Magnetoelectric(ME) composites and functional devices based on ME effect

Junqi Gao

Dissertation submitted to the faculty of the
Virginia Polytechnic Institute and State University
in partial fulfillment of the requirements for the degree of
Doctor of Philosophy
In
Materials Science and Engineering

Dwight D. Viehland (Chair)
Jiefang Li
David Clark
Guo-Quan Lu

May 06 2013
Blacksburg, Virginia

Keywords: Magnetoelectric, magnetic sensor, low noise circuit, noise modeling, geomagnetic field sensing, energy harvester

Magnetoelectric(ME) composites and functional devices based on ME effect

Junqi Gao

ABSTRACT

Magnetoelectric (ME) effect, a cross-coupling effect between magnetic and electric orders, has stimulated lots of investigations due to the potential for applications as multifunctional devices. In this thesis, I have investigated and optimized the ME effect in Metglas/piezo-fibers ME composites with a multi-push pull configuration. Moreover, I have also proposed several devices based on such composites.

In this thesis, several methods for ME composites optimization have been investigated. (i) the ME coefficients can be enhanced greatly by using single crystal fibers with high piezoelectric properties; (ii) the influence of volume ratio between Metglas and piezo-fibers on ME coefficients has been studied both experimentally and theoretically. Modulating the volume ratio can increase the ME coefficient greatly; and (iii) the annealing process can change the properties of Metglas, which can enhance the ME response as well. Moreover, one differential structure for ME composites has been proposed, which can reject the external vibration noise by a factor of 10 to 20 dB. This differential structure may allow for practical applications of such sensors in real-world environments.

Based on optimized ME composites, two types of AC magnetic sensor have been developed. The objective is to develop one alternative type of magnetic sensor with low noise, low cost and room-temperature operation; that makes the sensor competitive with the commercially available magnetic sensor, such as Fluxgate, GMR, SQUID, etc. Conventional passive sensors have been fully investigated, including the design of sensor working at specific frequency range, sensitivity, noise density characterization, etc. Furthermore, the extremely low frequency (< 10^{-3} Hz) magnetic sensor has undergone a redesign of the charge amplifier circuit. Additionally, the noise model has been established to simulate the noise density for this device which can predict the noise floor precisely. Based on theoretical noise analysis, the noise floor can be eliminated greatly. Moreover, another active magnetic senor based on nonlinear ME voltage coefficient is also developed. Such sensor is not required for external DC bias that can help the sensor for sensor arrays application.

Inspired by the bio-behaviors in nature, the geomagnetic sensor is designed for sensing geomagnetic fields; it is also potentially used for positioning systems based on the geomagnetic field. In this section, some works for DC sensor optimization have been performed, including the different piezo-fibers, driving frequency and magnetic flux concentration. Meanwhile, the lock-in circuit is designed for the magnetic sensor to replace of the commercial instruments. Finally, the man-portable multi-axial geomagnetic sensor has been developed which has the highest resolution of 10 nT for DC magnetic field. Based on the geomagnetic sensor, some demonstrations have been finished, such as orientation monitor, magnetic field mapping, and geomagnetic sensing.

Other devices have been also developed besides the magnetic sensor: (i) magnetic energy harvesters are developed under the resonant frequency condition. Especially, one 60 Hz magnetic harvester is designed which can harvester the magnetic energy source generated by instruments; and (ii) frequency multiplication tuned by geomagnetic field is investigated which potentially can be used for frequency multiplier or geomagnetic guidance devices.

To my parents, sister and wife

Acknowledgements

I would like to express my sincere gratitude to my advisor, Professor Dwight Viehland, for his support on my Ph.D study and research: for his patience, motivation, enthusiasm, and immense knowledge. His guidance helped me in all the time of research and writing of this thesis.

I have tremendous respect to Professor Dwight Viehland for his professional knowledge and passion for the research. I benefited a lot from his "Structure Properties Materials" class, the discussions about the project, the intelligent suggestions on my research, his patience on correcting my papers, and his valuable instruction on my presentation. His high enthusiasm and hard-work on research influenced me greatly and will be very helpful in my future career.

Equally important, Professor Jiefang Li has given me great help and guidance in almost all of the projects that I have worked during my Ph.D research. Professor Li gave me several suggestions on research ideas and experimental setup. She generously shared with me all her senior experience on sensor design and characterization without any reservations. I definitely would not be successful in many of my research without her help.

I would also like to thank my committee member Professor David Clark. I learned a lot on the knowledge of ceramic science from his "Advanced Physical Ceramics" class. Professor Clark gave me several professional instructions on presentations, and valuable training on research. I really appreciate his questions and comments on my Ph.D qualifier and preliminary exams.

My sincere thank also goes to Professor Guo-Quan Lu, who serves as my committee member for my defense. I benefited a lot from his "Advanced materials thermodynamics" class, especially the training about the proposal writing. I really appreciate the knowledge and skills obtained from Professor Lu.

I would like to thank Professor Shashank Priya. I benefited a lot from his "Energy Harvesting" class, especially the theoretical model and analysis on piezoelectric materials based vibration energy harvester. Dr. Priya also gave me significant guidance on my

project that is related to geomagnetic sensor design. I always acquired new knowledge each time I discussed with him.

I would like to thank Dr. Junyi Zhai and Dr. Zengping Xing. They have given me knowledge on the ME materials, measurement setup, and circuit design since I joined the research group. Their valuable experience made my research go much easier.

I would like to thank Dr. Davresh Hasanyan. He shared with me lots of hermetical models and calculations about the magnetoelectric effect, which gave me deep insight about the fundamental research on functional materials. His strong theory convinced my many ideas.

I would like to thank Dr. Yaodong Yang for his creative ideas on the optimizations and applications of ME composites. We collaborated together happily for lots of measurements.

I would like to thank Dr. Liangguo Shen for his great help on the lock-in circuit design that made my project run fast.

I would like to thank Dr. David Gray, David Berry for their great guidance and discussion on the experimental setup and magnetic sensor design.

I would like to thank Dr. Yaojin Wang, Menghui Li, and Ying Shen for great discussion on the ME materials and applications. We worked together to make great progress on the development of the ME sensor. It will always be good memory to work with you.

I would also like to thank Dr. Yan Li, Dr. Jianjun Yao, Dr. Wenwei Ge, Zhiguang Wang, Yanxi Li, and Chengtao Luo, members in Professor Dwight Viehland's group. They gave me a lot of knowledge on quite different research areas that extended my research experience widely.

Last, but most importantly, I wish to express my deepest appreciation to my family. I am eternally indebted to my parents, Zhenjin Gao and LiZhen Cao, for their endless support over the years. I would like to thank my sister, Yanqi Gao for her encouragement and help as it was most required. In particular, I would like to express my gratitude to my wife, Ying Shen. She gave me lots of support, help and encourage both in my Ph.D study and life.

Table of contents

ABSTRACT ..... **ii**

DEDICATION ..... **v**

ACKNOWLEDGEMENT ..... **vi**

TALBE OF CONTENTS ..... **viii**

LIST OF TABLE ..... **xi**

LIST OF FIGURES ..... **xii**

1. Introduction **1**

1.1 Development of Magnetoelectric effect 1

1.1.1 Magnetoelectric Materials 1

1.1.2 Workding mode of ME lamianted composites 11

1.2 Potential devices based on ME effect 18

1.2.1 Magnetic sensors 18

1.2.2 Energy harvesters 22

1.2.3 Other decices 24

1.3 Noise souruces and their elminations 26

1.3.1 External noise 26

1.3.2 Internal noise 29

1.4 Summary of this section 35

2. Purpose of thesis **36**

3.Magnetoelectric composites **41**

3.1 Metglas/Piezo-fbiers ME lamiantes composites 41

3.2 Improvement of ME coefficients 42

3.2.1 Compasrison of different piezo-fibers 42

3.2.2 Volume ratio effect 51
3.2.3 Heat treatments 64
3.3 Vibration noise rejection 67
3.4 Summary of this section 78
4. AC magnetic sensor 79
4.1 Introduction 79
4.2 Passive magnetic sensor unit 79
4.3 Extremely low frequency magnetic sensor 92
4.3.1 Charge amplifier circuit design 92
4.3.2 Charge noise model 98
4.3.3 ELF magnetic sensor optimization 105
4.4 Active magnetic sensor unit 122
4.4.1 Sensor design and characterization 122
4.4.2 Optimization of active magnetic sensor 134
4.5 Summary of this section 146
5. DC magnetic sensor 149
5.1 Introduction 149
5.2 Improvement of sensitivity 152
5.2.1 Different piezo-fibers 153
5.2.2 Magnetic flux concentration 159
5.3 Man portable magnetic sensor 166
5.3.1 Lock-in detection circuit 166
5.3.2 Sensor performances 171
5.4 Geomagnetic field detection 175
5.4.1 2-axial magnetic sensor 176
5.4.2 3-axial magnetic sensor 178
5.4.3 Mobile magnetic sensor unit 180
5.4.4 Demonstrations for geomagnetic field sensor 182
5.5 Summary of this section 188

6. Other devices based on ME effect 189

6.1 Introduction 189

6.2 Bi-layered ME composites 190

6.2.1 Design of bi-layered ME composites 191

6.2.2 Tunability of resonant frequency 199

6.3 Energy harvester 206

6.3.1 Multi-push pull ME harvester 206

6.3.2 Bi-layered ME harvester 210

6.4 Frequency multiplier 214

6.5 Summary of this section 224

LIST OF TABLES

Table 1.1 ME coefficients for different ME composites 10

Table 3.1 Piezoelectric properties of some materials 43

Table 3.2 Materials parameters for ME coefficients calculation 60

Table 4.1 ME composites properties 99

Table 4.2 Circuit components used for charge amplifier 99

Table 4.3 Comparisons of op-amp chips 112

Table 4.4 Components used for circuit design 113

Table 5.1 Critical piezoelectric properties for PZT and PMN-PT fibers 153

Table 5.2 Geomagnetic field measurements at two positions by using 3-axial sensor ... 178

Table 5.3 Geomagnetic field intensity along North direction 178

Table 5.4 Geomagnetic field intensity along Vertical direction 178

Table 5.5 Inclination Angle 178

Table 6.1 Materials parameters for Metglas, PZT used for theoretical modeling 204

Table 6.2 Geomagnetic field intensity of Virginia Tech area 219

LIST OF FIGURES

Figure 1.1 Schematic illuminations of idea ME coupling effect in multiferroic materials 2

Figure 1.2 Schematic illustrations of bulk composites with three common connectivity schemes: (a) 0-3 particulate composite, (b) 2-2 laminate composites, and (c) 1-3 fiber/rode composites. 6

Figure 1.3 Transverse and longitudinal ME voltage coefficients as function of dc magnetic field at 100 Hz for Zn-doped NFO and PZT multilayer structure. .. 7

Figure 1.4 (a) An optical and (b) scanning electron micrograph of the fractured surface of the sandwiched PZT/NFO/PZT ceramics. 8

Figure 1.5 Schematic illustration of the various ME coupling modes: (a) L-L; (b) T-L; (c) L-T; and (d) T-T. 12

Figure 1.6 Schematic of push-pull mode. 14

Figure 1.7 Schematic illustration of multi-push pull configuration. 15

Figure 1.8 Self biased Ni/Metglas/PZT ME composites: (a) Metglas/Ni/PZT configuration, (b) Ni/Metglas/PZT configuration; and (c) Magnetostriction coefficients for Ni, KNNLS-NZF, and KNNLS-NZF/Ni/KNNLS-NZF. 17

Figure 1.9 (a) Photograph of the prototype ME detection system. A: batteries (below the PCB board); B: optimized dc magnetic bias (NbFeB); C: Teflon tube (ME sensor is held inside); D: aluminum box; E: low noise charge amplifier; F: output jack; G: power switch; and (b) response of detection unit to small AC magnetic field at 1 Hz. 19

Figure 1.10 (a) Schematic illustration of DC magnetic sensor; (b) Photo of geomagnetic field detection; and (c) Output signals along different directions in Earth plain. 21

Figure 1.11 (a) Multimodal energy harvester; and (b) Vibration energy harvester prototype. 23

Figure 1.12 (a) Equivalent circuit of gyrator; (b) ME gyrator design; (c) Inductor converted to inductor; and (d) resistor to resistor with inverse resistance 25

Figure 1.13 (a) Schematic illustration of symmetrical structure design; and (b) comparison of output signals under thermal fluctuations in time domain 28

Figure 1.14 (a) Voltage noise model; and (b) current noise model. 31

Figure 1.15 (a) Equivalent noise model for magnetic sensor; and (b) Output noise level of circuit and sensor unit. 34

Figure 3.1 The ME voltage coefficient α_{ME} as a function of the static magnetic field H_{dc} for Metglas-PZT, Metglas-PMN-PT, and Metglas-PZN-PT laminate composites, as indicated. Inset shows a representative picture of a laminate composite. 45

Figure 3.2 (a) Picture of our low noise circuit along with the ME sensor in a box. The ME output voltage as a function of time for the (b) PZT, (c) PMN-PT and (d) PZN-PT based sensors, respectively. The corresponding field sensitivities are as indicated. (e) Noise level for various detection units. 48

Figure 3.3 Noise spectra for the PZT, PMN-PT, and PZN-PT laminates with wide band circuit. Inset shows the wide band circuitry response as the function of the frequency. 50

Figure 3.4 (a) Schematic diagram of ME composites configuration consisting of an ID electrodes, core composite and symmetric Metglas actuators on the bottom and top of the core composite. (b) Illustration of the numerous alternating push-pull mode units. (c) Optical microscopy image of a longitudinally poled push-pull element in the core composite. (d) and (e) Photographs of ME composites. 52

Figure 3.5 2-D ID electrode schematic showing the electric field lines. 54

Figure 3.6 Schematic of L-L model. 55

Figure 3.7 Magneto-electric voltage coefficients α_V as a function of the static dc magnetic field H_{dc} for various PZT fiber-Metglas laminate composites. The inset shows a schematic of the structure. 59

Figure 3.8 Comparison of experimental data and estimated values. 61

Figure 3.9 (a) Lowest detectable magnetic field for the PZT fiber-metglas laminate composites as a function of the number of metglas layers N on either side of PZT at 1 Hz for constant signal-to-noise ratio SNR > 2. (b)-(f) Output voltage waveforms for the laminates with different metglas layers N in the time domain. (g) Example voltage noise level for the low noise charge amplifier as a function of time. 63

Figure 3.10 ME voltage coefficient a as a function of the static dc magnetic field H_{dc} for various PZT fiber-Metglas laminate composites after heat treated with Metglas layer. 65

Figure 3.11 Comparison of AC magnetic sensitivity for the PZT fiber/Metglas laminated composites as a function of the different annealed temperature of Metglas layer. 66

Figure 3.12 (a) Schematic of our new differential mode ME laminate sensor; (b) poling profile of multi-push/pull, dual PZT composite structure; and (c) schematic of the experimental signal path. 70

Figure 3.13 (a) Time-domain equivalent magnetic response of differential mode sensor to incident vibrational signal; (b) power spectral density of top, bottom and time-domain summation of top and bottom; and (c) phase shift between top and bottom PZT layers as a function of frequency calculated from a linear time invariant transfer function. 73

Figure 3.14 (a) Time-domain response of top PZT layer, bottom and sum of individual signals in response to an incident magnetic field; and (b) power spectral density response of a sensor to a 10 Hz magnetic field..... 75

Figure 3.15 Comparison of noise cancellation for a differential ME structure sensor and a non-differential ME structure sensor..... 77

Figure 4.1 (a) Schematic illustrations of Metglas/PMN-PT ME composites; and (b) ME voltage coefficient α_{ME} and ME charge coefficient α_{me} for Metglas/PMN-PT laminates as function of H_{dc}. 81

Figure 4.2 Transfer function of detection circuit. 83

Figure 4.3 Equivalent magnetic noise density spectra: (a) Voltage noise density detected by dynamic signal analyzer; and (b) equivalent magnetic noise density after conversion. 84

Figure 4.4 Transfer function of low frequency detection circuit. 87

Figure 4.5 Output signal in response to the incident magnetic field: (a) low frequency detection sensor circuit, and (b) wide band frequency detection sensor unit. 88

Figure 4.6 Linearity of magnetic sensor assembled with low frequency circuit. 90

Figure 4.7 Equivalent magnetic noise spectra. 91

Figure 4.8 (a) Charge amplifier design for quasi-static magnetic sensor, and (b) predicted and measured transfer functions of the circuit. 94

Figure 4.9 ME charge coefficients at quasi-static frequency range. The insert is the output voltage of circuit in response to a 10 mHz input charge. 97

Figure 4.10 Estimated and measured equivalent magnetic noise of the magnetic sensor based on previous noise model..... 100

Figure 4.11 (a) Theoretical model for noise sources in our ME magnetic sensor; and (b) estimated and measured equivalent magnetic noise of the sensor. 104

Figure 4.12 (a) Transfer function of two sensors, and (b) coherency between two sensors. 106

Figure 4.13 Comparisons of equivalent magnetic noise with and without high vacuum conditions. 108

Figure 4.14 Comparison of equivalent magnetic noise spectra at normal and high vacuum conditions for ELF magnetic sensors. 110

Figure 4.15 Estimated and measured equivalent magnetic noise of the ELF magnetic sensor based on Metglas/PMN-PT ME composites. The insert is a schematic illustration of the ME composites. 111

Figure 4.16 (a) Calculated voltage noise densities for LMC6042 and LMC6442 operational amplifiers, and (b) comparisons of calculated magnetic noise spectra for magnetic sensors based on optimized and previously reported detection circuits. 114

Figure 4.17 (a) Predicted and measured transfer functions of the new detection circuit; and (b) estimated and measured equivalent magnetic noise floors of an optimized magnetic sensor. 116

Figure 4.18 Transfer functions of the 0.001 Hz detection circuit. 118

Figure 4.19 (a) Waveform of magnetic sensor in time domain, and (b) magnetic power spectra of magnetic sensor. The red dash line indicates the theoretical prediction result. 121

Figure 4.20 Modulation process of active mode ME sensor. 124

Figure 4.21 (a) Schematic of our custom-built lock-in circuit; and (b) photo of a lock-in circuit. 127

Figure 4.22 (a) Experimental setup for the active sensor test; and (b) H-coils calibration results at 1 Hz and 7.875 mHz 131

Figure 4.23 (a) Output signal from active sensor as function of incident magnetic field; and (b) sensitivity of sensor as frequency range from 7.8125 mHz to 1 Hz. 132

Figure 4.24 Equivalent magnetic noise density spectra of active magnetic sensor. 133

Figure 4.25 Equivalent magnetic noise density spectra of active magnetic sensor. 135

Figure 4.26 (a) Sensitivity of modulated sensor as frequency range from 6 mHz to 200 Hz; and (b) equivalent magnetic noise density spectra of active magnetic sensor. 136

Figure 4.27 (a) Sensitivity of modulated sensor as frequency range from 6 mHz to 200 Hz; and (b) equivalent magnetic noise density spectra of active magnetic sensor. 138

Figure 4.28 (a) Induced output signals in response to the incident magnetic field; and (b) noise spectra of the sensor at various driving signals, respectively. 140

Figure 4.29 Equivalent magnetic noise density spectra for the sensors under different driving signals. 141

Figure 4.30 Sensitivity, voltage noise density and equivalent magnetic noise density at 1Hz for active sensor as function of driving signals. 143

Figure 4.31 (a) Local geomagnetic field noise measurements along different directions; and (b) comparisons of noise spectra measured by active sensor and fluxgate. The insert of the figure indicates the experimental setup. 145

Figure 5.1 Geomagnetic sensing by sea turtles. 151

Figure 5.2 α_{ME}-H_{dc} for Metglas/PZT composites. 152

Figure 5.3 ME voltage coefficient of Metglas/PZT and Metglas/PMN-PT laminates: (a) α_{ME} as the function of dc bias H_{dc} at f = 1 kHz, and (b) α_{ME} as a function of ac magnetic drive frequency. 154

Figure 5.4 DC magnetic field sensitivities for (a) PZT based; (b) PMN-PT based composites. 156

Figure 5.5 Sensitivity of MEtglas/PMN-PT laminate to small DC magnetic field changes at ac drive field of H_{ac} = 0.1 Oe at the resonant frequency. 158

Figure 5.6 (a) Schematic representation of 3-D Mangetostatic model layout including large, permanent magnetic HDC bias generators, and (b) vector map of the y-z (axial-height) component of the H field in the presence of the high-mu Metglas. Insert: non-ideal B-H relationship used to define magnetostatic behavior of high mu Metglas in FEM. 160

Figure 5.7 (a) In-plane magnetic field strength along centerplane of Metglas foils in response to arbitrarily low DC bias field, as simulated by Maxwell 3D, and (b) line scan traces of magnetic flux density along the axially centerline of Metglas foils for 80mm and 100mm geometries. 162

Figure 5.8 ME voltage coefficient of laminate sensor with different Metglas lengths as a function of DC bias H_{dc} in response to a 1Oe, 1 kHz AC magnetic excitation. 164

Figure 5.9 Comparison of the sensitivity for Metglas/PZT laminates to small DC magnetic field changes under AC drive conditions of at f =1 kHz and H_{ac}=0.1

Oe: (a) ME sensor with 8 cm long Metlgas, and (b) ME sensor with 10 cm long Metglas. 165

Figure 5.10 (a) Schematic of our custom-built lock-in circuit; (b) photo of a prototype lock-in circuit. 167

Figure 5.11 Waveforms of driving signal generated by oscillator in time domain: (a) 1 kHz; and (b) 32.7 kHz. 169

Figure 5.12 Sensitivity of composites to small DC magnetic field changes under AC driving conditions at f=1 kHz and H_{ac}=0.1 Oe generated by (a) lock-in amplifier (SR-850); and (b) lock-in circuit. 170

Figure 5.13 Illustration of capability of our DC magnetometer to localize a magnetic dipole: (a) schematic of experimental setup, (b) magnetic flux distribution of the magnetic dipole, and (c) position measurement. 173

Figure 5.14 Real space DC magnetic field test: (a) photo of test location, and (b) output signal from DC magnetometer over spatial grid about test location. 174

Figure 5.15 Multi-axial detection magnetic sensor: (a) 2-axis; and (b) 3-axis. 175

Figure 5.16 (a) Experimental setup for 2-axial geomagnetic sensor; and (b) orientation determined based on geomagnetic field. 177

Figure 5.17 Geomagnetic field measurements around Blacksburg area. The insert shows the 3-axial magnetic sensor used in the test. 179

Figure 5.18 (a) Rigid package for 3-axial magnetic senor; and (b) characterization of sensitivity for each axis sensor. 181

Figure 5.19 (a) Labview program for rotation monitor; and (b) experimental setup for monitoring the orientation in 3-D space. 183

Figure 5.20 (a) magnetic field mapping demonstration performed at parking lot; and (b)-(d) magnetic field mapping results measured by the sensors. 185

Figure 5.21 (a) Geomagnetic field sensing in open environment; and (b) magnetic fields for the process. 187

Figure 6.1 Schematics of Metglas/PZT ME laminate sensors: (a) L-L mode sensor, and (b) bending mode. 192

Figure 6.2 ME voltage coefficients of L-L and bending mode ME laminates: (a) α_{ME} as a function of dc magnetic bias H_{dc} at f = 1 kHz, and (b) α_{ME} as a function of ac magnetic drive frequency. The insert shows α_{ME} for the L-L mode for $10^3 < f < 10^5$ Hz. 194

Figure 6.3 (a) Noise levels for the L-L and bending mode sensors; and (b) ME output voltage as a function of time for the L-L and bending mode sensors. The corresponding peak-to-peak ac field sensitivities are listed. 196

Figure 6.4 Equivalent magnetic noise spectra for the L-L and bending mode sensors for $10^2 < f < 10^3$ Hz. 198

Figure 6.5 (a) Impedance spectra of Metglass/PZT bending laminates with various tip masses; and (b) ME voltage coefficients for Metglas/PZT laminates as a function of frequency with various tip masses. The insert is a schematic of the bending mode laminates. 201

Figure 6.6 (a) Theoretical model for magnetoelectric bi-layer laminates, and (b) estimated ME voltage coefficients as a function of frequency. 205

Figure 6.7 Output voltage and power as a function of load resistance load for Metglas/PMN-PT laminates at the resonance frequency. 207

Figure 6.8 Illustration of ability to charge batteries of ME detection units by magnetic energy harvesting: (a) experimental setup, and (b) testing results. 209

Figure 6.9 (a) ME voltage coefficient of 60 Hz magnetic energy harvester as a function of AC magnetic drive frequency; and (b) output voltage and power as a function of resistance load at the bending mode resonance frequency..... 211

Figure 6.10 Demonstration of ability to capture 60 Hz electromagnetic energy by using ME magnetic harvester: (a) photo of experimental setup, and (b) output voltage signal in the time domain..... 213

Figure 6.11 (a) Waveforms of driving ac magnetic field and output signal in time domain; and (b) induced frequency doubling signal as a function of dc magnetic bias H_{dc}. The insert shows schematic of frequency multiplier based on Metglas/PZT ME composites. 216

Figure 6.12 Waveforms of driving ac magnetic field and output signal in the time domain at various frequencies: (a) 100 Hz, (b) 1 kHz, and (c) 2 kHz. 218

Figure 6.13 (a) Schematics of frequency multiplier under geomagnetic field; the ratio of the induced second to first harmonic signals V_{2f}/V_f along various directions: (b) in horizontal plane, and (c) in vertical plane. The inserts show the waveforms in the time domain. 221

Figure 6.14 Magnetostriction and effective linear piezomagnetic coefficient for the Metglas/PZT ME composites. 223

1. Introduction

1.1 Development of Magnetoelectric effect

1.1.1 Magnetoelectric Materials

Magnetoelectric (ME) effect is characterized by electric polarization changes in response to an applied magnetic field (H), or conversely, a magnetization changes with an applied electric field (E).[1-3] The direct ME coupling effect of the materials can be characterized by a parameter designed as ME voltage coefficient α_{ME}, which is described by the induced electric field (δE) by an applied magnetic field (δH):

$$\alpha_{ME} = \delta E / \delta H = \delta V / (t \delta H) \quad (1.1)$$

where δV is induced voltage as applied magnetic field, t is the thickness. On the other hand, the converse ME coupling effect is defined as induced magnetic field by an applied electric field.[4] Figure 1.1 shows the idea ME coupling effect in multiferroic materials. Ideally, electric (magnetic) polarization would show the hysteresis response to applied magnetic (electric) field.[5] Based on strong ME coupling effect, some novel multifunctional devices can be developed.

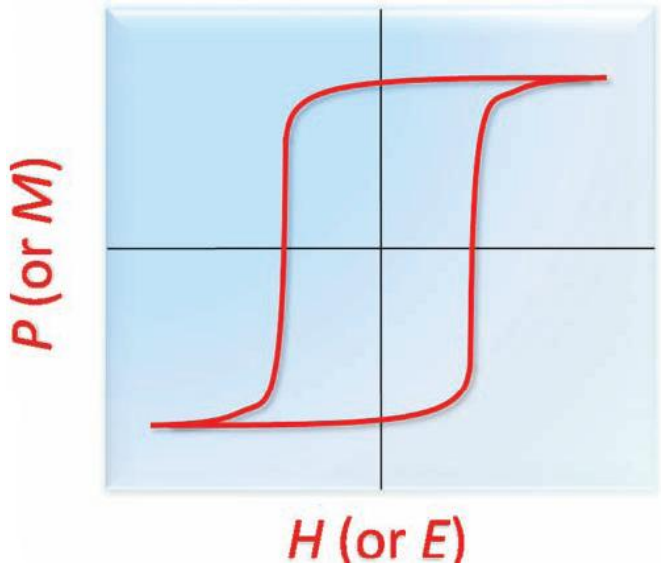

Figure 1.1 Schematic illuminations of idea ME coupling effect in multi-ferroic materials

The concept of magnetoelectric effect can be traced back to predictions based on crystal symmetry theory by Curie in 1894.[6] However, over half of century passed, and only was, the electrically induced and magnetically induced ME effects observed in anti-ferromagnetic single phase crystal of Cr_2O_3 by G.N.Astrov and G.T.Rado in 1960 and 1961,[7, 8] respectively. These works confirmed the reality of ME effect experimentally, which were the milestones in the research of ME effect. Later, more single phase ME materials were reported.

However, the ME voltage coefficients for single phase materials are not high: the values of α_{ME} for these materials are on the order of several mV/cm-Oe. For example, the ME voltage coefficient is only about 20 mV/cm-Oe in Cr_2O_3 single crystal. The basic problem in single phase materials is that the electronic configurations which favor magnetization are antagonistic to those that favor polarization. This problem makes the ME coupling effect is either weak or occurred at low temperature, in which case, makes it hard for single phase materials to be useful for devices in practical applications.

Obviously, it is necessary to explore possible composites when the reasonable ME effect could not be obtained or optimized in single phase materials. In 1972, van Suchtelen first proposed the concept of ME effect in ceramic composites. The composite materials contain one magnetostrictive phase and piezoelectric phase, achieving ME coupling effect via elastic interaction. The following expressions show the process of how to obtain direct or converse ME effect:[9]

$$\begin{aligned} ME_H\ \text{effect} &= \frac{\text{magnetic}}{\text{mechanical}} \times \frac{\text{mechanical}}{\text{electric}}, \\ ME_E\ \text{effect} &= \frac{\text{electric}}{\text{mechanical}} \times \frac{\text{mechanical}}{\text{magnetic}}. \end{aligned} \tag{1.2}$$

According to this design, some ME ceramic composites were first reported by the Philips Research Lab.[10] For example, they studied ME composites using $BaTiO_3$ as the piezoelectric phase and $Ni(Co,Mn)Fe_2O_4$, as piezomagnetic phase in 1978. In their study, the ME voltage coefficient for this composites was up to 80 mV/cm-Oe. Although it did not get the remarkable values (> 1V/cm-Oe) as expected, it did prove the design concept and possibility of obtaining higher ME coefficients. In the 1990s, several theoretical work on ME ceramics were developed to understand the coupling effect between two phases, and to predict the ME coefficient in ceramic composites. However, a rare giant ME coupling effect was reported experimentally at that time. Meanwhile, some groups prepared particulate ceramic composites by conventional processing. This method is much easier and cost effective. There are several challenges that limited the property of ME composites: (i) chemical reactions between the constituent phases or during sintering; (ii) non-ideal interfacial boundary makes the stress transfer inefficient, (iii) much smaller resistivity of the magnetostrictive phase compared to that of piezoelectric phase results in poor polarization of the piezoelectric phase and discharge as applied magnetic field; and (iv) non-optimum alignment of the magnetization of the magnetostrictive phase on applying DC bias.

Since 2000, ME laminated composites consisting of magnetostrictive and piezoelectric phases were reported to have giant ME voltage coefficients. The values

of α_{ME} for these laminated composites were enhanced by over 500× compared to other ME materials.[11-13] In detail, laminated composites are designed with "2-2" connectivity schemes, as shown in Figure 1-2.[9] The biggest advantage of 2-2 connectivity is that the leakage problem due to high concentration of the ferrite phase with low resistivity in the particulate composites can be reduced. So, 2-2 connectivity can improve the poling condition of a piezoelectric layer resulting in enhancement of the ME effect.

Laminated composites have been constructed by co-sintering or mechanical epoxy bonding methods.[13-16] Co-sintered ME laminated composites have been made from perovskite ferroelectric and ferrite magnetostrictive ceramics. For example, bi-layer or multi-layer Pb(Zr, Ti)O_3 (PZT) and $NiFe_2O_4$(NFO) and so on. Another characteristic for laminated composites is the anisotropic response to external magnetic bias.[14] Figure 1.3 shows the dc magnetic field dependent ME coefficient for NZFO and PZT composites. The ME voltage coefficients for transverse mode is around 400 mV/cm-Oe, while the value for longitudinal mode is less than 100 V/cm-Oe.

Although the co-sintering method is easy to perform, there are several limitations that influence the property of composites: (i) chemical reaction at higher sintering temperature; (ii) non-idea interfacial boundary between two phases, like porous in ceramics, as shown in Figure 1.4;[17] and (iii) limited materials selection.[18, 19] The first two reasons make the ME coefficients for laminated composites fabricated by co-sintering exhibit smaller values than the value predicted by model works.

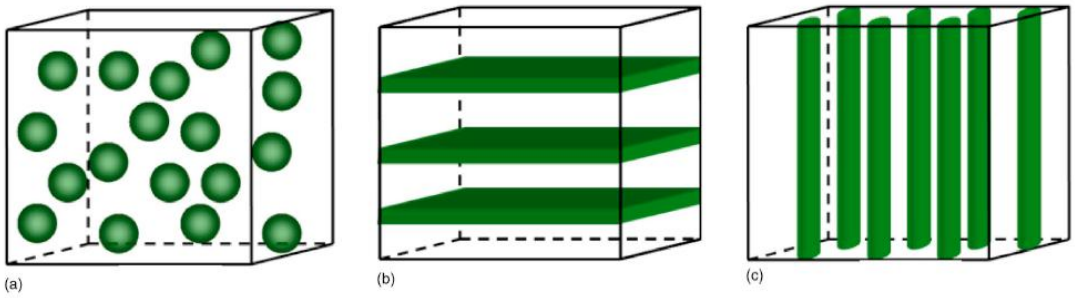

Figure 1.2 Schematic illustrations of bulk composites with three common connectivity schemes: (a) 0-3 particulate composite, (b) 2-2 laminate composites, and (c) 1-3 fiber/rode composites.

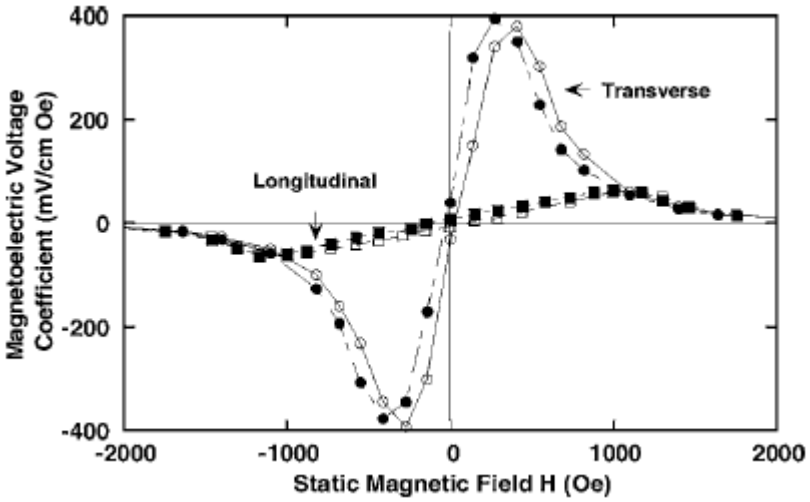

Figure 1.3 Transverse and longitudinal ME voltage coefficients as function of dc magnetic field at 100 Hz for Zn-doped NFO and PZT multilayer structure.

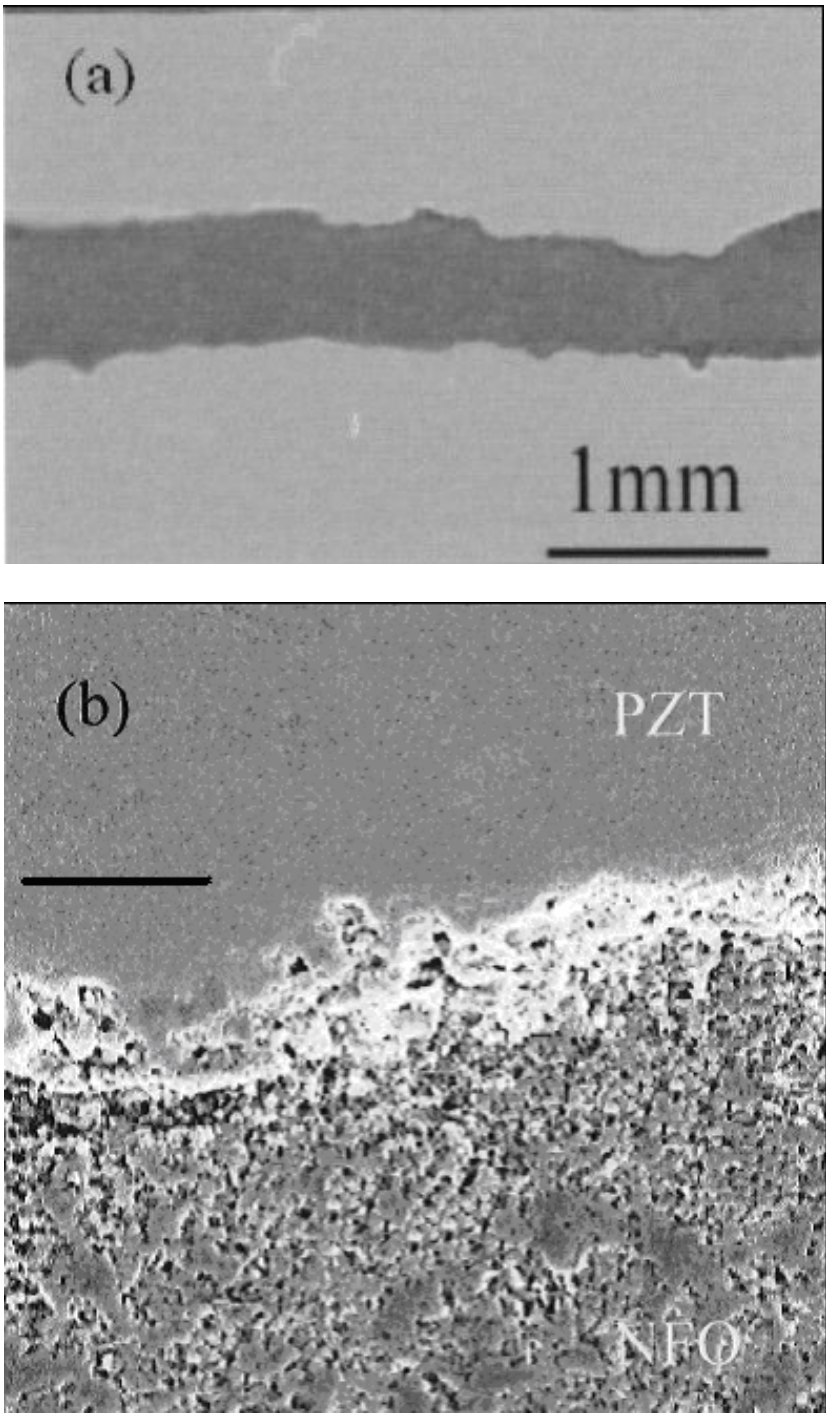

Figure 1.4 (a) An optical and (b) scanning electron micrograph of the fractured surface of the sandwiched PZT/NFO/PZT ceramics.

On the other hand, an epoxy bonding method is much more suitable for magnetic alloy and piezoelectric ceramic based ME laminated composites. By this method, materials with completely different properties can be bonded together mechanically,[20, 21] such as the PZT/ Terfenol-D alloy. Terfenol-D is a magnetostrictive alloy with extremely high magnetostriction coefficients that could enable the achievement of further enhancement in ME coefficients. However, it is impossible to form composites by using the co-sintering method: the high sintering temperature for PZT would oxidize Terfenol-D. Epoxy bonding can solve this problem easily without high temperature sintering. Dong *et al*. have reported that the giant ME coefficient in PZT/Terfenol-D laminated composites.[22] The value of α_{ME} can reach as high as 4.6 V/cm-Oe at quasi-static frequency and up to 40 V/cm-Oe at the electromechanical resonance drive conditions: this value is one order higher than the value of ferrite/PZT system. More investigations on magnetic alloys and ceramic systems have been developed, such as Fe-Ga alloy, Galfenol or Metglas and PZT, PMN-PT or PVDF layers. Table 1.1 list the ME coefficients for some ME composites.

Table 1.1 ME coefficients for different ME composites

ME composites	*ME coefficient (mV/cm-Oe)*	*Ref.*
Ceramic Composites:		
(0-3)NZFO/PZT	155@1kHz	Ref.[23]
(2-2) NCZF/PZT/NCZF	782@1kHz	Ref.[24]
Ceramic-Alloy Composites		
(2-2) Terfenol-D/PMN-PT	10.3×10^3@1kHz	Ref.[25]
(2-2) Terfenol-D/PVDF	1.43×10^3	Ref.[26]
(2-2) Metglas/PZT	22×10^3	Ref.[27]

1.1.2 Working mode of ME laminated composites

Besides the numerous types of materials that have been studied for enhanced ME effects, several investigations have focused on the geometry and the polarization or magnetization direction with respect to long axis of the laminated composites. The results show that different ways to bond the composites can generate significant different ME coefficients and optimum DC bias, even for the same phases. Basically, there are four operation modes according to the poling or magnetization directions with respect to long axis.[28]

Figure 1.5 shows four basic types of operation modes. These are the longitudinally magnetized and longitudinally poled (L-L) mode, the transversely magnetized and longitudinally poled (T-L) mode, the longitudinally magnetized and transversely poled (L-T) mode, and the transversely magnetized and transversely poled (T-T) mode.

As mentioned above, different operation modes can affect the ME response dramatically. Generally, the L-L mode normally shows the largest ME voltage coefficient among these four operation modes according to the experimental results. To explain it easily, we can say that the L-L mode uses the d_{33} of the piezoelectric phase while others operate using d_{31}. For typical piezoelectric ceramics, the value of d_{33} is larger than d_{31}. Take PZT-5, one of the commercially available piezoelectric phases, for example: d_{33} is 400 pC/N while d_{31} is just -175 pC/N.

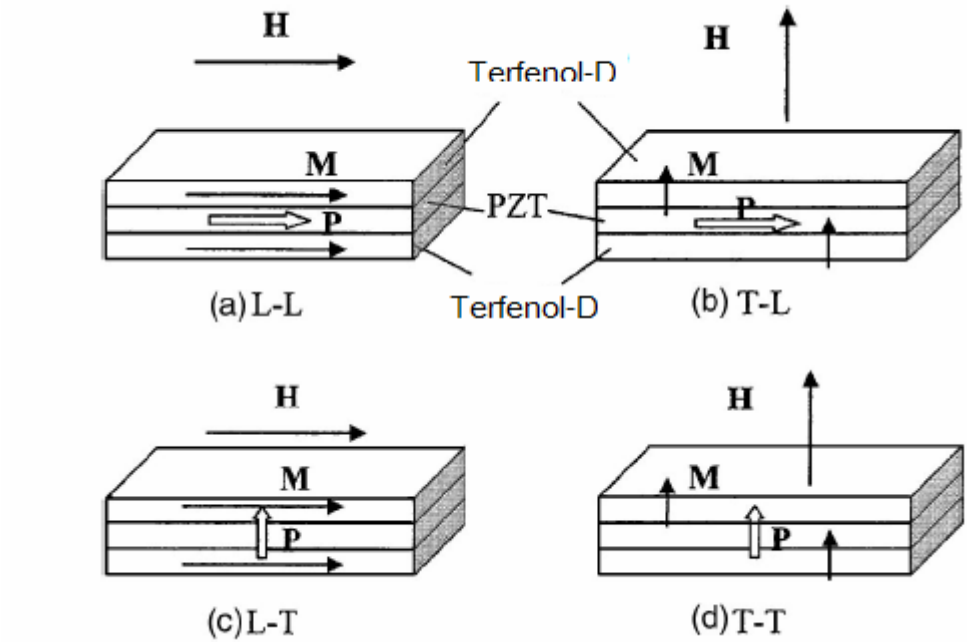

Figure 1.5 Schematic illustration of the various ME coupling modes: (a) L-L; (b) T-L; (c) L-T; and (d) T-T.

However, there are several limitations for this operation mode: (i) a high poling voltage. Due to the geometry of laminates (Length (l) >width (w)> thickness (t)), much higher poling voltage is required for L-L mode than that needed for L-T, T-T mode; (ii) a low capacitance, that makes the composites be affected by the stray capacitance of the measurement system, and low charge output. In order to solve these problems, the L-L push-pull mode was proposed, as shown in Figure 1.6.[16] Compared to traditional L-L mode, push-pull mode can enhance the capacitance by 4× with the same dimensions. Meanwhile, it decreased the poling voltage.

Interestingly, Dong *et al*. proposed a multi-push pull structure for Metglas/PZT laminated composites.[27] Figure 1.7 shows the structure of this design: PZT fibers of 100 um in thickness were oriented along their long axis to form a piezoelectric layer. Two interdigitated Kapton®-based electrodes were then bonded to the top and bottom surfaces of the piezoelectric layer. Metglas foils were then laminated to both the top and bottom surfaces of the PZT composite cores. In fact, we can separate this configuration into numerous small units, as shown in insert of Figure 1.7. Each unit can be taken as a "push-pull" mode. Due to the thickness of Metglas foils is very thin, the thin piezo-fiber used for this system is required to reach high ME voltage coefficient, such as 100 um in this case. This structure can enhance the capacitance dramatically, which is quite valuable for Metglas alloy based ME laminated composites.

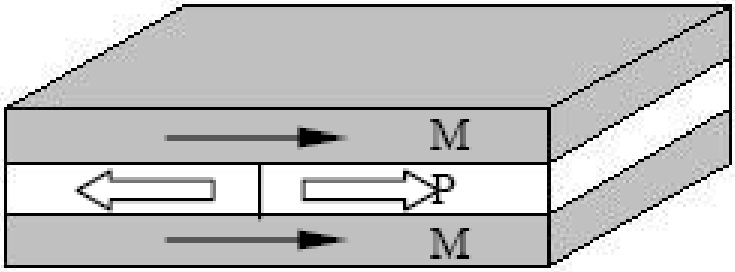

Figure 1.6 Schematic of push-pull mode.

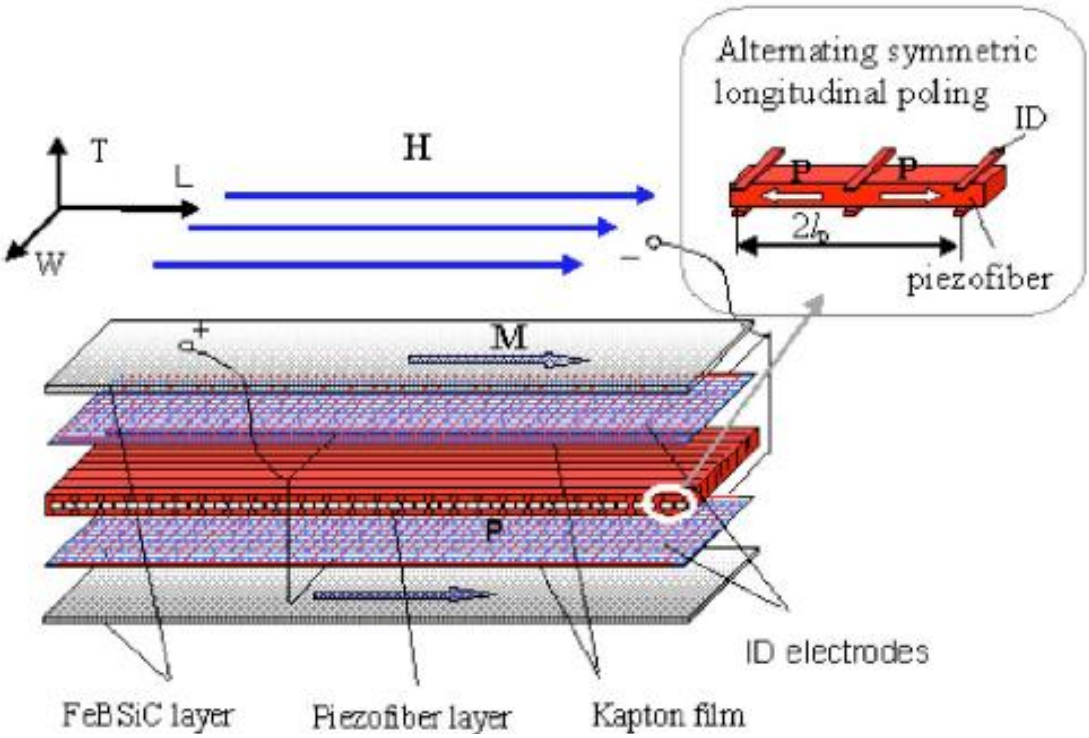

Figure 1.7 Schematic illustration of multi-push pull configuration.

Besides these typical symmetrical modes, there are also many asymmetric designs, such as the bi-layer bending structure.[29-32] Moreover, recently, graded magnetization ME composites have been proposed which show a non-zero ME coefficients at zero bias, as illustrated in Figure 1.8 (a) and (b).[33] Interestingly, the ME voltage can be tuned by changing the arrangement of magnetostrictive layers. The origin for a self bias effect comes from the different magnetic properties of two piezomagnetic phases and the strain-mediated coupling between them. One direct observation for KNNLS-NZF/Ni/KNNLS-NZF composites is present in Figure 1.8 (c).[34] From this figure, one can see, compared to pure Ni or KNNLS-NZF individually, the magnetostriction coefficient curve for combination of KNNLS-NZF and Ni was shifted to the left resulting in the remaining strain at zero dc magnetic bias. This shift could be the reason for the non-zero ME effect at zero magnetic field.

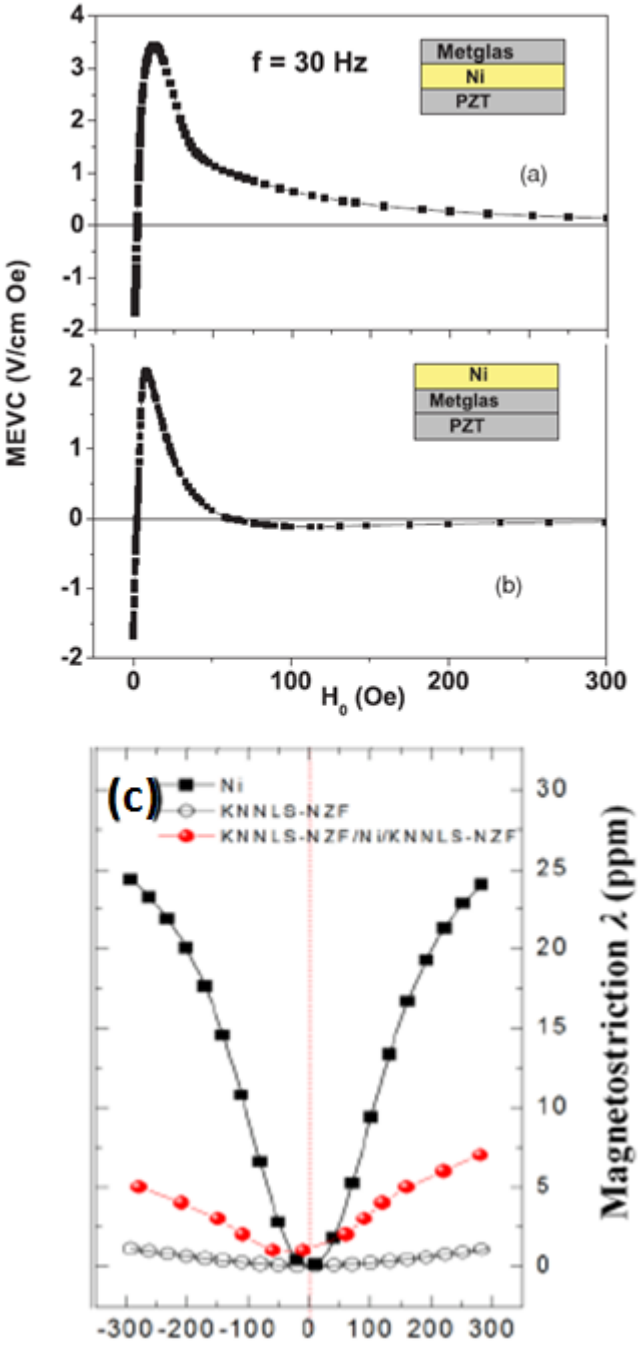

Figure 1.8 Self biased Ni/Metglas/PZT ME composites: (a) Metglas/Ni/PZT configuration, (b) Ni/Metglas/PZT configuration; and (c) Magnetostriction coefficients for Ni, KNNLS-NZF, and KNNLS-NZF/Ni/KNNLS-NZF.

1.2 Potential devices based on ME effect

Giant ME coupling effects in laminated composites gives the material the potential for applications as multifunctional devices, such as sensors,[35, 36] memory devices,[37, 38]energy harvesters,[39, 40] transducer[41] and so on.

1.2.1 Magnetic Sensors

There are some commercially available magnetic sensors in the market: giant magneto-resistive (GMR), flux-gate, and superconducting quantum interference devices (SQUID). They have low noise floors in the order of $10^{-10}\ T/\sqrt{Hz}$, $10^{-12}\ T/\sqrt{Hz}$ and $10^{-14}\ T/\sqrt{Hz}$ respectively, in the frequency range of $1<f<10^3$ Hz.[42-44] However, there are some limitations to these conventional magnetic sensors in applications. For example, SQUIDs require extremely low operational temperatures, fluxgates have magnetic hysteresis and offset values under zero magnetic fields, and both fluxgate and GMRs require considerable power. So, one novel AC magnetic sensor is highly desired to satisfy the following requirements: (i) high sensitivity or low noise at static frequency range (~pT/√Hz at 1 Hz); (ii) low power: long-term operation; (iii) compact size; and (iv) low cost.

Xing et al. designed one passive AC magnetic sensor based on charge amplifier circuit. Based on Terfenoal-D/PZT composites with L-T mode, the sensitivity of 2.6 nT at 1 Hz can be measured, as shown in Figure 1.9.[45] Later, using push-pull mode, Zhai *et al* have proposed one passive AC magnetic sensor with much lower noise density (20 *p*T/√Hz @ 1 Hz) at room temperature.[46]

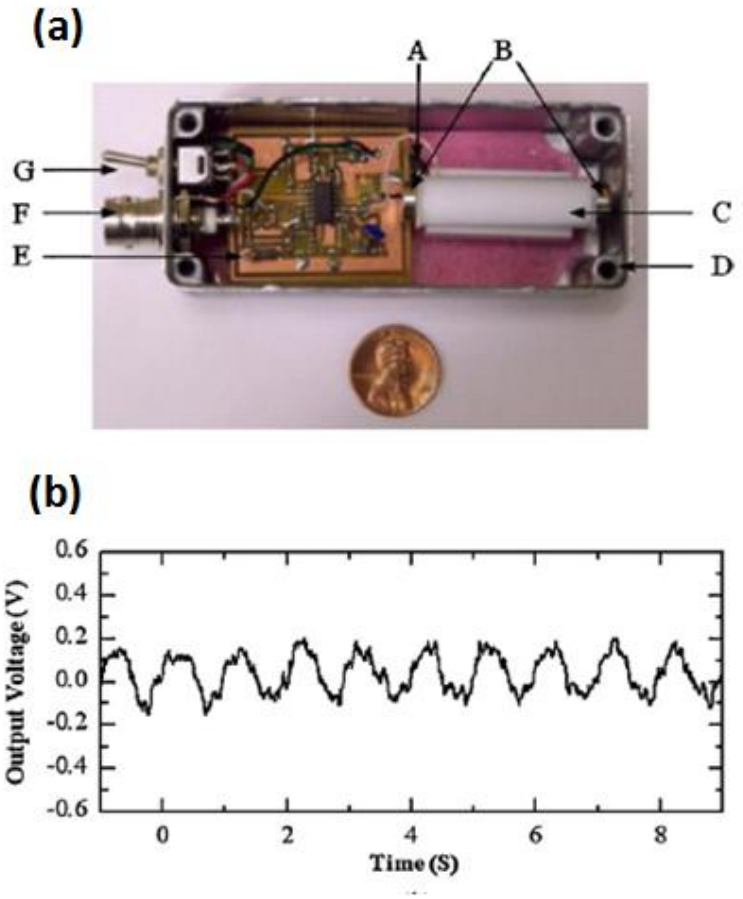

Figure 1.9 (a) Photograph of the prototype ME detection system. A: batteries (below the PCB board); B: optimized dc magnetic bias (NbFeB); C: Teflon tube (ME sensor is held inside); D: aluminum box; E: low noise charge amplifier; F: output jack; G: power switch; and (b) response of detection unit to small AC magnetic field at 1 Hz.

However, there are still researches needed to further improve the AC magnetic sensor: (i) increase the sensitivity; (ii) decrease the equivalent magnetic noise at the quasi-static frequency range; (iii) external noise rejection; and (iv) small package.

Besides AC magnetic sensors, an active DC magnetic sensor was also developed. In this measurement, Dong *et al*. developed a lock-in amplifier method to drive the ME composites, as shown in Figure 1.10.[47] A small AC current was generated from a lock-in amplifier to directly excite the driving coils wrapped around the composites. The incident magnetic field was applied along a long axial direction. Based on the ME effect, the composites can convert the small DC magnetic field to an electric signal monitored by a lock-in amplifier as well. By this method, the small DC magnetic field variations as small as 10 nT can be detected using Terfenol-D/PZT composites driving at frequency of 84 kHz and H_{ac} = 71 mOe. Moreover, Zhai *et al*. used the similar method to design one geomagnetic detection sensor based on Metglas/PZT laminated composites.[35] Figure 1.10 (b) shows the experimental setup: the sensor was placed on the inside of the globe which can rotate along three different directions. Thus, the geomagnetic intensity along the north-south axis, east-west axis, and earth plan can be detected. Figure 1.10(c) presents the test result of the Earth plane. These results confirm that the ME composites also have the potential for applications in DC magnetic field sensor. However, in spite of this potential, an actual application has not yet been achieved. One of the biggest problems is using a lock-in amplifier in this method. This method limits the mobility as a detection unit. A different method is highly desired to develop which would have the similar functions as the lock-in amplifier.

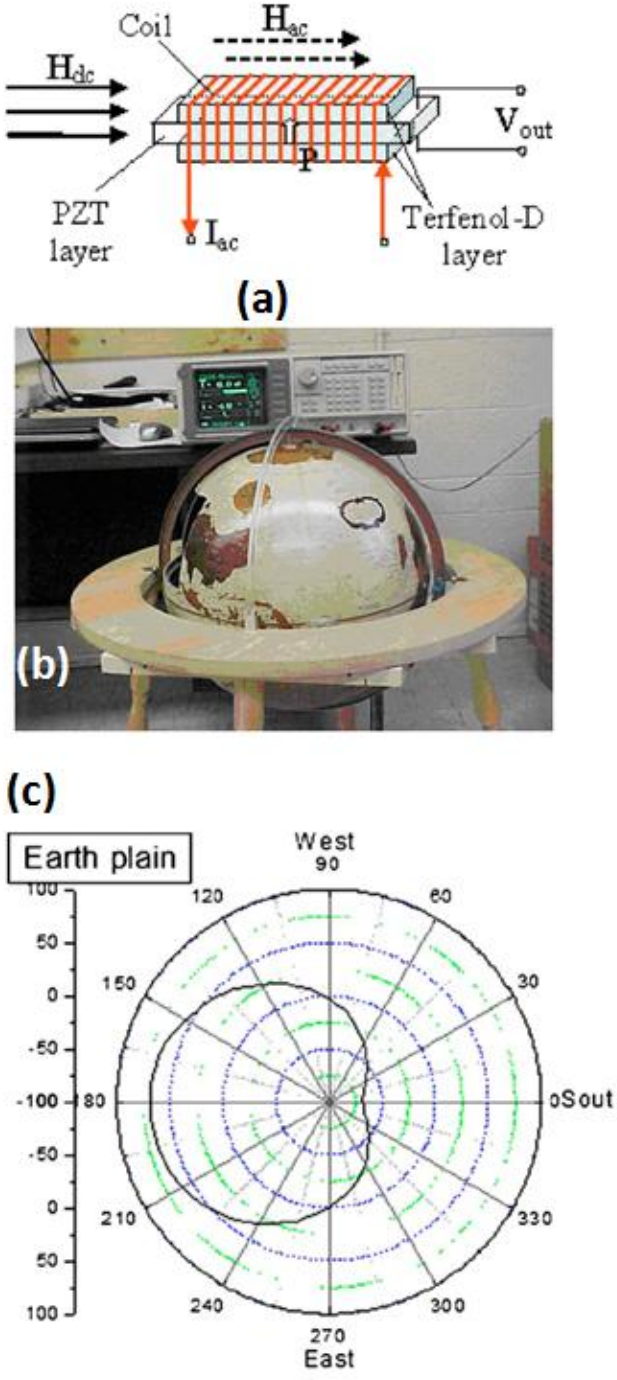

Figure 1.10 (a) Schematic illustration of DC magnetic sensor; (b) Photo of geomagnetic field detection; and (c) Output signals along different directions in Earth plain.

1.2.2 Energy harvesters

Magnetoelectric bulk composites can be also used for energy harvesting devices which can generate useful electric energy by harvesting energy sources that cannot be utilized directly in the environment, such as solar, thermal, vibration, and magnetic energies. Specifically, for ME laminated composites, it would be possible to harvest vibration energy via piezoelectric effect and electromagnetic energy via ME effect. These hybrid harvesters are expected to enhance energy collection and conversion efficiency.

For example, by using an ME laminated composites attached to a cantilever beam with a tip mass, a multimodal energy harvester was developed which can harvest energy from both of magnetic field and mechanical vibration.[48] By driving the harvester at 20 Hz with a magnetic field of 2 Oe and mechanical vibration amplitude of 50 mg, an open-circuit output voltage of 8 V can be generated, as shown in Figure 1.11 (a). Also, other groups designed a prototype of vibration energy harvester by using a Terfenol-D/PZT sandwich structure ME transducer which can generate a load power of 1.05 mW across a 564.7 kohm electric load driving with an acceleration of 1 g at resonance frequency of 51 Hz (Figure 1.11 (b)).[49, 50]

Compared to piezoelectric or electromagnetic harvesters, the conversion efficiency of an ME harvester is still at a lower level.[51] There is a lot of room for enhancement.

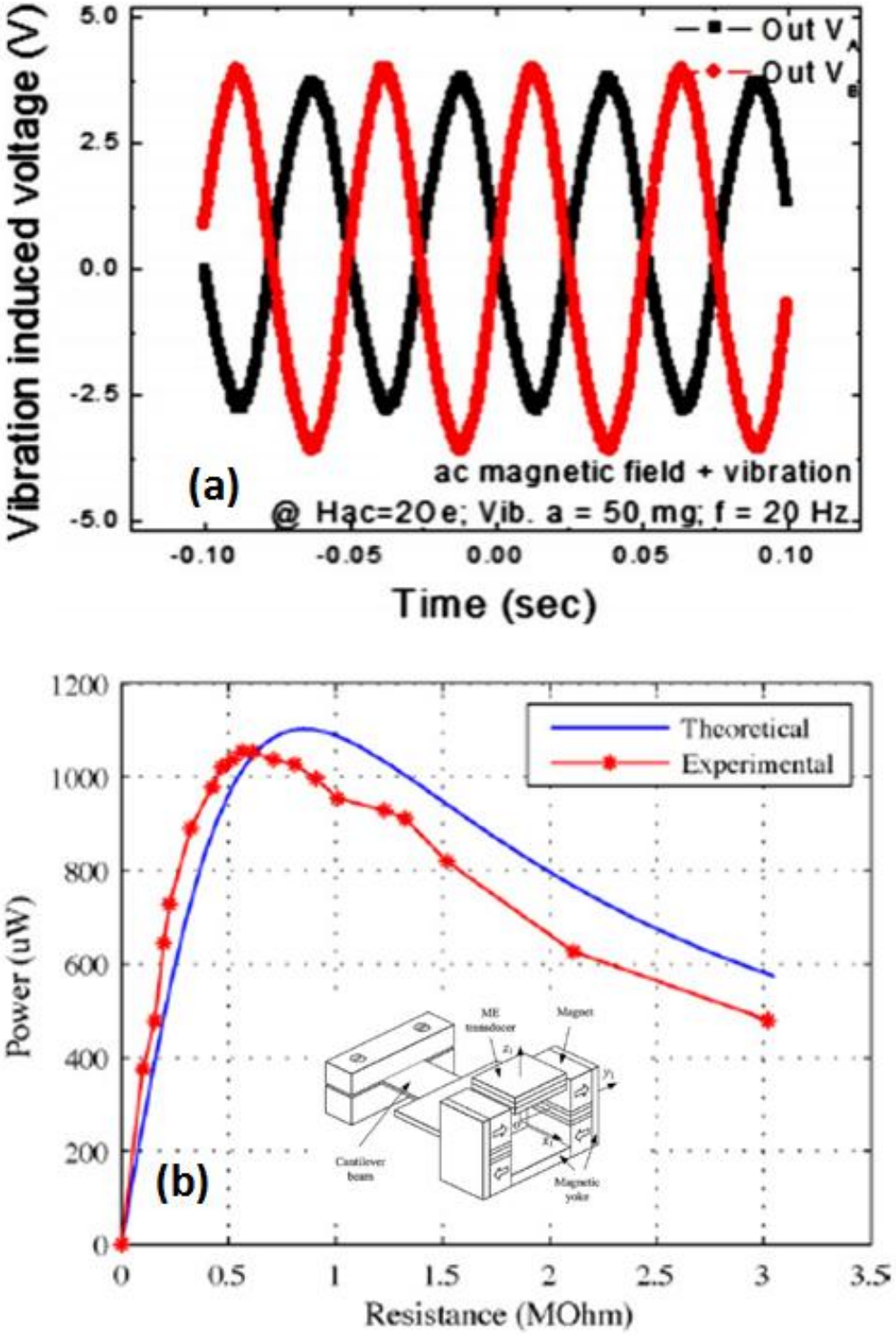

Figure 1.11 (a) Multimodal energy harvester; and (b) Vibration energy harvester prototype.

1.2.3 Other Devices

Besides these main applications, some other multifunctional devices based on ME composites have been designed as well. For example, ME composites based gyrator was developed.[52] A gyrator is a passive, two-port electric network. Figure 1.12 (a) shows the equivalent circuit of gyrator. The gyrator looks like the voltage transformer via inductive interaction between coils. The gyrator can achieve the impedance inversion function, which means that it can convert an inductor (capacitor) to a capacitor (inductor). Through calculations, ME composites are predicted to have this function. Figure 1.12 (b) shows the device's design according to the equivalent circuit. (c) and (d) present through ME gyrator, the capacitor can be converted to inductor, resistor to resistor with an inverse resistance.

Recently, a simple ME-based frequency multiplier made up of FeBSiC and PZT wrapped with a coil has been proposed.[53] It shows the steady frequency doubling behaviors at various frequencies. Moreover, the small DC bias can switch device on or off. Zhang *et al*. designed one resonance frequency multiplier.[54] The multiplying signal can be generated when the input frequency of AC magnetic field is around 1/n of mechanical resonance frequency of device. Interestingly, such frequency multiplying behavior can be tuned by using external DC bias. Compared to traditional frequency multipliers, these devices are passive components and can be used in broad frequency range, probably offering a potential application in the electric industry

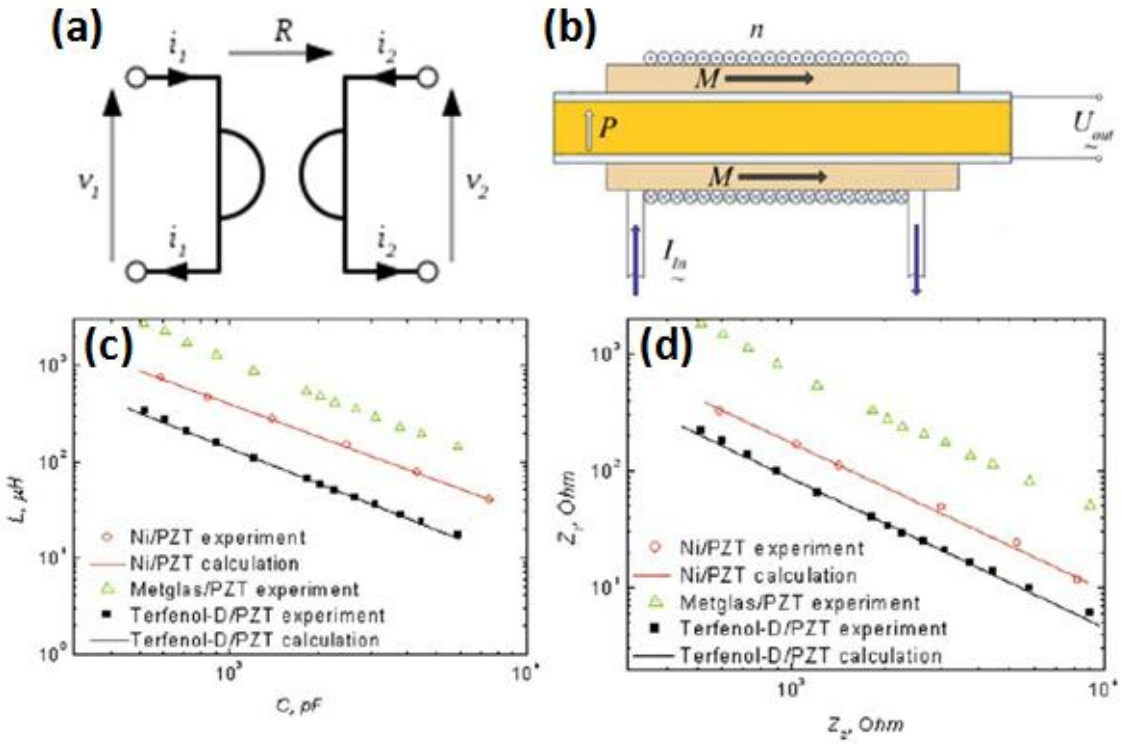

Figure 1.12 (a) Equivalent circuit of gyrator; (b) ME gyrator design; (c) Inductor converted to inductor; and (d) resistor to resistor with inverse resistance.

1.3 Noise sources and their eliminations

The main research for my thesis is about the improvement of AC and DC magnetic sensors based on ME laminated composites. So, the noise analysis is mainly considered for these detection units. Generally, *noise* is referred to as any unexpected or unwanted disturbance that reduces the resolution of signal.[55] It plays an important role in electronic devices, especially for the measurement of minute signals. The sensitivity of sensors is limited by noise level: so, reducing the noise is quite helpful for enhancement in sensitivity of detection unit. According to sources, noise can be classified as external noise and internal noise. We will discuss these classification separately to show how they can affect the ME detection unit, and what some works have been done to reject their influences.

1.3.1 External noise

External noise is referred to as the interactions between a detection unit and the environment. These interactions can be electric, magnetic, chemical, thermal, vibration, and so on. Due to an AC magnetic sensor that contains materials and electronic circuit parts, the noise sources that affect any parts would influence the detection unit. The main noise sources that can disturb materials are vibrations and external thermal noises. On the other hand, electromagnetic coupling, electrochemical noises are the main factors for circuit parts. Although conductive coupling is also common as noise sources for electrics, it has little effect due to individual circuit used for each sensor without sharing common grounding or common power supply.

Thermal noise should be named as external thermal noise or thermal fluctuation noise. That noise affects the ME-based magnetic sensor via pyroelectric effect which refers to the fact that some materials with lower crystal symmetry can generate an electrical potential when they are heated or cooled.[56] In our case, PZT belongs to a 4mm point group, which just has the pyroelectric effect. Thus, most of PZT-based magnetic sensors would be affected by thermal fluctuation noise. Previous investigation show designs of one symmetrical bimorph structure for Terfenol-D/PZT laminated composites which shows great thermal noise rejection ability, as shown in Figure 1.13.[57] The idea is to separate the signal and noise with different deformations resulted from a magnetic field and thermal fluctuations. We can see that the sensor is used in a mechanically symmetrical design that would generate elongating or shrinking deformation along horizontal plane. However, the bending mode deformation would be excited as applied magnetic field due to reversed magnetization directions two pieces of Terfenol-D plates by using U-shape magnets. The comparative results clearly exhibit the ability of noise rejection.

Vibration noise affects the ME-based sensor via piezoelectric effect. Because piezoelectric effect is a natural phenomenon of the materials, it is impossible to remove by changing other materials unless new ME materials systems are found. In lab conditions, we can use a vibration isolation table to reject the effect of vibration noise. However, for real environments, there is no effective method to reject the vibration noise: thus, this lack of effective method has limited the ME sensor applications greatly. Xing *et al.* analyzed the external noise effect on ME composites

with various configurations and proposed potential methods to design the sensor which can reject vibration or thermal noise.[58]

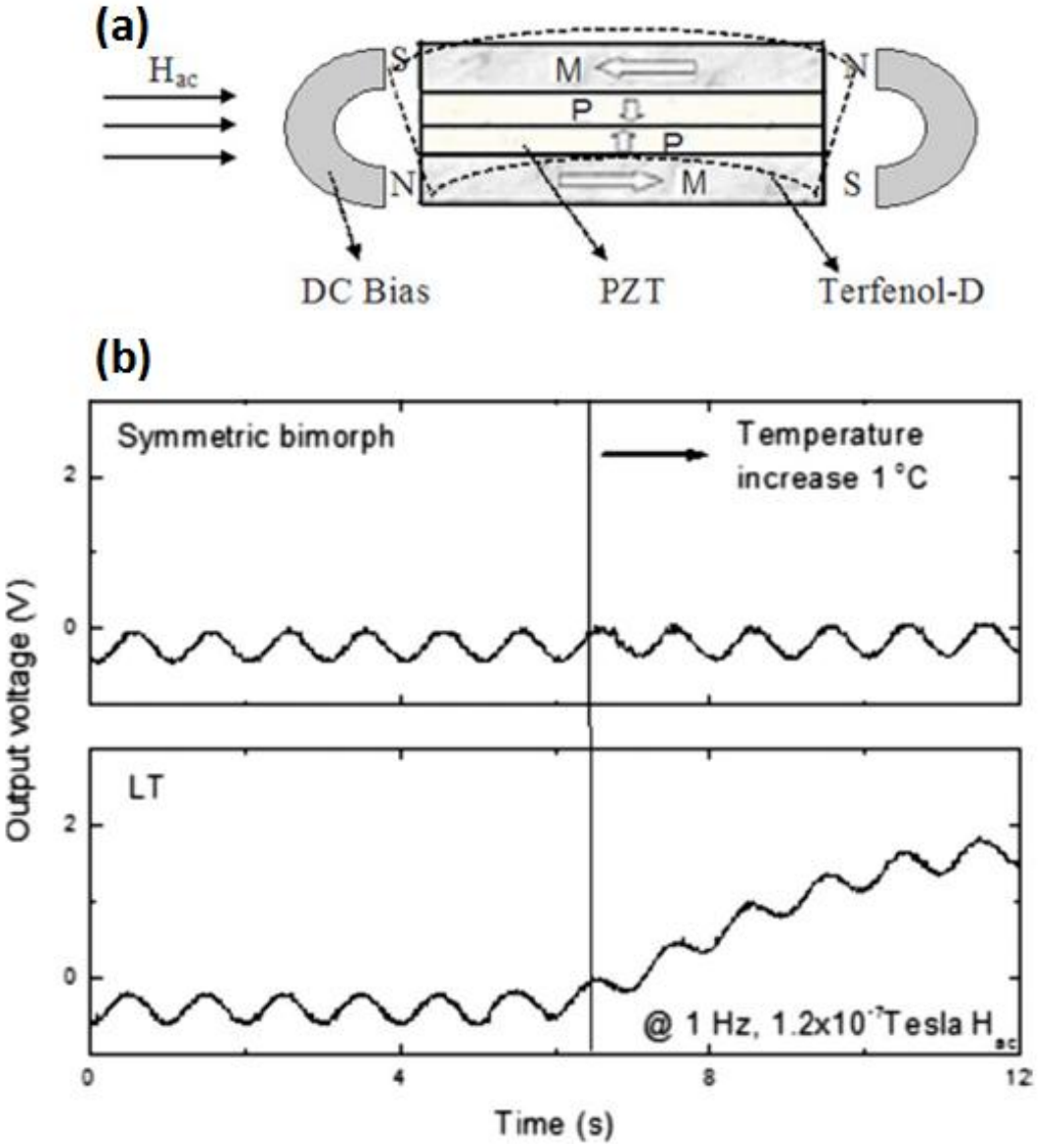

Figure 1.13 (a) Schematic illustration of symmetrical structure design; and (b) comparison of output signals under thermal fluctuations in time domain.

For the circuit portion, Electromagnetic Interference (EMI) is occurred almost all over the Earth due to the development of communication techniques. For example, we have strong 60 Hz EMI noise due to the power supply all over America. EMI noise can be reduced by proper shielding, grounding, and filtering techniques. Electrochemical noise[59] refers to a fluctuation in corrosion potential or corrosion current flow. This effect takes place as a chemical reaction occurs between two different inductors, forming micro batteries. At high humanity environment, the sensor or the front end of the amplifier is contaminated, this electrochemical noise always appears. To reduce this effect, it is very important to keep the detection unit clean and dry.

1.3.2 Internal noise

Even if we can eliminate or reject all external noise mentioned above, a circuit or ME composites would still exhibit inherent noise. This form of noise is random in nature, such as thermal agitation of electrons in resistors and the random generation and recombination of electron-hole pairs in semiconductors. This inherent noise is also defined as intrinsic or internal noise. Basically, we have thermal noise, shot noise, Flicker noise, and Avalanche noise.[60, 61]

Thermal noise, or Johnson noise, is present in all passive resistance components, including the stray resistances of non-ideal capacitor and capacitor.[62, 63] The origin of thermal noise is from random thermal motion of electrons (or holes in p-type semiconductor). From the name, it is easy to see that this noise is directly related to temperature. In fact, thermal noise in a resistor can be described as a voltage noise

source with power density of e_R in series with a noiseless resistor, as shown in Figure 1.14 (a). The voltage noise density of thermal noise can be calculated by:[60]

$$e_R(V/\sqrt{Hz}) = \sqrt{4kTR}; \tag{1.3}$$

where k = 1.38×10^{-23} J/K is Boltzmann's constant, T is absolute temperature in kelvins, and R is resistance value. From the formula, one can see that the voltage noise density is independent with frequency, but directly affected by temperature and resistance used. By using an equivalent circuit mode, the voltage noise model can be transferred to a current noise source in parallel with an ideal resistor, as shown in Figure 1.14 (b). The current noise density can be expressed as:

$$i_R(A/\sqrt{Hz}) = \sqrt{\frac{4kT}{R}}; \tag{1.4}$$

Shot noise arises whenever charges cross a potential barrier, such as in transistors. As electrons encounter a potential barrier, energy will accumulate until they have enough energy to pass the barrier. Shot noise has uniform power density given as:[60]

$$i_n(A/\sqrt{Hz}) = \sqrt{2qI}; \tag{1.5}$$

where q=1.6×10^{-19} C is an electron charge, and I is the dc current through a barrier. Once again, the shot noise is also independent with frequency, and also not related to temperature.

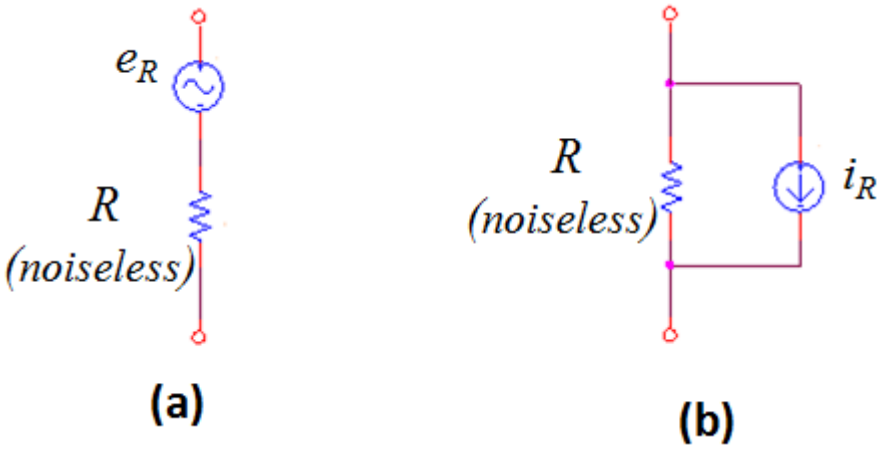

Figure 1.14 (a) Voltage noise model; and (b) current noise model.

Flicker noise, also called 1/*f* noise, or contact noise, is present in all active and some passive devices. The origins of Flicker noise are various, depending on the device type. Basically, it is related to the capture or release charge carrier as current flows in the active devices. That can result in random fluctuation in the current. The noise power density can be written as:[60]

$$i_n(A/\sqrt{Hz}) = K\frac{I^a}{f}; \tag{1.6}$$

where *K* is a device constant, *I* is the dc current, and *a* is another device constant in range from ½ to 2.

The biggest difference between Flicker noise and the previous two noises is the frequency dependent power density. The power density can be increased sharply at low frequency range. That is a big problem for our low frequency measurement (*f* < 1 Hz), because it is also found in some resistors as a flowing current. In this case, this noise is also called excess noise because it appears in addition to the thermal noise, and it would have a main contribution on noise density as extremely low frequency. Different types of resistors have various excess noises. The resistor of the wirewound type is the quietest in terms of 1/*f* noise; however, it is high cost. Carbon composition types can be noisier by as much as an order of magnitude. Carbon-film and metal film types have intermediated performance compared to wirewound and carbon composition.

Avalanche noise is found in p-n junctions as operated in reverse breakdown mode. Under the strong reverse electric field in p-n junction, electrons have enough kinetic energy to create additional election-hole pairs by collision against the atoms

of the crystal lattice. These additional pairs can create other pairs that result in noise spikes as current flowing through the reverse biased junction.

All of these noises have limited the signal-to-noise ratio (SNR) for magnetic sensors based on ME composites. Since the external noise can be reduced dramatically in lab conditions, the internal noises are the dominant factors that need to be optimized.

Previously, Xing *et al*. designed the charge amplifier based AC magnetic sensor that can be operated at quasi-static frequency (0.16 Hz ~ 10 Hz).[45] This design is a passive device with high sensitivity. Moreover, they also analyze the internal noise in this detection unit at quasi static frequency range, as shown in Figure 1.15 (a).[64] In the model, ME composites was considered as a charge source induced as applied magnetic field in parallel with a capacitor and resistor. Another part is the detection circuit consisting of an op-amp, feedback resistor, and capacitor. The thermal noise, shot noise and other internal noise sources were analyzed in this model. The output noise level was characterized for the circuit itself and connected with one ME composites (Figure 1.15 (b)). The results showed that the dominant noise source of detection unit was from the ME composites part. Thus, more investigations have been focused on how to optimize that portion, including external noise rejection, capacitance and dimension effects,[65] and array study.[66] These works can increase the ME coefficient or decrease noise level, in another word, it can enhance the SNR value of the detection unit.

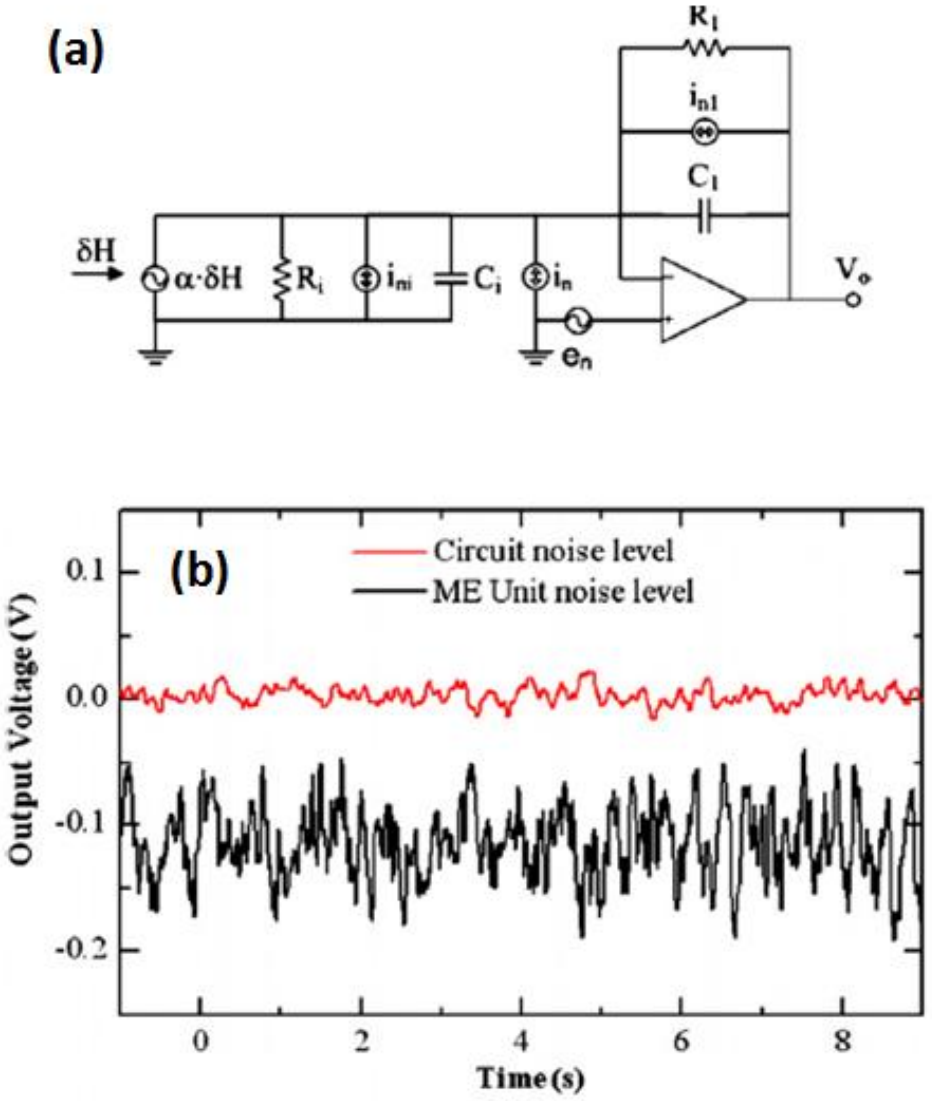

Figure 1.15 (a) Equivalent noise model for magnetic sensor; and (b) Output noise level of circuit and sensor unit.

1.4 Summary of this section

In the past ten years, ME laminated composites have been developed rapidly due to giant ME coefficients compared to other connectivity schemes, especially for Metglas/piezo-fibers with multi-push pull structure. Meanwhile, several multifunctional devices based on ME effect have been proposed, such as sensors, harvester and so on. However, there is significant work to be done, including (i) further improvement of ME voltage coefficients; (ii) external noise rejection; (iii) optimum of detection circuit; and (iv) new detection method for DC sensor. These are the purposes of my thesis.

2. Purpose of the thesis

The purpose of my dissertation is to optimize the ME coupling effect for Metglas/piezo-fiber laminate composites, and develop devices based on ME composites. Specifically, the following topics are the main area I studied in the thesis.

(1) ME composites

Previous investigations have found ME laminate composites consisting of Metglas foils with high magnetic permeability and piezo-fiber with great piezoelectricity have giant ME coefficient of of $\alpha_{ME} \approx 22$ V/cm-Oe under small optimum DC magnetic biases. Such ME composites have the potential to develop the multifunctional devices, such as magnetic sensors, memory storages. All of my researches were focused on improving the ME coefficients for Metglas/piezo-fiber composites, including different piezoelectric materials, volume ratio, thermal treatment, and preliminary array study.

Besides improving the ME coefficient, another challenge for the ME composites is to reduce the equivalent magnetic noise floor, which is impacted by environmental or external noise sources. Some examples include thermal fluctuations coupled into the noise via the pyroelectric effect and mechanical vibrations coupled via the piezoelectric effect pose significant obstacles for practical application of ME composites based devices. In my thesis, I have proposed a

symmetric differential structure for Metglas/Pb(Zr,Ti)O_3 (PZT) fiber-based ME composites which can reject the vibration noise effectively.

(2) AC magnetic sensor

Previously, the passive AC magnetic sensor based on ME composites has been developed; this passive device is quite highly sensitive to small AC magnetic fields. The practical application of such magnetic sensor is determined not only by the output signal of the sensor in response to an incident magnetic field, but also by the equivalent magnetic noise which limits the detection sensitivity in principle. In Section 3.2, I have shown the works on improving ME coefficient that can optimize the sensor's output signal to an incident magnetic field. Moreover, reducing the equivalent magnetic noise is another important part of this thesis. In my research, I developed a new method to characterize the sensor's noise: taking materials and circuit as a whole unit to study. In this method, the detection circuit noise is also the important factor that needs to be taken into account.

To understand the main noise sources in this unit, a static charge model for the sensor was developed. The effect of composites and electronic circuit on the equivalent magnetic noise was studied and optimized. Based on the noise model, the extremely low frequency magnetic sensor (<1 mHz) with low noise level was proposed. Furthermore, one active magnetic sensor based on amplitude modulation-demodulation method has been also developed. The motivation for using this technique is to modulate the low frequency magnetic signal to the relative high frequency range which has lower noise floor. Accordingly, the signal to noise ratio is expected to be enhanced.

(3) DC magnetic sensor

The DC magnetic sensor has been designed in previous works. By using the active method, the sensor can sense small DC magnetic field variations driven by AC magnetic field. Interestingly, the novel global positioning system (GPS) based on geomagnetic field was proposed. Previous investigations have shown the DC magnetic sensor can sense the intensity and inclination angle for local geomagnetic field accurately. This capability offers the potential application on underwater guidance system based on geomagnetic field. However, in these reports, only 1-axis sensor was developed that required to rotate the sensor to sense the magnetic field along a different direction. Moreover, the traditional method needs to use a commercial lock-in amplifier (SR-850) to drive the sensor and process induced signal from ME composites that is not convenience for application. In my research, I proposed a man-portable multi-axial DC magnetic sensor that can be operated anywhere easily.

Firstly, some works were focused on the improvement of DC magnetic sensitivity for ME composites, including different piezoelectric materials, magnetic flux concentration, and driving frequency. Meanwhile, in order to replace the commercial lock-in amplifier, I fabricated a battery operated multi-axial lock in the circuit which had the comparable capacity of commercial one. After assembling the sensor and circuit in a compact box, some measurements were performed, such as target localization, and magnetic field distribution mapping. More importantly, I took the DC magnetic sensor to test the geomagnetic field outside which show the great accuracy compared to the database.

(4) Other devices and applications

Previously, ME composites have been approved to have ability of harvesting the vibration and magnetic energy. However, the output power for the previous harvester was not high enough. In my research, a magnetic energy harvester based on Metglas/PMN-PT composites can be used to charge a Ni-Mn hybrid battery pack as driving at resonance frequency. Meanwhile, based on bending mode ME composites, I proposed one 60 Hz magnetic energy harvester which had potential to integrate on power supply to harvest energy.

3. Magnetoelectric composites

3.1 Metglas/Piezo-fibers ME laminated composites

Metglas is a thin amorphous metal alloy ribbon produced by using a rapid solidification process.[67] The amorphous alloy $Fe_{81}B_{13.5}Si_{3.5}C_2$ is specially designed as Metglas 2605SC[68], and has been used to serve as the magnetostrictive phase in my investigations. Metglas 2605SC, which exhibits strong magnetic flux concentration effect, has an extremely high relative permeability that is over 40,000.[27] Moreover, Metglas 2605SC can reach a maximum magnetostriciton of $\lambda >$ 40 ppm at very low magnetic field biases of $H_{dc} <$ 2 Oe.[69] On the other hand, $Pb(Zr,Ti)O_3$ (PZT), $Pb(Mg_{1/3},Nb_{2/3})O_3$-30at%$PbTiO_3$ (PMN-PT) and $Pb(Zn_{1/3},Nb_{2/3})O_3$-4.5at%$PbTiO_3$ (PZN-PT) were used as the piezoelectric phase in my research.

Previous investigations have indicated long-type sandwiched laminate structures comprised of Metglas and $Pb(Zr,Ti)O_3$ (PZT) fiber layers with multi-push pull configurations had several advantages compared to other ME composites and structures: (i) high ME voltage coefficients, (ii) small required DC magnetic biases, and (iii) an anisotropic response to incident magnetic field.

There still remains some factors needing study in order to optimize the ME coefficients. I studied several questions in my research:

i) Are there any methods to further improve the ME voltage coefficient for Metglas/PZT ME composites? We already know that Metglas/PZT has a high ME coefficient. High permeability Metglas foils can reduce the DC magnetic field biases dramatically compared to Terfenol-D. PZT is a commercially available piezoelectric material with good properties. For this specific structure, I wanted to know if it was possible to improve the ME effect by using other piezo-fibers. What is the best volume ratio between magnetostrictive and piezoelectric phases? Can Metglas layers be improved?

ii) Can we design different configurations that can reject external noise, such as thermal and vibration noises? External noise is one of the biggest challenges for sensor application based on piezoelectric materials. We know that piezoelectric materials will introduce thermal fluctuation noise via the pyroelectric effect, which can generate charges that influence the signal to incident magnetic field. Moreover, piezoelectric layers will couple to vibration noises in practical applications, due to the strain induced by this noise source. Thus, it is highly desired to design a structure that can reject these noise sources without losing ME voltage coefficients.

3.2 Improvement of ME coefficients

3.2.1 Comparison of different piezo-fibers

Different piezo-fibers have various piezoelectric properties and mechanical coupling effects. This can result in enhancements of the ME voltage coefficients by using better raw materials. In this study, three piezoelectric fibers was selected for research: $Pb(Zr,Ti)O_3$ (PZT), $Pb(Mg_{1/3},Nb_{2/3})O_3$-30at%$PbTiO_3$ or PMN-PT, and

$Pb(Zn_{1/3},Nb_{2/3})O_3$-4.5at%$PbTiO_3$ (PZN-PT). Table 3.1 lists the basic properties for these materials.

Table 3.1 Piezoelectric properties of some materials

Piezo-fibers	d_{33} ***(pC/N)***	d_{31}***(pC/N)***	g_{33} ***(mV-m/N)***	g_{31} ***(mV-m/N)***	k_{33}
PZT 3195 STD [a)]	350	-175	24.2	-11.0	0.70
PMN-PT [b)]	2365	-1283	39.11	-21.22	0.93
PZN-PT [c)]	2400	-1400	45.9	-20.9	0.90

a) Cited from CTS, Albuquerque, NM

b) Cited from Ref [70]

c) Cited from Microfine Materials Technologies Pte Ltd, Singapore

To compare the ME effect for the three different ME composites, I obtained PZT (CTS, Albuquerque, NM), PMN-PT single crystals (Shanghai Institute of Ceramics, Shanghai, China), PZN-PT single crystals (Microfine Materials Technologies Pte Ltd, Singapore), and Metglas foils (Metglas Inc, Anderson, SC). Piezoelectric fibers of 200μm thickness were then cut to the dimensions of 2.5cm $\times$ 0.4cm, and both surfaces of the fibers were adhered to thin polymer-insulating films with inter-digitated (ID) electrodes using an epoxy resin. This electrode pattern allowed us to symmetrically pole the piezoelectric fibers in a back-to-back pattern along their length axis. Next, these structures were laminated together between four Metglas layers of dimension 8cm$\times$0.4cm using an epoxy. The thickness of each Metglas layer was 25 μm, as shown in the insert of Figure 3.1.

The ME coefficient α_{ME} was first measured as a function of DC magnetic field H_{dc} for various laminates using a lock-in amplifier method. A pair of Helmholtz

coils was used to generate an AC magnetic field of H_{ac}=1 Oe at a frequency of f=1 kHz. The H_{dc} was applied along the longitudinal axis of the laminates. Figure 3.1 shows α_{ME} as a function of H_{dc} for Metglas-PZT, Metglas-PMN-PT, and Metglas-PZN-PT laminates. We can see that for all three laminates, α_{ME} increases with increasing dc magnetic bias up to about H_{dc}=3 Oe, reaches a maximum, and subsequently decreases as H_{dc} increases further. The values of α_{ME} for the Metglas-PMN-PT and Metglas-PZN-PT fiber laminates are nearly equal and both are notably higher than that for Metglas-PZT. The maximum value of α_{ME} for PMN-PT and PZN-PT-based laminates is about 8.5V/cm-Oe, which is about 2.8 times larger than that for the PZT based ones of similar size. Higher ME coefficients are expected to get better sensitivity and lower noise floors for the AC magnetic sensor.

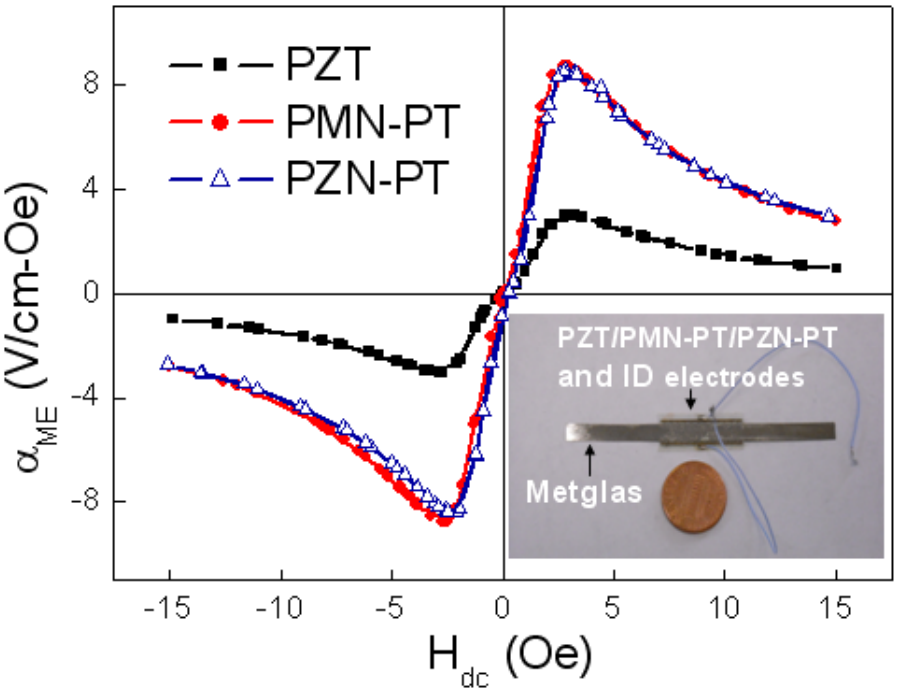

Figure 3.1 The ME voltage coefficient α_{ME} as a function of the static magnetic field H_{dc} for Metglas-PZT, Metglas-PMN-PT, and Metglas-PZN-PT laminate composites, as indicated. Inset shows a representative picture of a laminate composite.

I then assembled the ME composites and charge amplifier circuits into battery operated sensor detection units (Figure 3.2 (a)). In order to bias the ME laminate to the highest value of α_{ME} near the inflection point in the α_{ME}–H curve, small permanent magnets were attached to the composites. The detection units were designed to operate over the bandwidth of $1<f<10^3$Hz. Firstly, the AC magnetic-field sensitivity was characterized. A small AC magnetic field was applied along the longitudinal direction of the sensors by inputting an AC signal generated by a lock-in amplifier (SR-850) at a frequency of f = 1Hz into the Helmholtz coils. The output voltages from the sensors in response to the small incident magnetic field and the noise levels of sensors without any external magnetic field were measured in the time domain using an oscilloscope (Agilent 54624A). The peak-to-peak voltage noise level was about 6 mV. Thus, the applied AC magnetic field was varied to keep the peak-to-peak output voltage constant at about 12 mV where the signal magnitude was 2 times larger than the value of noise level: this was done in order to compare the magnetic field sensitivity for different sensors under the same conditions.

Figure 3.2 shows the magnetic field sensitivity results. Panel (a) shows a photo of the detection circuit. This box contains the ME laminate, the low noise detection circuit, and several batteries that served as the power supply for the circuit. Panels (b), (c), and (d) show the time domain output waveforms for the Metglas-PZT, Metglas-PMN-PT, and Metglas-PZN-PT laminates, respectively. The corresponding magnetic field sensitivities are also provided in the graphs. The magnetic-field sensitivities are 0.6 nT for both the PMN-PT and PZN-PT based laminates, which are about 1.7 times higher than the 1 nT for PZT based ones. This increase in

sensitivity originates from the increase in α_{ME} for PMN-PT and PZN-PT laminated composites. Panel (e) shows an example noise level from the low noise circuit in real time for H_{ac}=0 Oe. One can see that the peak-to-peak noise level is about 6 mV yielding a signal-to-noise ratio above 2, which again has been kept constant during the sensitivity measurements for the various laminates.

Finally, the noise floors for the three sensor units were measured in the frequency range of $10<f<10^3$ Hz by using dynamic analyzer. Over this frequency range, the gain factor (V/pC) was characterized, as shown in the insert of Figure 3.3. I then obtained the following sensor transfer function, by which to convert the noise floor in $V/\sqrt{Hz}$ to that in $T/\sqrt{Hz}$ using the gain:

$$\begin{aligned} Conversion\ factor(V/Oe) &= \frac{\alpha_{me}(pC/Oe)}{1pC/V} \\ Noise\ floor(T/\sqrt{Hz}) &= \frac{Noise\,floor(V/\sqrt{Hz})}{Conversion\ \ factor(V/Oe)} \times 10^{-4} \end{aligned} \tag{4.1}$$

Please note that I included a 60 Hz notch filter in the circuit to reject 60 Hz electromagnetic induction. In order to obtain the real noise floor for the ME sensor units, rather than that of the environment, the sensor units were tested in a mu-metal chamber without any signal input.

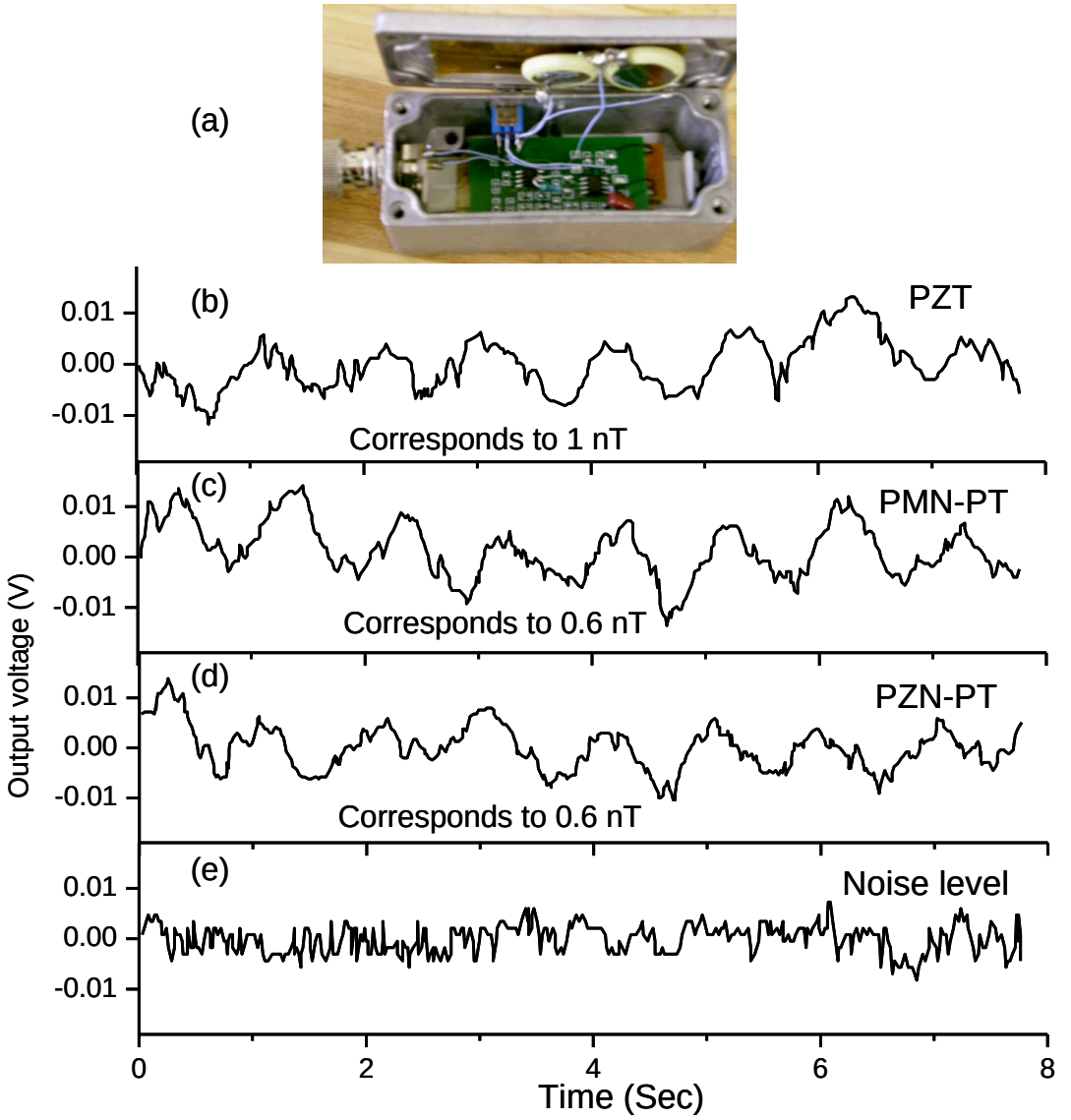

Figure 3.2 (a) Picture of our low noise circuit along with the ME sensor in a box. The ME output voltage as a function of time for the (b) PZT, (c) PMN-PT and (d) PZN-PT based sensors, respectively. The corresponding field sensitivities are as indicated. (e) Noise level for various detection units.

Figure 3.3 shows the noise floor spectra for all three sensor units. From this figure, we can observe that the noise floors for the Metglas-PMN-PT and Metglas-PZN-PT laminates are about $6\times10^{-11}\,T/\sqrt{Hz}$ in the frequency range of f =10-100 Hz and about $2\times10^{-11}\ T/\sqrt{Hz}$ in the range of f=100-1000 Hz. This was much lower than that for the Metglas-PZT laminate which is $1.5\times10^{-10}\,T/\sqrt{Hz}$ and $7\times10^{-11}\,T/\sqrt{Hz}$ in the low and high frequency range, respectively. The reduction of the noise floor resulted from the increase of α_{ME} for the laminates that had single crystal fibers, due to the much larger piezoelectric d_{33} coefficient for PMN-PT and PZN-PT relative to PZT.

The findings demonstrate that selection of better materials can enhance the ME coefficients dramatically, resulting in the improvement of sensitivity and decrease of noise floors for the AC magnetic sensors based on laminated composites. However, the cost of single crystals was much higher than that of PZT fibers, and the operational temperature span for single crystals based sensor would be narrower compared to PZT based ones. Recently, highly orientated PMN-PT fibers were commercialized that can decrease the cost without sacrificing much in terms of the piezoelectric properties.

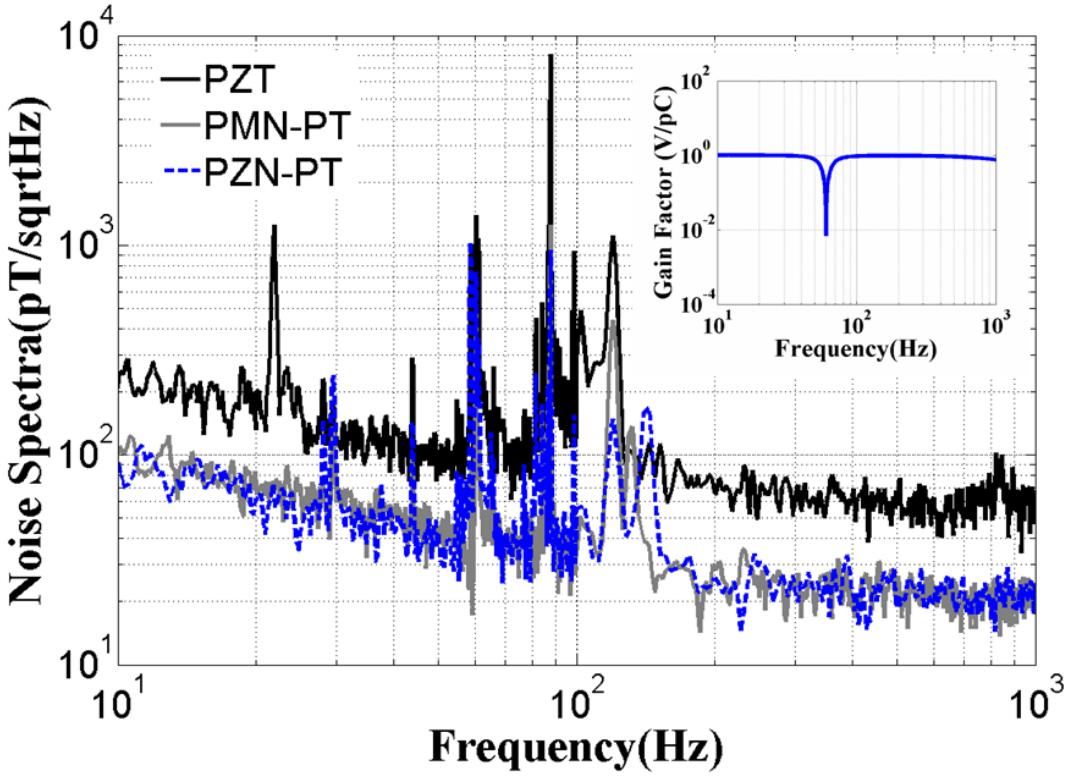

Figure 3.3 Noise spectra for the PZT, PMN-PT, and PZN-PT laminates with wide band circuit. Inset shows the wide band circuitry response as the function of the frequency.

3.2.2 Volume ratio effect

As mentioned in the introduction part, the volume ratio between piezoelectric and magnetostrictive phases is an important parameter for ME composites. The ME voltage coefficients can be enhanced greatly at optimum volume ratio. However, no previous report has focused on the study of the volume ratio effect on Metglas/piezo-fibers composites.

The schematic structure of our Metglas/PZT laminated composites is shown in Figure 3.4.[71] It is a more complicated structure than traditional modes, not only due to numerous units, but also to the non-ideal poling current. Typically, for poling along the thickness direction, the electrodes need to deposit on both top and bottom surfaces; for poling along the length direction, the electrodes are placed two edges. However, it is impossible to do such an ideal design. The fibers used in this structure were only 180 um in thickness and 4 cm in length. Thus, it is not easy to put electrode directly, which furthermore would require extremely high voltages to pole. By using Interdigitated (ID) electrodes, poling along the length direction can be achieved by smaller voltage, as the PZT layer was separated into small poling unit with a push-pull mode configuration. Each push-pull unit can be considered as two L-L modes in parallel connection.

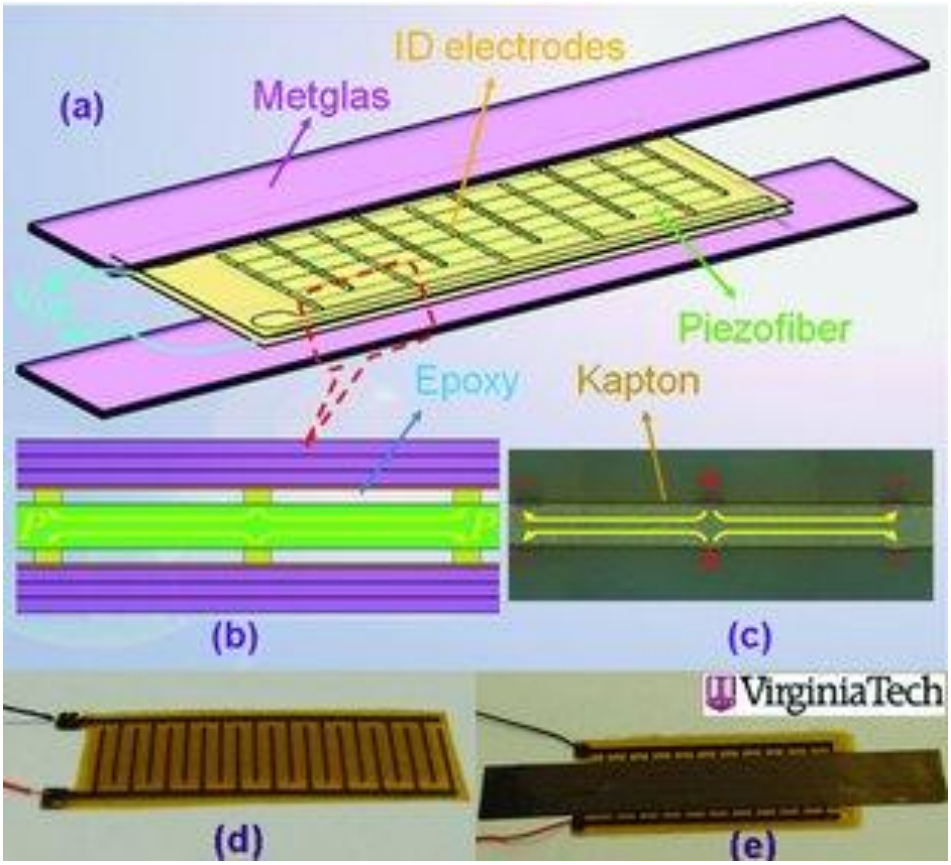

Figure 3.4 (a) Schematic diagram of ME composites configuration consisting of an ID electrodes, core composite and symmetric Metglas actuators on the bottom and top of the core composite. (b) Illustration of the numerous alternating push-pull mode units. (c) Optical microscopy image of a longitudinally poled push-pull element in the core composite. (d) and (e) Photographs of ME composites.

However, I need to make some assumptions in dividing an “L-L mode” theory that describes the real case. (i) Homogenous poling current between the two electrodes. This is an important assumption in the model development, because the poling current of the ID electrodes was not uniform. In fact, it had a dead zone and active zone, as shown in Figure 3.5. [72] (ii) The epoxy between each Metglas layers is uniform, and this has identical mechanical properties. Figure 3.6 indicates the conceptual model used to analyze the problem.

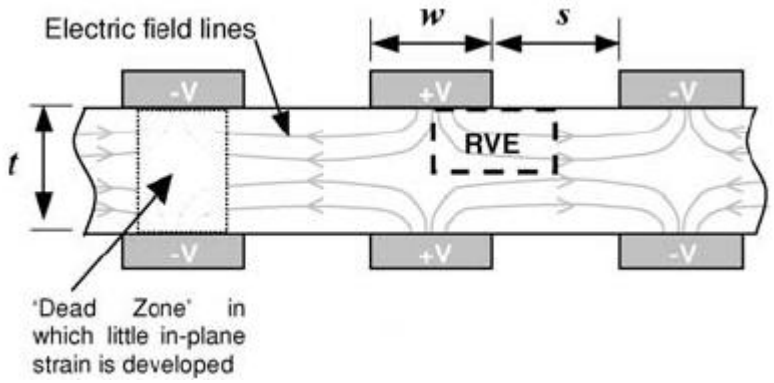

Figure 3.5 2-D ID electrode schematic showing the electric field lines.

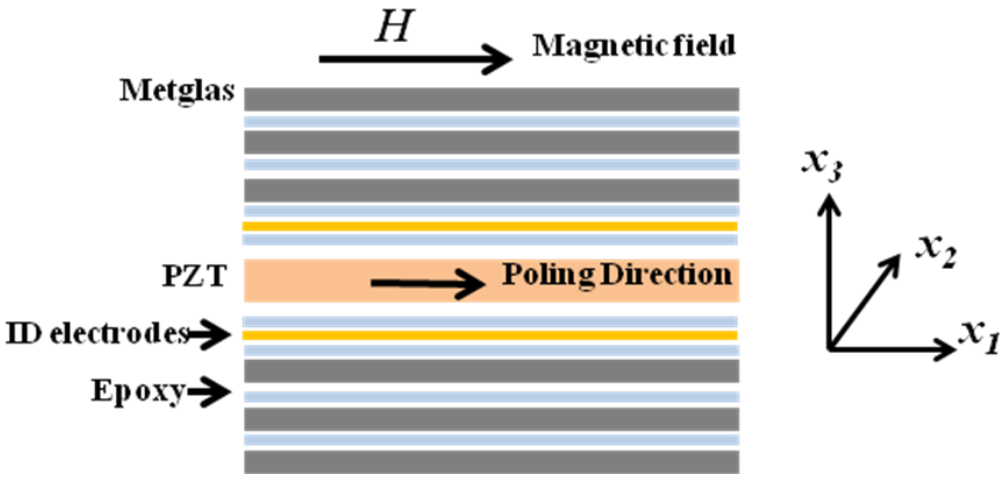

Figure 3.6 Schematic of L-L model.

In this model, I considered N layers of Metglas foils in ME composites on each side, 2 ID electrodes and 2 (N+1) layers epoxy. More considerations complicate the model more than previous static model.

The constitutive equations for the piezoelectric phase can be written as:

$$ {}^{p}S_i = {}^{p}s_{ij}\,{}^{p}T_j + {}^{p}d_{ki}\,{}^{p}E_k \tag{3.2} $$

$$ {}^{p}D_k = {}^{p}d_{ki}\,{}^{p}T_i + {}^{p}\varepsilon_{kn}\,{}^{p}E_n \tag{3.3} $$

where ${}^{P}S_i$ and ${}^{p}T_j$ are strain and stress tensor components of the piezoelectric phase. ${}^{p}E_k$, ${}^{p}E_n$ and ${}^{p}D_k$ are the vector components of the electric field and electric displacement. ${}^{p}s_{ij}$ and ${}^{p}d_{ki}$ are compliance and piezoelectric coefficient, and ${}^{p}\varepsilon_{kn}$ is the permittivity matrix of the piezoelectric phase.

The n-th Metglas layer is described by the following constitutive equations:

$$ {}^{m}S_i = {}^{m}s_{ij}^{(n)}\,{}^{m}T_j^{(n)} + {}^{m}q_{ki}^{(n)}\,{}^{m}H_k \tag{3.4} $$

$$ {}^{m}B_k = {}^{m}q_{ki}^{(n)}\,{}^{m}T_i^{(n)} + {}^{m}\mu_{kn}^{(n)}\,{}^{m}H_n \tag{3.5} $$

where n=(1,2,…,2N) ${}^{m}S_i$ and ${}^{m}T_j$ are strain and stress tensor components of the piezoelectric phase. ${}^{m}H_k$, ${}^{m}H_n$ and ${}^{m}B_k$ are the vector components of the magnetic field and magnetic flux induction. ${}^{m}s_{ij}$ and ${}^{m}q_{ki}$ are compliance and piezomagnetic coefficients, and ${}^{m}\mu_{kn}$ is the permittivity matrix of the magnetostrictive phase.

Besides the traditional equations for piezoelectric and magnetostrictive phase, I need to consider the stains in epoxy layers and electrode layers:

$$ \begin{aligned} {}^{g}S_i &= {}^{g}s_{ij}^{(n)}\,{}^{m}T_j^{(n)} \\ {}^{e}S_i &= {}^{e}s_{ij}\,{}^{m}T_j \end{aligned} \tag{3.6} $$

where n=(1,2,…,2(N+1)) ${}^{g}S_i$ and ${}^{g}T_j$ are strain and stress tensor components of the epoxy layers. ${}^{e}S_i$ and ${}^{e}T_j$ strain and stress tensor components of the electrode layer.

In order to simplify the equations, the following assumptions were made firstly: (i) no stress in "2" direction; (ii) no shear stress; and (iii) homogenous mechanical property for epoxy and electrode layers.

Boundary conditions:

$$ {}^{m}S_1^n = {}^{p}S_1 \tag{3.7} $$

$$ {}^{m}S_3^n = {}^{p}S_3 \tag{3.8} $$

$$ {}^{g}S_1^n = {}^{p}S_1 \tag{3.9} $$

$$ {}^{g}S_3^n = {}^{p}S_3 \tag{3.10} $$

$$ {}^{e}S_1 = {}^{p}S_1 \tag{3.11} $$

$$ {}^{e}S_3 = {}^{p}S_3 \tag{3.12} $$

$$ 2\sum_{n=1}^{N} {}^{m}T_1^n h_m^n + 2\sum_{n=1}^{N+1} {}^{g}T_1^n h_g^n + 2\,{}^{e}T_1 h_c + {}^{p}T_1 h_p = 0 \tag{3.13} $$

$$ 2\sum_{n=1}^{N} {}^{m}T_3^n h_m^n + 2\sum_{n=1}^{N+1} {}^{g}T_3^n h_g^n + 2\,{}^{e}T_3 h_c + {}^{p}T_3 h_p = 0 \tag{3.14} $$

$$ {}^{p}D_3 = 0 \tag{3.15} $$

Through the equations 3.7-3.12, I can express the stress in Metglas, epoxy and electrode by using the terms of ${}^{p}T_1$, ${}^{p}T_3$. By using equations 3.13-3.14, ${}^{p}T_1$, ${}^{p}T_3$ can be written as the function of E_3 and H_3.

Finally, based on open circuit condition, the ME voltage coefficients can be calculated by following equations:

$$ \alpha_{ME,L-L} = \frac{E_3}{H_3} = \frac{-d_{31}[B_2A_4 - B_4A_2] + d_{33}[B_4A_1 - B_2A_3]}{\varepsilon_{33}[A_1A_4 - A_2A_3] + d_{31}[B_3A_2 - B_1A_4] + d_{33}[B_1A_3 - B_2A_1]}. \tag{3.16} $$

where,

$$A_1 = 2a_1 h_m N + 2g_1 h_g (N+1) + 2\tau_1 h_c + h_p$$
$$A_2 = 2a_2 h_m N + 2g_2 h_g (N+1) + 2\tau_2 h_c$$
$$A_3 = 2a_3 h_m N + 2g_4 h_g (N+1) + 2\tau_4 h_c$$
$$A_4 = 2a_4 h_m N + 2g_5 h_g (N+1) + 2\tau_5 h_c + h_p$$
$$B_1 = 2f_1 h_m N + 2g_3 h_g (N+1) + 2\tau_3 h_c$$
$$B_2 = 2f_2 h_m N$$
$$B_3 = 2f_3 h_m N + 2g_6 h_g (N+1) + 2\tau_6 h_c$$
$$B_4 = 2f_4 h_m N$$

Then, I did experiments to compare the model data. The fabrication for ME composites is the same as previous process. The difference is the dimensions for PZT is 4 cm × 1cm and Metglas is 8cm × 1 cm. And the cut Metglas pieces were then stacked one on top of each other, bonded with epoxy resin, and were pressed using a hydraulic press to minimize the epoxy thickness in-between Metglas foils. To study the effect of Metglas layers, various layers of Metglas stacks were made (2, 4, 6, 8, and 10). Metglas stacks with equal number of layers were then attached at the top and bottom of the ID electrode-PZT-ID electrode structure with epoxy, in order to obtain the ME laminate layered structures.

Figure 3.7 shows the ME voltage coefficients as functions of DC magnetic field H_{dc}. From this figure, it can be seen that α_{ME} is nearly zero at $H_{dc} = 0$; increased as H_{dc} was increased; reached a maximum at a particular field point; and subsequently decreased as H_{dc} was further increased. One can also clearly see that the maximum value of α_{ME} increased with increasing number of Metglas layers until $N = 6$, after which it began to decrease with further increase in N. Furthermore, the H_{dc} required for the maximum α_V response also increased with N.

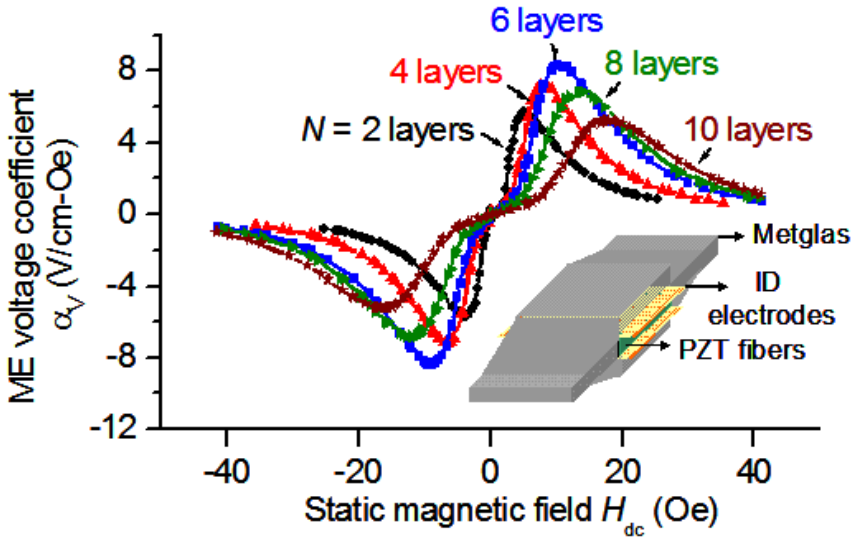

Figure 3.7 Magneto-electric voltage coefficients α_V as a function of the static dc magnetic field H_{dc} for various PZT fiber-Metglas laminate composites. The inset shows a schematic of the structure.

I recorded the maximum α_{ME} values at the optimum H_{dc} bias, and compared the data to the model predications. The materials parameters are given in Table 3.2.

Table 3.2 Materials parameters for ME coefficients calculation

	PZT [a]	***Metglas*** [b]	***Electrode*** [c]	***Epoxy*** [c]
Elastic constants $(10^{-12}\ m^2N^{-1})$	15.3 ($^{p}s_{11}$) 17.3 ($^{p}s_{11}$) -5 ($^{p}s_{13}$)	10 ($^{m}s_{11}$,$^{m}s_{33}$) -5.2 ($^{m}s_{12}$)	440 ($^{e}s_{11}$,$^{e}s_{33}$) -110 ($^{e}s_{12}$)	315($^{g}s_{11}$,$^{g}s_{33}$) -78 ($^{g}s_{12}$)
Piezoelectric constant $(10^{-12}$ pC/N)	-185($^{p}d_{31}$) 440($^{p}d_{33}$)			
Piezomagnetic coefficient $(10^{-9}$ m/A)		-21.3($^{m}q_{31}$) 50.3($^{m}q_{33}$)		
Dielectric constant ($^{p}\varepsilon_{33}/\varepsilon_0$)	1750			
Thickness (μm)	180	25	20	20

a) Cited from CTS, Albuquerque, NM
b) Cited from Ref [73]
c) Cited from Ref [74]

Figure 3.8 presents a comparison of the experimental results and estimated values. We can see that the measured data follow the trend predictions, although the values were smaller compared to the predicted behavior. The reasons may be: (i) the poling of the PZT was not sufficient compared to the model assumption; (ii) the epoxy layer reduced the strain transfer between the interfaces. To reduce the thickness of the epoxy, a spin coating method has been used. Such an optimized fabrication process can reduce the thickness of the epoxy from 20 μm down to 4 μm, as observed by optical microscopy.[75] The ME coefficient for the composites fabricated by this process was improved by a factor of 1.5× compared to previous method; and (iii) strain transfer across interfaces results in energy loss.

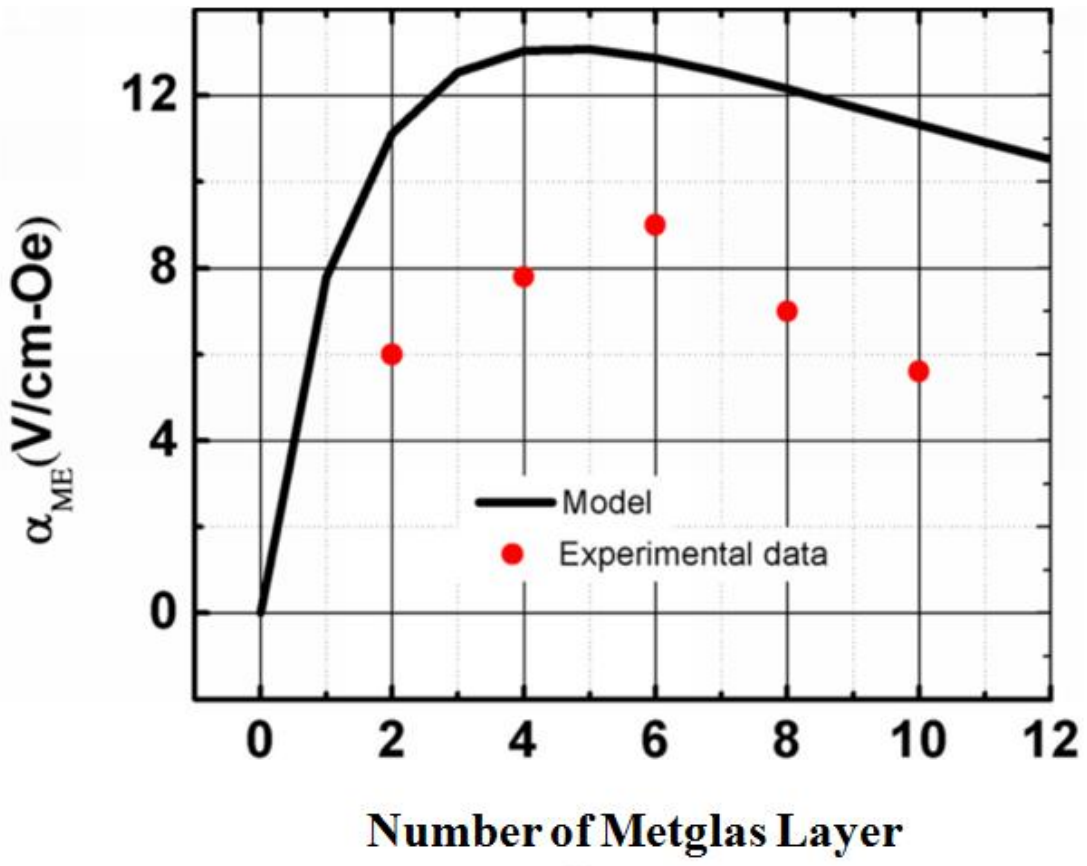

Figure 3.8 Comparison of experimental data and estimated values.

Moreover, I also found a sensitivity improvement by using an optimized volume ratio. Figure 3.9 presents the magnetic field sensitivity results. Part (a) shows the lowest detectable magnetic field as a function of the number of Metglas layers *N*. Parts (b) through (f) show the output waveform as a function of real time for the structures with different number of Metglas layers *N*, as shown in the figures. The corresponding field sensitivities are also marked in the graphs. Part (g) shows an example of the voltage noise spectrum in real time from our low noise charge amplifier. From part (a), we can see that the structure with 2 Metglas layers can detect a magnetic field of 0.8 nT with a SNR > 2. With increasing *N*, the magnetic field sensitivity increased almost linearly with *N* up to 6 layers. The structure with $N = 6$ was capable of detecting a magnetic field as small as 0.3 nT (with a SNR > 2). This is a 2.7 times increase in sensitivity relative to the 2 layered structure. This increase in sensitivity is a direct consequence of the increase in the ME voltage and charge coefficients that resulted from an increase in the effective interfacial volume with increasing Metglas thickness. In parts (b) - (f), one can see that the noise level is much smaller than the peak-to-peak output waveforms. The graphs also clearly show that the waveform profile for $N = 6$ was much cleaner than that for $N = 2$, even though the applied H_{ac} was much smaller.

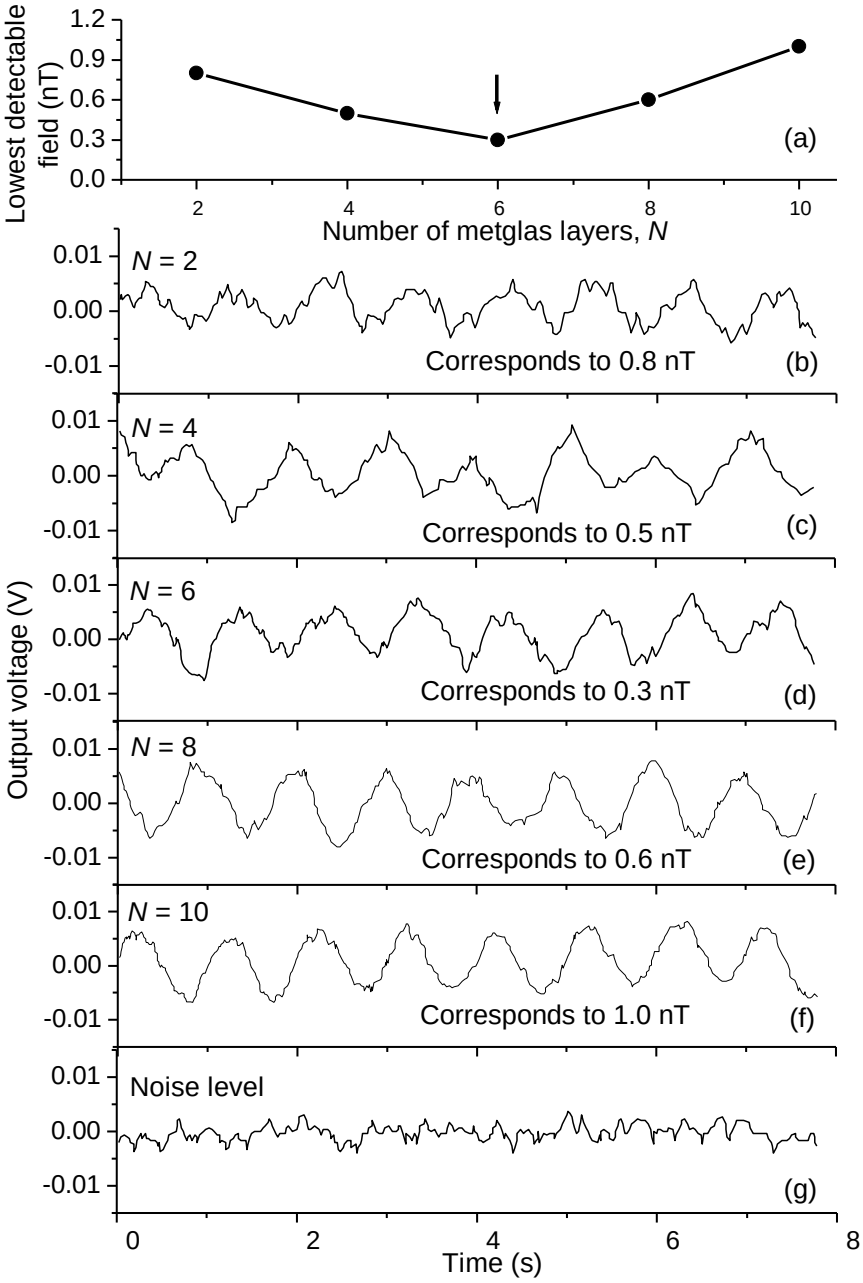

Figure 3.9 (a) Lowest detectable magnetic field for the PZT fiber-metglas laminate composites as a function of the number of metglas layers *N* on either side of PZT at 1 Hz for constant signal-to-noise ratio SNR > 2. (b)-(f) Output voltage waveforms for the laminates with different metglas layers *N* in the time domain. (g) Example voltage noise level for the low noise charge amplifier as a function of time.

3.2.3 Heat treatments

In addition to the piezo-fiber phase, the Metglas phase was also studied with regards to how to improve the ME coefficient.[76] Some previous investigations have shown that the electromechanical factor k_{33} of Metglas 2605 can be improved by heat treatment.[77] The value of the k_{33} was found to be increased with increasing annealing temperature between 385 ℃ and 400 ℃, and to decline sharply above 400 ℃. Thus, it may be possible to improve the ME coefficients by increasing the magnetomechanical factors of Metglas.

I used Metglas 2605 from Metglas Inc (Conway, SC) and annealed the foils at different temperatures: 300 ℃, 350 ℃ and 400 ℃. After heat treatment, the foils were bonded to PZT to fabricate the laminated composites. Figure 3.10 shows the ME coefficient as a function of H_{dc}. One can see that the ME coefficient was increased with increasing annealing temperature from 300 ℃ to 350 ℃, and was dramatically decreased by annealing at 400 ℃. This trend agrees with the experimental data for k_{33} in Ref 69.

Next, the magnetic field sensitivity and output noise measurements for the heterostructures were characterized. The output voltage and the noise level for the different structures with various Metglas layers were then measured using an oscilloscope. The noise amplitude of our charge amplifier detection circuit was about 7 mV. The applied H_{ac} was varied to keep the peak-to-peak output voltage constant at about 15 mV (to maintain a signal to noise ratio SNR > 2). This allowed us to compare the field sensitivities measured at constant SNR for the different structures. In Figure 3.11, it can be seen that the ME sensors with Metglas

annealed under 350 ℃ had larger magnetic-field sensitivity than the others. The value was almost 1.4 times larger than for the laminate annealed at 300 ℃, and about 1.5 times than the one annealed at 400 ℃.

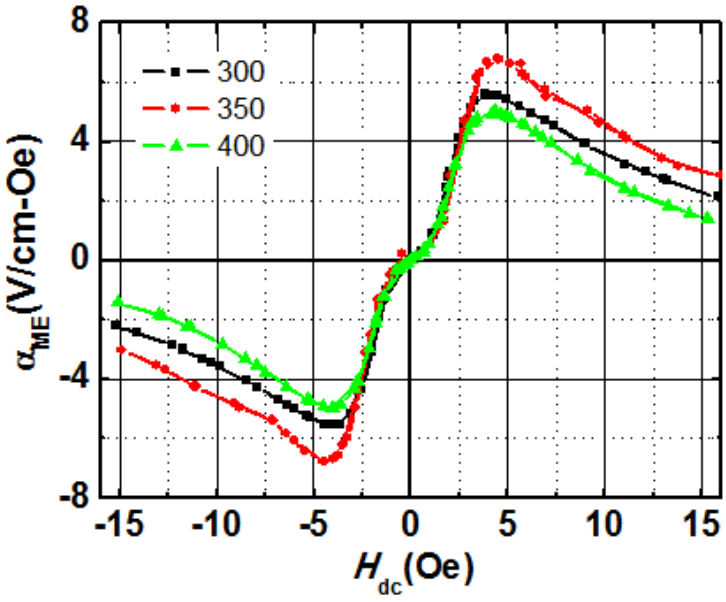

Figure 3.10 ME voltage coefficient a as a function of the static dc magnetic field H_{dc} for various PZT fiber-Metglas laminate composites after heat treated with Metglas layer.

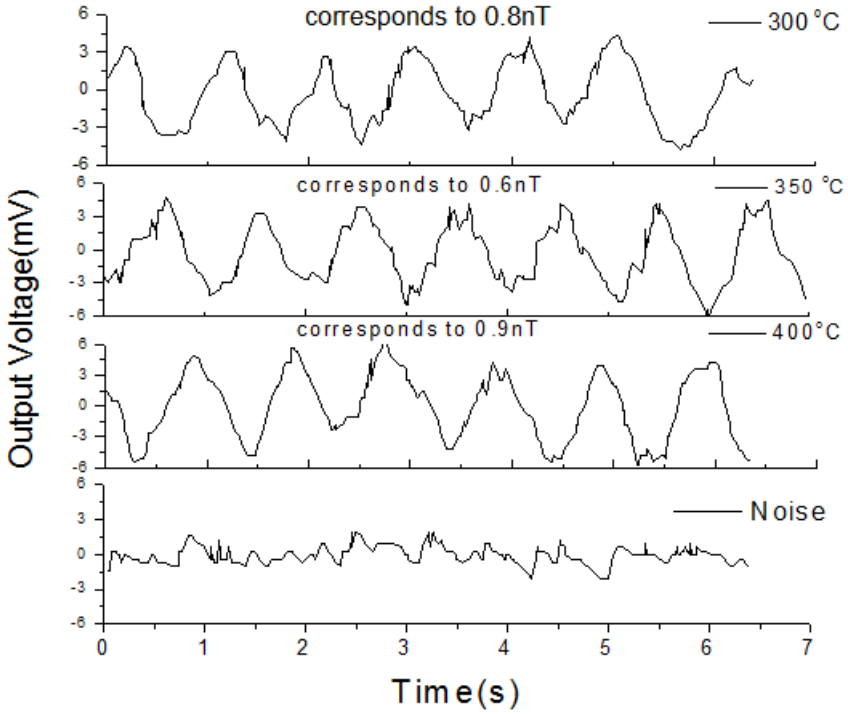

Figure 3.11 Comparison of AC magnetic sensitivity for the PZT fiber/Metglas laminated composites as a function of the different annealed temperature of Metglas layer.

.

3.3 Vibration noise rejection

One of the biggest challenges for ME sensors is to reduce the equivalent magnetic noise floor, which are impacted by environmental or external noise sources. Thermal fluctuation coupled into the noise via the pyroelectric effect and mechanical vibration coupled via the piezoelectric effect pose significant obstacles for practical applications of ME sensors.

To eliminate vibration noise, I proposed a differential structure for Metglas/PZT laminates.[78] Sensors fabricated with this differential mode structure can attenuate external vibration noise by about 10-20dB at different frequencies, while simultaneously having a doubled ME voltage coefficient. Interestingly, in additional to offering a means of mitigating vibration noise, this ME structure offers the potential to be a hybrid sensor, separating magnetic and acoustical signals.

Figure 3.12 (a) illustrates our new laminate structure design for vibrational noise cancellation. Unlike other Metglas/PZT/Metglas sandwich structures, two layers of PZT were used to create a differential symmetric structure. Five PZT fibers were oriented along the longitudinal axis to form composite PZT layers 10 mm wide and 40 mm long. Two such PZT layers were fabricated, and epoxied to either side of a double-sided ID electrode. A single-sided electrode with identical geometry was then bonded bare to the top and bottom surfaces of the PZT layers in a multi-push-pull geometry. The PZT composite was then poled under 2 kV/mm for 15 minutes at room temperature. Metglas foils (Vitrovac Inc. Hanau, German) were cut to 10 mm in width and 80 mm in length. Three Metglas foils were then laminated to both the top and bottom of the dual PZT laminate core.

Figure 3.12 (b) shows the poling configuration of the structure. In our design, the two PZT fiber layers were poled along the same orientation. Due to the symmetrical nature of the structure, the double-sided electrode in the middle acts as a neutral plane. Application of a magnetic field along the longitudinal direction of the laminate will cause the sensor to contract or elongate longitudinally. Contraction or expansion in the plane of the sensor will result in an identical charge in each PZT layer. Parallel electrical connection of the PZT layers would therefore result in a doubling of the signal. Conversely, an applied external vibration signal will tend to cause an asymmetric (bending mode) deformation. Simultaneous elongation of the top PZT and contraction of the bottom PZT will result in charges of opposite polarity in the PZT layers. Parallel electrical connection of the PZT, therefore, results in an attenuation of the output signal.

A schematic of the experimental setup for the evaluation of the differential mode structure of the Metglas/PZT laminates is shown in Figure 3.12 (c). Information about the relative amplitude of and the phase shift between the top and bottom PZT layer is important to understanding the different deformation modes excited by an applied magnetic signal relative to those excited by an applied vibrational signal. In order to analyze the signal from each PZT layer individually, the charge generated by each PZT layer was converted to a voltage, via integration using custom-built charge amplifier circuits. The raw voltage signals were recorded using a CR 5000 Datalogger and uploaded to a PC for analysis using MATLAB. Vibrational signals were generated using an LDS V203 10/32 shaker. The shaker was driven by a 10 Hz sinusoidal output signal from a SR850 lock-in amplifier augmented by an LDS

PA25E power amplifier. Magnetic test fields of frequency 10 Hz were generated using the output of the lock-in amplifier, and then fed into a custom-built 100 turn Helmholtz coil with a 45 mm radius.

To compare the two signals generated by each sensor, the charge outputs were converted into equivalent magnetic signals using a calibration factor. The magnetoelectric charge coefficient (α_{MEQ}) was measured for each sensor by exposing the sensor to a calibrated magnetic field.

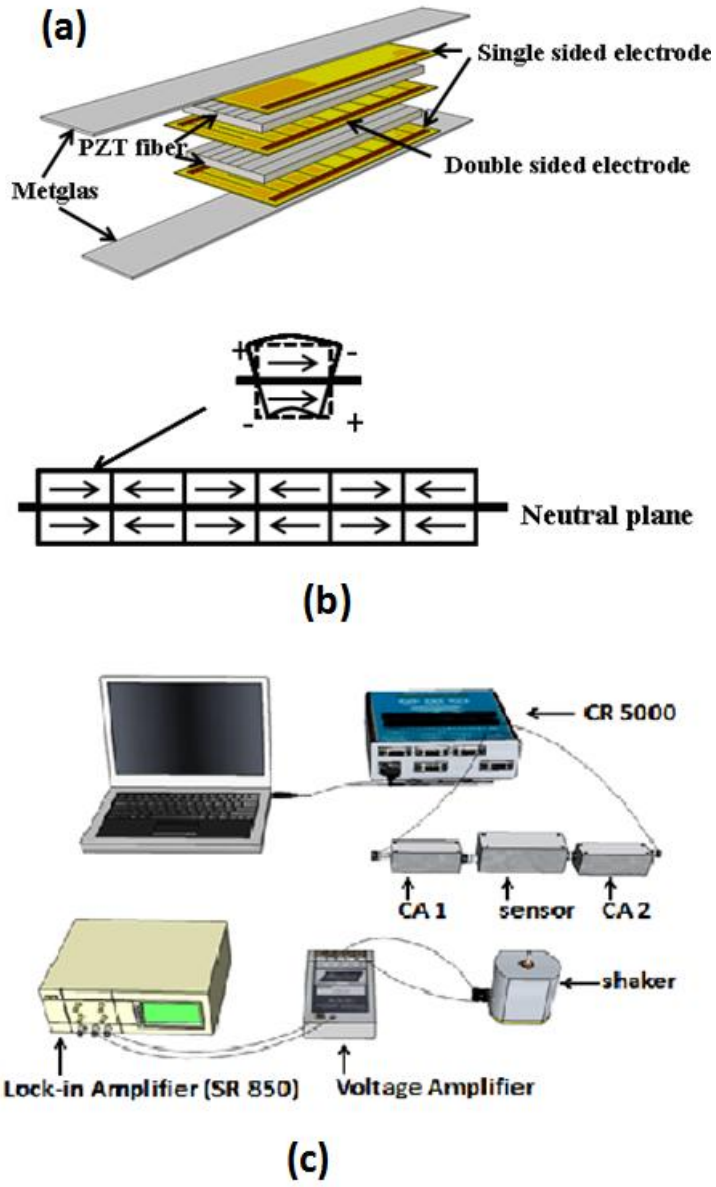

Figure 3.12 (a) Schematic of our new differential mode ME laminate sensor; (b) poling profile of multi-push/pull, dual PZT composite structure; and (c) schematic of the experimental signal path.

First, the response of the sensors to an induced vibration signal was measured and analyzed. Using the calibration factor given above, the equivalent magnetic signal was calculated from the output voltage of each charge amplifier.

The response of each layer of the differential sensor, as well as the summation of the constituent signals, is presented in Figure 3.13 (a). In this figure, the blue line shows the output signal from the top PZT layer, the red dashed line is the signal generated by the bottom PZT layer, and the black dashed line is the time-domain summation of the top and bottom PZT layers. Figure 3.13 (a) shows that the amplitude of the combined signal (black trace) is significantly attenuated relative to either of the two constituent output signals (red and blue traces). In order to more accurately analyze the data, the power spectral density (PSD) of each component signal and of the time-domain summation of the two signals was calculated using MATLAB. Additionally, a linear, time-invariant transfer function between the constituent output signals was estimated using built-in MATLAB commands. The phase shift between top and bottom PZT layers as a function of frequency can then be calculated from the estimated transfer function.

Figure 3.13 (b) shows the power density of the output signals of the top, bottom and time-domain summation over the frequency range from DC to 55 Hz. At the vibration drive frequency of 10 Hz, the amplitude of the summation signal was 5 times smaller than either that of the top or bottom PZT layers (10^{-8} T/√Hz versus 5×10^{-8} T/√Hz, respectively). In addition, the second, third, fourth and fifth harmonic signals (20, 30, 40, and 50 Hz) exhibited the same trends. The summation signal of the third harmonic was tenfold attenuated. In fact, the differential structure ME

sensor also shows the significant cancellation to the vibration noise at frequency range from 10 Hz to hundreds Hz.

Figure 3.13 (c) shows the calculated phase shift between the output signals as function of frequency upon exposing the differential ME structure to a 10 Hz vibrational signal. At 10 Hz, as well as at the higher order harmonics, the phase shift between the top and bottom PZT layers was quite close to 180˚. This phase shift data supports our hypotheses that vibration signals tend to excite the differential ME structure in a bending mode deformation, where the top and bottom layers are phase shifted, and enabling cancellation of that vibration signal in summation.

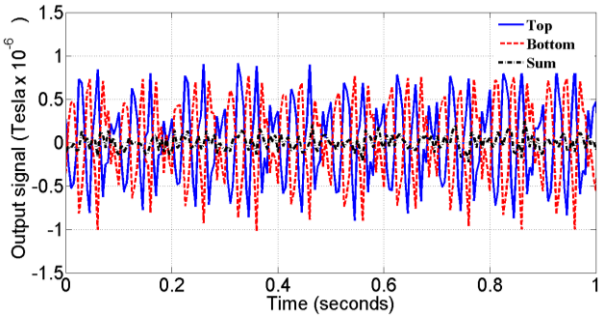

(a)

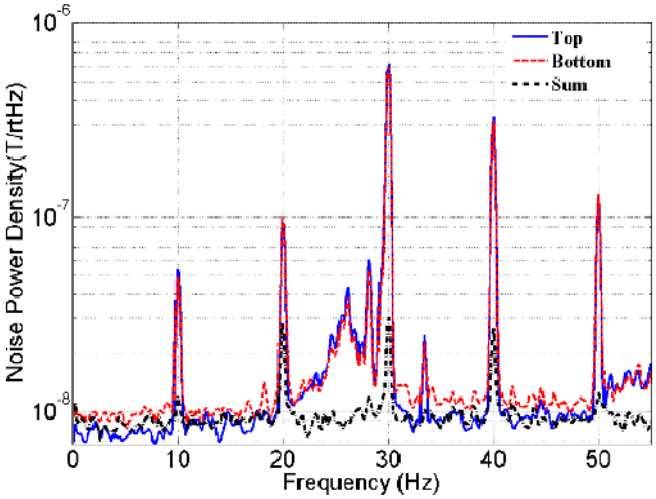

(b)

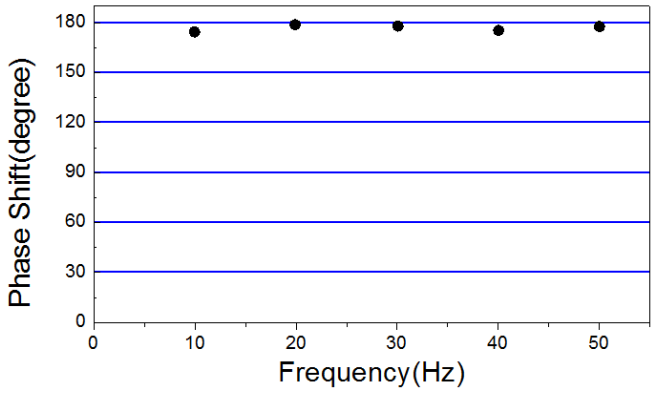

(c)

Figure 3.13 (a) Time-domain equivalent magnetic response of differential mode sensor to incident vibrational signal; (b) power spectral density of top, bottom and time-domain summation of top and bottom; and (c) phase shift between top and bottom PZT layers as a function of frequency calculated from a linear time invariant transfer function.

To examine the response of the sensor to an incident magnetic field, the shaker was replaced by a 90 mm, 100 turn Helmholtz coil driven at a frequency of 10 Hz by a SR850 lock-in amplifier. Figure 3.14 (a) shows the time domain response of the sensor to an incident 10 Hz magnetic field. The signals from the top and bottom PZT layers are nearly in-phase, resulting in an approximate doubling of the output signal upon summation. The relative phase shift between top and bottom PZT layers at 10 Hz was only 0.6˚, which evidences the fact that incident magnetic fields result in a longitudinal mode deformation of the differential ME structure.

The power spectral density response to the 10 Hz magnetic field over the range of DC to 55 Hz is shown in Figure 3.14 (b). Characteristic of the ME laminate sensor's magnetic response, the 10 Hz first harmonic signal was dominant relative to the higher harmonic signals (20 Hz, 30 Hz, etc.). The power spectral density of the summation signal was doubled in amplitude relative to the individual component layers at 10 Hz (1.4 μT/√Hz vs. 0.7 μT/√Hz, respectively).

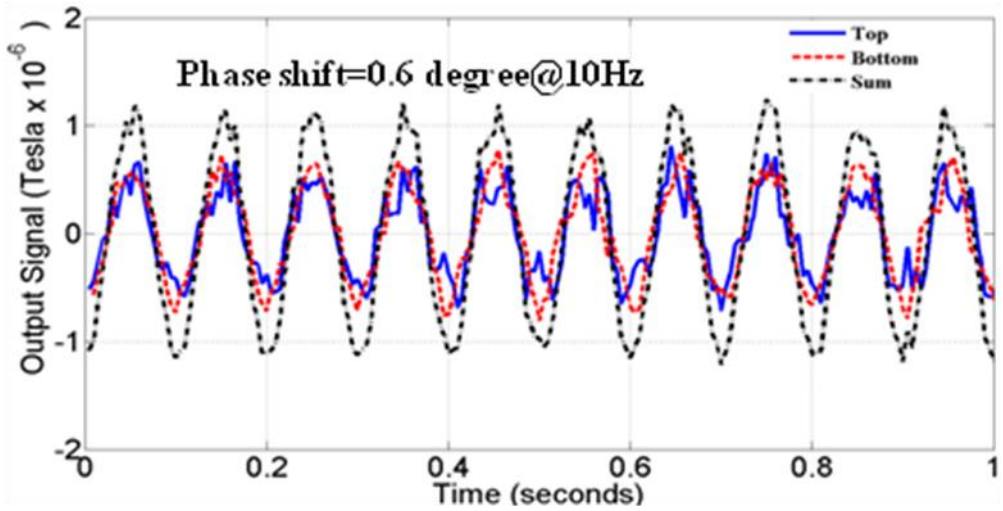

(a)

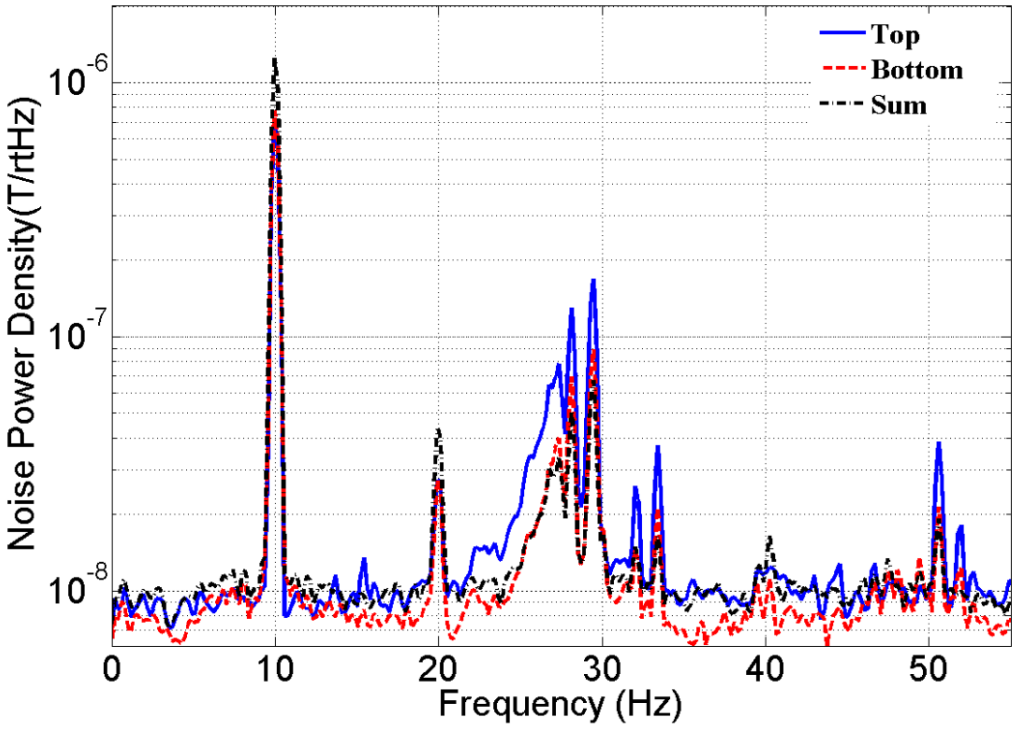

(b)

Figure 3.14 (a) Time-domain response of top PZT layer, bottom and sum of individual signals in response to an incident magnetic field; and (b) power spectral density response of a sensor to a 10 Hz magnetic field.

Finally, the capability for vibration signal cancellation of our new differential ME structure was compared to that of a non-differential one of similar geometry. Following analysis similar to that above, the different working modes under various excitation sources were studied. The results demonstrate that the new differential structure has the ability to reject an incident vibration signal by summation of the signals of top and bottom PZT layers. In this measurement, the top and bottom PZT layers were connected in parallel at first, and a single charge amplifier was used to collect the signal. Simultaneously, a second non-differential ME laminate connected to another charge amplifier was used as a control group. Both of these two signals were observed together by an oscilloscope. The shaker was put in the middle of the differential and non-differential ME structures and a 10 Hz driving signal was excited.

Figure 3.15 shows the signals from the differential and non-differential ME sensors, obtained directly from the oscilloscope. In this figure, the signal amplitude of the non-differential sensor was about 80 mV, whereas, that of the differential ME structure was only about 20 mV.

Clearly, our new differential structure shows excellent capacities with regards to vibration signal cancellation. Furthermore, the fact that we can separate magnetic and vibration signals is important in and of itself. Hybrid sensors capable of data fusion between two separated signals of an environment could be enabled.

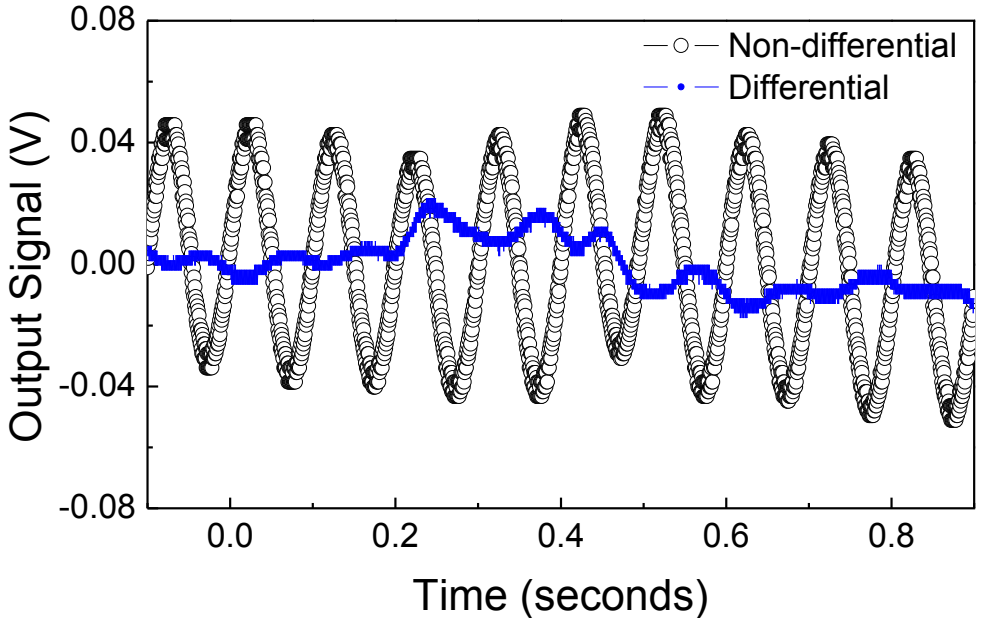

Figure 3.15 Comparison of noise cancellation for a differential ME structure sensor and a non-differential ME structure sensor.

3.4 Summary of this section

In summary, investigations directed at enhancing the ME voltage coefficient have been performed, such as different piezo-fibers, volume ratios, and heat treatments. In addition, I have proposed a differential structure for Metglas/PZT laminate to reject the external vibration noise.

(i) Using PMN-PT and PZN-PT single crystal fibers, one can improve the ME voltage coefficient by over 2× compared to PZT fibers. The sensitivity for magnetic sensors based on those single crystal fibers is likewise enhanced. The drawback is the high cost of the crystals, which can be reduced a little by using highly orientated PMN-PT fibers that also have high piezoelectric properties.

(ii) The volume ratio between Metglas and PZT layers was found to have a significant influence on the ME effect. The findings show that the ME coefficient can be increased by 1.4×, offering another effective means by which to optimize the ME laminates.

(iii) Heat treatment can affect the electromechanical factor for Metglas 2605. By annealing the Metglas foils at 350℃, the ME coefficients of the laminate was found to be increased.

(iv) A differential structure was developed that can notably reject the vibration noise. Additional investigations are needed to optimize this structure to realize its full rejection efficiency.

4. AC magnetic sensor

4.1 Introduction

I have developed a novel type of AC magnetic sensor, based on ME composites, which has advantages over the presently available ones. The sensors need to meet the following requirements: (i) high sensitivity or low noise at quasi-static frequencies (~pT/√Hz at 1 Hz); (ii) low power consumption offering the potential for long-term operation; (iii) compact size; and (iv) low cost.

In addition to the external noise that I mentioned in the last chapter, the internal noise in the detection unit needs investigations. Such internal noise is an important aspect to identifying the potential of ME laminate as AC magnetic sensors. In this chapter, I will discuss the internal noise sources in AC magnetic sensors and address some methods by which to attenuate the spectral noise density.

4.2 Passive magnetic sensor unit

Considering the giant internal impedance of ME laminates, an induced charge detection method has been developed to detect the induced signals from ME composites in response to the incident magnetic field. Quasi-static models of the ME composite and detection circuit have been investigated in previous studies.[45, 64] Figure 4.1 (a) shows a photograph of a passive magnetic sensor detection unit: it contains an analog charge amplifier circuit and a ME laminated composites. Two

small dc magnets were used to bias the laminate to work at the optimized α_{me} value, as shown in Figure 4.1 (b). Based on different application requirements, the detection circuit can be modified to optimize the ME magnetic sensor unit to particular frequency ranges.

One of the most important parameters to evaluate magnetic sensors is the spectra noise density (SND) which limits the detection sensitivity of a sensor unit. Previous measurements were mainly concerned themselves with the SND over a broad frequency range, which is not necessarily accurate to describe a sensors performance at a specific frequency. Meanwhile, the SND was measured using a commercially available charge amplifier (Kistler 5015). Though this method is capable of detecting the noise, one must bear in mind that the charge amplifier noise itself cannot be neglected.

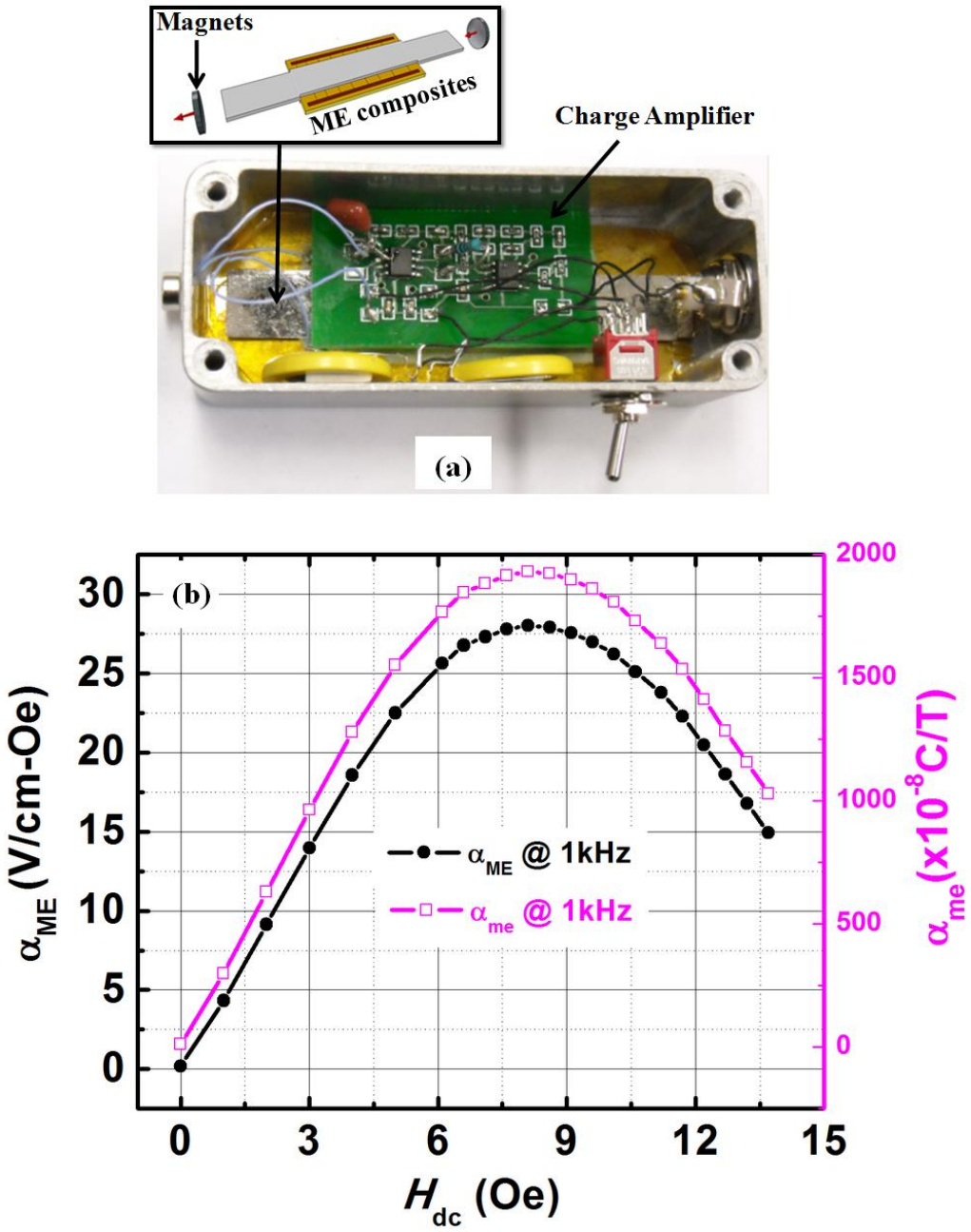

Figure 4.1 (a) Schematic illustrations of Metglas/PMN-PT ME composites; and (b) ME voltage coefficient α_{ME} and ME charge coefficient α_{me} for Metglas/PMN-PT laminates as function of H_{dc}.

In this thesis, a low noise charge amplifier was developed and assembled with ME composites to form a magnetic sensor unit, and the noise sources were characterized for the unit instead of only the composites part. Based on this method, the transfer function in units of V/pC for each magnetic sensor unit has been identified. Figure 4.2 shows the transfer function of a detection circuit with designed to have a frequency bandwidth of 1 to 1600 Hz. Considering the strong Electromagnetic Interference (EMI) at 60 Hz resulting from power lines, a notch filter was induced in the circuit to attenuate the signal at this specific frequency. Clearly, my lab-made circuit has demonstrated to have a uniform gain factor of about 1 V/pC over the frequency range from 1 Hz to 1600 Hz, except near 60 Hz.

A Metglas/PZT ME laminate was then assembled with this wide band frequency circuit as the magnetic sensor unit shown in Figure 4.1. The intrinsic magnetic noise for this unit was characterized in a magnetic shielding chamber to reject the external magnetic noise and EMI. The SND was detected by using a dynamic signal analyzer in units of V/√Hz. The detected signal was then converted to equivalent magnetic noise in units of T/√Hz by the following equation:[79]

$$\begin{aligned} Conversion\ factor(V/Oe) &= \frac{\alpha_{me}(pC/Oe)}{1pC/V} \\ Noise\ floor(T/\sqrt{Hz}) &= \frac{Noise\,floor(V/\sqrt{Hz})}{Conversion\ factor(V/Oe)} \times 10^{-4} \end{aligned} \tag{4.1}$$

where, α_{me} is the ME charge coefficient at the optimized bias. For this detection unit, the ME charge coefficient was α_{me} = 200 pC/Oe.

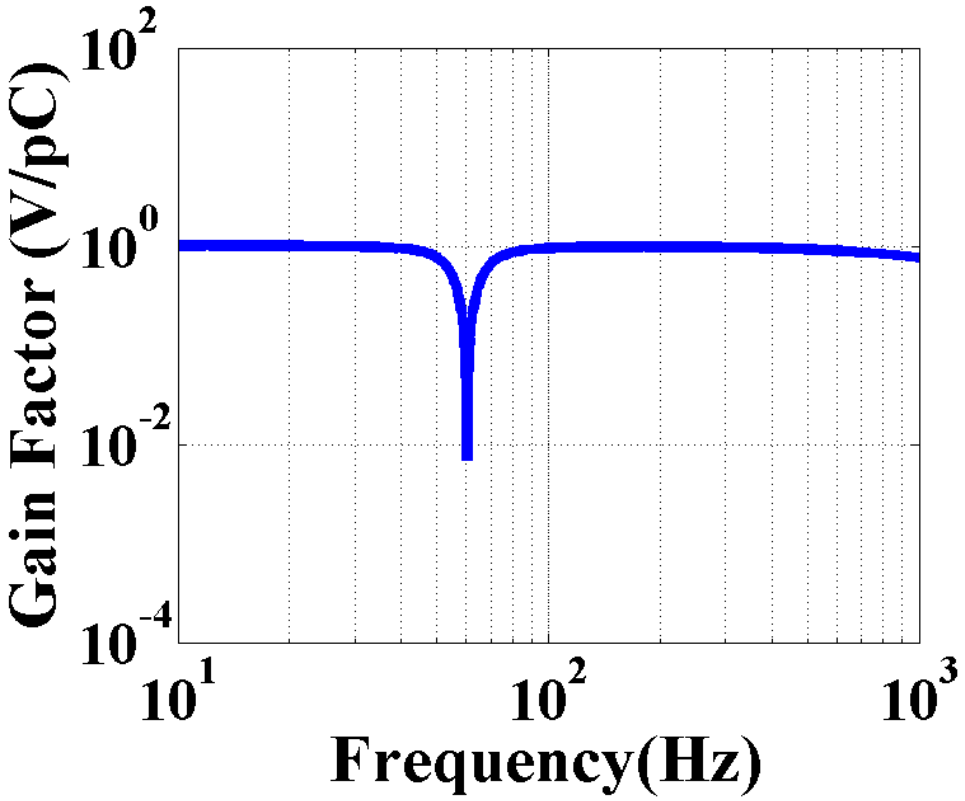

Figure 4.2 Transfer function of detection circuit.

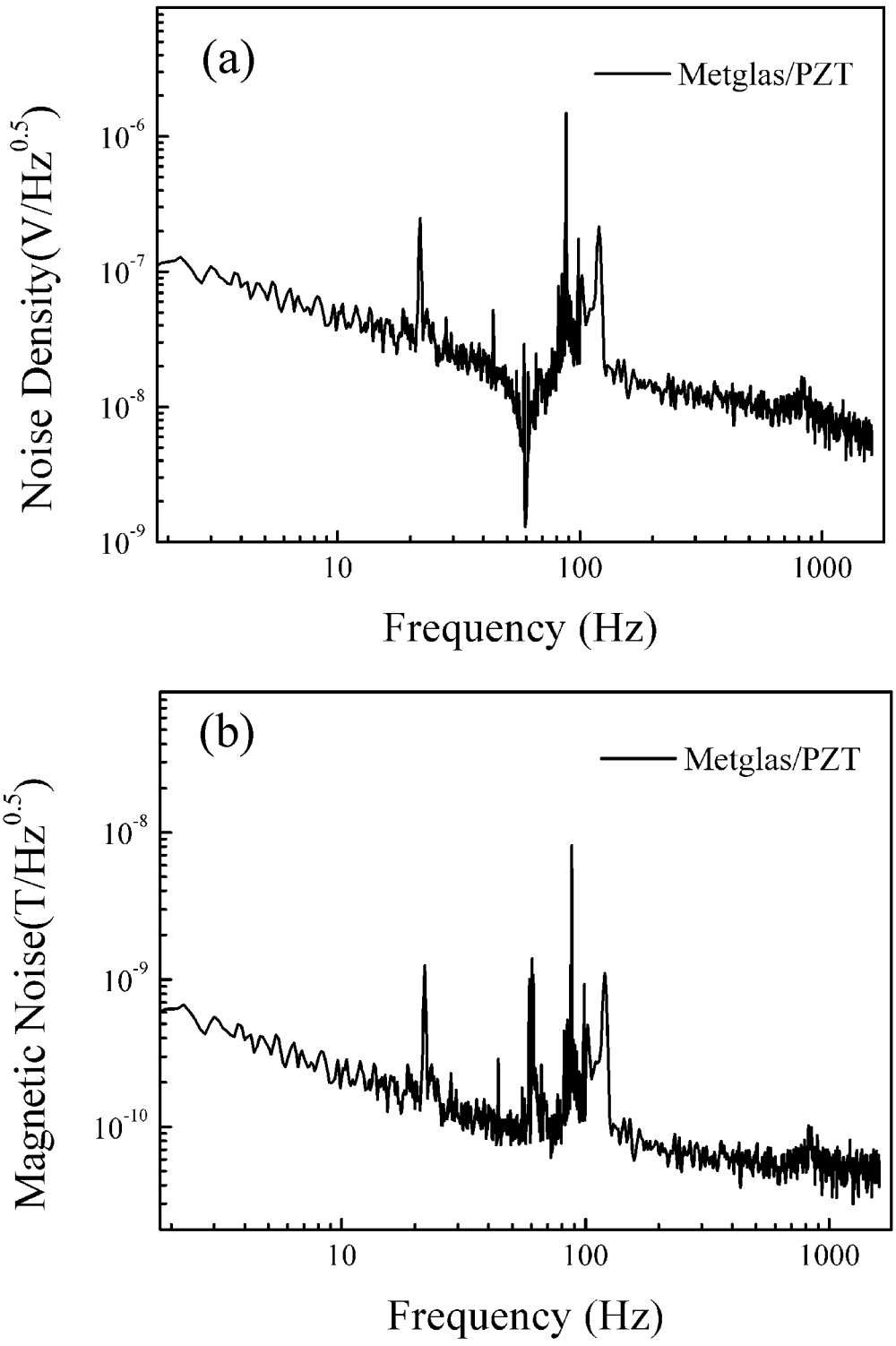

Figure 4.3 Equivalent magnetic noise density spectra: (a) Voltage noise density detected by dynamic signal analyzer; and (b) equivalent magnetic noise density after conversion.

Figure 4.3 (a) shows the direct measurement of the voltage noise density of the sensor unit by using a dynamic signal analyzer (SR-785) over the frequency range from 1.8 Hz to 1600 Hz. From this figure, the noise density near 60 Hz was decreased sharply due to the notch filer mentioned above: the noise density was only about 1.49 nV/√Hz at 60 Hz. However, the intrinsic magnetic noise density calculated using Equation 4.1 presents a different noise sources from that of the voltage noise density, as shown in Figure 4.3 (b). From the spectrum, one can see the magnetic noise at 60 Hz was still much higher than the values at other frequencies. This was a direct result of EMI interference, although the sensor unit was placed in a magnetic shielding chamber. In detail, the magnetic noise at 1.8 Hz was almost 7×10^{-10} T/√Hz, which decreased with frequency increasing. The noise density was about 5×10^{-11} T/√Hz at 1000 Hz, which was dominantly influenced by the 1/*f* noise in the electronic circuit and materials. The detailed noise model will be discussed in the following section.

In addition to the wide band detection unit, a low frequency detection unit has also been designed to work over the frequency range from 0.8 Hz to 10 Hz. This narrower bandwidth detection unit was developed to reduce the noise floor. The output voltage noise as function of frequency bandwidth can be described as:

$$E_n = (\int_{f_L}^{f_H} e_n^2(f)df)^{1/2}; \tag{4.2}$$

where E_n is the mean square value of voltage noise, $e_n(f)$ is the spectral noise density which is dependent on frequency f, and f_L, f_H are the lower and upper limits of the frequency band of interest, respectively.

Equation 4.2 clearly indicates that a narrower frequency bandwidth may have a lower output noise, as given a similar voltage noise density. Figure 4.4 shows the gain factor of a low frequency detection circuit. It can be seen that the circuit had a totally different transfer function than the wide band ones. It had a homogenous gain only over the frequency range of 1 Hz to 10 Hz, with a 3-dB point near 12.5 Hz. This type of circuit, assembled with a ME laminates, can be used for low frequency magnetic field detection with reduced equivalent magnetic noise floors.

In order to demonstrate the benefit of the low frequency circuit, a Metglas/PZT laminates was assembled with both the low frequency and wide bandwidth circuits. During the measurements, a pair of H-coils driven by lock-in amplifier was used to generate AC magnetic fields at 1 Hz and 10 Hz for these two sensor units. The output signals from the sensors were monitored by an oscilloscope in the time domain. The AC magnetic field was modulated to keep the signal-to-noise ratio constant at the value of SNR=2.

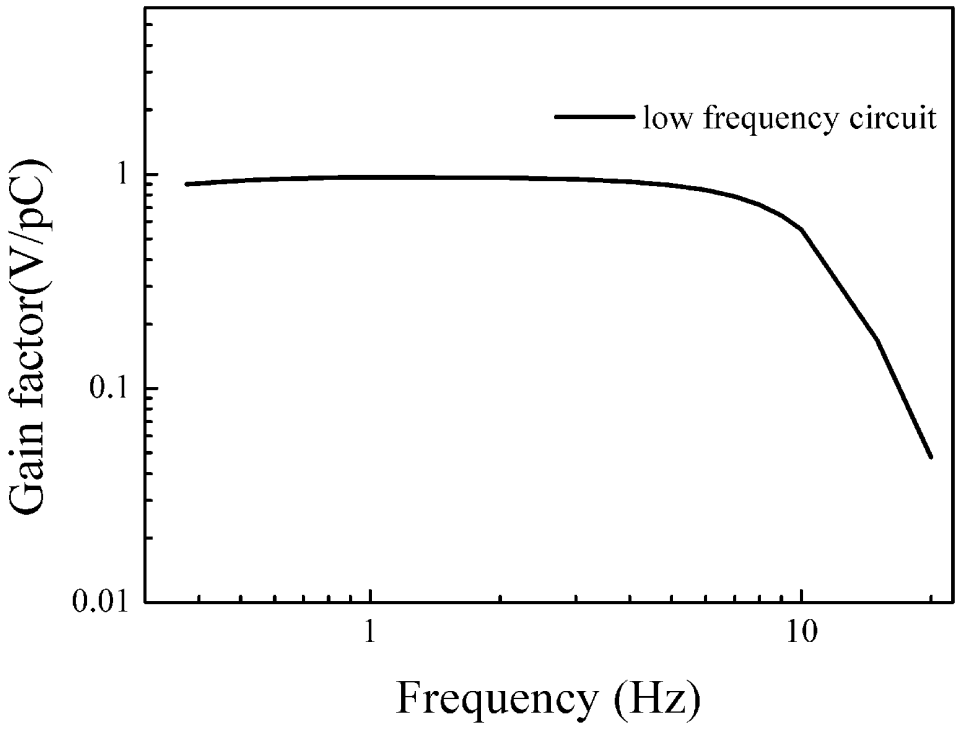

Figure 4.4 Transfer function of low frequency detection circuit.

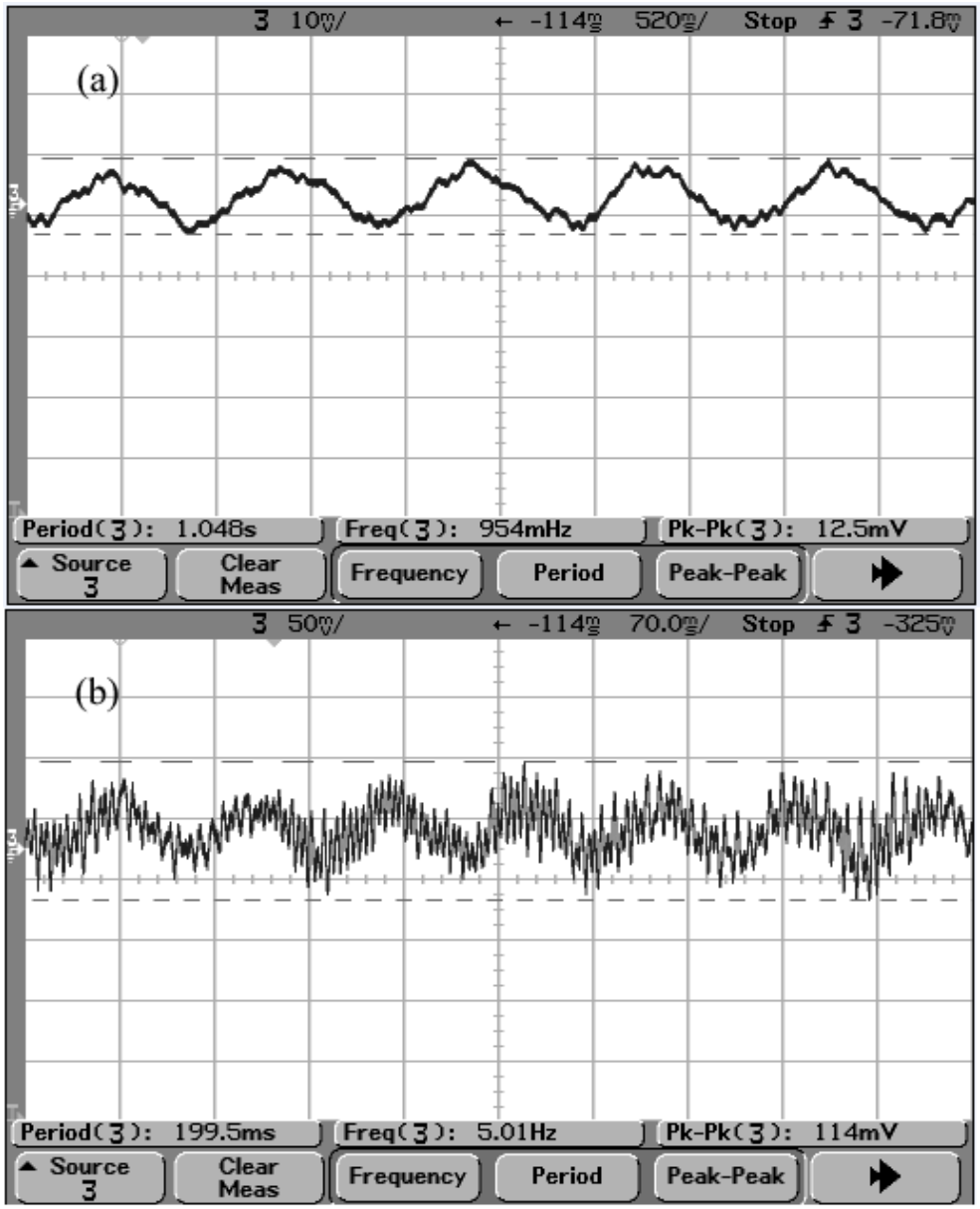

Figure 4.5 Output signal in response to the incident magnetic field: (a) low frequency detection sensor circuit, and (b) wide band frequency detection sensor unit.

Figure 4.5 shows the measurement results for these two magnetic sensors. Panel (a) indicates the low frequency magnetic sensor in response to AC magnetic field at frequency of 1 Hz with the amplitude of 0.4 nT. The amplitude of signal is about 12.5 mV, which is two times larger than output noise. Panel (b) shows the output signal from the wide band magnetic sensor in response to AC magnetic field at frequency of 10 Hz with amplitude of 2.5 nT, that corresponds to an amplitude of 114 mV in order to satisfy the SNR=2. From this comparison, it can be seen that the wide band magnetic sensor has a larger voltage noise compared to the low frequency one. Moreover, the small spikes at 60 Hz were also observed in this unit due to the detectable frequency range from 1 Hz to 1600 Hz, although 60 Hz notch filter has been designed in detection circuit. The specific detection circuit can enhance the performance of magnetic sensor according to the practical application.

Considering that the low frequency circuit has better performance, more characterizations have been performed to study the sensor assembled with low frequency circuit. Firstly, the linearity of the sensor was measured. During the test, an incident magnetic field as small as 0.88 nT at 1 Hz was applied to the magnetic sensor, and then the amplitude of the field was increased gradually. Figure 4.6 shows the output signal as function of incident magnetic field. From the figure, one can see that the ME composites based sensor shows great linearity in response to the external field with the dynamic range. Moreover, the dynamic range can be determined by using the similar measurement. In detail, the waveform of the magnetic sensor indicated the distortion as applied the field over 106 nT. Thus, the dynamic range was considered as below 100 nT.

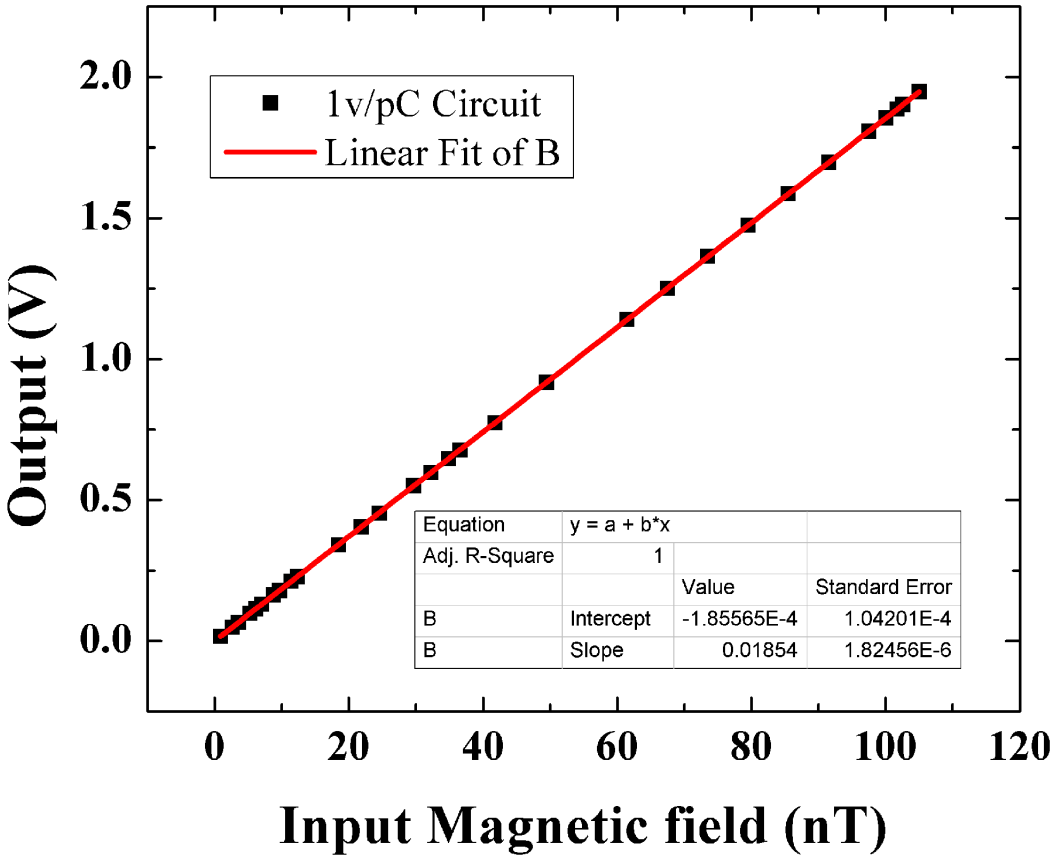

Figure 4.6 Linearity of magnetic sensor assembled with low frequency circuit.

The equivalent magnetic noise density spectra were then measured as absence of magnetic field. The result was shown in Figure 4.7. From the figure, one can see the magnetic noise was about 15 pT/√Hz at 1 Hz.

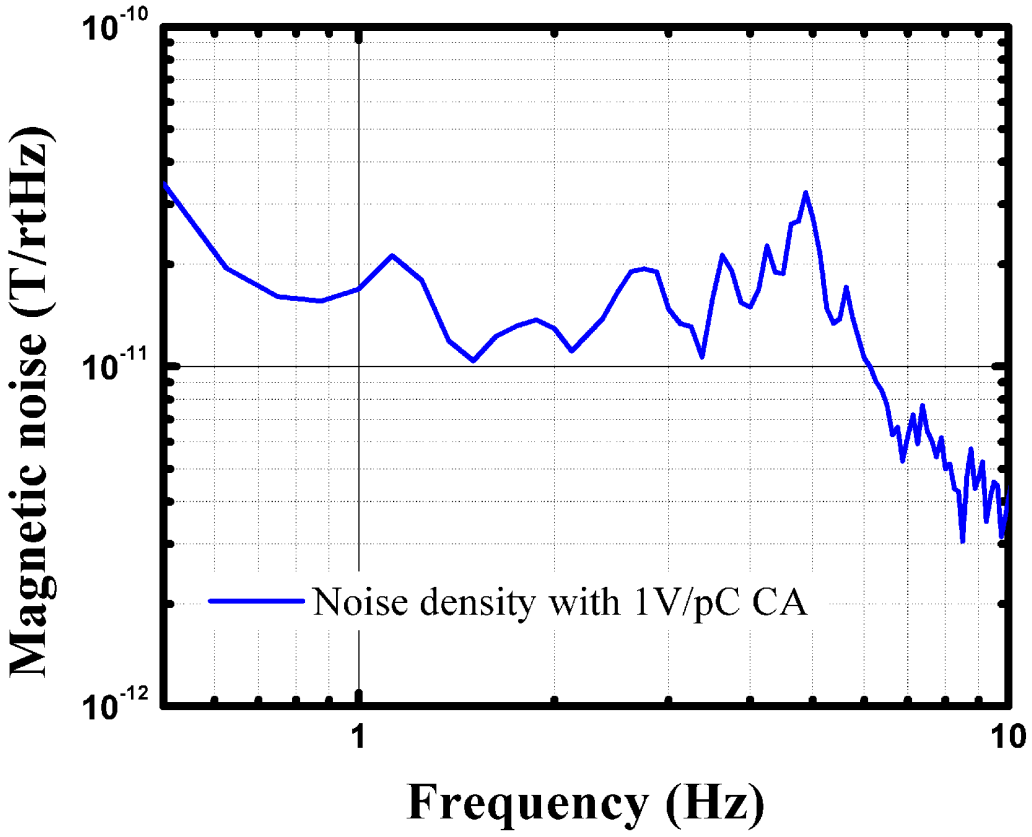

Figure 4.7 Equivalent magnetic noise spectra.

4.3 Extremely low frequency magnetic sensor

Besides the noise floor, another important consideration for design of magnetic sensor is the frequency bandwidth of detectable magnetic fields. Some specific applications require extremely low frequency detection. For example, the magnetoencephalography (MEG) measurements span a frequency range from about 10 mHz to 1 kHz.[80] However, previous investigations show the frequency bandwidth of 1 Hz < f <1 kHz.[81] In this section, one quasi-static frequency detection sensor unit based on Metglas/Pb($Mg_{1/3}Nb_{2/3}$)O_3-$PbTiO_3$ (PMN-PT) ME laminated composites was developed.[82] In detail, an extremely low frequency (ELF) charge amplifier circuits were designed with cutoff frequencies of f <1 mHz, which allowed us to characterize ME effect at frequency range down to $f \leq 1$ mHz.

4.3.1 Charge amplifier circuit design

Firstly, the 10 mHz magnetic sensor was developed. In order to characterize the ME effect for Metglas/PMN-PT laminated composites and to fabricate the magnetic sensor at quasi-static frequency, a charge amplifier with extremely low cut-off frequency ($f_c \leq 10$ mHz) was proposed. The circuit design was partially based on a previous report,[45] as illustrated in Figure 4.8 (a). The biggest challenge for this circuit design was to reduce the cut-off frequency to be $f_c \leq 10$ mHz, while maintaining a reasonable circuit transfer function (V/pC), otherwise the output voltage would be significantly reduced. In addition, the circuit noise was another important factor that needed to be taken into account.

Figure 4.8 (a) illustrates the charge amplifier as containing two parts: pre-amplifier and band-pass filter stages. The transfer function in (V/pC) of the preamplifier part can be written as:

$$H_1(s) = \frac{1}{C_f}\frac{sR_fC_f}{1+sR_fC_f}; \tag{4.3}$$

where the R_f and C_f are the feedback resistor and capacitor, respectively. *s* is a complex frequency. For a sine wave signal drive, $s = j\omega$: where $\omega = 2\pi f$ is the angular frequency. Meanwhile, the cut-off frequency of the pre-amplifier part was determined by R_f and C_f as well, given as:

$$f_c = \frac{1}{2\pi R_f C_f}. \tag{4.4}$$

In order to design an extremely low frequency charge amplifier, the value of f_c should be smaller than 10 mHz. However, one is not free to choose arbitrary values of R_f and C_f to control f_c. There are several other factors that need to be considered. For example, the bias current of the op-amp needs to be sufficient to avoid saturation, and also the leakage charge from the capacitor must be small.[45] As the circuit is operated at the bandwidth range: $f > f_c$ for preamplifier part, the transfer function can be simplified as:

$$H_1(s) \approx \frac{1}{C_f}. \tag{4.5}$$

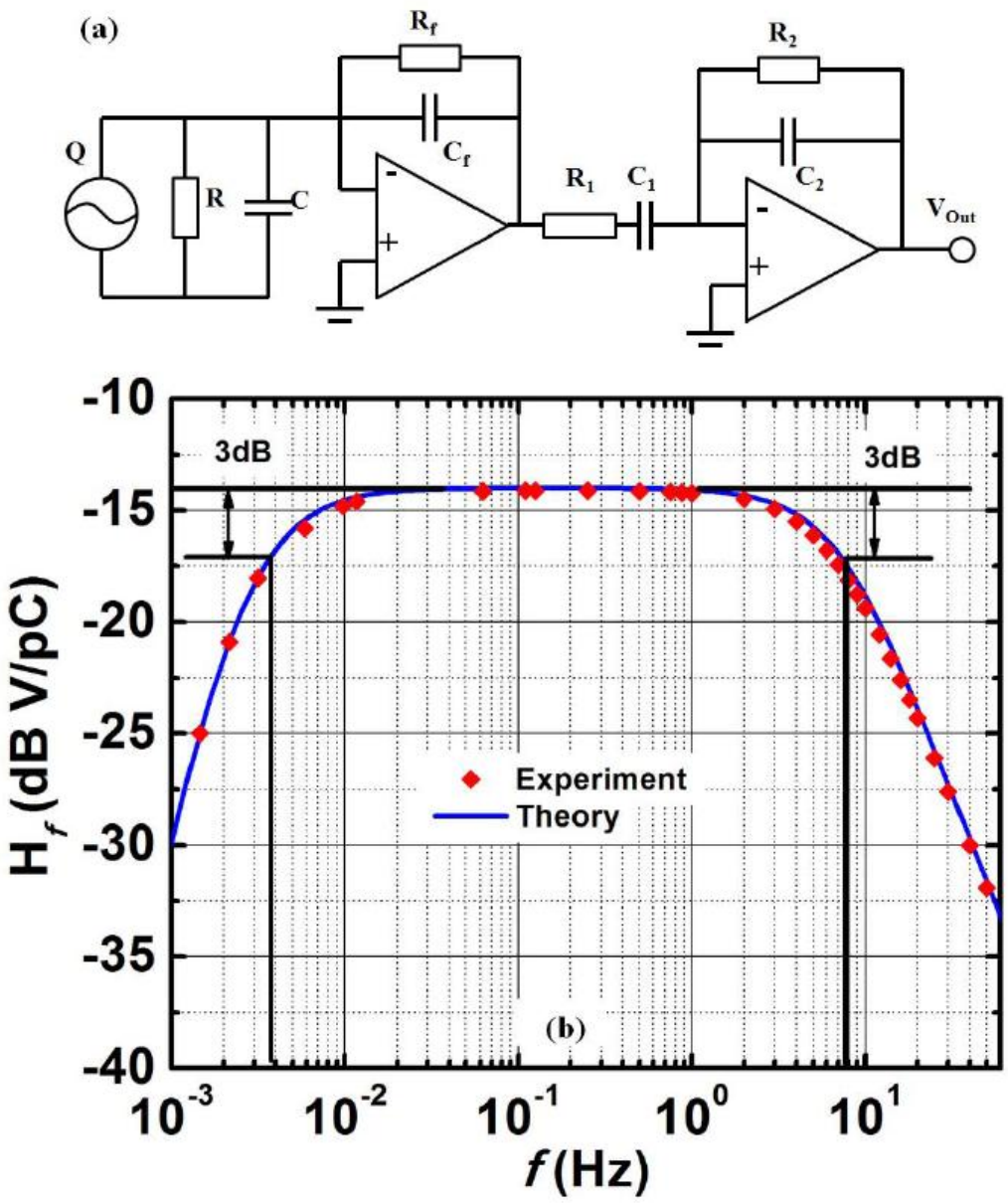

Figure 4.8 (a) Charge amplifier design for quasi-static magnetic sensor, and (b) predicted and measured transfer functions of the circuit.

In my design, I chose feedback capacitors and resistors with values of C_f = 1000 pF and R_f =50 Gohm, respectively. Thus, the cut-off frequency was fixed at *f*c = 3.184 mHz, which satisfied the requirements for detection of magnetic signals for frequencies as low as $f = 10^{-2}$ Hz. Unfortunately, the amplitude of the transfer function given in (3) for this pre-amplifier stage was decreased by a factor of 10×, compared to previously reported detection circuit.[29] However, the filter stage of the circuit (see Figure 2(a)) can be used to increase the transfer function. The transfer function in (V/V) of this filter can be written as:

$$H_2(s) = -\frac{R_2}{R_1}\frac{R_1C_1s}{R_1C_1s+1}\frac{1}{R_2C_2s+1}. \tag{4.6}$$

This second stage was a single bandpass filter which sets the bandwidth of the signal to be:

$$\frac{1}{2\pi R_1C_1} < f_{bp} < \frac{1}{2\pi R_2C_2}. \tag{4.7}$$

In considering these two functions for the filter stage, I set the bandpass filter to work over the frequency bandwidth of 1.59 mHz <f_{bp} <7.96 Hz. The transfer function was then designed to be 200 (V/V), and the overall gain factor for both stages together in (V/pC) was:

$$H(s) = |H_1(s)| \times |H_2(s)| = \frac{1}{1000p} \times 200 = 0.2\ (\frac{V}{pC}). \tag{4.8}$$

Figure 4.8 (b) shows the predicted and experimental values for the transfer function of the charge amplifier detection unit. During the measurement, one 440 pF capacitor was connected to the charge amplifier circuit. An AC signal with amplitude of 10 mV_{rms} was applied to the capacitor at various frequencies, and the output

voltage from circuit was then monitored by a dynamic signal analyzer (SR-785). Finally, the transfer function was calculated by using the output voltage divided by the input charge. From the figure, one can see that the values match quite well. The experimentally-observed cut-off frequencies were 3.56 mHz and 7.58 Hz, which are quite closed to the predicted ones.

Finally, I assembled the ME laminated composites and charge amplifier circuit together into battery-operated magnetic sensor detection units, as shown in Figure 4.1 (a). In this unit, two small dc magnets were used to bias the composites with optimum α_{me} value.[82] I then characterized the ME charge coefficients at extremely low frequency range. During the test, the *H*-coils was used to generate 10 nT AC magnetic field to the magnetic sensor at various frequencies, the signals were monitored by dynamic signal analyzer to analysis the amplitudes and then were displayed by an oscilloscope to present the waveforms. Figure 4.9 present the values of α_{me} over the frequency range of 7×10^{-3} Hz < f < 20 Hz: the values of α_{me} were constant around 1900×10^{-8} C/T which was closed to the value at 1 kHz. The insert shows the waveform of sensor's response to a 10 mHz ac magnetic field signal in the time domain.

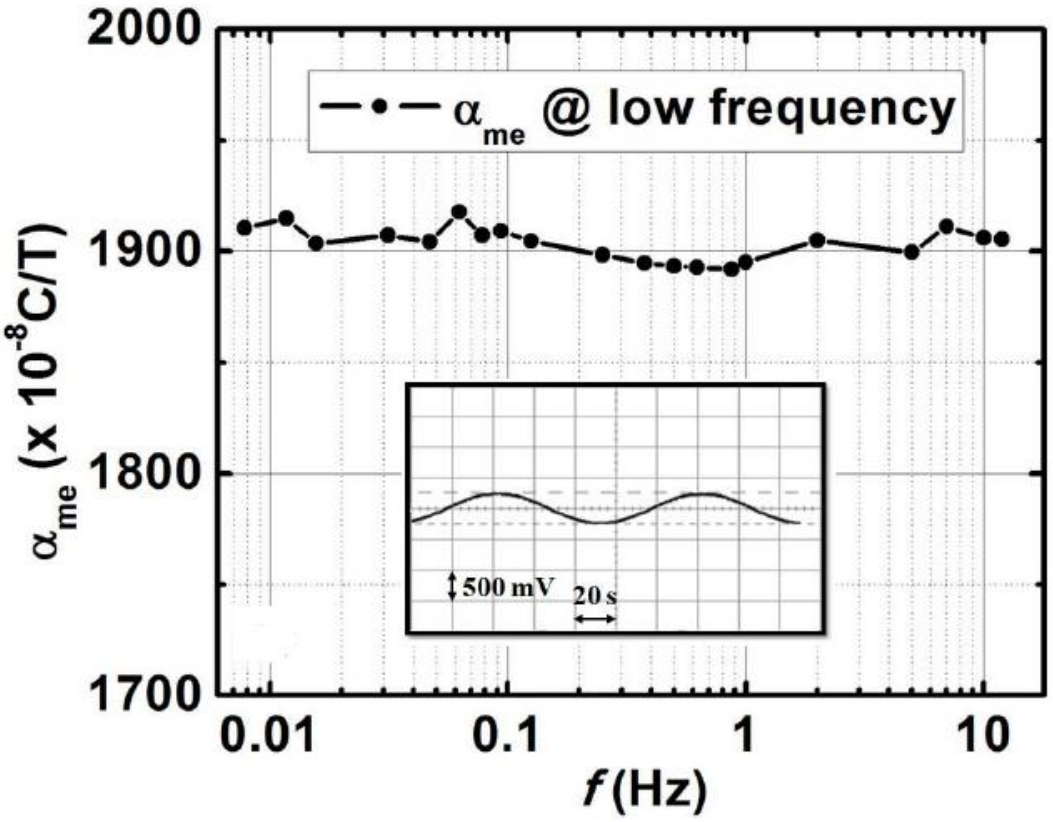

Figure 4.9 ME charge coefficients at quasi-static frequency range. The insert is the output voltage of circuit in response to a 10 mHz input charge.

4.3.2 Charge noise model

As described before, the equivalent magnetic noise density is a very important parameter which limits the detection sensitivity at a specific frequency. Thus, I also characterized the noise density spectra of the extremely low frequency magnetic sensor. Previously, the current noise model has been proposed, which considered the noise source in both of ME composites and detection circuit as the current noise source.[64] Most recently, the charge noise model has been also developed.[83, 84] Considering the charge induced by ME composites in response to incident magnetic field, the charge noise model was applied in this research. However, the previous models were not accurate to describe the magnetic noise for sensor units. Normally, the literatures considered the noise sources for ME magnetic sensor were contributed from ME composites and detection circuit. In detail, the noise sources from ME composites were considered as dielectric loss noise and leakage resistance noise. For the circuit part, the noise sources were considered to be dominated by the charge preamplifier part, including the thermal noise from feedback resistor, current noise and voltage noise in op-amp chips.[64, 71, 81, 83] Thus, a total of five noise sources were analyzed in these literatures, and the investigations show the estimated noise density spectra were quite closed to the measured results.

However, the model presented before indicated the limitation as an extension of the detectable frequency range of magnetic sensor down to 0.01 Hz. Figure 4.10 shows the results of one Metglas/PMN-PT with extremely low frequency circuit with frequency range from 0.01 Hz to 10 Hz. Table 4.1 lists the parameters of the Metglas/PMN-PT ME composites, and Table 4.2 lists the parameters of the circuit.

Table 4.1 ME composites properties

ME composites	C (pF)	R (GΩ)	Tanδ	α_{me}@ 1 kHz
Metglas/PMN-PT	175	195	1.2%	1.930×10^{-5} C/T

Table 4.2 Circuit components used for charge amplifier

Op-amp	$e_{n,1Hz}$ (nV/√Hz)	$e_{n,1kHz}$ (nV/√Hz)	i_n (fA/√Hz)	R_f (GΩ)	C_f (pF)	R_1 (MΩ)	R_2 (MΩ)
LMC6042 [a)]	230	83	0.2	50	1000	10	2000

a) Cited from LMC 6042 Operational Amplifier, Texas Instruments

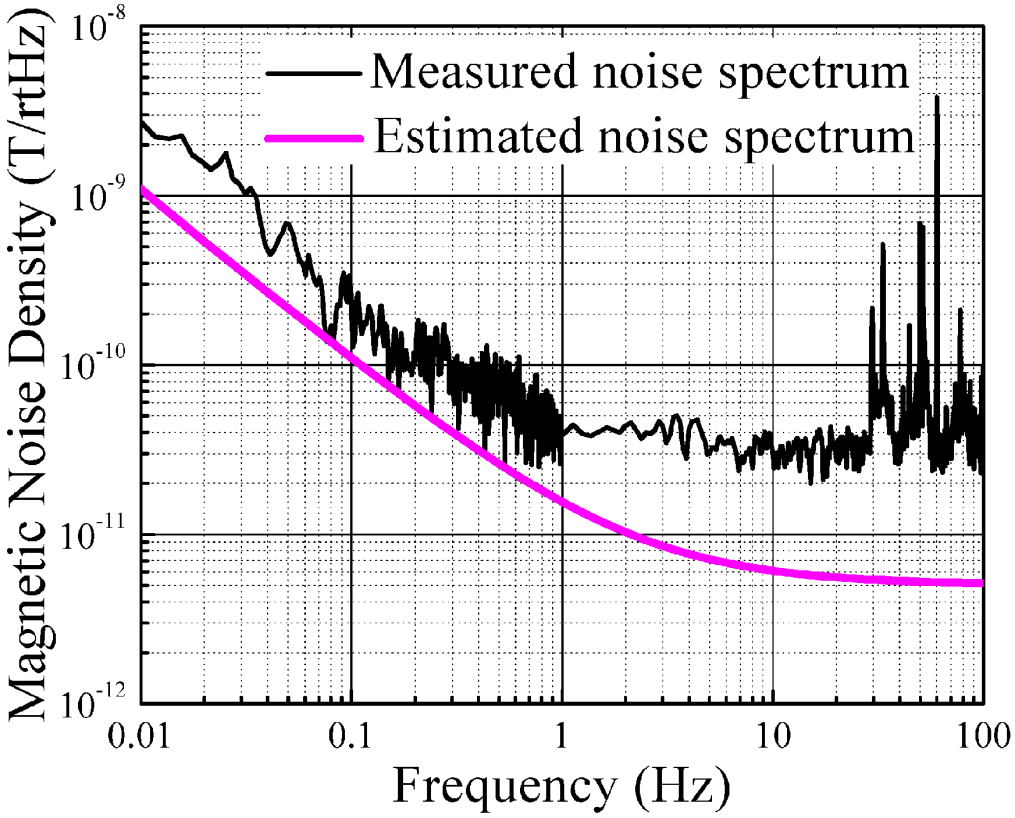

Figure 4.10 Estimated and measured equivalent magnetic noise of the magnetic sensor based on previous noise model.

From Figure 4.10, one can see that the estimated magnetic noise is much lower than that of measured values, especially at frequency range of f > 1Hz. Below frequency of 0.07 Hz, the measured noise was higher than estimated due to the low frequency vibration that wasn't being rejected clearly by floating table. That would be investigated in the following study. However, it was hard to explain the frequency above 1 Hz. At frequency of f > 10 Hz, the measured values were almost consistent larger than predicted by a factor of 6×. I considered the proposed model has some limitation that could not describe the sensors' noise for the magnetic sensor unit. Thus, more detailed investigations were performed to optimize the charge noise model.

In this modulated noise model, I still considered five noise sources which have main contributions to the total noise density. For ME composites, there are dielectric loss noise (N_{loss}), thermal noise of the leakage resistor (N_{R}).[65] The current (N_{i}), voltage (N_{e}) noises from op-amp and thermal noise (N_{Rf}) from feedback resistor were the main noise sources in electronic part.

The noise charge density in (C/√Hz) for the preamplifier part can be expressed as:

$$
\begin{aligned}
&N_R = \frac{1}{2\pi f}\sqrt{\frac{4k_bT}{R}}; N_{loss} = \sqrt{\frac{4k_bTC\tan\delta}{2\pi f}};\\
&N_{R_f} = \frac{1}{2\pi f}\sqrt{\frac{4k_bT}{R_f}}; N_{i1} = \frac{1}{2\pi f}i_n; N_{v1} = e_n(1+\frac{Z}{Z_f})/\left|H_1(s)\right|; \qquad (4.8)\\
&e_n = (e_{n,1Hz} - e_{n,1kHz})/\sqrt{f} + e_{n,1kHz};
\end{aligned}
$$

where k_b is the Boltzmann constant, T is the absolute temperature, tanδ and R is the dielectric loss factor and leakage resistance of the ME composites, i_n is the current noise density and v_n is the voltage noise density of the amplifier.

Besides the preamplifier part, the noise sources from bandpass filter part were also considered to have the contributions to the total noise as well, including thermal noise from feedback resistors of R_1 and R_2, current and voltage noises in op-amp chips, as shown in Figure 4.11 (a). The noise charge density in (C/√Hz) for this stage can be written as:

$$N_{R_1} = \frac{\sqrt{4k_bTR_1}}{|H_1(s)|}; N_{R_2} = \frac{\sqrt{4k_bTR_2}}{|H_1(s)|\times|H_2(s)|};$$

$$N_{i2} = \frac{i_n \times Z_2}{|H_1(s)|\times|H_2(s)|}; N_{v2} = \frac{e_n(\frac{Z_1+Z_2}{Z_1})}{|H_1(s)|\times|H_2(s)|}; \quad (4.9)$$

$$e_n = (e_{n,1Hz} - e_{n,1kHz})/f + e_{n,1kHz}.$$

Thus, the total noise density in (T/√Hz) can be written as:

$$N_T = \frac{1}{\alpha_{me}}\sqrt{N_R^2 + N_{loss}^2 + N_{R_f}^2 + N_{i1}^2 + N_{v1}^2 + N_{R_1}^2 + N_{R_2}^2 + N_{i2}^2 + N_{v2}^2}. \quad (4.10)$$

The parameters given in Table 4.2 were then used to calculate the equivalent magnetic noise using equation (4.10).

Figure 4.11 (b) shows the equivalent magnetic noise density. This figure shows both the measured data and the predicted values. One can see that the experimental results matched the predicted ones by modulated charge noise model quite closely over the frequency range of 0.07 Hz < f < 100 Hz. However, below 0.07 Hz, the measured value increased more rapidly with decreasing frequency than the predicted

one due to the environmental noise in nature. The equivalent magnetic noise density at 10 mHz was around 3 nT/√Hz, which decreased significantly with increasing frequency to around 30 pT/√Hz at 1 Hz.

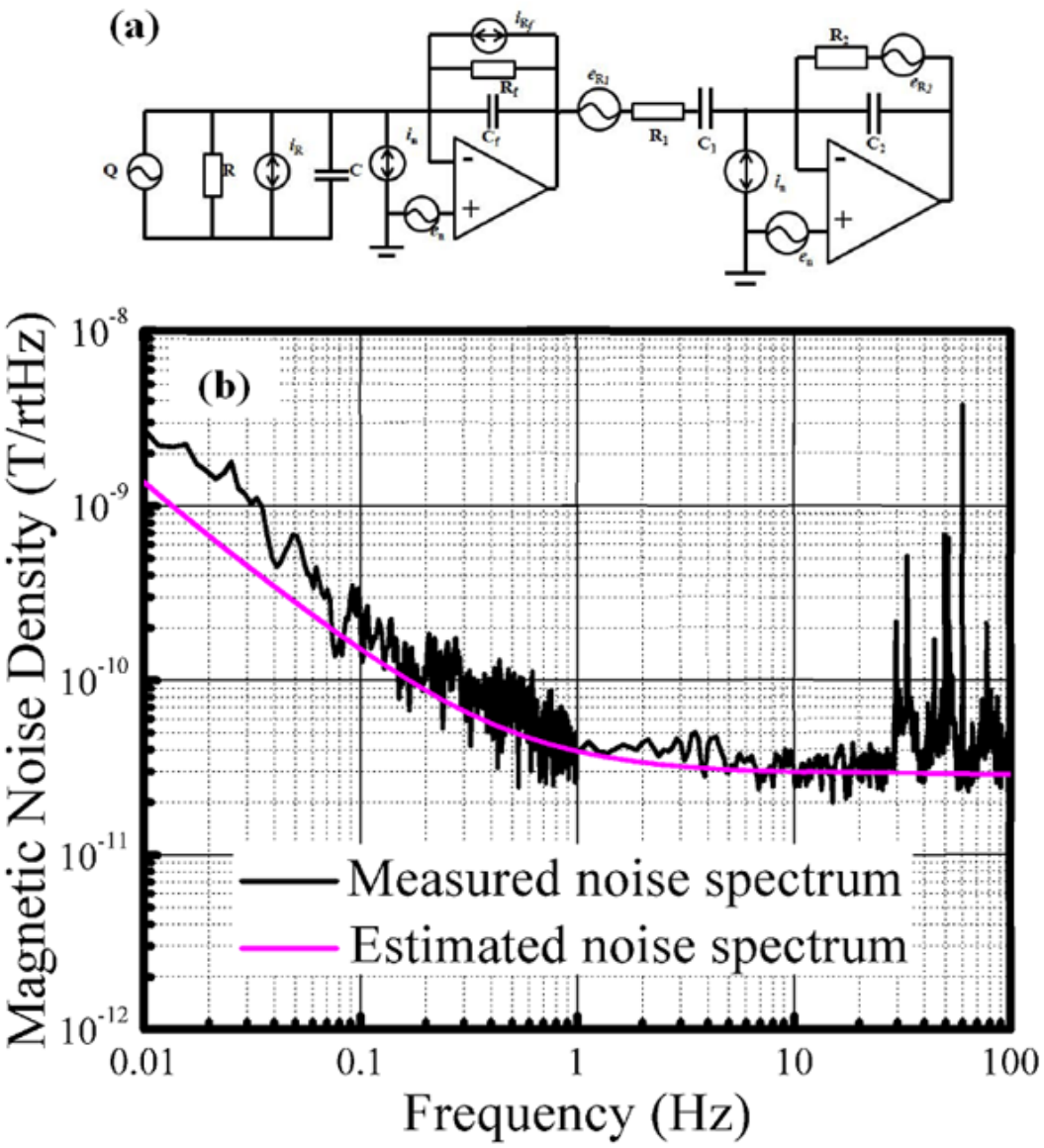

Figure 4.11 (a) Theoretical model for noise sources in our ME magnetic sensor; and (b) estimated and measured equivalent magnetic noise of the sensor.

4.3.3 ELF magnetic sensor optimization

In the previous section, an ELF magnetic sensor which can work down to 0.01 Hz was proposed. Moreover, a more accurate charge noise circuit model was also established which can predict the sensors' performances much more precisely. However, the noise floor at low frequency range is still much higher than estimated values, which indicated there were still some external noise sources as placed the sensor inside chamber on top of vibration shielding table. In order to confirm this assumption, one pair of sensors were setup inside of chamber to analyze the common external noise.[85] The fundamental signal processing can be found in Ref.[85]. Through analysis of coherency between two sensors, one can see if there is a common noise inside the chamber. First of all, the transfer function of the sensors was measured to eliminate the influence from circuits. Figure 4.12 (a) shows the transfer function of two sensors as function of frequency. In this measurement, two low frequency circuits were used which had the uniform gain factors over frequency range from 1 to 10 Hz. The transfer functions at 1 Hz were very identical with the amplitudes of over 7×10^6 V/T. During the test, the output signals from sensors were collected by digitizer SR 1000 and then the signal processing was applied to analyze the coherence between them at frequency domain, as shown in Figure 4.12 (b).

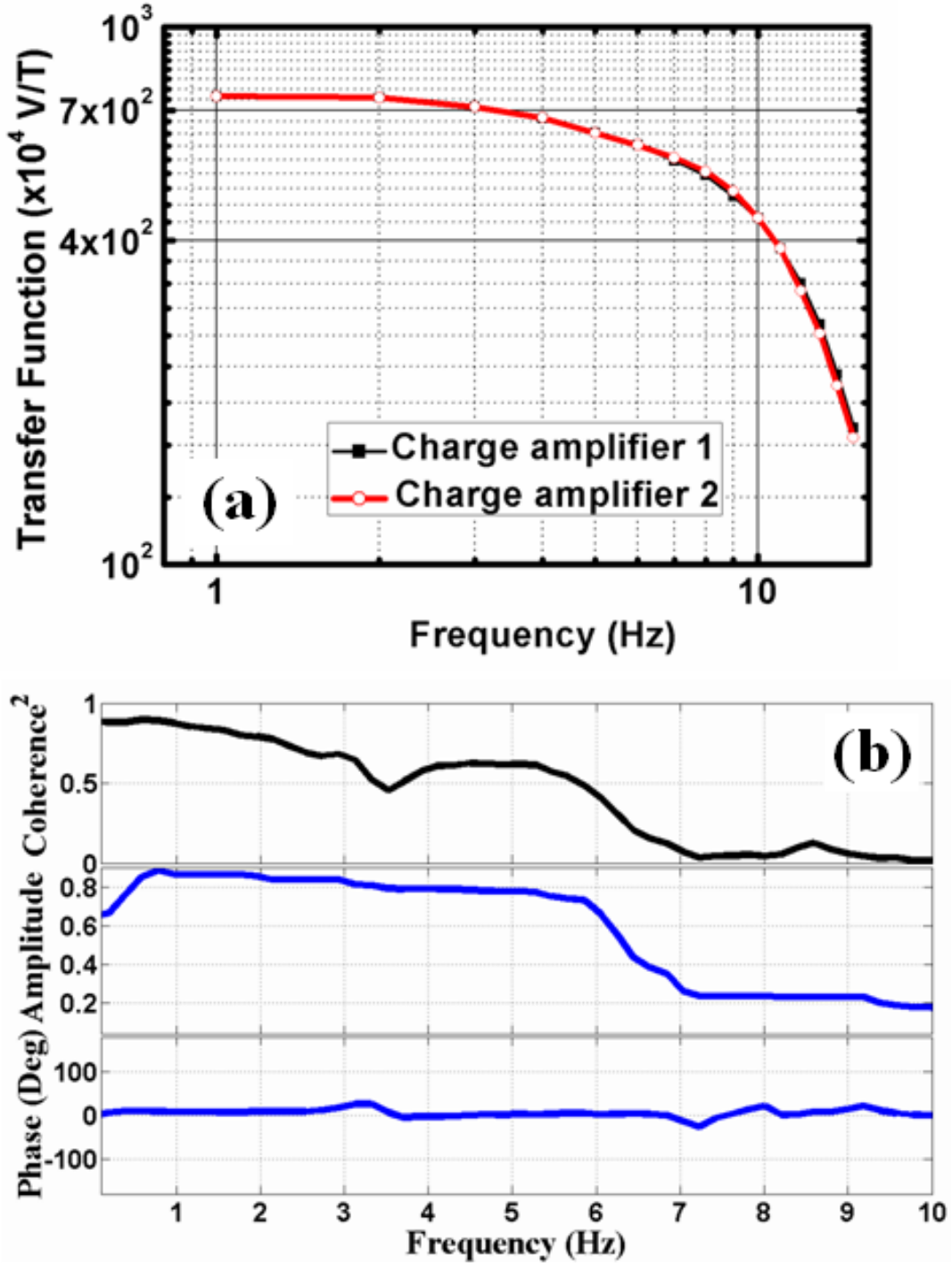

Figure 4.12 (a) Transfer function of two sensors, and (b) coherency between two sensors.

Figure 4.12 (b) shows the coherency analysis between two sensors at frequency domain. From the result, one can see that the amplitude of coherence above 7 Hz shows very low values which were quite closed to 0. This means the external noise at this frequency range was very limited, so the influence from external noise could be neglectful. However, the strong coherence was observed at frequency of f <7 Hz. The amplitudes of two sensors at this range were closed to 1, and phase shift was closed to 0. Considering the intrinsic noise in the detection unit was random, it was not impossible to result in high coherence between two sensors. So, the results can demonstrate that there is still external noise inside chamber, even if placed on top of vibration shielding table.

Inspired by the wafer-level MEMS magnetic devices installed in a vacuum chamber,[86] it is possible to utilize the vacuum chamber to isolate the acoustic noise. During the test, the magnetic sensor was placed in a vacuum chamber and the installment was pumped to high vacuum condition. The equivalent magnetic noise of the sensor was characterized at high vacuum condition.

Figure 4.13 shows the results of magnetic sensors at vacuum condition and compared to the noise floor without vacuum. From the figure, one can see that the equivalent magnetic noise for magnetic sensor at vacuum condition shows much lower noise floor compared to the test results at normal condition. Simply installing the sensor at vacuum chamber can reduce the noise floor by a factor of over 8× at relative low frequency range which is dominated by external noise. Moreover, the estimated noise floor was quite closed to the values measured at high vacuum condition.

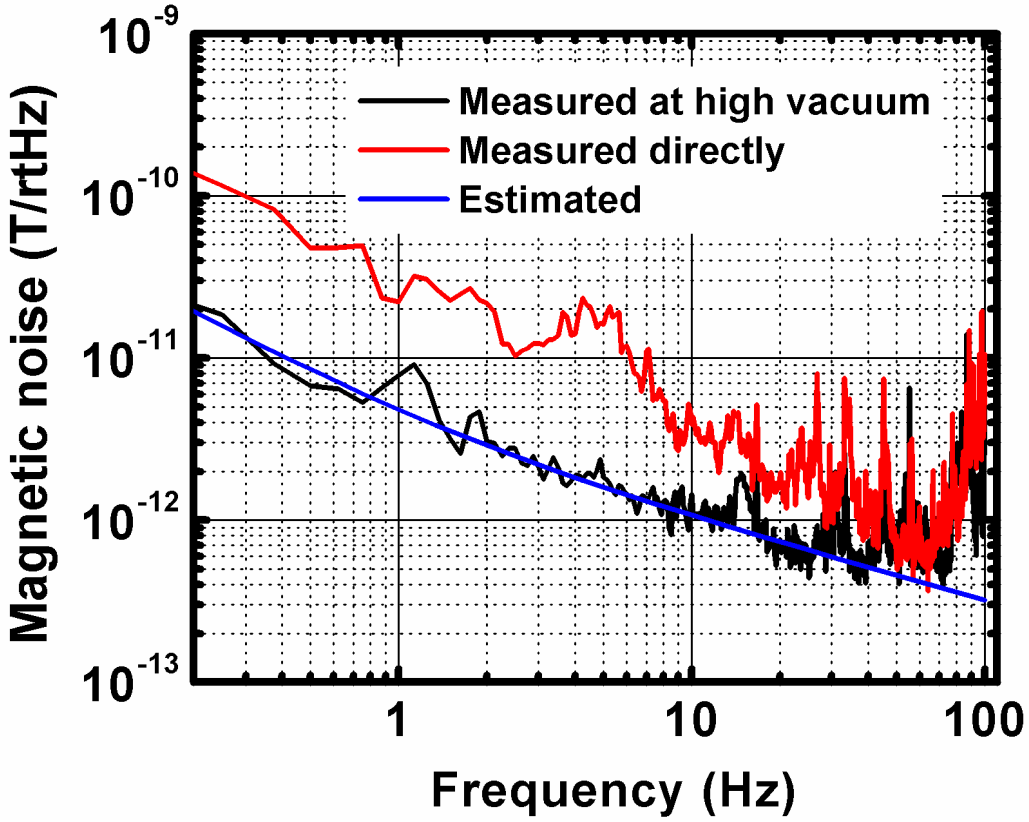

Figure 4.13 Comparisons of equivalent magnetic noise with and without high vacuum conditions.

Moreover, the vacuum chamber can work for the ELF magnetic sensor as well, which can reduce the external noise down to 10 mHz. During this demonstration, the ELF magnetic sensor with bandwidth from 0.01 Hz to 10 Hz has been placed in the vacuum chamber and pumped to high vacuum condition. The whole installment was then put in the magnetic shielding chamber. The equivalent magnetic noise spectra at high vacuum and normal conditions were measured, respectively. Figure 4.14 present the comparisons of the noise floors at two different measuring conditions.

Clearly, the noise floor at high vacuum conditions shows much smaller noise density at frequencies below 0.3 Hz. The noise floor was about 2 nT/√Hz at 0.008 Hz, which was 3 times smaller than the value tested at normal condition. Meanwhile, at high frequency range, the noise density spectra for two measurements were overlapped perfectly. This test was also confirmed that the influence of external noise inside chamber was occurred at relative low frequency range, and can be eliminated by vacuum chamber greatly.

Besides that, the investigations on the reduction of electronic noise have been also performed. According to the noise charge model proposed in section 4.2.2, noise contributions from nine sources were identified, including two intrinsic sources in the ME laminates and 7 sources from the electronic components in the detection circuit. Good agreement was reported between predicted and measured equivalent magnetic noise floors for Metglas/PMN-PT ME composites based on magnetic sensor, as illustrated in Figure 4.15. The red line represents the noise from the electronic portion and the black line shows the total noise of the sensor unit.

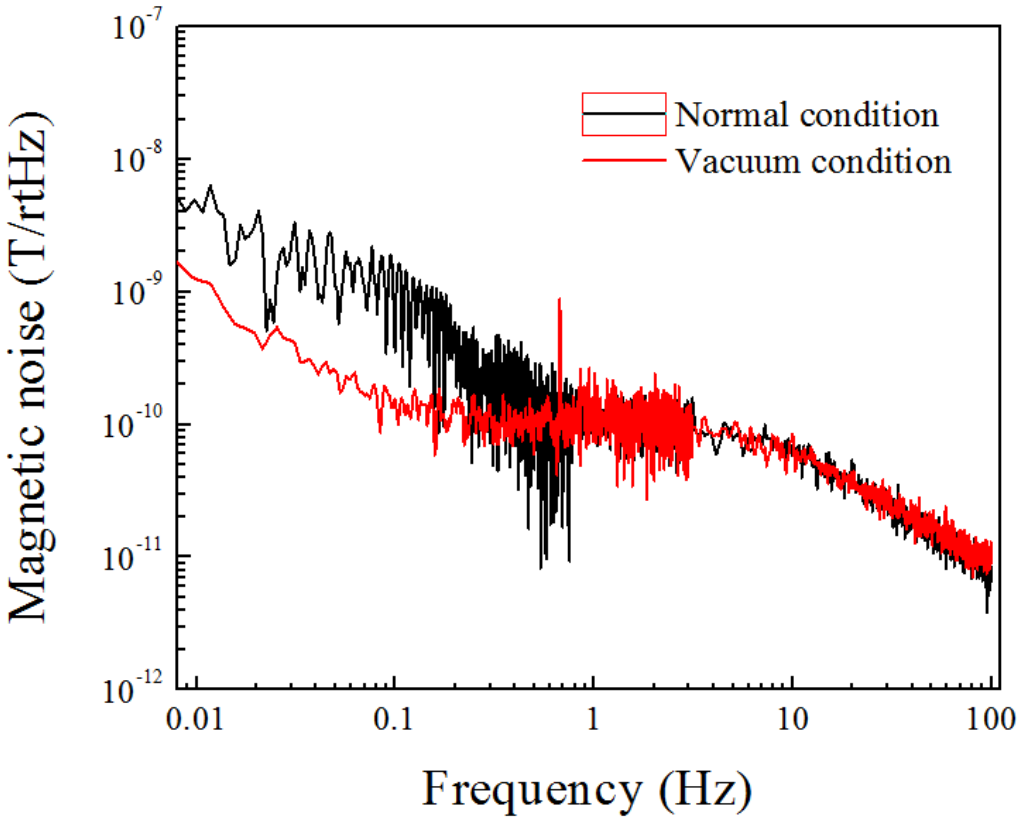

Figure 4.14 Comparison of equivalent magnetic noise spectra at normal and high vacuum conditions for ELF magnetic sensors.

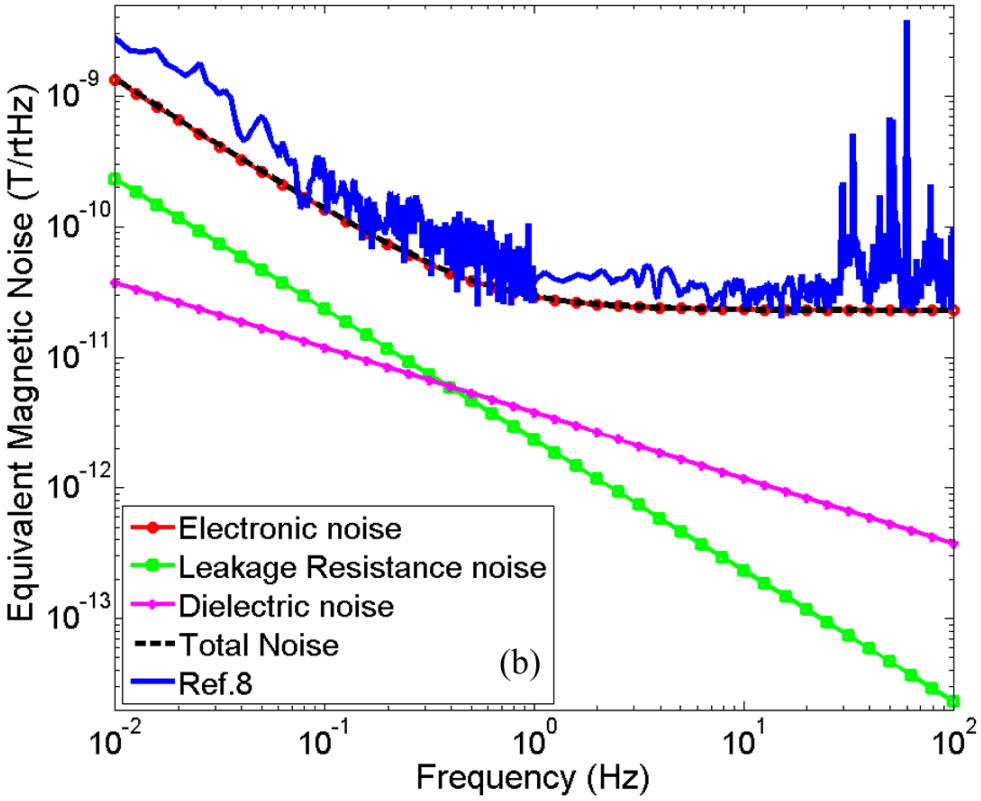

Figure 4.15 Estimated and measured equivalent magnetic noise of the ELF magnetic sensor based on Metglas/PMN-PT ME composites. The insert is a schematic illustration of the ME composites.

From Figure 4.15, it can be clearly observed that the dominant noise source was the electronic contribution, which means the noise floor could potentially be reduced if a charge amplifier detection circuit with reduced noise was identified. First of all, the alternative op-amp chips were changed with lower voltage noise density, without increasing current noise density. Op-amp LMC6042 (Texas Instruments) was used in previous design which actually was suitable for wide band frequency range. A different op-amp chip of LMC6442 was much better candidate for low frequency applications which have lower voltage noise density. Table 4.3 summarizes the comparisons of these two op-amps.

Table 4.3 Comparisons of op-amp chips

Op-amp	$e_{n,1Hz}$ (nV/√Hz)	$e_{n,100\ Hz}$ (nV/√Hz)	i_n (fA/√Hz)
LMC6042 a)	230	90	0.2
LMC6442 b)	190	180	0.2

a) Cited from LMC 6042 Operational Amplifier, Texas Instruments
b) Cited from LMC 6442 Operational Amplifier, Texas Instruments

In this table, the LMC 6442 has a lower voltage noise at 1 Hz, and a similar current noise compared to that of LMC 6042. Based on the data in Table 4.3, the electronic contribution to the voltage noise density as a function of frequency was determined, as shown in Figure 4.16 (a). From this figure, one can see that LMC6442 has much lower voltage noise density below frequency of 1.5 Hz. However, LMC6042 has better performance at frequency of $f > 1.5$ Hz. In detail, the LMC6442 has voltage density of 1.2×10^3 nV/√Hz at 0.01 Hz, which is 10× smaller than that of LMC6042. Thus, the LMC6442 based circuit was expected to have

lower noise floor at extremely low frequency range. In addition, some of the other passive components used in the detection circuit were changed, in order to further reduce the voltage noise: for example, the feedback resistor was increased from 50 Gohm to 500 Gohm. Thus, the corresponding voltage noise was reduced by a factor of $\sqrt{10}$ according to the Johnson noise equation.[60] Table 4.4 summarizes the electrical parameters of the modified detection circuit design.

Table 4.4 Components used for circuit design

Op-amp	R_f(GΩ)	C_f(pF)	R_1 (MΩ)	R_2 (MΩ)
LMC6442	500	100	10	100

Figure 4.16 (b) gives the predicted equivalent magnetic noise power density for our ME sensor and modified detection circuit which was based on the previously reported noise model. It can be seen that the equivalent magnetic noise density of the new detection unit was dramatically reduced for 10^{-2} Hz < f < 1 Hz, approaching that of the dielectric loss and dc resistance contributions from the laminates. In this figure, the black dashed line represents the total equivalent magnetic noise of the sensor unit using LMC 6442 and the blue solid line shows that of the sensor unit using LMC 6042. Clearly, the total equivalent magnetic was reduced by a factor of about 5-10× for 10^{-2} Hz < f < 1 Hz compared to previous reports.

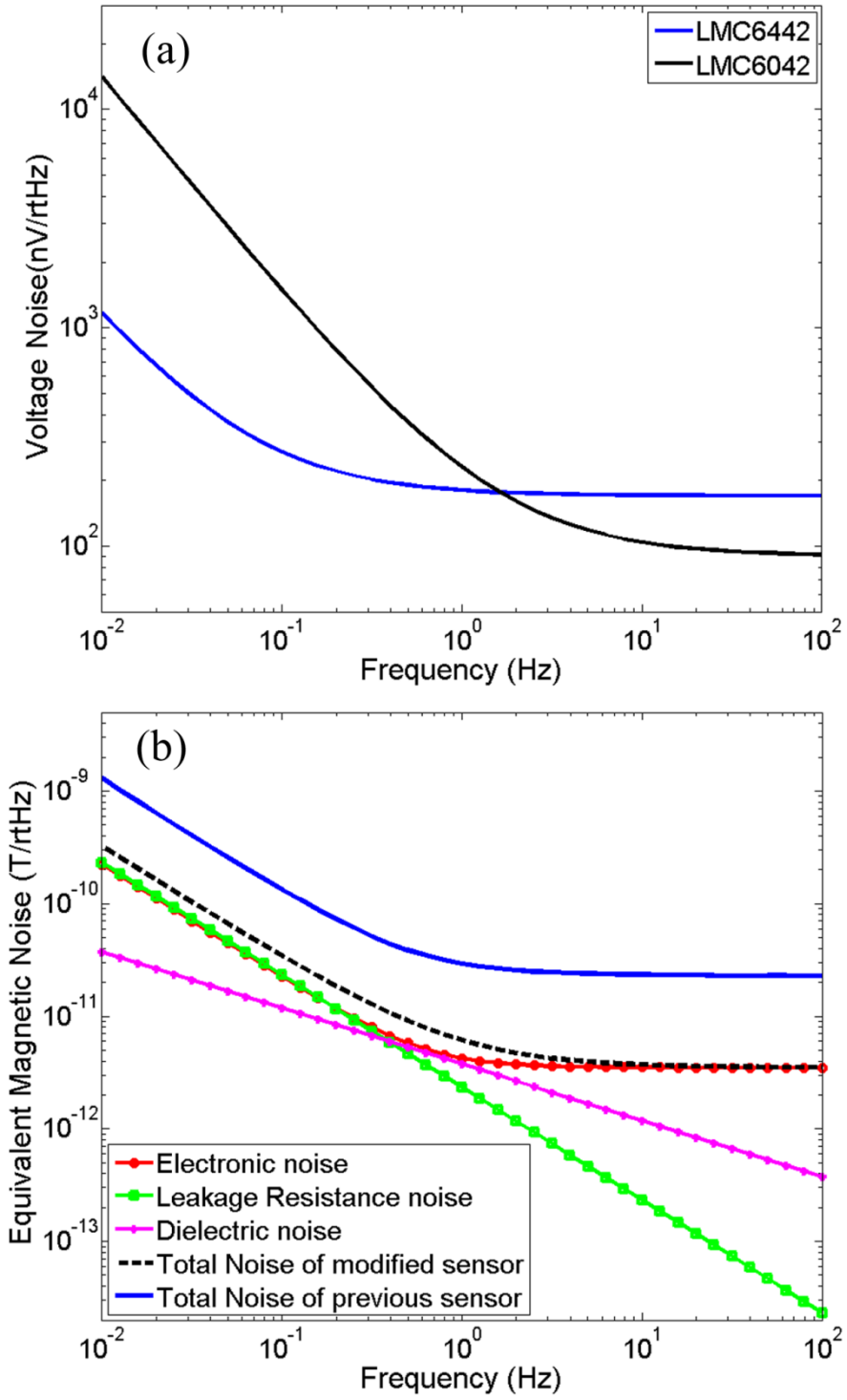

Figure 4.16 (a) Calculated voltage noise densities for LMC6042 and LMC6442 operational amplifiers, and (b) comparisons of calculated magnetic noise spectra for magnetic sensors based on optimized and previously reported detection circuits.

According to this prediction, a modified charge amplifier circuit was fabricated and the transfer function of the circuit characterized. During measurements, a 440 pF capacitor was connected to the charge amplifier circuit. An ac signal with amplitude of 10 mV_{rms} was applied to the capacitor at various frequencies, and the output voltage from the circuit was monitored by a dynamic signal analyzer (SR-785). The transfer function was calculated by using the output voltage divided by the input charge. Figure 4.17 (a) shows the predicted and experimental values for the transfer function of the detection unit. In this figure, it can be seen that the predicted and measured values matched well. The transfer function was nearly constant for 10^{-2} Hz $< f <$ 7 Hz.

Finally, the ME composites and modified charge amplifier circuits were assembled together into a battery operated magnetic sensor detection unit. The equivalent magnetic noise floor was measured for 10^{-2} Hz $< f <$ 10 Hz using a dynamic signal analyzer (SR-785). In order to characterize the intrinsic noise, the sensor unit was placed in a high mu-metal shielding chamber to reject the influence of electromagnetic interference (EMI). Figure 4.17 (b) shows the equivalent magnetic noise density spectra. It can be seen that the experimental results and the predicted values are in good agreement over the entire frequency range. The equivalent magnetic noise density was around 0.3 nT/√Hz at 10 mHz, which was almost 10 times smaller than that previously reported.[82] Furthermore, the noise density was also reduced by a factor of 5× to 8 pT/√Hz at f = 1 Hz. So, the equivalent magnetic noise density of ELF magnetic sensors based on Metglas/PMN-PT ME composites was reduced by optimizing the detection circuit.

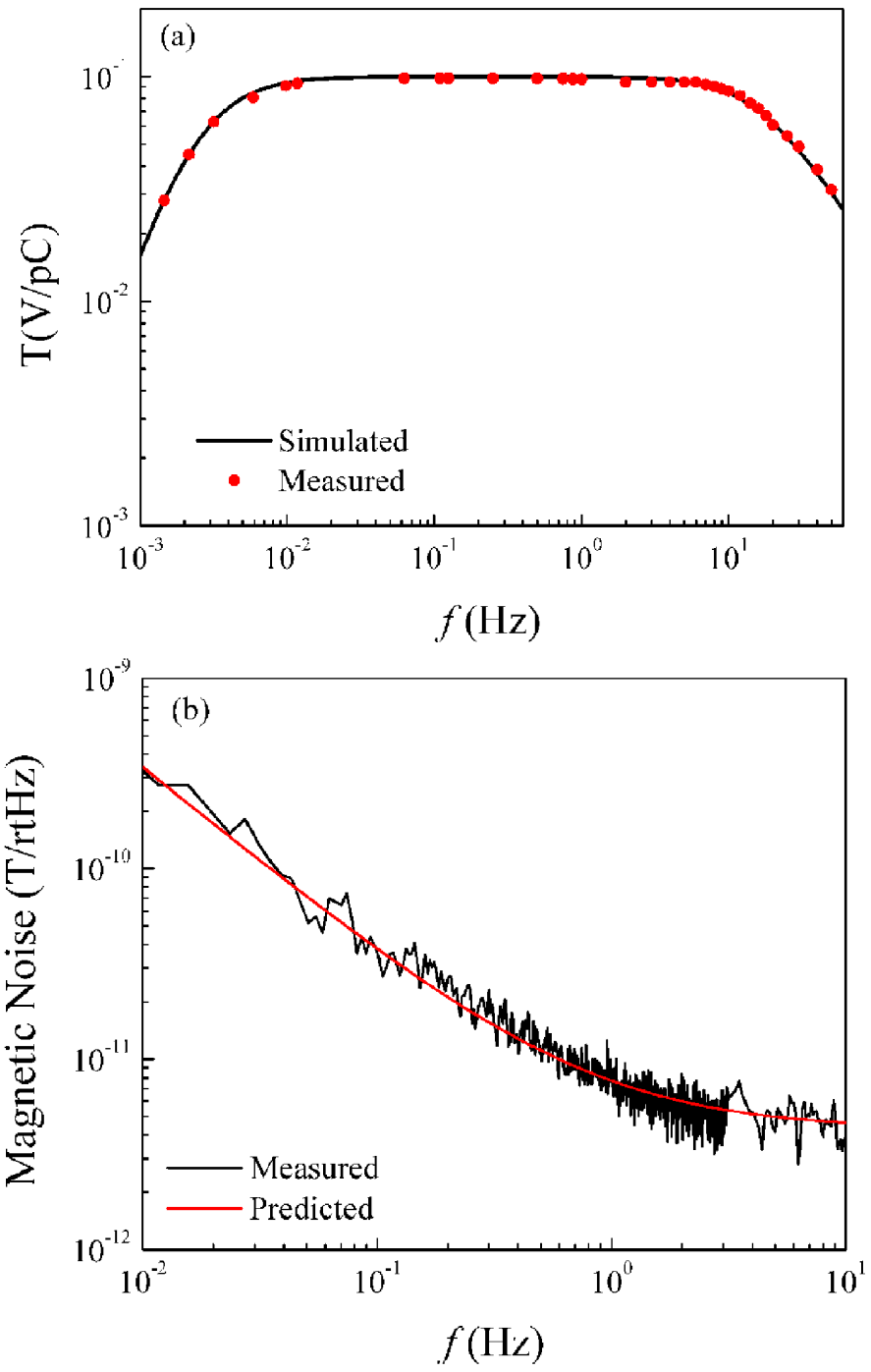

Figure 4.17 (a) Predicted and measured transfer functions of the new detection circuit; and (b) estimated and measured equivalent magnetic noise floors of an optimized magnetic sensor.

Meanwhile, the circuit was redesigned to work down to frequency as low as 0.001 Hz in order to apply the sensor for medical treatment application. The design was based on the similar layout, and the cutoff frequency was calculated through the equations 4.3-4.8. The feedback resistor R_f and capacitor C_f were used for 500 Gohm and 1000 pF, respectively. Accordingly, the resistors used in bandpass part were setup at 100 Meg and 2 Gohm, respectively. So, the approaching gain factor for this circuit can be calculated by the following equation:

$$H(s) = |H_1(s)| \times |H_2(s)| = \frac{1}{1000\,p} \times 20 = 0.02\ (\frac{V}{pC}). \qquad (4.11)$$

After fabricating the circuit, the gain factor in unit of V/pC was characterized firstly. The characterization process was followed the above process, and the gain factor at frequency from 0.007 Hz to 1 Hz was shown in Figure 4.16. From the figure, one can see the transfer function is homogenous from 0.007 Hz to 1 Hz which was not attenuated below 0.01 Hz. The circuit can work down to extremely low frequency. However, the gain below 0.07 Hz is really hard to characterize due to the quite long measuring time required.

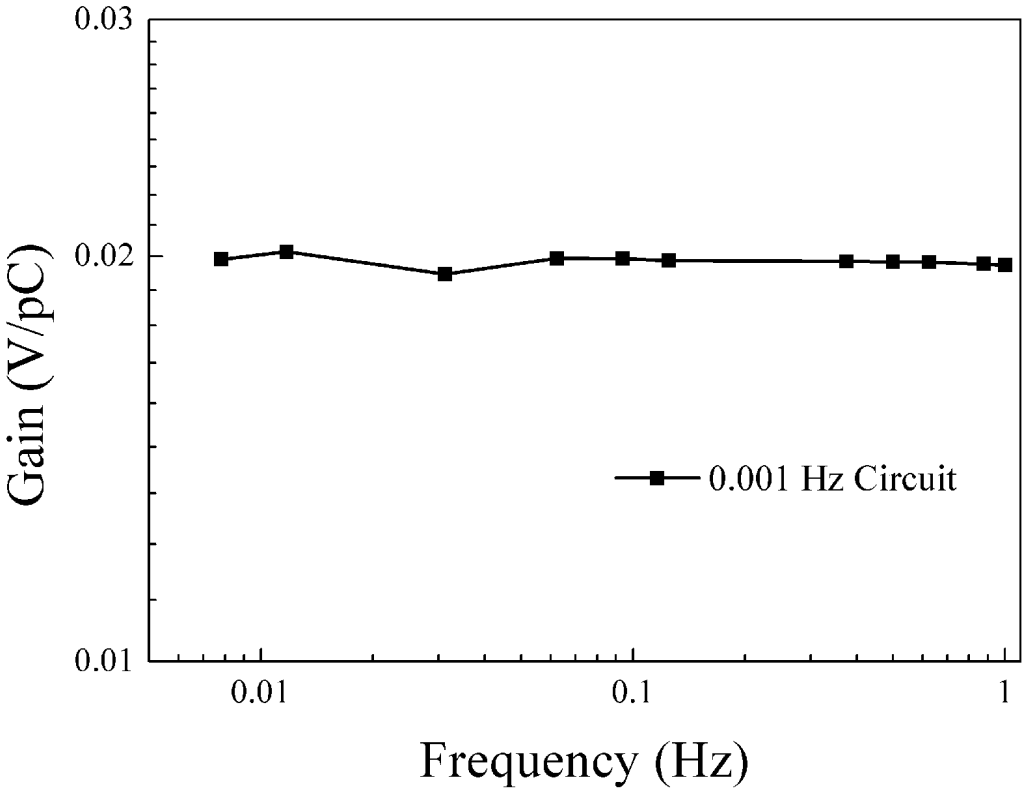

Figure 4.18 Transfer functions of the 0.001 Hz detection circuit.

As discussed in the previous section, the equivalent magnetic noise density spectrum for a 0.001 Hz magnetic sensor was also measured. However, a dynamic signal analyzer is not a good choice since the whole instrument requires a low noise condition. Otherwise, it would be saturated easily. In order to characterize the magnetic noise for this sensor, the digitizer CR 1000 was used during the test. The magnetic sensor was placed inside the vacuum chamber and the whole package was then installed in magnetic shielding chamber. In order to measure the noise down to 0.001 Hz and to have the sufficient data points to do the further signal processing, the datalogger was operated for over 3 hours with the sample rate of 100 Hz. During the whole process, an AC magnetic field at frequency 1 Hz was applied to the magnetic sensor by one pair of H-coils. Figure 4.19 (a) shows the waveform of magnetic sensor in time domain. One can see the strong output signal can be observed with slight variation. After collecting the raw data, MATLAB was used to perform the signal processing to convert the raw data in time domain to power density in frequency domain. In order to enhance the frequency resolution closed to 0.001 Hz, all the 1,200,000 data points were used. After processing, the noise density spectra are shown in Figure 4.19 (b). From this figure, one can see the measured noise floor is very close to estimated values over the whole frequency range except the frequency below 0.0015 Hz, and strong spike at 1 Hz due to the incident magnetic field. The blue line shows larger variations at frequency of $f > 0.05$ Hz which is a direct result of high frequency resolution. Moreover, the magnetic noise density below 0.0015 Hz is higher than predicated one, which is probably limited by insufficient data points. So, the ELF magnetic sensor based on ME composites has

been successfully proposed which can work at frequency down to 0.001 Hz. The noise density is around 2 nT√Hz below 0.002 Hz.

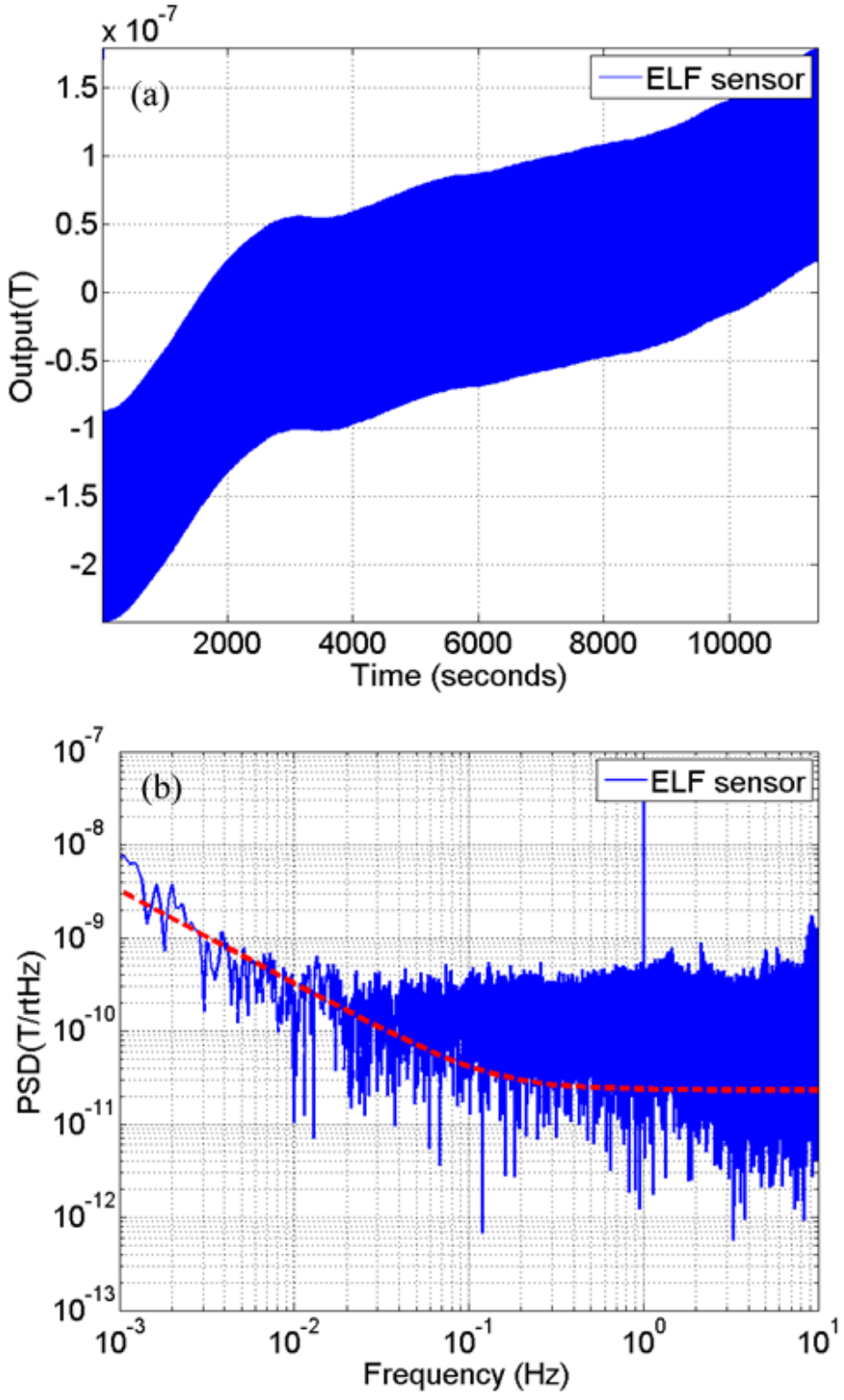

Figure 4.19 (a) Waveform of magnetic sensor in time domain, and (b) magnetic power spectra of magnetic sensor. The red dash line indicates the theoretical prediction result.

4.4 Active magnetic sensor unit

In addition to developing a passive magnetic sensor, an alternative AC magnetic sensor was also designed based on the nonlinearity of ME composites.[87, 88] The modulation technique was utilized in order to modulate the low frequency magnetic signal to the relatively high frequency range which has a lower noise floor. Accordingly, the signal-to-noise ratio was expected to be enhanced in this way.[87]

4.4.1 Sensor design and characterization

The modulation processing of an active mode ME sensor is shown in Figure 4.20. First, a solenoid coil was wrapped around an ME composites to work as driving coil in order to carry the high frequency (f_0) magnetic field B_0, after which the incident magnetic field B_1 at low frequency (f_1) was applied through the external H-coils (not shown in this figure). As a result of the nonlinear ME effect, the induced output from the ME composites would contain signals at a frequency of (f_0 +/- f_1). This process represents how one can modulate a low frequency incident magnetic field to relatively high frequency range.

The origin of the nonlinear ME effect stems from the fact that the magnetostriction of Metglas is non-linear to the applied magnetic field, as described by equation (4.11):

$$\lambda \propto B^2 \tag{4.11}$$

where λ is the magnetostrictive coefficient, and B is the applied magnetic field. Considering the sine wave signals used to drive the carrier magnetic field and the incident magnetic field, the induced magnetic field can be expressed as:

$$B_0 = A_0 \sin(2\pi f_0 t + \theta_0);$$
$$B_1 = A_1 \sin(2\pi f_1 t + \theta_1). \tag{4.12}$$

where A_0, A_1 correspond to the amplitudes of the driving magnetic field and incident magnetic field, respectively; θ_0, θ_1 represent the phase angles of the two fields. So, the λ under two magnetic fields can be presented as:

$$\lambda \propto (B_0 + B_1)^2 = B_0^2 + B_1^2 + 2B_0 \cdot B_1;$$
$$B_0^2 = A_0^2 \sin^2(2\pi f_0 t + \theta_0) = \frac{1}{2} A_0^2 (1 - \cos(4\pi f_0 t + 2\theta_0));$$
$$B_0 \cdot B_1 = A_0 A_1 \sin(2\pi f_0 t + \theta_0) \cdot \sin(2\pi f_1 t + \theta_1) \tag{4.13}$$
$$= -\frac{1}{2} A_0 A_1 [\cos(2\pi(f_0 + f_1)t + \theta_0 + \theta_1) - \cos(2\pi(f_0 - f_1)t + \theta_0 - \theta_1)];$$
$$B_1^2 = A_1^2 \sin^2(2\pi f_1 t + \theta_1) = \frac{1}{2} A_1^2 (1 - \cos(4\pi f_1 t + 2\theta_1)).$$

Clearly, under two AC magnetic fields, the magnetostrition was influenced by both the applied fields, as well as the the cross-modulation between two AC fields. By adjusting the relative amplitudes of B_0 and B_1, λ can show strong a relationship with the magnetic field at frequencies of (f_0 +/- f_1). Considering that the output signal from piezo-fiber was directly related to the strain transferred from Metglas, the induced voltage from ME composites displayed the cross modulation elements under two AC magnetic field conditions.

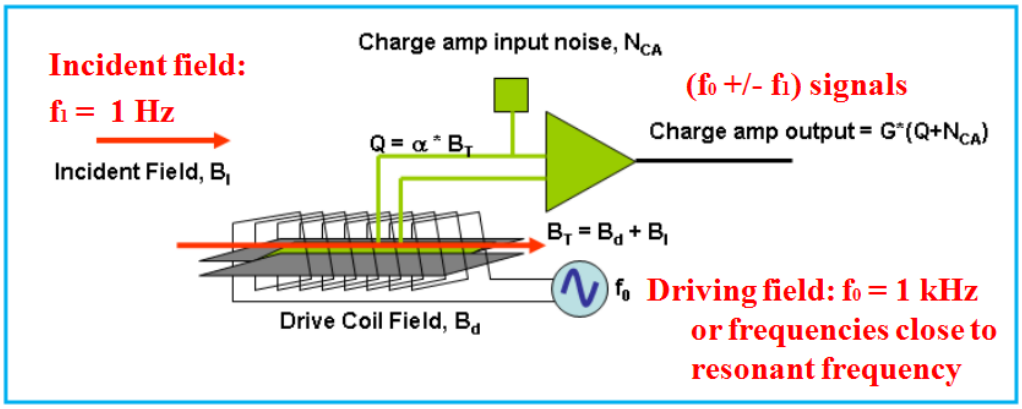

Figure 4.20 Modulation process of active mode ME sensor.

In order to characterize nonlinear ME effects, the nonlinear ME voltage coefficient was defined as:

$$\alpha_{ME}^{nonlinear} = \frac{E_{f_1 \pm f_0}}{B_0 \cdot B_1}. \quad (4.14)$$

where E is the induced electric field at frequencies of (f_0 +/- f_1). Theoretically, these two values should be equal.

Nonlinear coefficients as a function of DC magnetic bias have been reported in previous literature. Specifically, it was realized that nonlinear ME coefficients show a completely different trend under a DC magnetic field compared to linear or primary ME coefficients. Typically, the primary ME coefficients display the smallest values at a zero DC bias, but increase to optimized values at a DC bias of 8 Oe. In contrast, the nonlinear ME coefficients show the largest values at approximately zero DC bias, but decrease with increasing DC magnetic bias. Therefore, in order to observe the maximum nonlinear ME effect, the active sensor was placed inside the magnetic shielding chamber, which was considered to be zero magnetic field.

Normally, most prior investigations have used the induced signal at frequencies of f_0 +/- f_1 to indicate the response to the incident magnetic field under a consistent driving magnetic field. This approach was also considered to be a reasonable characterization method according to Equation 4.14 which indicates that the output signal was proportional to the incident magnetic field as fixing the amplitude of the driving field. However, this method does not elucidate the relationship between output signal and incident magnetic field in any direct way. Accordingly, the demodulation process was required to convert signals in the high frequency range back to the low frequency area, which then can be used to accurately represent the

sensors' response to the incident magnetic field. In fact, by using a demodulator, one is able to fully decode the signal process, which unrelated to the nature of the materials. Specifically, during this process, the signal from the sensor and one reference signal with the same frequency as the driving signal are applied to the demodulator. By comparing the output signal and the driving signal, essential information at low frequency range can be obtained. Most of previous investigations have concluded by using a commercial lock-in amplifier to drive the sensor and perform the demodulation process. However, due to the large size and significant power consumption of demodulator, this method tends to be feasible only for certain fundamental research applications or for demonstration purposes. In other words, it is impossible to propose one alternative magnetic sensor based on this process; thus, one analog circuit with similar functions was determined to be sufficient.

For this investigation, therefore, I proposed one simple analog circuit apparatus that was easily-operated by two 4.5 V batteries packs with differential mode input. The schematic illustration of the signal process in the circuit is shown in Figure 4.21, where, one oscillator is designed to generate a consistent sine wave driving signal at a frequency of 10 kHz, which is an adjustable gain through the buffer stage. This high frequency signal was applied to the excitation coil to drive the sensor. Meanwhile, it served as the reference signal for the demodulation process. It should also be noted that the circuit was integrated with a voltage amplifier to collect the induced voltage from the ME sensor, after which the signal went to the demodulator. Once the process performed by the demodulator and the low pass filter occurs, the low frequency signal can be observed by oscilloscope or other instruments.

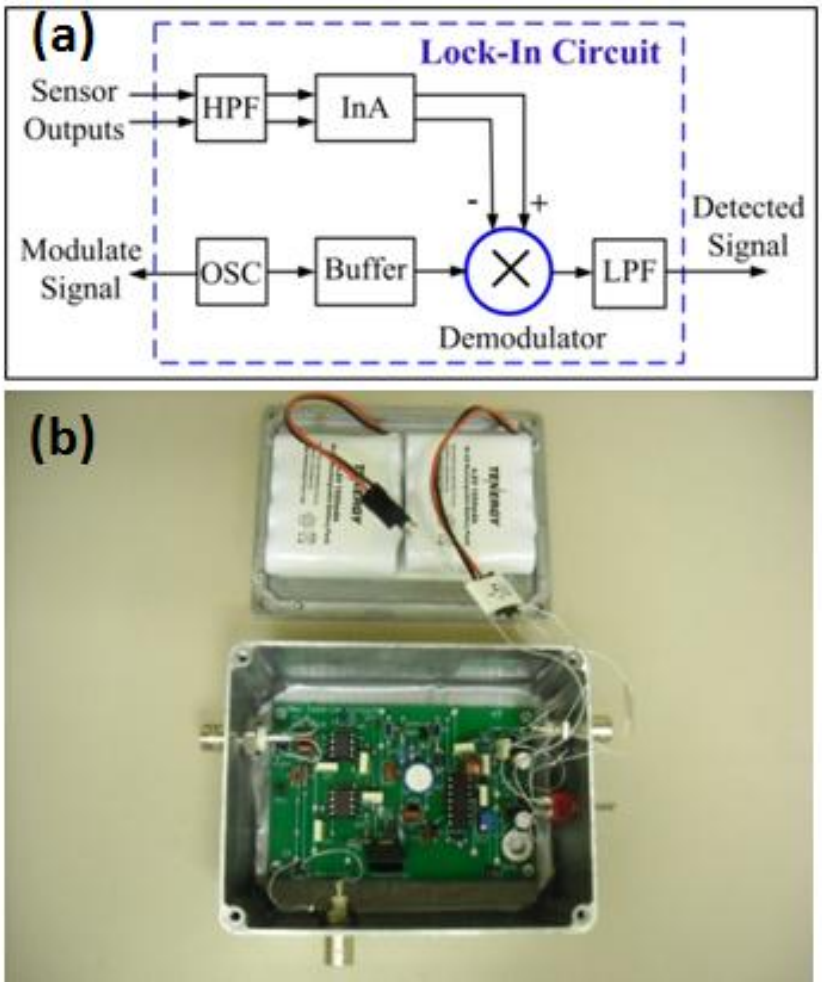

Figure 4.21 (a) Schematic of our custom-built lock-in circuit; and (b) photo of a lock-in circuit.

For the present investigation, the commercial multiplier AD835 (Analog Devices) was used to perform the demodulation process, which basically can achieve the function of multiplying the signals applied to the X and Y input ports. I tested three high frequency signals in this study: f_0 - f_1, f_0, and f_0 - f_1. Assuming these three induced signals and reference signal can be expressed as:

$$\begin{aligned} V_{f_0-f_1} &= A_1 \sin(2\pi(f_0 - f_1)t); \\ V_{f_0} &= A_2 \sin(2\pi f_0 t); \\ V_{f_0+f_1} &= A_1 \sin(2\pi(f_0 + f_1)t); \\ V_{ref} &= A_3 \sin(2\pi f_0 t). \end{aligned} \tag{4.15}$$

where A_1, A_2, A_3 correspond to the amplitude of the signals. To simplify the calculation, the phase shift for each signal is neglected.

According to this expression, the signals through the AD835 demodulator can be transferred to the low frequency signal as:

$$\begin{aligned} V_{out} &= (V_{f_0-f_1} + V_{f_0} + V_{f_0+f_1}) \cdot V_{ref}; \\ V_{f_0-f_1} \cdot V_{ref} &= -\frac{1}{2} A_1 A_3 [\cos(2\pi(2f_0 - f_1)t) - \cos(2\pi f_1 t)]; \\ V_{f_0} \cdot V_{ref} &= -\frac{1}{2} A_2 A_3 [\cos(4\pi f_0 t) - 1]; \\ V_{f_0+f_1} \cdot V_{ref} &= -\frac{1}{2} A_1 A_3 [\cos(2\pi(2f_0 + f_1)t) - \cos(2\pi f_1 t)]. \end{aligned} \tag{4.16}$$

Clearly, the signal processed by the AD835 contained signals at the incident frequency f_1 and at the double-frequency range. The low pass filter after the modulator stage was able to reject signals at high frequency range; thus, only low frequency signal could be detected. Typically, the low pass filter is designed to have cutoff frequency around 1.6 Hz. However, it can be extended to higher frequency in order to obtain a broader detectable frequency range.

Figure 4.21 (b) shows the prototype of our custom-built lock-in circuit, which features small battery packs power supply. Given that the complete lock-in circuit was relatively compact (12 cm × 9 cm × 6 cm), it was quite portable. This size factor has positive implications for developing an active magnetic sensor based on the nonlinear ME effect that is easily transportable.

Similar to a passive magnetic sensor, the sensitivity and noise floors remain two important parameters to evaluate for an active magnetic sensor as well. Here, the sensitivity in units of μV/nT for the active magnetic sensor was defined as overall output signal divided by input magnetic field; in other words, we did not take into account the complicated circuit process. The experimental setup for sensitivity characterization is shown in Figure 4.22 (a). For this test, the ME sensor was wrapped with 100 turn coils and placed inside the big *H*-coils which was used to apply the incident magnetic field with small amplitude.

The H-coils was first characterized using a commercially available fluxgate, which had a known sensitivity. During the calibration, the driving signal applied to the big H-coils was generated by dynamic signal analyzer. Subsequently, the induced output signal from the fluxgate was also monitored by the dynamic signal analyzer. In order to reduce system noise, the results were averaged 12 times, after which the recorded data was converted to magnetic field results according to the sensitivity of the fluxgate. Figure 4.22 (b) presents H-coils calibration results, which indicate the relationship between induced magnetic field and applied voltage. In order to study the performance of the active sensor down to extremely low frequencies, the calibrations were conducted at 1 Hz and 7.875 mHz. Form this figure it can be seen

that the amplitudes of the generated magnetic fields excited by an arbitrary voltage at 1 Hz and 7.875 mHz overlapped each other perfectly. Thus, we were able to demonstrate that the magnetic fields generated by the H-coils were consistent at varying frequencies.

The performance of active sensor was then characterized, including linearity to the magnetic field, sensitivity and noise floor. First of all, the linearity of the sensor was measured. This was accomplished by generating the driving voltage by dynamic signal analyzer at different amplitudes and at a frequency of 1 Hz, after which the induced output signal from the sensor was monitored. According to the H-coils characterization results, the driving voltage was then converted to the magnetic field. Figure 4.23 (a) illustrates the output signals from the sensor as a function of incident magnetic field at a frequency of 1 Hz. From the figure it can be seen that the sensor's output was fairly linear to the amplitude of the incident magnetic field. The slope of the fitting curve was 12.09 μV/nT, which indicated sensitivity at 1 Hz. Using similar methods, sensitivity over frequencies ranging from 7.8125 mHz to 2 Hz were then characterized (Figure 4.23 (b)).

One can see from the figure that the sensitivity for the active magnetic sensor was consistent at a value of 12 μV/nT at a frequency as low 7.8125 mHz, and up to 1 Hz. After that upper limit, the sensitivity was attenuated as a direct result of the low pass filter, which has a cutoff frequency of 1.6 Hz. These findings indicate that the sensor was able to detect magnetic fields in an extremely low frequency range or DC up to 1 Hz.

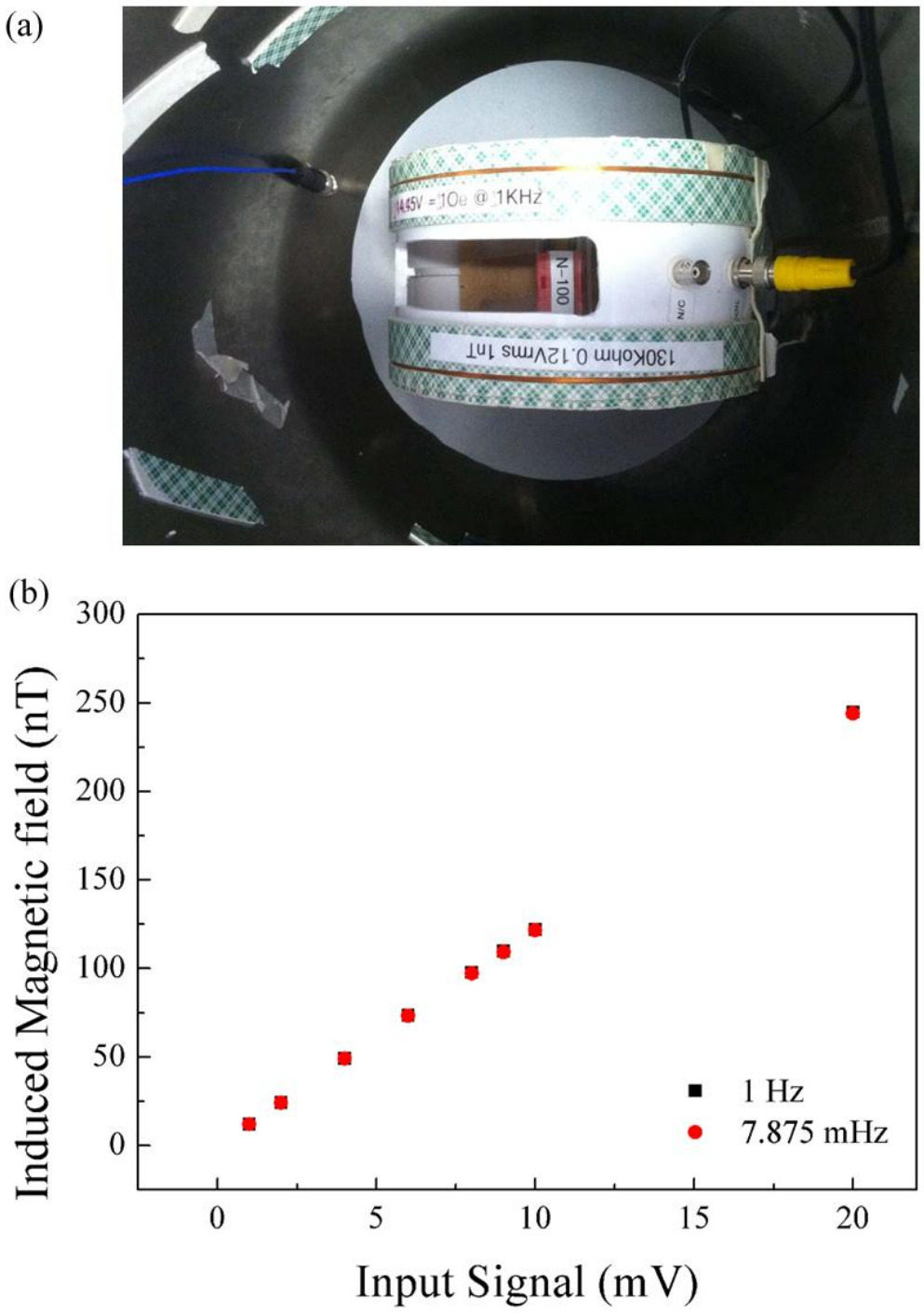

Figure 4.22 (a) Experimental setup for the active sensor test; and (b) H-coils calibration results at 1 Hz and 7.875 mHz.

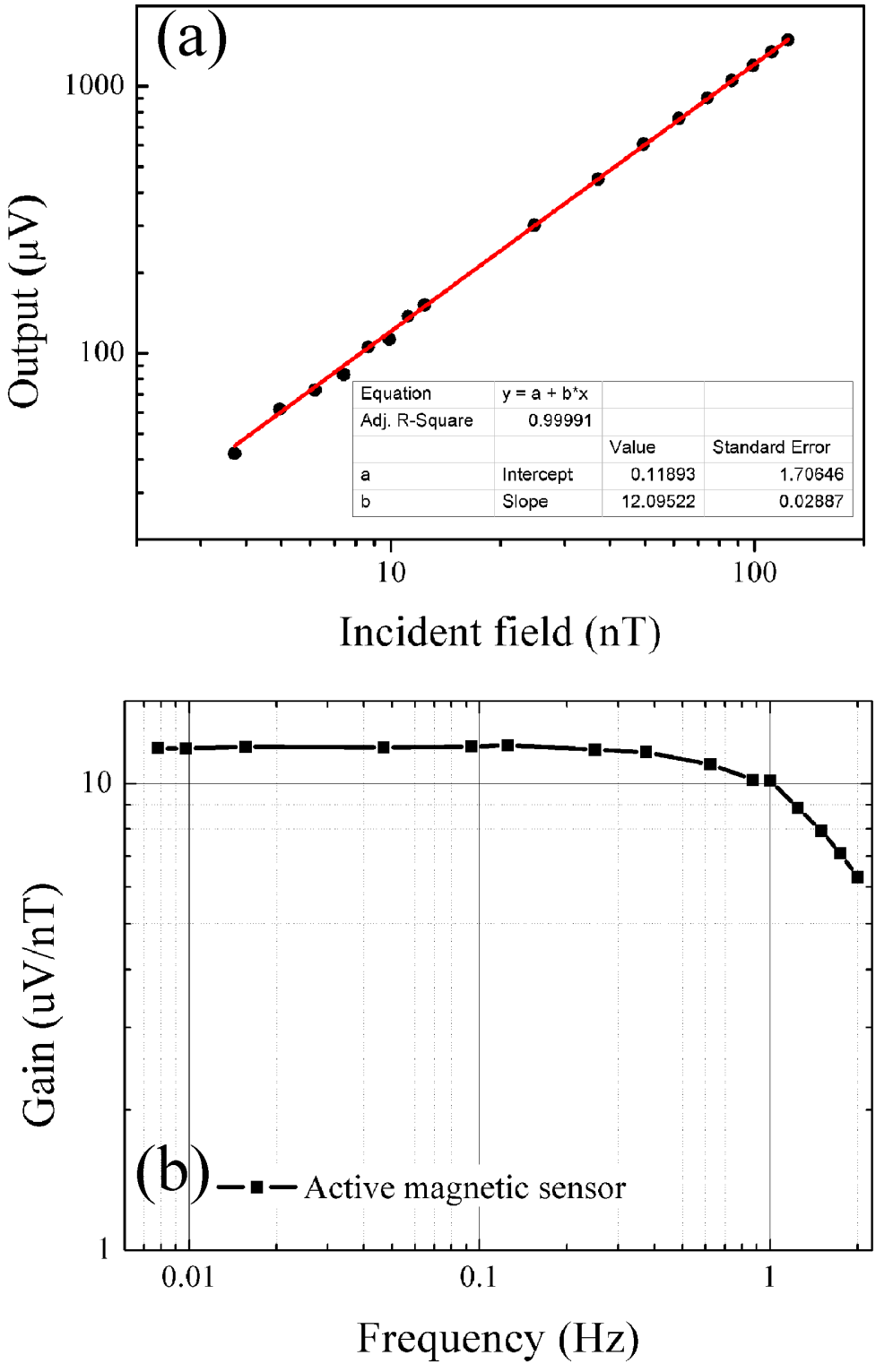

Figure 4.23 (a) Output signal from the active sensor as function of incident magnetic field; and (b) sensitivity of the sensor at a frequency range from 7.8125 mHz to 1 Hz.

Finally, the equivalent magnetic noise of the active sensor was measured via the following protocol. First, the active sensor was placed inside the chamber in order to reduce any electromagnetic interference. Then, the H-coil was activated by an AC signal with amplitude of 8 mV at frequency of 7.8125 mHz to check the sensor's response. Figure 4.24 graphically illustrates the noise density spectra of the magnetic sensor. The noise density at 2 mHz was around 18 nT/√Hz, and decreased gradually with increasing frequency. The noise density was reduced to around 0.4 nT/√Hz at a frequency of 0.78125 Hz. Moreover, the sharp spike observed at a frequency of 7.8125 mHz was attributed to the incident magnetic field.

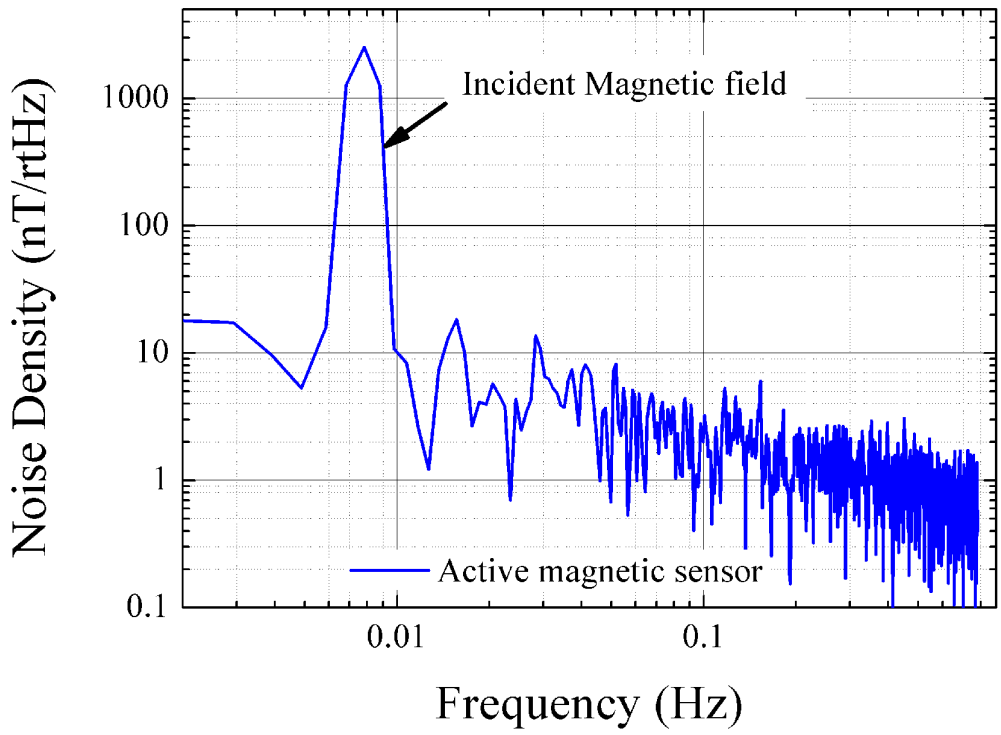

Figure 4.24 Equivalent magnetic noise density spectra of the active magnetic sensor.

4.4.2 Optimization of active magnetic sensor

Although the present active sensor can work only from DC to 1 Hz, the bandwidth of the sensor can be extended by changing the low pass filter during the final stage. Additionally, the noise floor can be reduced by enhancing the gain factor of the circuit. By simply changing the resistor or capacitor components during the filter stage, the bandwidth can be modulated. Figure 4.25 shows the bandwidth extended to 10 Hz and the noise density spectra. According to gain factor test results, one can see that the gain factor displayed consistent values of about 6.8 μV/nT from 0.004 Hz to 4 Hz, while the 3-dB cutoff frequency was around 12 Hz. Based on noise spectra density comparisons, the extended bandwidth of the magnetic sensor had a similar noise floor as the original sensor. This finding indicates that the modulated sensor was not influenced by changing the bandwidth at a specific frequency range. Furthermore, the detectable frequency range was extended up to 100 Hz.

Figure 4.26 shows the detectable frequency range of a magnetic sensor that was designed to work up to 100 Hz. From Panel (a), one notes that the 3-dB cutoff frequency point was around 120 Hz. However, the noise density spectra of the sensor were increased significantly compared to the previous sensors. One possible reason for the inferior noise spectra could be reduced gain factor which limits the signal-to-noise ratio. Considering this limitation, the gain factor was increased while maintaining the 100 Hz bandwidth.

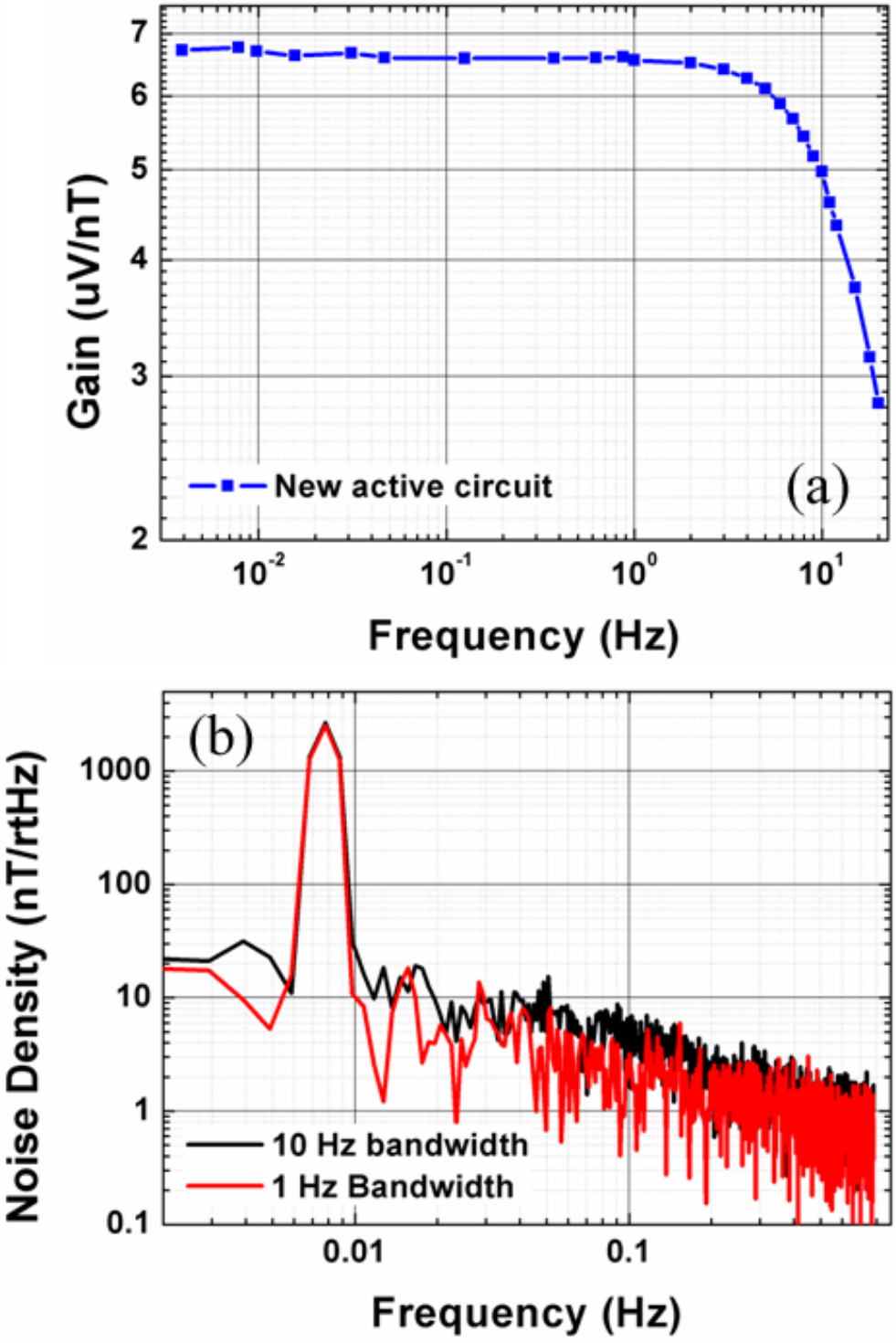

Figure 4.25 Equivalent magnetic noise density spectra of active magnetic sensor.

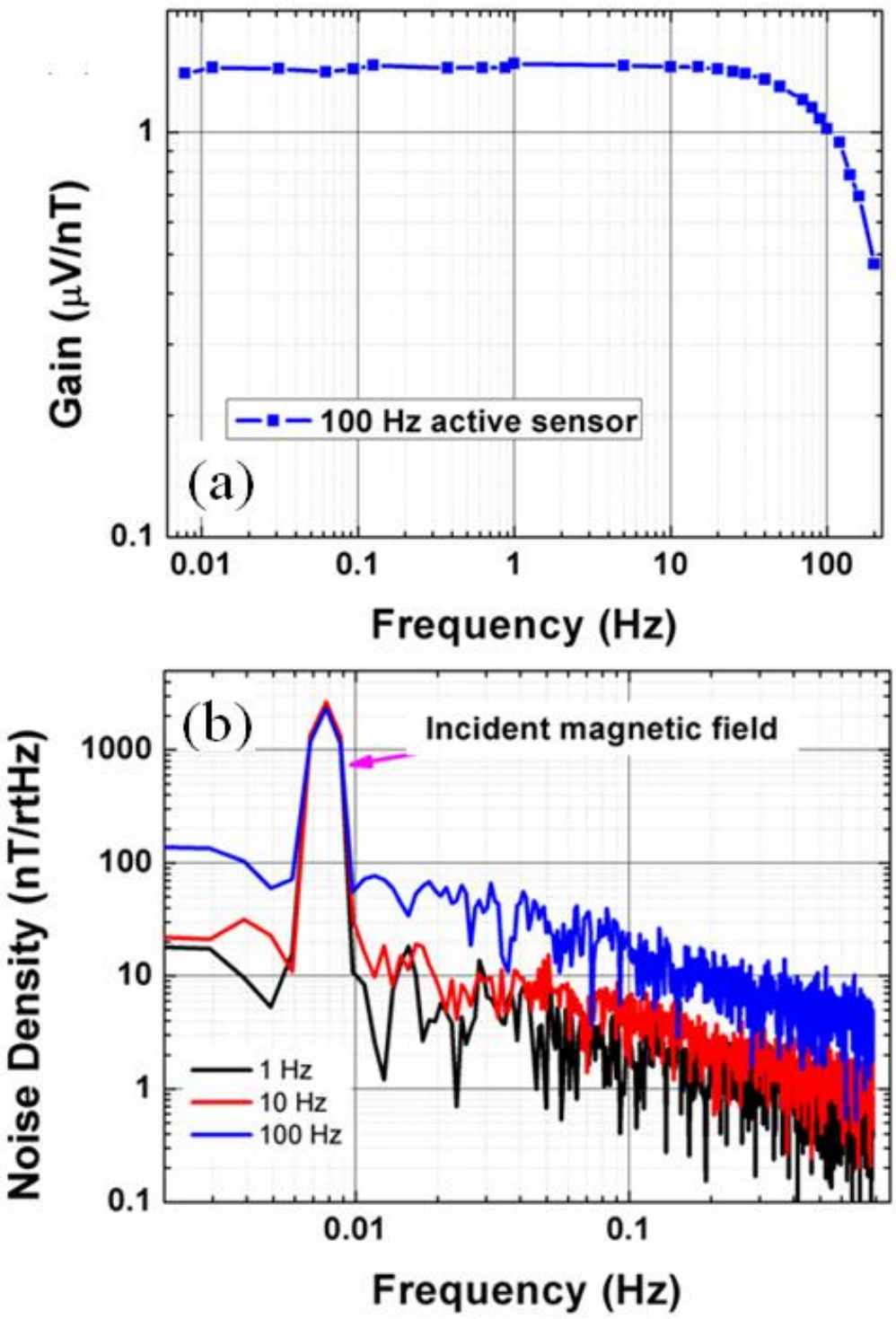

Figure 4.26 (a) Sensitivity of the modulated sensor in the frequency range of 6 mHz to 200 Hz; and (b) equivalent magnetic noise density spectra of the active magnetic sensor.

Figure 4.27 illustrates the modulated 100 Hz magnetic sensor. In this assay, the gain factor was increased from 1.2 μV/nT to 110 μV/nT. Accordingly, the noise density spectra were decreased from over 100 nT/√Hz to around 10 nT/√Hz, which was closed to the values of the previous sensors.

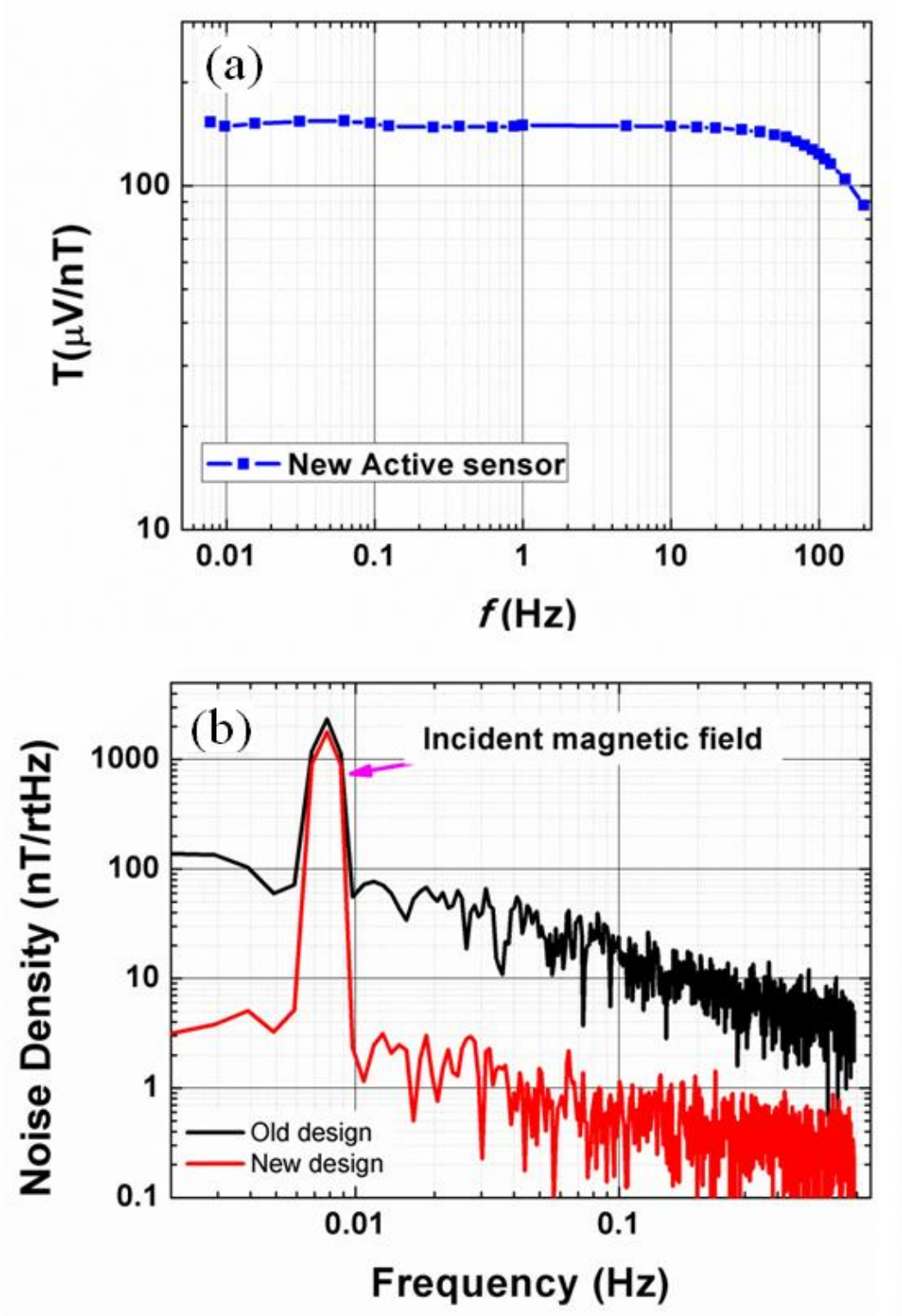

Figure 4.27 (a) Sensitivity of the modulated sensor in the frequency range of 6 mHz to 200 Hz; and (b) equivalent magnetic noise density spectra of the active magnetic sensor.

In addition to modifying the bandwidth, the driving signal was also optimized for the specific ME sensor due to the fact that driving signal played an important role in this active sensor design. From the Figure 4.21 (a), one notes that the driving signal was not only applied to the excitation coils to drive the ME sensor, but also served as the reference signal during the demodulation process. For this study, the frequency of the driving signal was fixed at 10 kHz. Another parameter that needs to be studied is the amplitude of the signal. From Equation 4.14 and 4.16, we can see that the amplitude of the signal affects the nonlinear output and the output through the demodulator.

To obtain the desired measurements, I adjusted the rheostat in the circuit, which caused the amplitude of the driving signals to vary from 0.57 V to 1.45 V. Meanwhile, a 100 nT incident magnetic field at a frequency of 1 Hz was applied to the active sensor through the H-coils, after which the output signals from the sensor and the noise floor were monitored by dynamic signal analyzer under each driving signal, as shown in Figure 4.28.

As clearly indicated, the output voltage from the sensor was enhanced by increasing the amplitude of the driving signal. However, it should be noted that the relationship between these two factors was not linear. Specifically, the output signal shows saturated values when the driving signal was over 1.20 V. Meanwhile, voltage noise tests were also conducted in the absence of incident magnetic field conditions; results showed that the noise level of the sensor increased when the amplitude of the driving signal was increased. On the basis of these two findings, we were able to confirm the driving signal should have an optimized value for the active sensor.

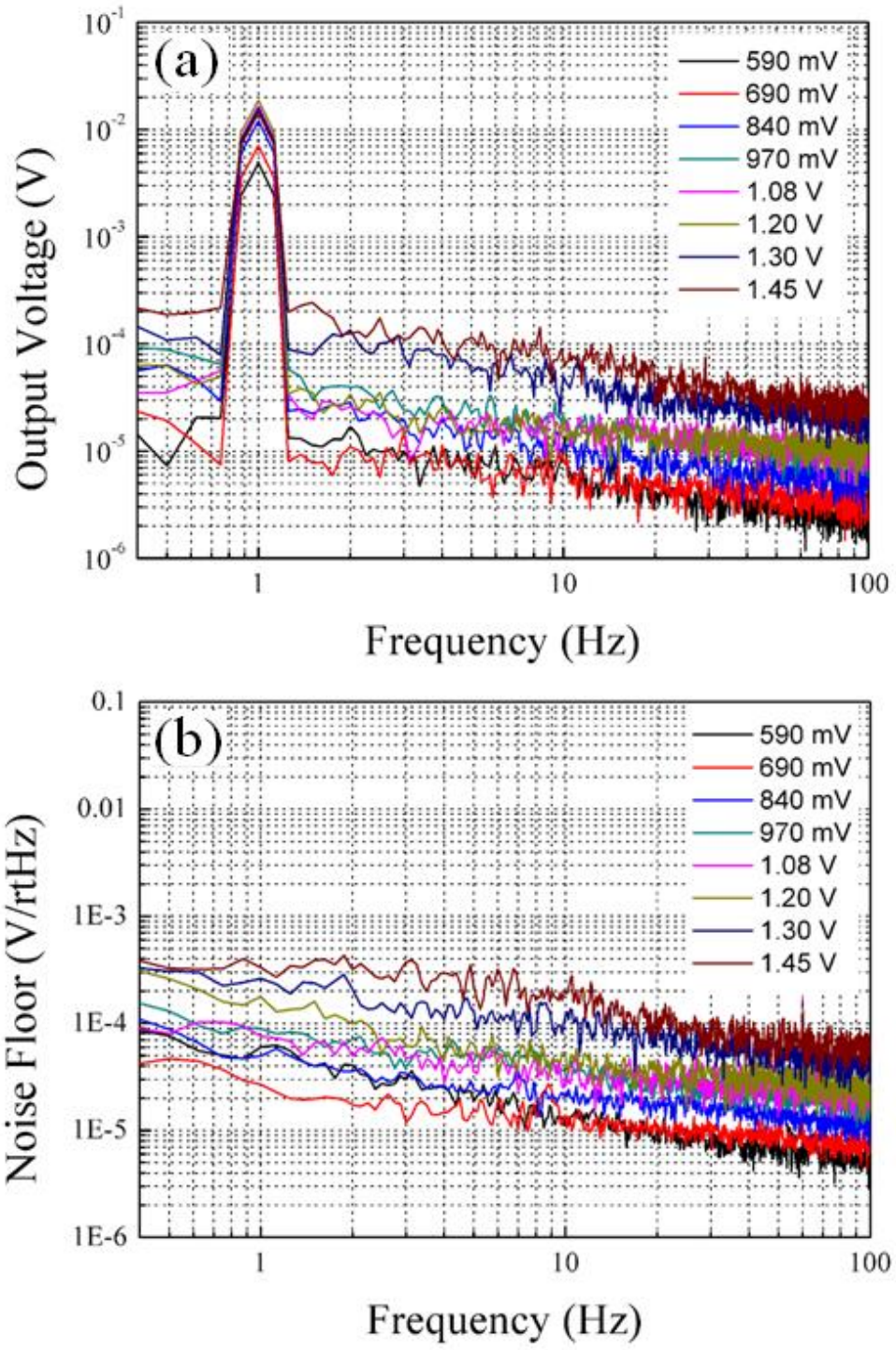

Figure 4.28 (a) Induced output signals in response to the incident magnetic field; and (b) noise spectra of the sensor at various driving signals.

Based on prior results, the equivalent magnetic noise density spectra for each condition were also calculated. As shown in Figure 4.29, the largest driving signal resulted in the highest noise level. Moreover, noise floor results for the sensor driven by the signals with amplitudes of 0.69 V, 0.84 V, 0.97 V and 1.08 V had the similar noise levels form 0.4 Hz to 100 Hz.

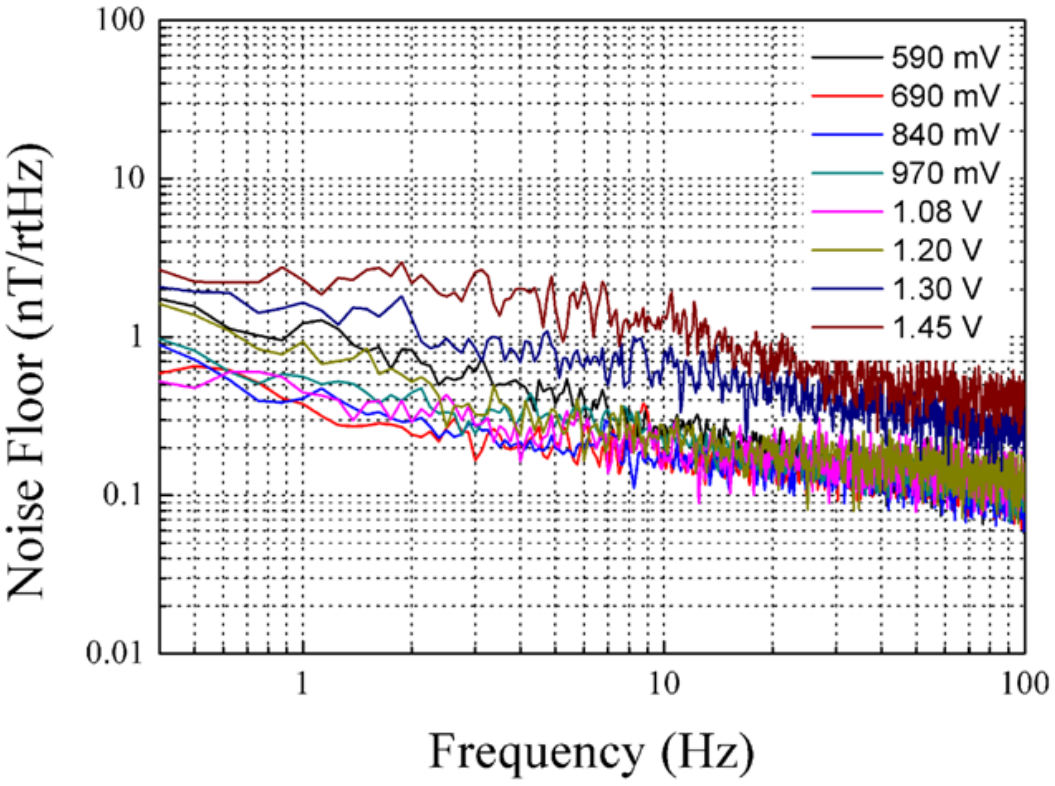

Figure 4.29 Equivalent magnetic noise density spectra for the sensors under different driving signals.

I also calculated results for sensitivity, voltage noise and equivalent magnetic noise at 1 Hz as a function of driving signal amplitudes, as shown in Figure 4.30. With respect to sensitivity, this parameter increased by increasing the amplitude of the driving signal, reaching maximum value at 1.20 V. Past this driving signal level, however, the value became smaller. Similarly, the output voltage noise also increased when the amplitude of the driving signal was elevated, which was somewhat analogous to our findings for magnetic noise. Finally, taking into account both sensitivity and voltage noise, the equivalent magnetic noise at 1Hz was calculated. We can see that the equivalent magnetic noise first decreased and then increased. Moreover, in reviewing my findings for noise density at levels of at 0.69 V, 0.84 V, 0.97 V and 1.08 V, I confirmed that the lowest values were at approximately 0.4 nT/√Hz at 1 Hz. This means that, in principle, the highest resolution results for these conditions should be in keeping with SNR = 1. However, by driving the sensor with 1.08 V, we were able to generate the largest output signal which was much more convenient for practical detection methods using other instruments. Therefore, results from this study confirmed the effective methods for optimizing the active sensor. Additionally, driving the sensor under optimal conditions can significantly decrease the equivalent magnetic noise.

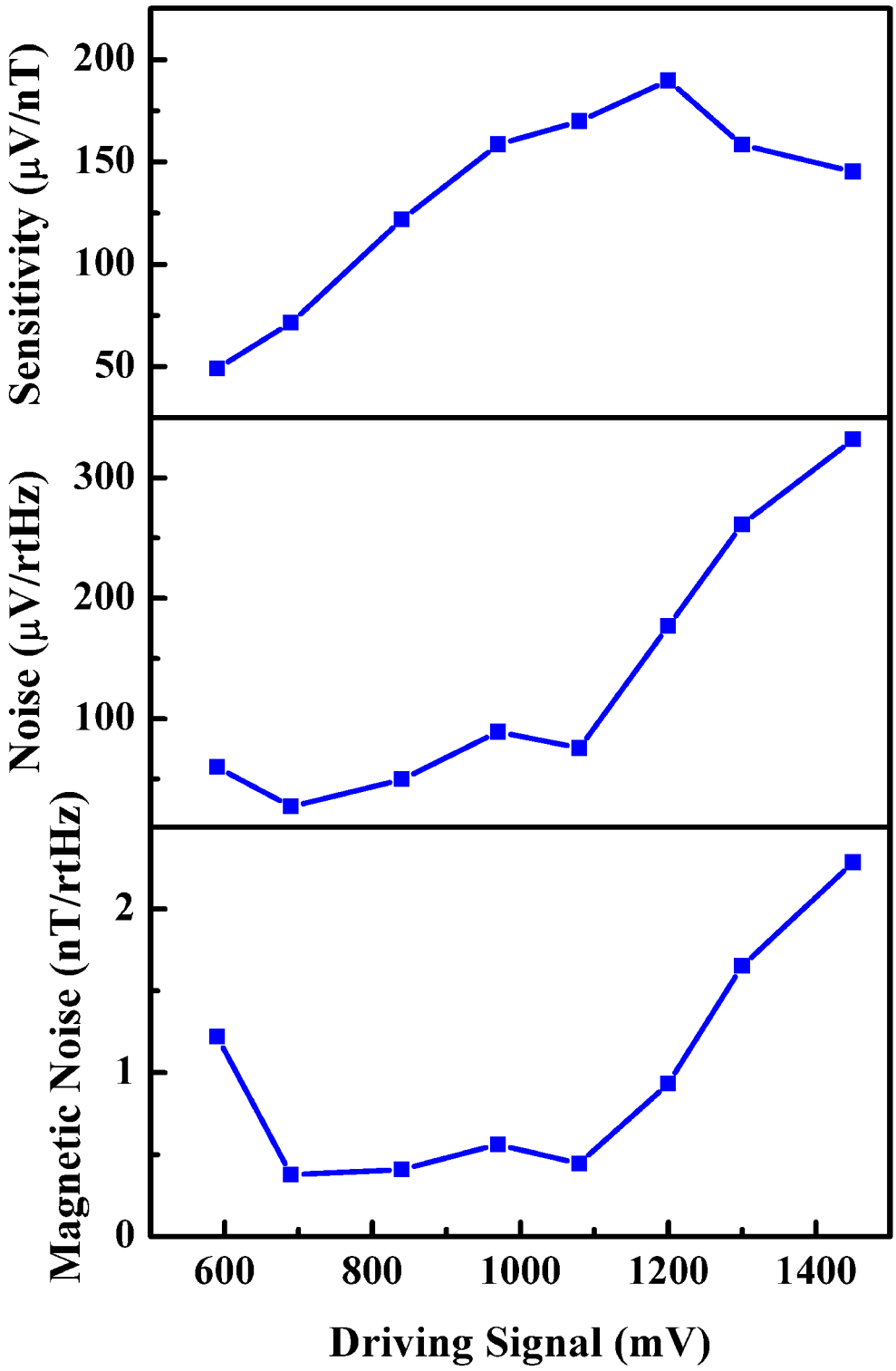

Figure 4.30 Sensitivity, voltage noise density and equivalent magnetic noise density results at 1Hz for the active sensor as a function of driving signal.

The biggest advantage of an active sensor in comparison to a passive one is that there is no need for an external dc bias. So, it allows us to directly measure the geomagnetic field noise without considering the interactions between the field and the dc bias. The photo insert in Figure 4.31 shows the experimental setup. Initially, the sensor was placed along the magnetic north direction, but was then rotated to the east direction. The results are shown in Figure 4.31 (a). Clearly, one can observe the geomagnetic noise along different directions. In detail, the noise level for north direction was higher than the noise along east direction. It should be noted that both of the sensors presented the strong 60 Hz magnetic noise due to the EMI in the open environment. In addition to the spikes observed at around 60 Hz, there were also several strong spikes at a frequency range of 20 Hz. To confirm the noise source from this range, the fluxgate was used to measure the geomagnetic field along the north direction as well, and subsequent data were used to compare the two sensors.

Figure 4.31 (b) shows the comparison of both sensors. As depicted, the active sensor had a similar noise level compared to the fluxgate along north direction. Moreover, the fluxgate also presented strong spikes at 20 Hz range, which may be used to confirm that the noise was not a result of vibration since it had little response to vibration. Instead, the strong spikes at 20 Hz were probably the result of electromagnetic noise induced by the AC power.

These measurements confirm that the active sensor has the ability to measure geomagnetic field noise precisely. Additionally, our results also imply that one needs to consider environmental magnetic noise along different orientations when performing research involving magnetic field testing.

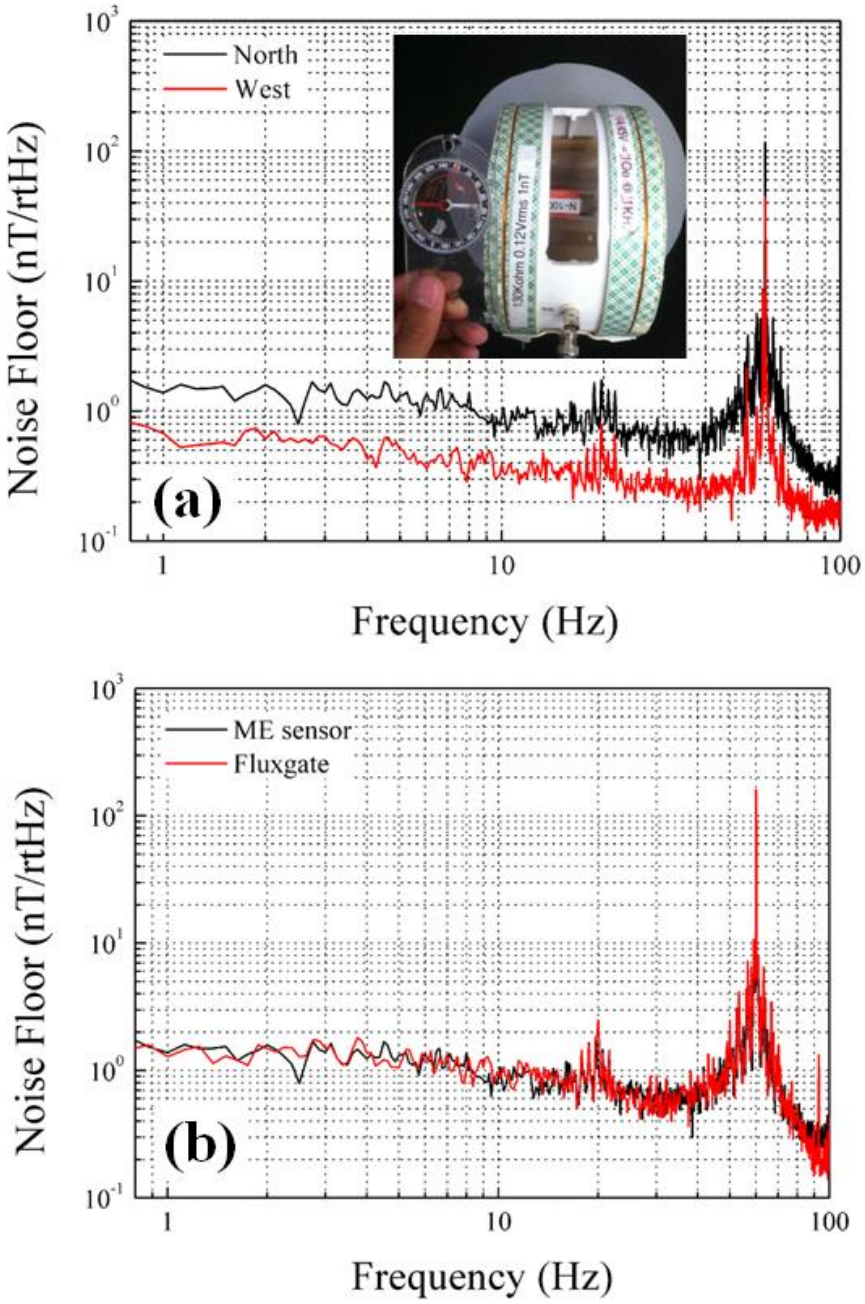

Figure 4.31 (a) Local geomagnetic field noise measurements along different directions; and (b) comparisons of noise spectra measured by active sensor and fluxgate. The photo insert of in upper portion of this figure depicts the experimental setup.

4.5 Summary of this section

In summary, two types of AC magnetic sensors based on ME composites were developed and optimized, including both passive and active modes. Moreover, the charge noise circuit model has been established to analyze the passive magnet sensors with more reasonable simulation results. Additional, detailed results are summarized as follows:

(i) A passive magnetic sensor based on ME composites was assembled into one battery-operated detection unit. Considering its practical applications, different bandwidth circuits were designed for the ME sensor. For example, a wide bandwidth circuit can help the sensor detect a magnetic field from 1 Hz up to 1.6 kHz. In order to reduce the 60 Hz EMI, a specific notch filter was integrated into the circuit as well, which can work effectively for obtaining practical measurements. Additionally, one low frequency circuit was designed for a specific low frequency field test, which was conducted at 0.6 Hz to 10 Hz. The advantage of the low frequency circuit is that it can significantly reduce output noise.

(ii) A more accurate charge noise model for the passive sensor was developed, which can predict noise density for the magnetic sensor more precisely. Moreover, a magnetic sensor capable of functioning at extremely low frequency range (< 1 mHz) has been successfully proposed. Using data from my noise model, some optimization results have been achieved that reduce the equivalent magnetic noise density by a factor of 10.

(iii) Based on the nonlinear ME effect, an active magnetic sensor has also been developed that can work from DC to 100 Hz. Instead of using direct measurement, an active sensor was designed according to modulation-demodulation processes, which were investigated mathematically and described in this section. Furthermore, the detection bandwidth of the active sensors has been successfully modulated, which confirmed that the sensors can be used for different applications. Finally, by adjusting the amplitude of the driving signal, I determined that the circuit can reduce the equivalent magnetic noise effectively, which offers one good method for optimizing the sensor.

5. DC magnetic sensor

5.1 Introduction

Previous investigations have also confirmed that ME composites can be used to detect DC magnetic fields by using an active method. In fact, reports have indicated that the sensitivity can reach the ~nT level. One of the main applications for a DC magnetic sensor is to detect the geomagnetic field. For example, this type of sensor could be used in an underwater positioning system that is based on a geomagnetic field or a local magnetic field. Interestingly, the motivation for such application was inspired by bio-behaviors in nature and, in particular, the sea turtle, which is able to sense geomagnetic fields and use them to navigate vast underwater distances. Research has shown that sea turtles can detect subtle variations of intensity and inclination angle of geomagnetic field, as shown in Figure 5.1. This finding, in part, led us to develop a new guidance system based on geomagnetic fields.

Based on this idea, prior members of our research group attempted to use a DC sensor to sense magnetic fields under laboratory conditions. Although their results confirmed that the sensor was able to detect changes in magnetic field intensity along different rotation planes (Figure 1.10), there were four critical shortcomings that need to be addressed, as follows:

(i) Improve sensitivity to small DC magnetic fields.

Higher sensitivity allows a sensor to detect smaller changes in a geomagnetic field. Considering that the geomagnetic field gradient is, on average, around 0.02 nT/m in the Virginia area, a highly sensitive sensor could improve spatial resolution.

(ii) New detection device

Although previous studies have demonstrated the ability to detect a geomagnetic field with some accuracy, those measurements tend to be based on the lock-in amplifier detection method. This process requires one commercial lock-in amplifier to drive the sensor, as well as detect the induced signals. However, it is not feasible to use this instrument in outside conditions for testing guidance devices of the future. It is highly desirable, therefore, to develop a new detection circuit that has the similar ability of commercial lock-in amplifier.

(iii) Multi-axial detection sensor

A multi-axial detection sensor allows us to acquire geomagnetic field information along different directions quickly. The quick response is essential for localization and navigation.

(iv) Applications for geomagnetic field sensor

Since no prior reports have described the real-world applications for geomagnetic sensors based on the magnetoelectric effect, one challenge for the current study was to perform and outside field test to sense a geomagnetic field, including magnetic field mapping and subsequent motion monitoring based on the detected field.

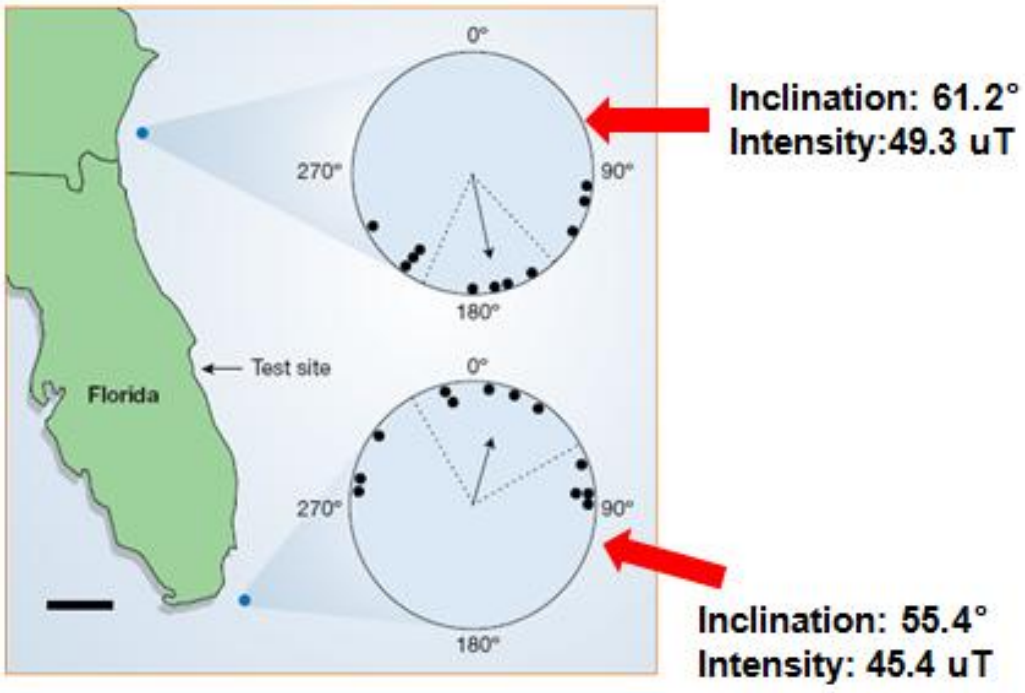

Figure 5.1 Geomagnetic sensing by sea turtles.

5.2 Improvement of sensitivity

The detection principle associated with DC testing is quite different in comparison to AC testing. For the AC sensor, the goal is to improve optimum ME voltage coefficients that can increase the output signal in response to an incident magnetic field. In contrast, a DC sensor requires larger voltage changes to detect the larger DC magnetic field variations under geomagnetic field range (-0.65 gauss to 0.65 gauss). Take one α_{ME}-H_{dc} curve as an example: Figure 5.2 presents the typical curve for Metglas/PZT composites. The optimum α_{ME} at the magnetic bias of 8 Oe is related to AC detection sensitivity, while the slope value of the linear part affects DC detection sensitivity.

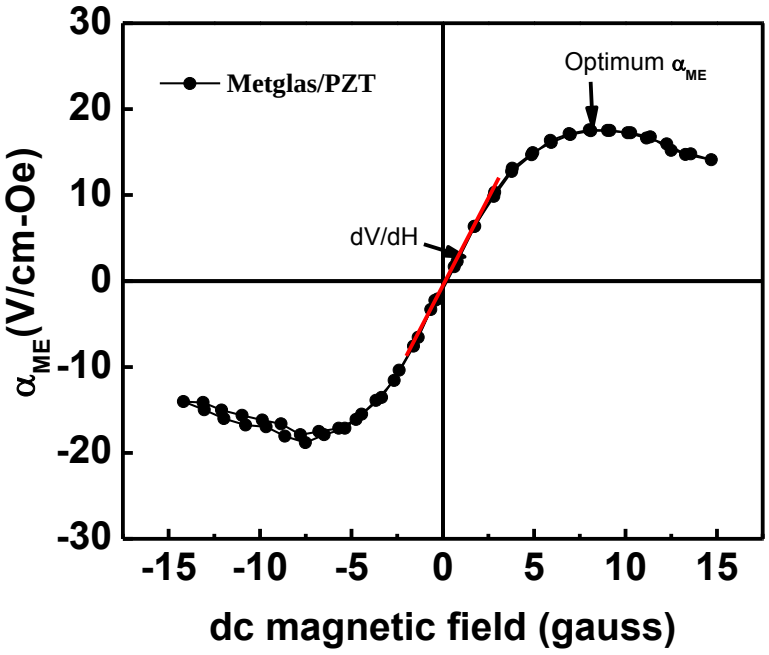

Figure 5.2 α_{ME}-H_{dc} for Metglas/PZT composites.

5.2.1 Different piezo-fibers

In this section, I compared highly orientated Metglas/Pb($Mg_{1/3}Nb_{2/3}$)O_3-$PbTiO_3$ (PMN-PT) fibers with PZT fibers based sensor's sensitivity. I used PZT (Smart Materials, Sarasota, FL) and PMN-PT (Ceracomp Co., Ltd., Korea) fibers to make different ME composites. The fabrication process and the geometry for each composite was exactly the same. The piezoelectric properties for these PZT and PMN-PT fibers are provided in Table 5.1. Higher g_{33} and k_{33} coefficients for PMN-PT fibers were expected to improve the ME effect. However, as previously indicated, that is not the only factors for DC sensitivity; detailed characterizations were required.

Table 5.1 The critical piezoelectric properties for PZT and PMN-PT fibers

	$d_{33,p}$	$g_{33,p}$	k_{33}
PZT[a)]	440pC/N	25.5mV·m/N	0.72
PMN-PT[b)]	2000pC/N	32.4mV·m/N	0.93

a) Cited from Smart Material Corp., USA
b) Cited from Ceracomp Co., Ltd., Korea

Figure 5.3 (a) shows α_{ME} as a function of H_{dc} for Metglas/PMN-PT and Metglas/PZT laminates. From this figure, we can see that α_{ME} for the two ME laminates had similar trends with H_{dc}; however, the values of α_{ME} for the Metglas/PMN-PT laminate were notably higher in comparison to those for Metglas/PZT. In particular, the maximum value of α_{ME} for the Metglas/PMN-PT laminate was 45 V/cm-Oe, which was about 3 times larger than that for the PZT based one of similar size (i.e., 15 V/cm-Oe). This represents the highest value of α_{ME} reported to date for any ME composite, by a factor of 2×.

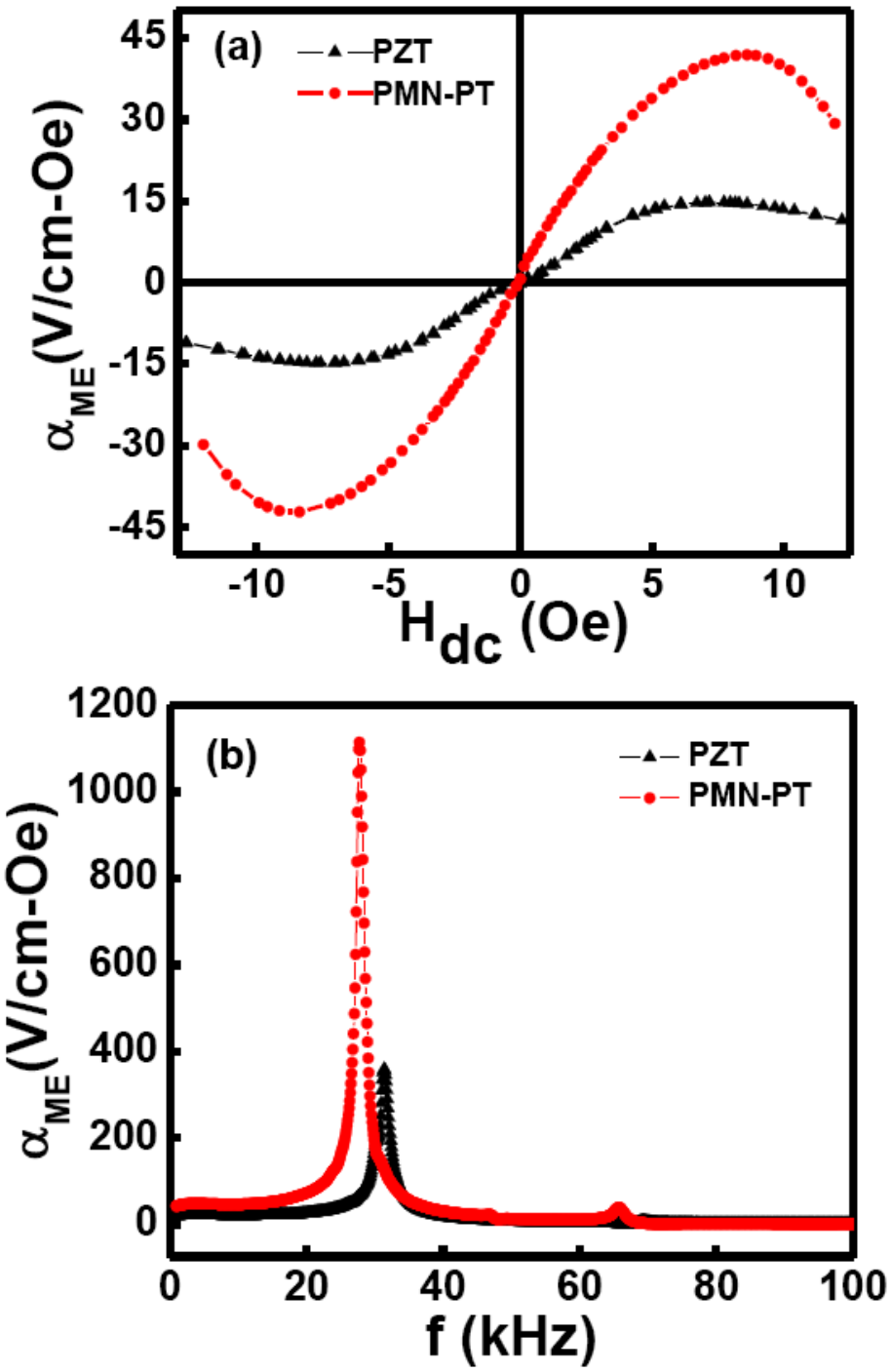

Figure 5.3 ME voltage coefficient of Metglas/PZT and Metglas/PMN-PT laminates: (a) α_{ME} as the function of dc bias H_{dc} at f = 1 kHz, and (b) α_{ME} as a function of ac magnetic drive frequency.

Figure 5.3 (b) shows the ME voltage coefficient for Metglas/PZT and Metglas/PMN-PT laminates as a function of AC magnetic field frequency, while sweeping through the electromechanical resonance (EMR). The fundamental resonant frequencies for the PZT and PMN-PT based sensors were 31.5 kHz and 27.8 kHz, respectively. In this figure, we can see (i) a strong EMR enhancement in α_{ME} that was previously reported; and (ii) that values of α_{ME} > 1100 V/cm-Oe can be achieved for PMN-PT laminates, which was about 3× larger than that for PZT ones.

The DC magnetic field sensitivity was characterized for both sensors using an active method: a 100 turns coil was wrapped around the sensor which carried a small AC current provided by the lock-in amplifier to drive the ME sensors. Voltages were then induced in the piezoelectric layer by small changes in H_{dc}, which were measured by the amplifier. Figure 5.4 presents the comparison of the DC magnetic field sensitivity of two ME composites.

Figures 5.4 (a) shows the induced output voltages from the Metglas/PZT laminates in response to small changes in H_{dc} at driving frequencies of f=1 kHz. It can be seen that DC magnetic field variations as small as H_{dc}=15 nT can be detected. Figures 5.4 (b) shows similar sensitivity measurements to small changes in H_{dc} for Metglas/PMN-PT laminates. In this figure, one can see that the sensitivity for the Metglas/PMN-PT laminates was significantly enhanced relative to that for the Metglas/PZT ones. The sensitivity to DC magnetic field changes for PMN-PT lamiantes can be seen to be 5 nT at 1 kHz and H_{ac}=0.1 Oe: which was 3 times higher than that for PZT based ones.

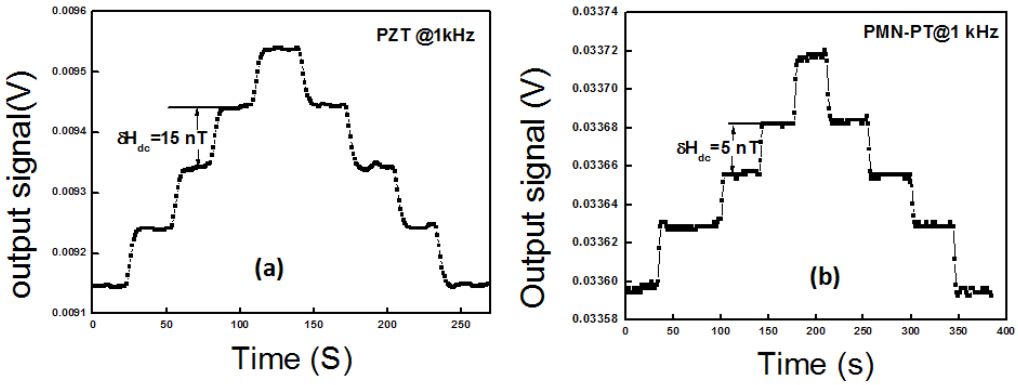

Figure 5.4 DC magnetic field sensitivities for (a) PZT based; (b) PMN-PT based composites.

Finally, the sensitivity to small DC magnetic field changes for Metglas/PMN-PT laminates was studied under the EMR conditions (f =27.8 kHz). Since α_{ME} is extremely high in this case (see Figure 5.3 (b)), it was believed that the sensitivity could be improved even further under EMR driving condition. During the test, the ME sensor was placed in a magnetically shielded chamber to reduce exposure to environmental noise. Figure 5.5 shows the induced output voltage to small step changes in DC magnetic field. Clearly, the Metglas/PMN-PT laminates can detect changes of $H_{dc}\leq$1 nT. This represents a notable improvement in DC field sensitivity relative to lower frequencies.

However, the principal limitation for driving the sensor under resonant frequency is the unstable response outside of the chamber. A small level of magnetic field bias could affect the output signal. That is the reason we put the above test in the chamber. Moreover, the resonant frequencies for different sensors are quite various that require different driving frequency for individual one. It is definitely not convenience for practical applications considering more driving sources are required.

Therefore, I am able to achieve a significant enhancement in α_{ME} (by 3×) and the DC magnetic field sensitivity (by up to 10×) by using PMN-PT fibers in heterostructured composites, relative to the analogous values for the PZT fibers. The ME voltage coefficient for Metglas/PMN-PT laminates reached values of 45 V/cm-Oe at f=1 kHz, and of 1100 V/cm-Oe at the EMR. The DC field sensitivity of these Metglas/PMN-PT laminates was then found to be 4 nT under a constant drive of H_{ac}=0.1 Oe at f =10 kHz. Even smaller DC field changes of ≤1 nT were also detected at the EMR.

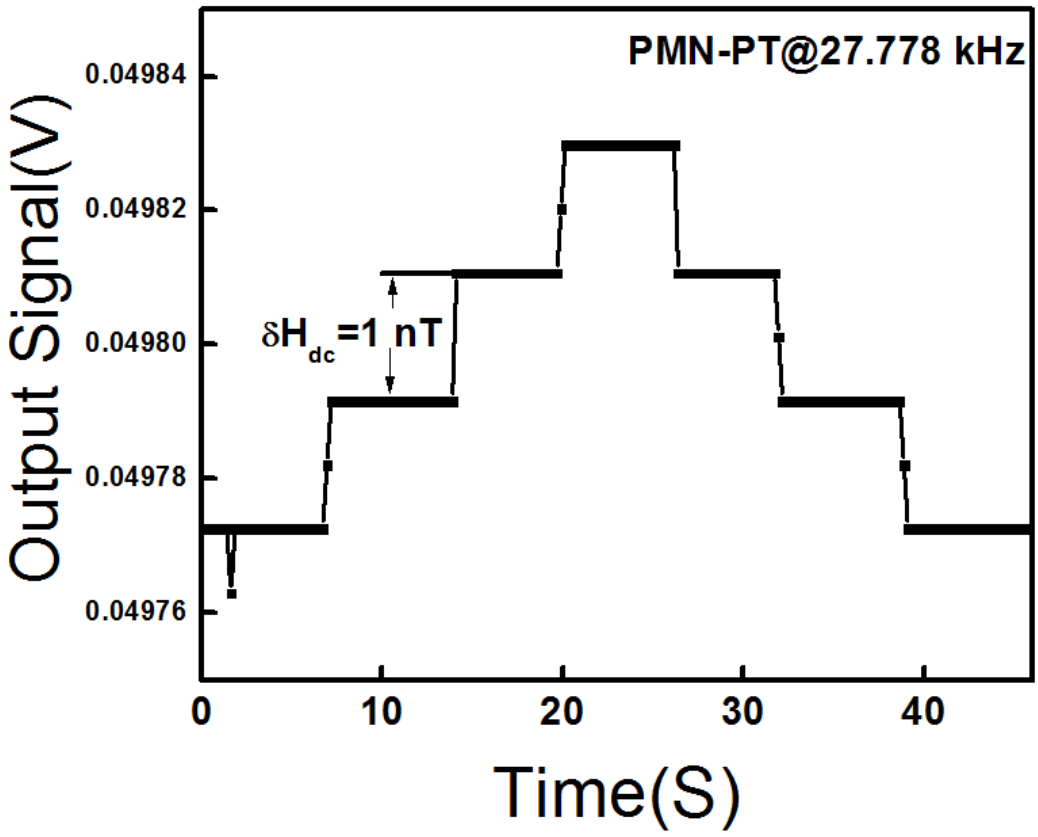

Figure 5.5 Sensitivity of MEtglas/PMN-PT laminate to small DC magnetic field changes under ac drive field of H_{ac} = 0.1 Oe at the resonant frequency.

5.2.2 Magnetic flux concentration

This study was based in part on the assumption that the flux concentration associated with a DC magnetic field measurement is quite important. Therefore, any method that could improve this factor would be able to increase induced signal changes at the same DC field variations. In response, I developed a magnetostatic finite element model to study the effects of in-plane magnetostrictive phase geometry on the magnetic flux concentration within high-mu layers. According to subsequent simulation results, we then redesigned the geometry of the sensors.

Magnetostatic modeling was performed using a commercial finite element modeling (FEM) package (Ansoft's Maxwell 3D). A uniform DC magnetic field was simulated by using a pair of neodymium permanent magnets separated by 25 cm at either end of the axial direction of the Metglas ribbons, as illustrated in Figure 5.6 (a). The strength of the neodymium magnets was adjusted to provide a sufficiently small H field, so as not to reach saturation (H_{sat}) within the high mu material. A 1 cm wide by 25 um thick ribbon of high-mu material was placed between the bias magnets, and then the length was changed for various laminates between 80 and 100 mm. The mu-metal was assigned a non-linear B-H curve (see insert in Figure 4.6) from the Ansoft materials library file to approximate the real behavior of the Metglas. An automatic 1000 point mesh was generated within a control volume with appropriate boundary conditions, located sufficiently far from regions of interest within the material. The simulation was completed to within 0.5% accuracy after 100 iterations of the code.

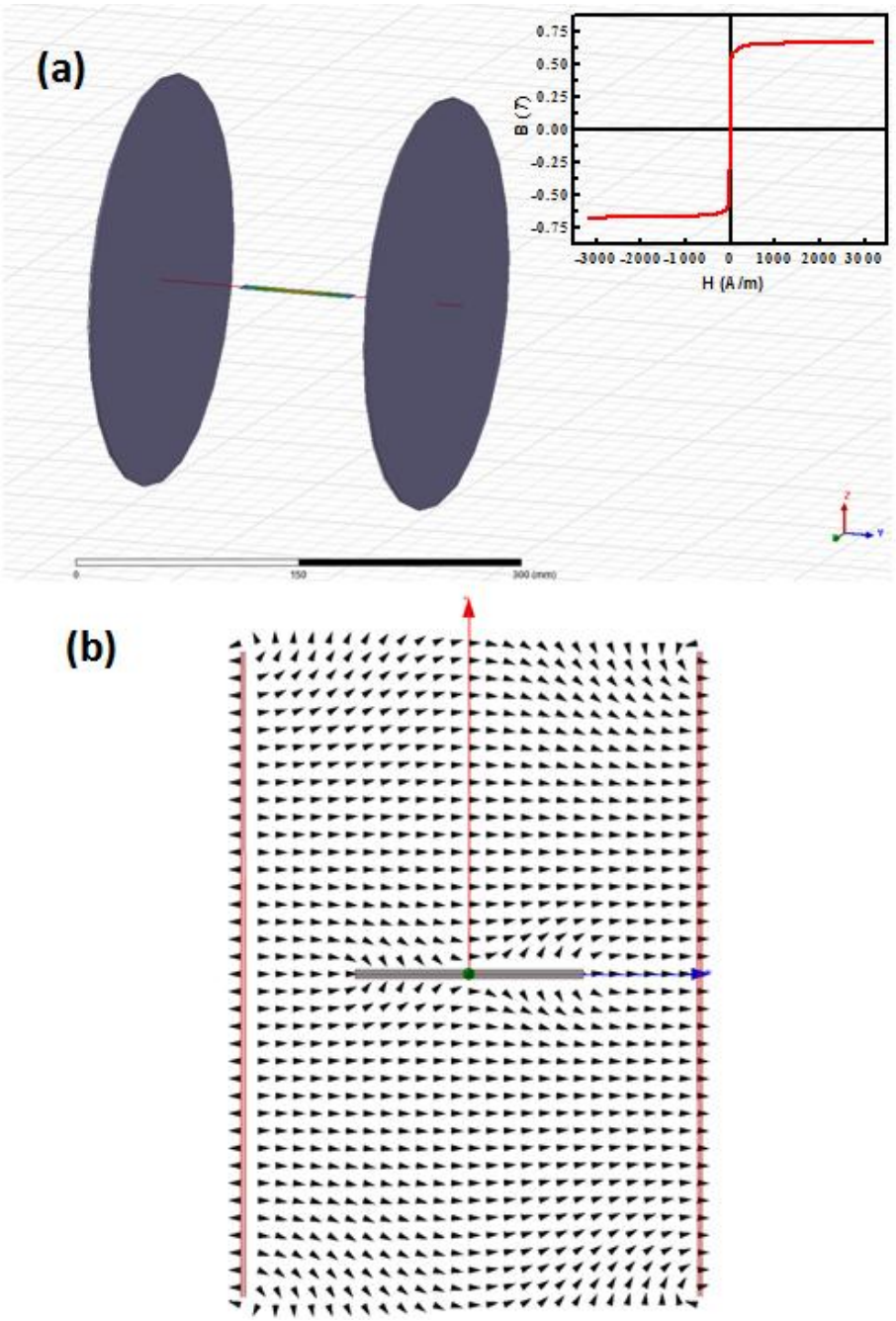

Figure 5.6 (a) Schematic representation of 3-D Mangetostatic model layout including large, permanent magnetic HDC bias generators, and (b) vector map of the y-z (axial-height) component of the H field in the presence of the high-mu Metglas. Insert: non-ideal B-H relationship used to define magnetostatic behavior of high mu Metglas in FEM.

The magnetic flux in the space close to the Metglas was found to be dramatically influenced by the high permeability of the foils. A planar representation of the H field in the space surrounding the Metglas is shown in Figure 5.6 (b). The magnetizing field (and corresponding flux density) was distorted in regions of close proximity to the Metglas in the Y-Z plane. The flux density was similarly distorted in all three dimensions surrounding the Metglas, although only a single plane is shown in Figure 5.6 (b) for illustration. The net effect of the flux concentration of the high-mu material was evidenced by a relative change in the internal field characteristics.

As shown in Figure 5.7 (a), the in-plane magnetic field strength for longer Metglas foils was larger than that of shorter ones, especially in the center portion of the foil. Line scans along the axial center-line of the Metglas foils (See Figure 5.7 (b)) with increasing length of the foil from 80 to 100 mm resulted in a 36% increase in field strength at the center of the Metglas ribbon. While the model has not been configured to allow for accurate determination of the absolute value of the flux density within the material, we believe that the relative increase in field strength is physically correct, and supportive of the experimental results to be shown below.

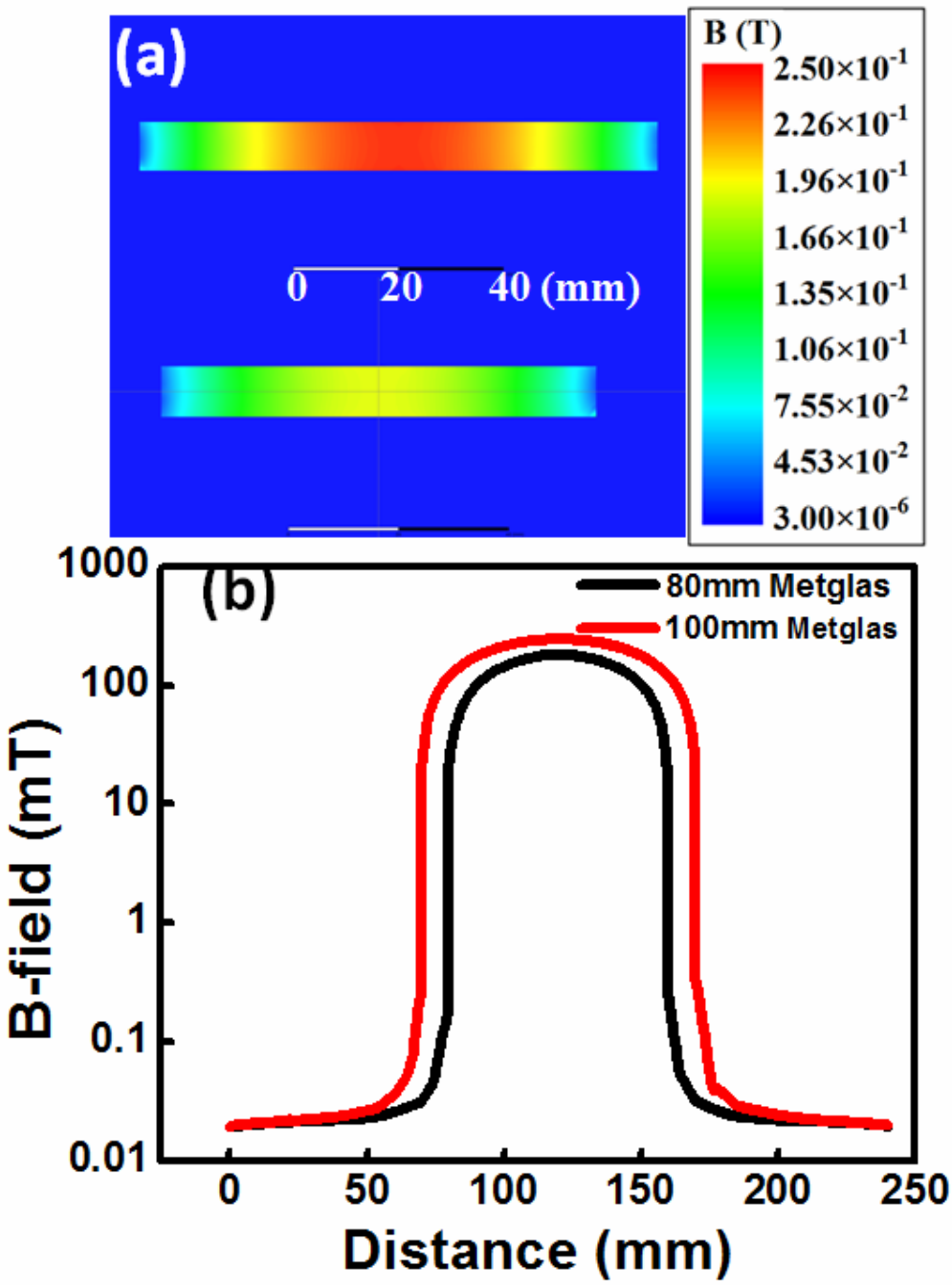

Figure 5.7 (a) In-plane magnetic field strength along center plane of Metglas foils in response to arbitrarily low DC bias field, as simulated by Maxwell 3D, and (b) line scan traces of magnetic flux density along the axially centerline of Metglas foils for 80mm and 100mm geometries.

Based on these simulation results, we fabricated composites with different lengths (8 cm and 10 cm) of Metglas foils for comparison. Figure 5.8 present the values of α_{ME} for ME laminates of different length that exhibited similar trends with H_{dc}. In both cases, α_{ME} increased from roughly 0 V/cm-Oe at zero bias to a maximum value at an optimum bias condition, and subsequently decreased as H_{dc} was increased further. The value of α_{ME} for the laminates with the longer Metglas foils was notably higher than that for shorter ones, while also requiring smaller magnetic biases. For example, under H_{dc} =2.5 Oe, the value of α_{ME} was 10 V/cm-Oe for 100 mm long Metglas laminates, relative to 5 V/cm-Oe for 80 mm Metglas ones. Following the above magnetostatic modeling results, the enhancement of α_{ME} for longer Metglas directly results from higher magnetic flux concentration.

Moreover, the DC magnetic field sensitivity for both composites was characterized. Figure 5.9 shows the measured result: DC magnetic field variations as small as H_{dc}=15 nT could be detected under a 0.1 Oe, 1 kHz drive for the sensor with Metglas foils of 80 mm in length. However, the DC magnetic field changes as small as 6 nT were detectable by using a ME sensor with longer Metglas foils (100 mm): please note that similar drive conditions were used. This represents a 250% increase in the DC field sensitivity.

In summary, we found that lengthening the Metglas layer increases the magnetic flux density over the central portion of the sensor that contains the core piezoelectric layer. A redesign of the Metglas/PZT sensor was notably enhanced over the bias range of -2.5 Oe<H_{dc}<2.5 Oe. This resulted in a 250% increase in the detection threshold (from 15 nT to 6 nT), measured under a constant SNR=10.

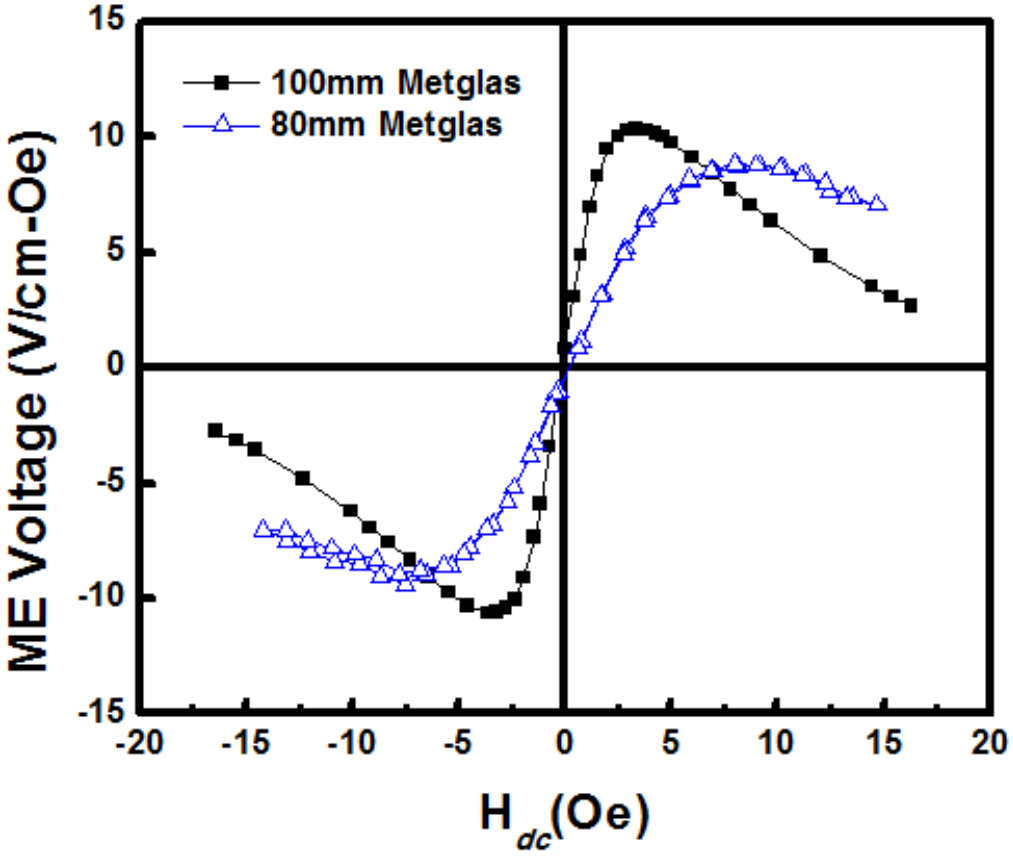

Figure 5.8 ME voltage coefficient of laminate sensor with different Metglas lengths as a function of DC bias H_{dc} in response to a 1Oe, 1 kHz AC magnetic excitation.

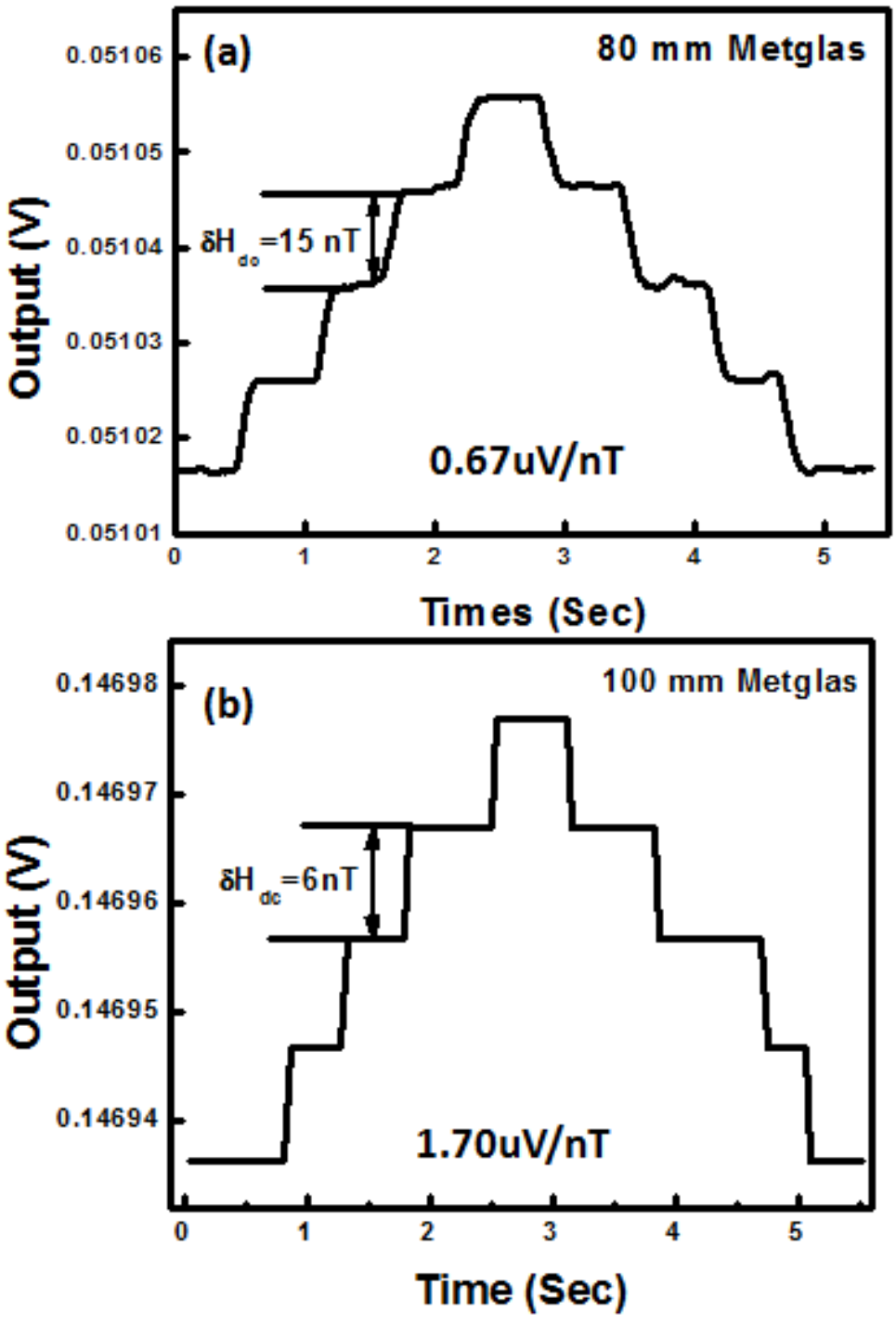

Figure 5.9 Comparison of the sensitivity for Metglas/PZT laminates to small DC magnetic field changes under AC drive conditions of at f =1 kHz and H_{ac}=0.1 Oe: (a) ME sensor with 8 cm long Metlgas, and (b) ME sensor with 10 cm long Metglas.

5.3 Man portable magnetic sensor

5.3.1 Lock-in detection circuit

In addition to working on improvements in sensitivity, we also designed a new circuit detection unit to replace the commercial lock-in amplifier. Figure 5.10 (a) shows a lay-out for the custom designed lock-in circuit. An analog sine wave oscillator (OSC) provided a modulation AC signal at frequency of 1 kHz to drive ME composites. The sensor output signals firstly passed a high-pass filter (HPF), and then were amplified by an instrumentation amplifier (InA). The amplified signals were demodulated by a demodulator with the help of a reference signal provided by the oscillator. A low pass filter (LPF) was used to provide a stable output. A second-order low pass filter (LPF) was used to filter out high frequency components of the demodulator output signal.

Figure 5.10 (b) provides a photo of single axis lock-in circuit prototype. In this prototype, two 4.8-V batteries were used as the power supply. The dimensions of the circuitry were 9 cm × 6 cm × 12 cm, while the power consumption was only 96 mW. The OSC provided a 1 kHz sine wave, while the corner frequency of the second-order LPF was set at 1.6 Hz. Bottom, left and right BNC connectors were used for the modulation signal, sensor outputs and detected signal, respectively. A switch was also used to turn off the lock-in circuit to save power.

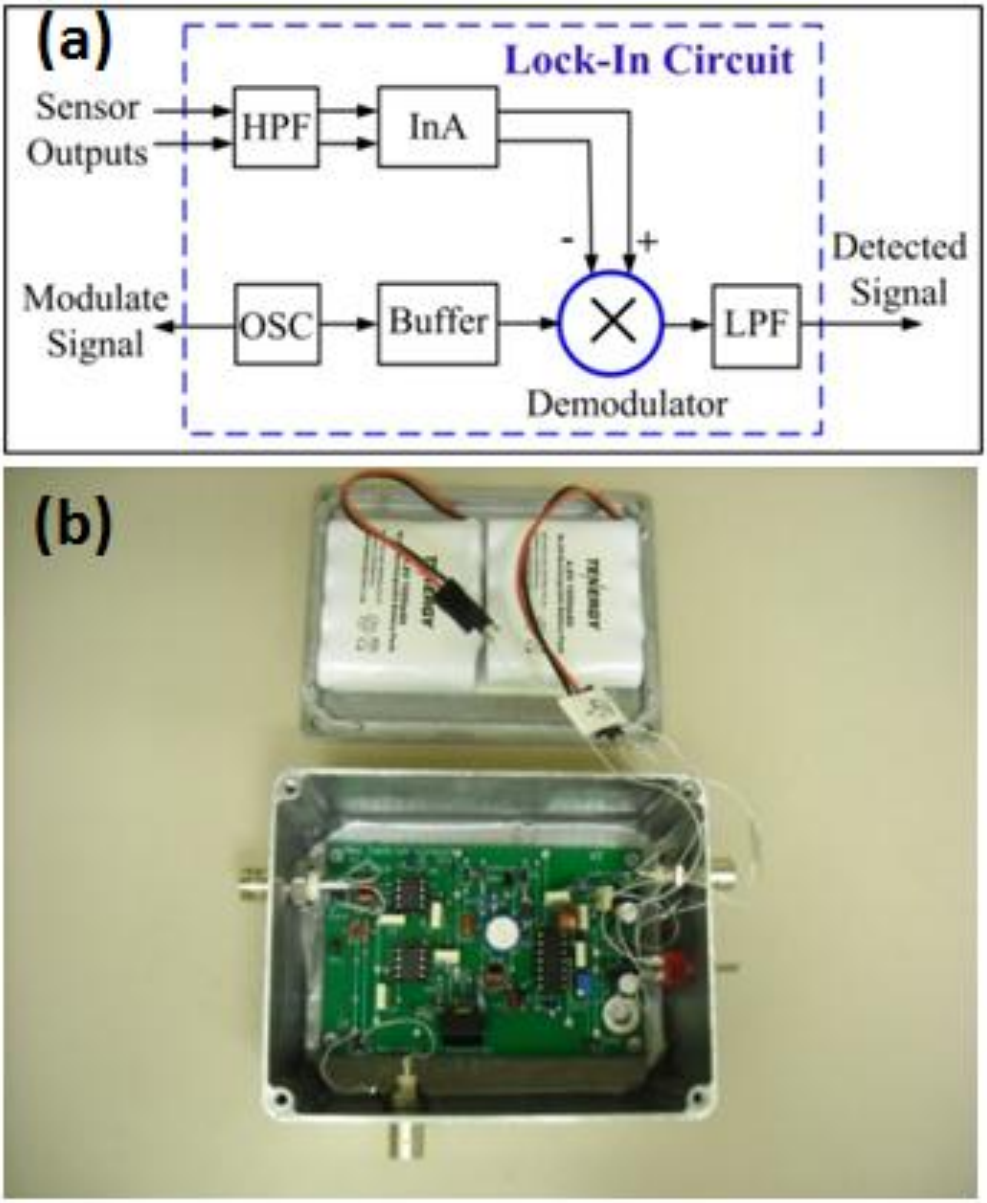

Figure 5.10 (a) Schematic of our custom-built lock-in circuit; (b) photo of a prototype lock-in circuit.

After fabricated the circuit, we checked the function of each part to make sure the circuit works well. First, we tested the oscillator, which is used to generate the driving signals and reference signals for the demodulation process. If this part did not work well, the circuit would not perform the expected functions. To examine the oscillator, we simply connected the driving signal port to the oscilloscope using a BNC cable. Figure 5.11 shows the output signals in time domain. One can see that a perfect sine wave signal can be generated by the circuit. Moreover, by adjusting a couple of components in the circuit, the frequency of the AC signal can be tuned from 1 kHz to over 30 kHz. This means we can drive the sensor under off resonant and resonant conditions depending on application requirements.

After this inspection, we compared the detection sensitivity of our fabricated lock-in circuit and the commercial lock-in amplifier using the same ME composites. Figure 5.12 (a) and (b) shows the DC magnetic field sensitivity detected by using the lock-in amplifier and lock-in circuit, respectively. From this measurement, one can see that the lab-made circuit has quite similar detection sensitivity as the lock-in amplifier. This outcome confirmed that we would be able to assemble the composites and the circuit in a relatively compact unit.

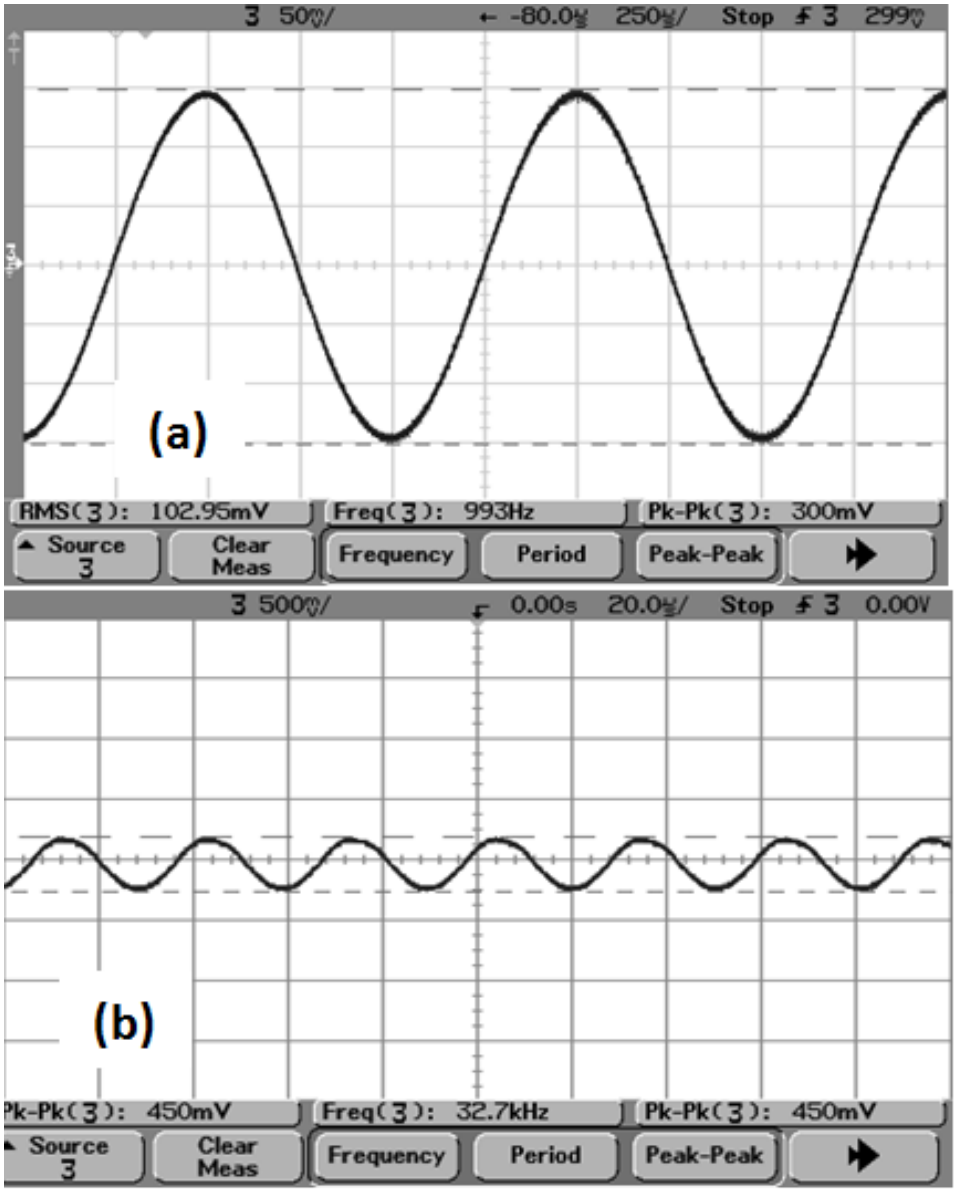

Figure 5.11 Waveforms of driving signal generated by oscillator in time domain: (a) 1 kHz; and (b) 32.7 kHz.

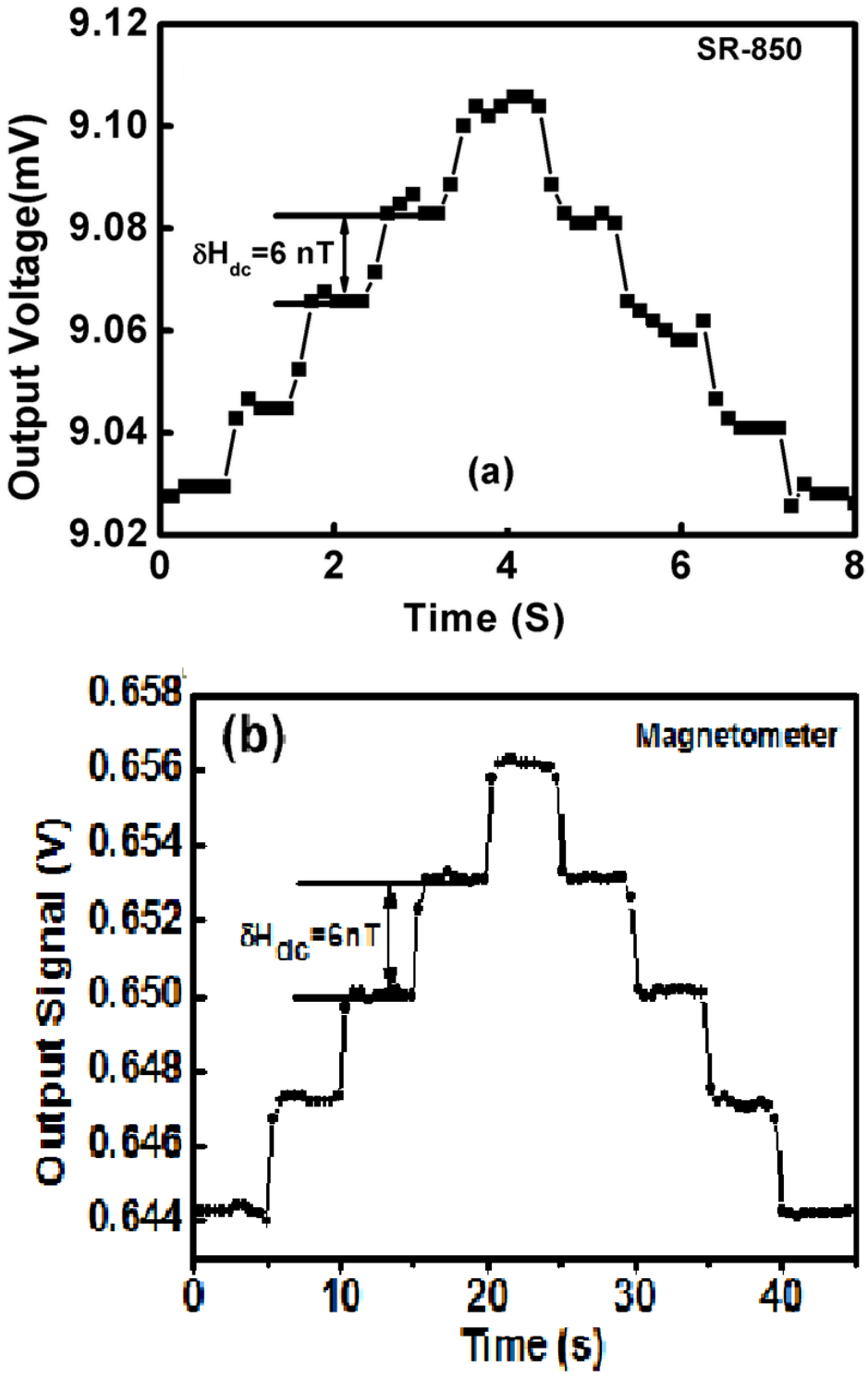

Figure 5.12 Sensitivity of composites to small DC magnetic field changes under AC driving conditions at f=1 kHz and H_{ac}=0.1 Oe generated by (a) lock-in amplifier (SR-850); and (b) lock-in circuit.

5.3.2 Sensor performance

As a DC magnetic sensor, our detection unit can be used for DC magnetic target localization, magnetic field mapping, and so on. The following section summarizes the process I utilized to obtain the essential measurements need to demonstrate the function of our DC magnetic sensors.

Firstly, I performed magnetic dipole localization. Figure 5.13(a) shows the schematic of experimental setup. In this test, a magnetic dipole was placed at an "unknown" position along y-axis, and the 1-axis DC magnetometer was placed 10 cm away and moved around the dipole over a 2-D grid of 50 cm by 20 cm. Since the magnetometer was quite sensitive to H_{dc} along the longitudinal direction but essentially, insensitive along the transverse direction, the detected magnetic field was mainly along the y direction. By detecting the magnetic field generated by the magnetic dipole, we were able to localize its position along the y-axis. Figure 5.13 (b) shows the magnetic field distribution of the dipole simulated by Vizimag software. Along the center, one can see that the symmetric magnetic flux lines flowed from the north pole to the south pole, and that the magnetic intensity reached its maximum vale around the two edges. Moreover, the magnetic flux direction was reversed over the center of dipole. Figure 5.13 (c) shows magnetic field data obtained from the magnetometer, which confirmed that the output signal from the magnetometer became larger when it was moved towards the dipole due to higher magnetic field intensity closer to the dipole. Since the magnetometer was quite sensitive to the orientation of the magnetic field, the output signal changed quickly from positive maximum to negative maximum values as it passed by the dipole source. All of these

characteristics matched the model results perfectly; in other words, there should be no magnetic field along the y direction at the middle of dipole. In Figure 5.13 (c), the "zero" point was located at 36.9 cm along the y axis. In order to reference this data, the actual distance between the mid-point and the initial position was measured by a ruler. The measured result shows the dipole was placed at 37.0 cm. Clearly, my DC magnetometer was able to localize the dipole with little error.

Furthermore, I used the DC magnetometer to measure the DC magnetic field distribution in real space. Figure 5.14 (a) shows the location where the field distributions were mapped using the portable DC magnetometer. It should be noted that this particular location had some iron pipes in vicinity, which could have distorted the magnetic field distribution, as indicated by the arrows in the figure. The test was performed over a spatial area of 1.2 m by 6.0 m. As shown in Figure 5.14(b), the results verified that a magnetic field distribution could be mapped by moving the magnetometer over this area. As expected, maximum values were detected at places closest to the pipes at (0.3m, 4.5m). Using our portable DC magnetometer, the maximum magnetic field change detected over this range was about 4800 nT, and the magnetic field was increased from 0 m to 6 m.

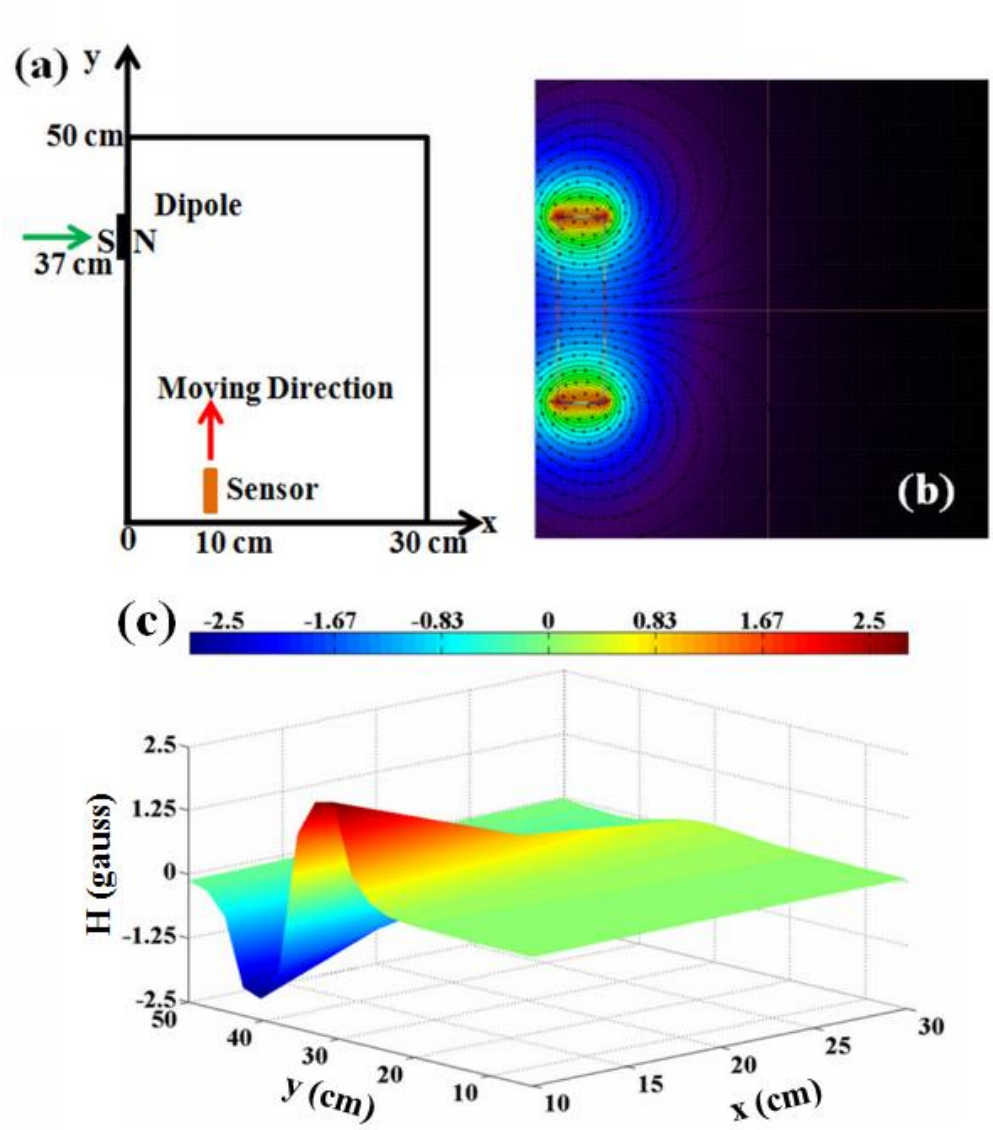

Figure 5.13 Illustration of capability of our DC magnetometer to localize a magnetic dipole: (a) schematic of experimental setup, (b) magnetic flux distribution of the magnetic dipole, and (c) real position measurement.

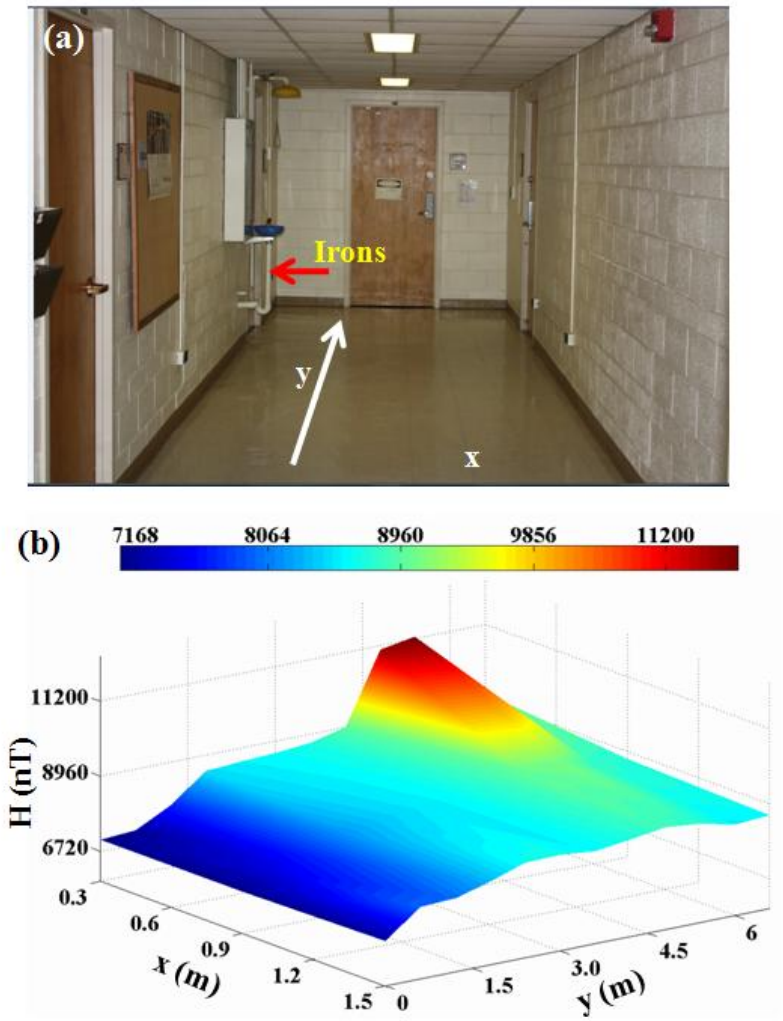

Figure 5.14 Real space DC magnetic field test: (a) photo of test location, and (b) output signal from DC magnetometer over spatial grid about test location.

5.4 Geomagnetic field detection

An important aspect of this study involved using the newly-developed and highly-sensitive DC magnetic sensor to detect a geomagnetic field, and then use resulting data to understand how to use this information to improve guidance functions. As previously indicated, in order to achieve geomagnetic field intensity along different directions, I have developed multi-axial detection unit, as shown in Figure 5.15. Specifically, 2-axial sensors were found to be useful for the horizontal plane test, while a 3-axial sensor was better for the 3-D space test.

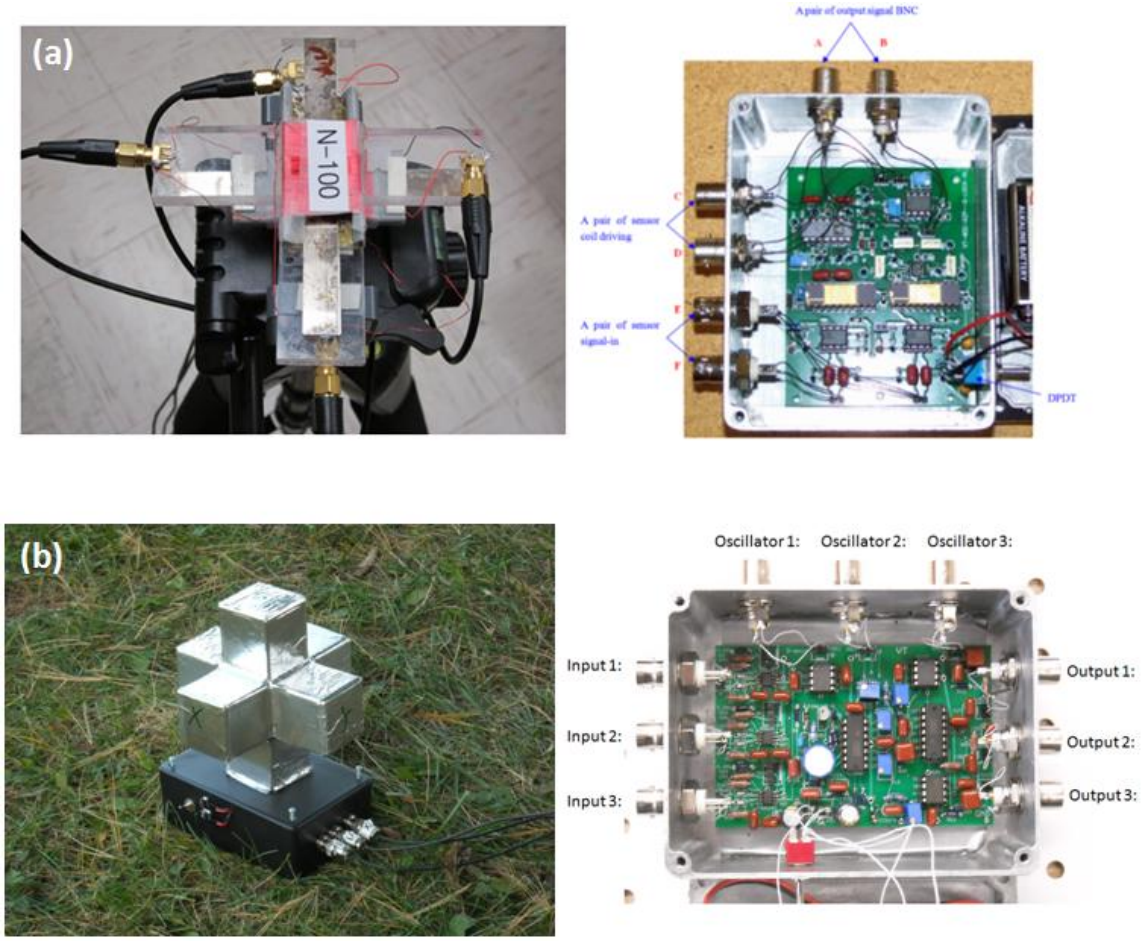

Figure 5.15 Multi-axial detection magnetic sensor: (a) 2-axis; and (b) 3-axis.

5.4.1 2-axial magnetic sensor

As shown in Figure 5.15, one 2-axial magnetic sensor was designed. Fundamentally, a magnetic sensor can monitor a magnetic field in the horizontal plane. According to the detected magnetic field, the sensor can be used for an orientation-based monitoring in a vehicle. In a 2-D plane, the geomagnetic field can be considered as the constant vector field in the absence of any external magnetic field interference, as shown in this figure. Ideally, when one rotates the 2-axial sensor along the Z-axis, the output signal of one sensor would show the sine waveform, while the other would show the cosine waveform. So, according to the output signal for each individual component, the orientation can be obtained.

For my measurement, the magnetic sensor was placed in a tripod which has two inclinometers to control the sensor along the horizontal plane without tilting. Initially, the y-axis sensor was positioned along the north direction and the angle between the y-axis sensor and the north direction was defined as θ, as shown in Figure 5.16 (a). To evaluate performance, the sensor was orientated in a gradual motion along north, northeast, east, southeast, south, southwest, west and northwest directions. During the process, the output signals from 2-axial sensor were recorded individually, and the angle θ and orientation was determined.

Figure 5.16 (b) shows the results according to the detected signals. Ideally, the angle should be equal to 45 degrees. And indeed, one can see that we were able to calculate the orientation from the geomagnetic field with relatively high accuracy. The observed deviations may have resulted from the measurement system, and/or the influence of any external magnetic field.

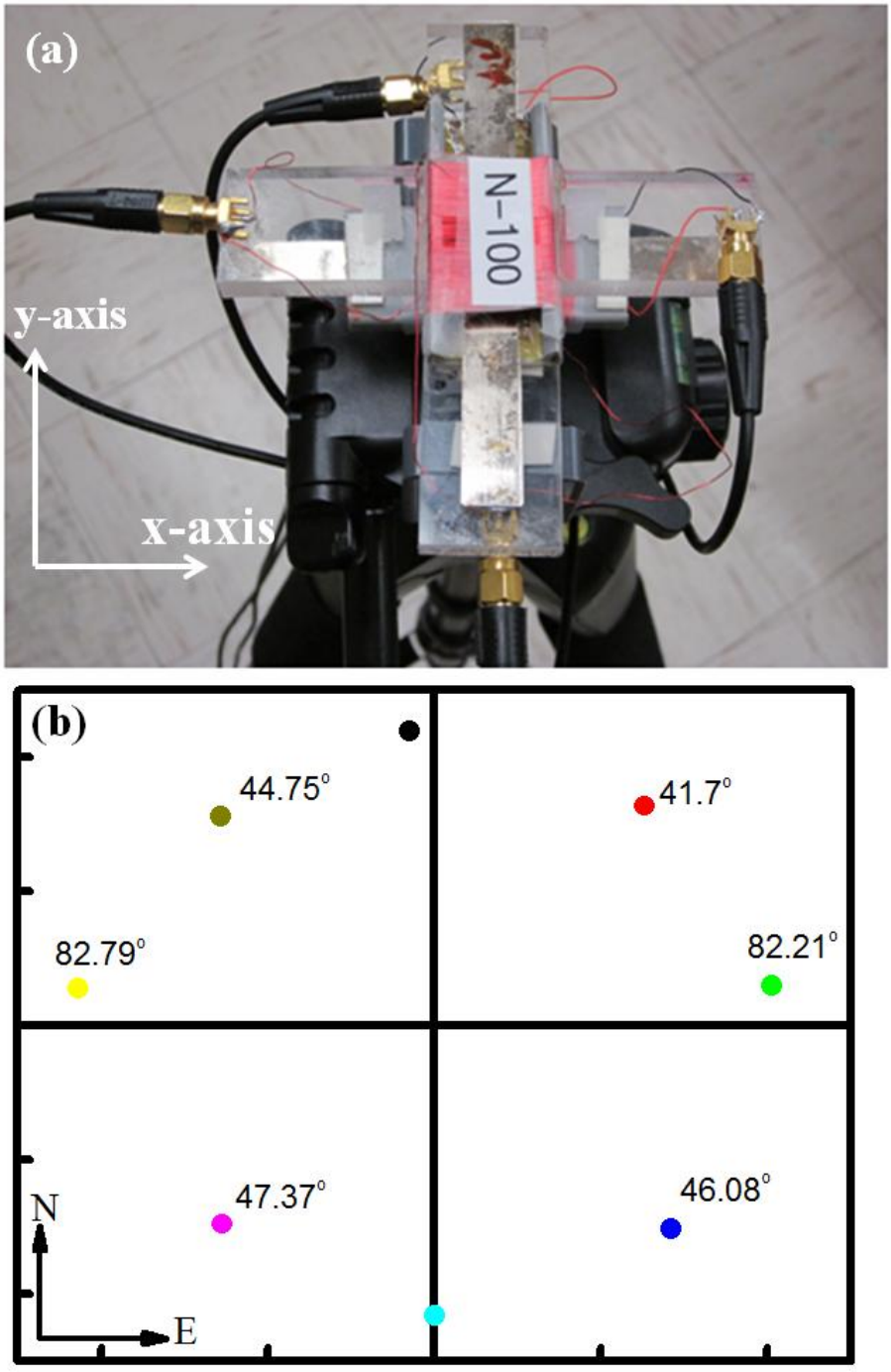

Figure 5.16 (a) Experimental setup for 2-axial geomagnetic sensor; and (b) orientation determined based on geomagnetic field.

5.4.2 3-axial magnetic sensor

Next, I utilized my 3-axial detection unit to do some exterior testing of geomagnetic fields in two locations around Blacksburg, Virginia. Figure 5.17 shows the detection locations and the sensor used in the test. The raw data for each position is listed in Table 5.2.

Table 5.2 Geomagnetic field measurements at two positions using the 3-axial sensor.

Location	N	W	Elevation	Earth's North	Vertical Component
A	37˚14.52'	80˚24.72'	2173 ft	1.1874 V	2.5882 V
B	37˚12.99'	80˚24.99'	2105 ft	1.1916 V	2.5871 V

By using the calibrated sensitivity of 55.56 uV/nT, I was able to convert the raw into magnetic field components. Meanwhile, the inclination angle could be calculated as well. Tables 5.3-5.5 summarize the comparisons and errors between test results and database values. From the test, it was able to confirm that my magnetic sensor could sense geomagnetic fields with small errors. Thus, such a system has potential for application in guidance systems based on geomagnetic field.

Table 5.3 Geomagnetic field intensity along North direction

Location	Earth's North	Database Value*	Error
A	21,371.5 nT	21,446.9 nT	0.35%
B	21,447.1 nT	21,457.9 nT	0.05%

Table 5.4 Geomagnetic field intensity along Vertical direction

Location	Earth's North	Database Value*	Error
A	46,583.9 nT	46,748.2 nT	0.35%
B	46,564.1 nT	46,728.9 nT	0.05%

Table 5.5 Comparisons of inclination Angle

Location	Earth's North	Database Value*	Error
A	65˚21'	65˚21'	0.35%
B	65˚18'	65˚20'	0.05%

* Cited from World magnetic model 2010-2015, National Geophysical Data center

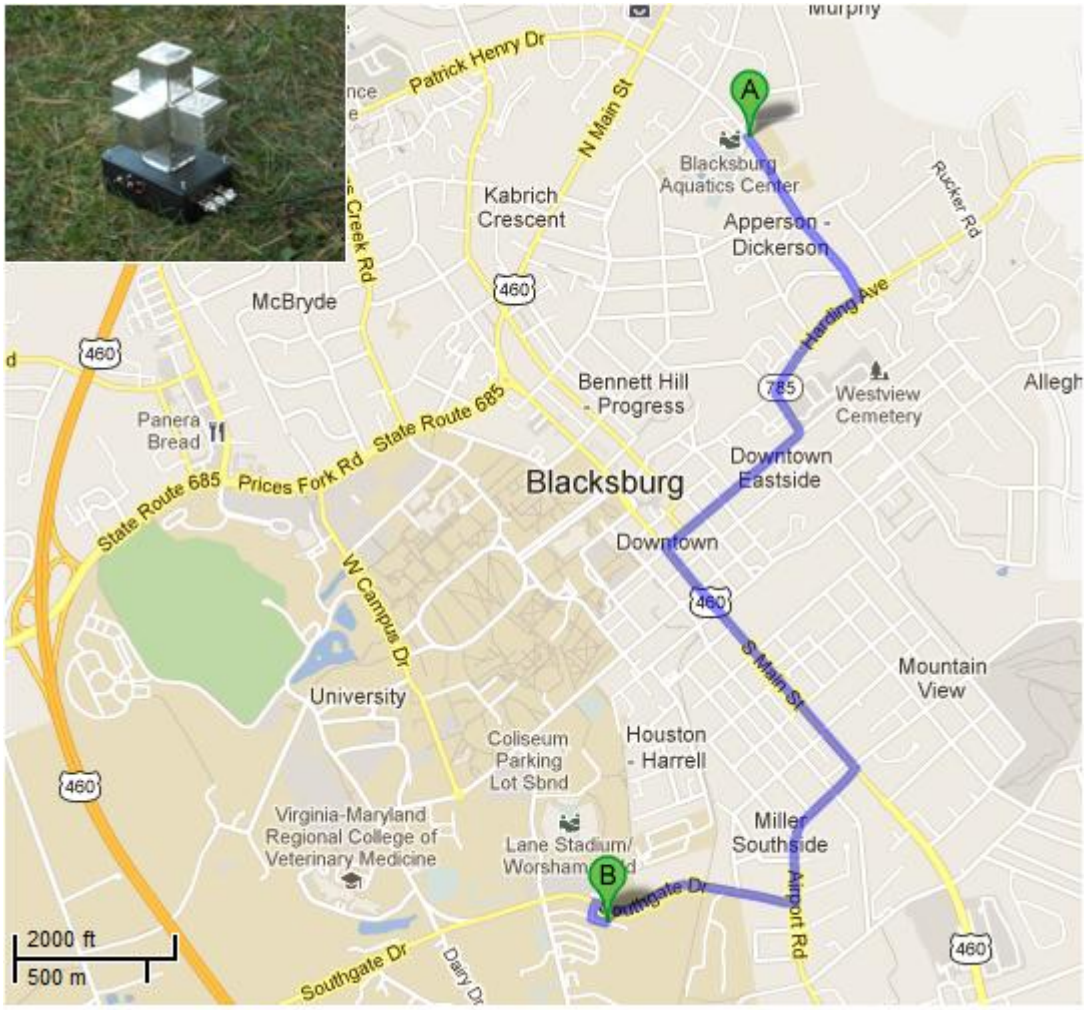

Figure 5.17 Geomagnetic field measurements around Blacksburg area. The insert shows the 3-axial magnetic sensor used in the test.

5.4.3 Mobile magnetic sensor unit

Due to the fact that prior measurements represent “static” data, they cannot be applied in ay reliable way to a real-time monitoring system for real-world applications. In order to overcome this limitation, a rigid, yet mobile, sensor package is highly desirable. Moreover, any “smart” data collection system needs to be developed for monitoring output signals continuously.

For this research phase, the 3-axial sensor was assembled in one box which can protect the sensor in an open environment and reject any electromagnetic interference, as shown in Figure 5.18 (a). The positive direction for each sensor is described in this figure as well. First, the sensitivity for each sensor was characterized by using one H-coils pair. During the characterization, the magnetic coil was driven by the DC output port from a lock-in amplifier. By adjusting the output signal, the DC field was controlled within the range from -0.11 Oe to 0.11 Oe. Then, the magnetic field was changed incrementally in measurement units as small as 0.01 Oe in the measurements. The results are shown in Figure 5.18 (b).

From the figure, one can see that the output signals from all 3 sensors are linear to the external magnetic field in the measured range. However, the sensitivities for the sensors were not exactly the same: there were small variations between each other. In detail, the sensitivities for x-axis, y-axis and z-axis were 51.45 μV/nT, 45.37 μV/nT, and 61.56 μV/nT, respectively. These magnetic sensor values were used to convert the measured voltage to the equivalent magnetic field.

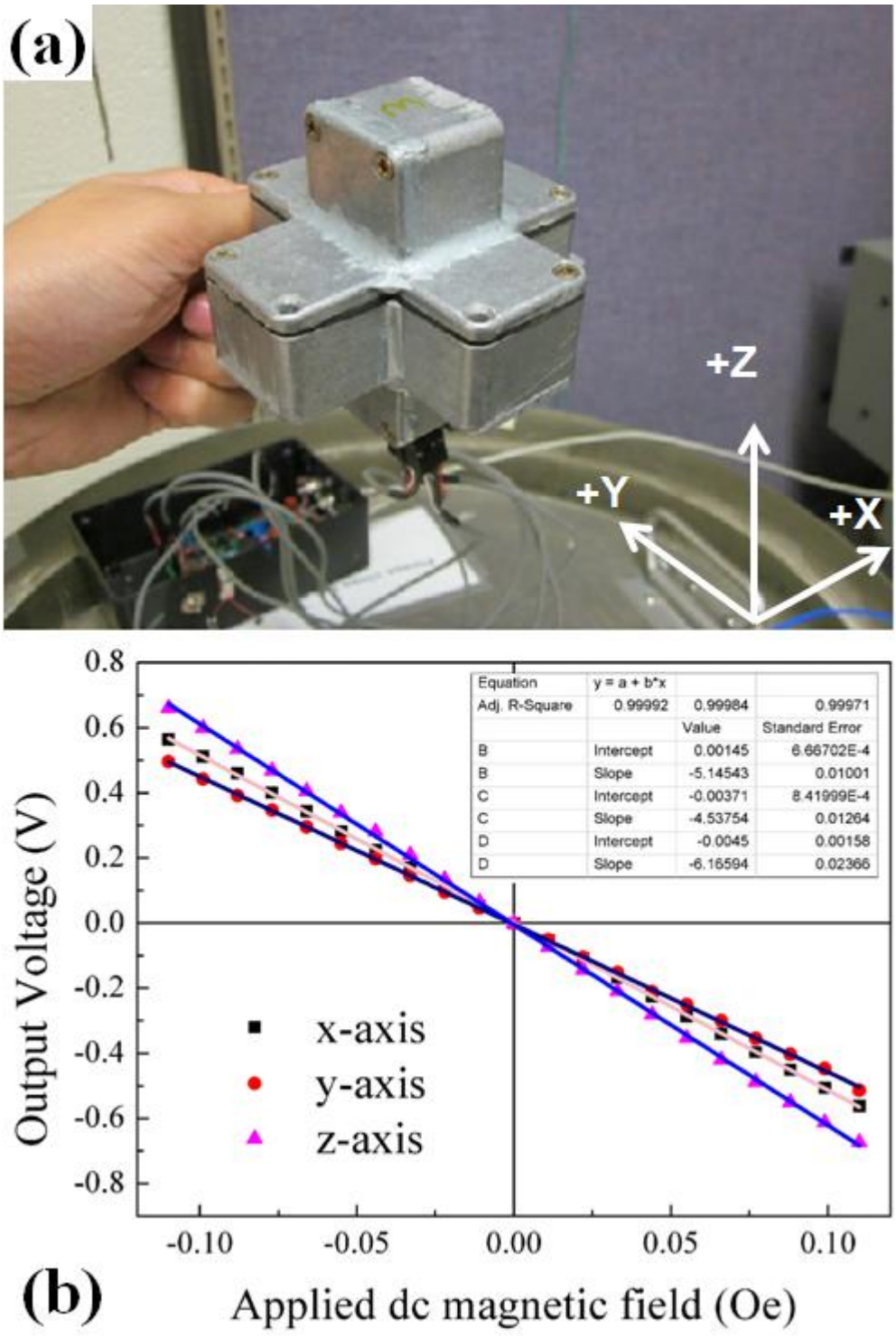

Figure 5.18 (a) Rigid package for 3-axial magnetic senor; and (b) characterization of sensitivity for each axis sensor.

5.4.4 Demonstrations for geomagnetic field sensor

First of all, a 3-D orientation monitoring system was proposed based on geomagnetic field. For this measurement, the 3-axial magnetic sensor was placed on the tripod described in the prior section. Meanwhile, the Labview code was compiled to monitor the orientation along different axes. The front panel of program is shown in Figure 5.19 (a). In detail, the graph displays the original data obtained directly from the sensors. And the three panels at the bottom shows the rotation angles which are defined as Yaw, Pitch, Roll angles corresponding to the rotating along Z, Y, and X axes, respectively.

Initially, the y-axis of the sensor was fixed along the north direction, so that the x-axis and z-axis were situated along the east and up directions, respectively. From this first panel, one can see that the angle is 0, which corresponds to prior assumptions. In other words, this finding directly resulted from the sensor being placed along the magnetic north direction. However, the second panel indicates a huge shift which means that the local magnetic field was not exactly along the up-down direction. By checking the parameters of the local magnetic field from the website, one can find that the geomagnetic field showed an inclination angle of around 65 degrees, which corresponds to the angle between the magnetic field and the horizontal direction. In my system, the second panel should display the magnetic field with respect to the vertical direction, which means the angle should be around 25 degrees. That can be corroborated by the data shown in Figure 5.19 (b). Moreover, by using the Labview, I was able to collect the data as the sensor rotated, so that I could monitor the rotation of the sensor in real time.

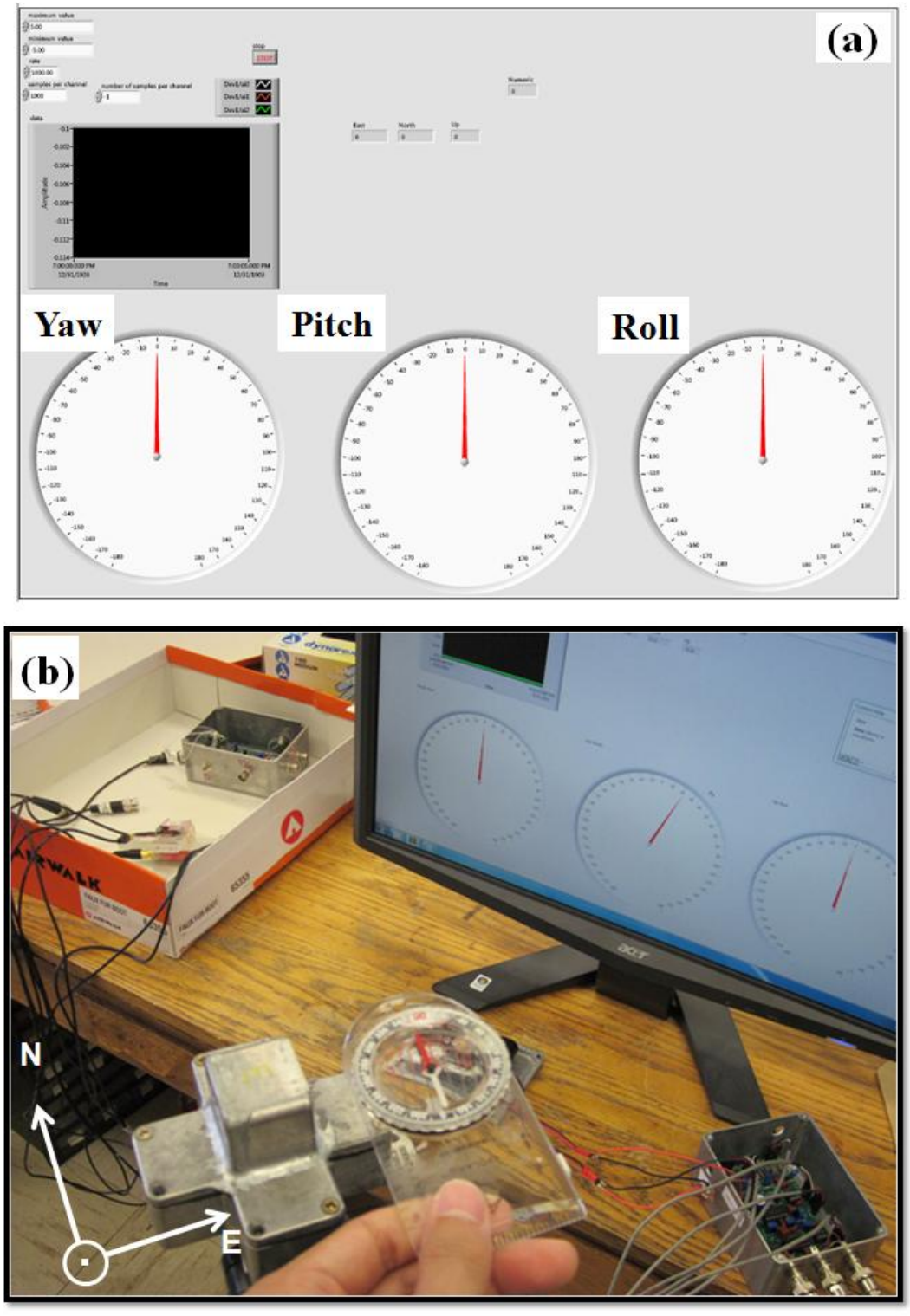

Figure 5.19 (a) Labview program for rotation monitor; and (b) experimental setup for monitoring the orientation in 3-D space.

In addition to capturing orientation measurements, I also developed a mobile magnetic sensor that enabled us to do wide range magnetic field sensing. For this design, a multi-axial magnetic sensor, detection circuit and one wireless digitizer were assembled in a rigid alumina bar. In terms of function, the digitizer was able to collect the data from the magnetic sensor and then send it to a laptop through a wireless network. With the help of this digitizer, this hand-held device can be used for magnetic field detection over 100 m. Moreover, all of the devices can be powered by a simple battery pack, thus eliminating the need for an external power.

A demonstration trail for magnetic field mapping was initially performed in a parking lot over 200 m^2. Figure 5.20 (a) shows a schematic illustration of magnetic field mapping test. The sensor was taken along the path lane from a starting point to an ending point, and then repeated in an adjacent lane location. During the measurement, there were 4 vehicles parked in the lot and their relative positions are shown in Figure 5.20 (a). The data was recorded with a laptop, after which the magnetic field could be calculated.

Figure 5.20 (b)-(d) show the magnetic field mapping results for x, y and z directions. From the figures, we can see that the magnetic fields along 3 directions were almost homogenous for the area furthest away from the vehicles, and the background magnetic fields measured by sensors varied. However, for the results associated with the path lane closed to the vehicles, the magnetic fields were influenced greatly. That was direct a result of high permeability materials which induced the magnetic field distortion.[89,90]

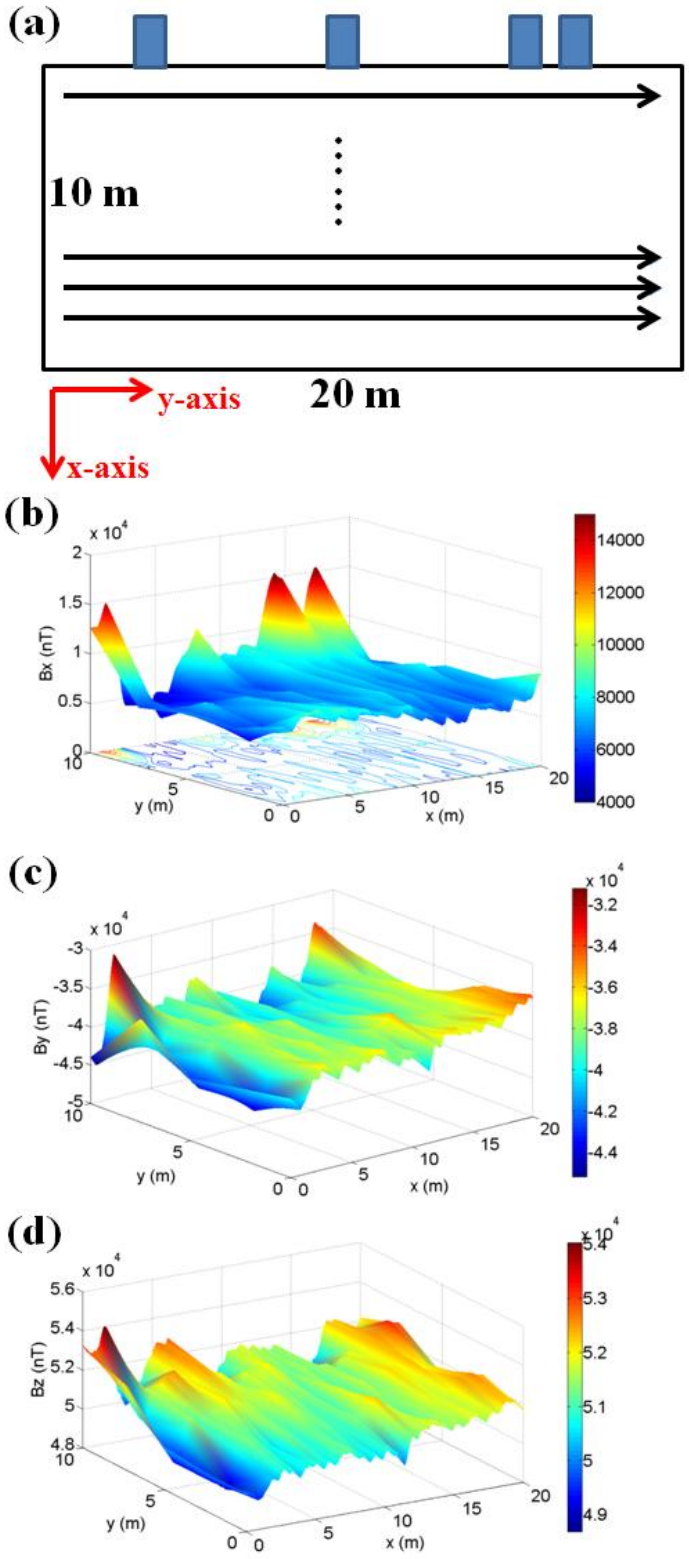

Figure 5.20 (a) magnetic field mapping demonstration performed at parking lot; and (b)-(d) magnetic field mapping results measured by the sensors.

In addition to the field mapping test, the geomagnetic sensor can be also used for field sensing in large area. For this assay, the sensor was taken to a soccer field in an open environment in order to reduce the influence of other noise sources. As shown in Figure 5.21 (a), the sensor was moved around along the penalty area, According to the previous results, the sensor was expected to be able to sense the motion of turning.

Figure 5.21 (b) shows the magnetic field changes for the whole process. One can see that the magnetic fields along all three directions did not change significantly at the very beginning since the motion was just along the straight path lane. Moreover, the magnetic field values varied due to the different geomagnetic fields along x, y and z directions. Noticeable changes emerged with the first left turn motion. Since this motion involved 90-degree turn, the y-direction changed to –x, and the x-direction changed to y. Thus, the amplitude of the y-axis was changed to the value of –x, and the amplitude of the x-axis was equaled to the value of y. The motions in the whole process could be observed from the measured signals.

This resulting data indicates that the sensor was highly sensitive to presence of the geomagnetic fields, as well as to turning motions. Potentially, if installed in a vehicle, this geomagnetic sensor would be useful for magnetic field mapping and for controlling the orientation of a vehicle, especially in case where no strong GPS signals were available.

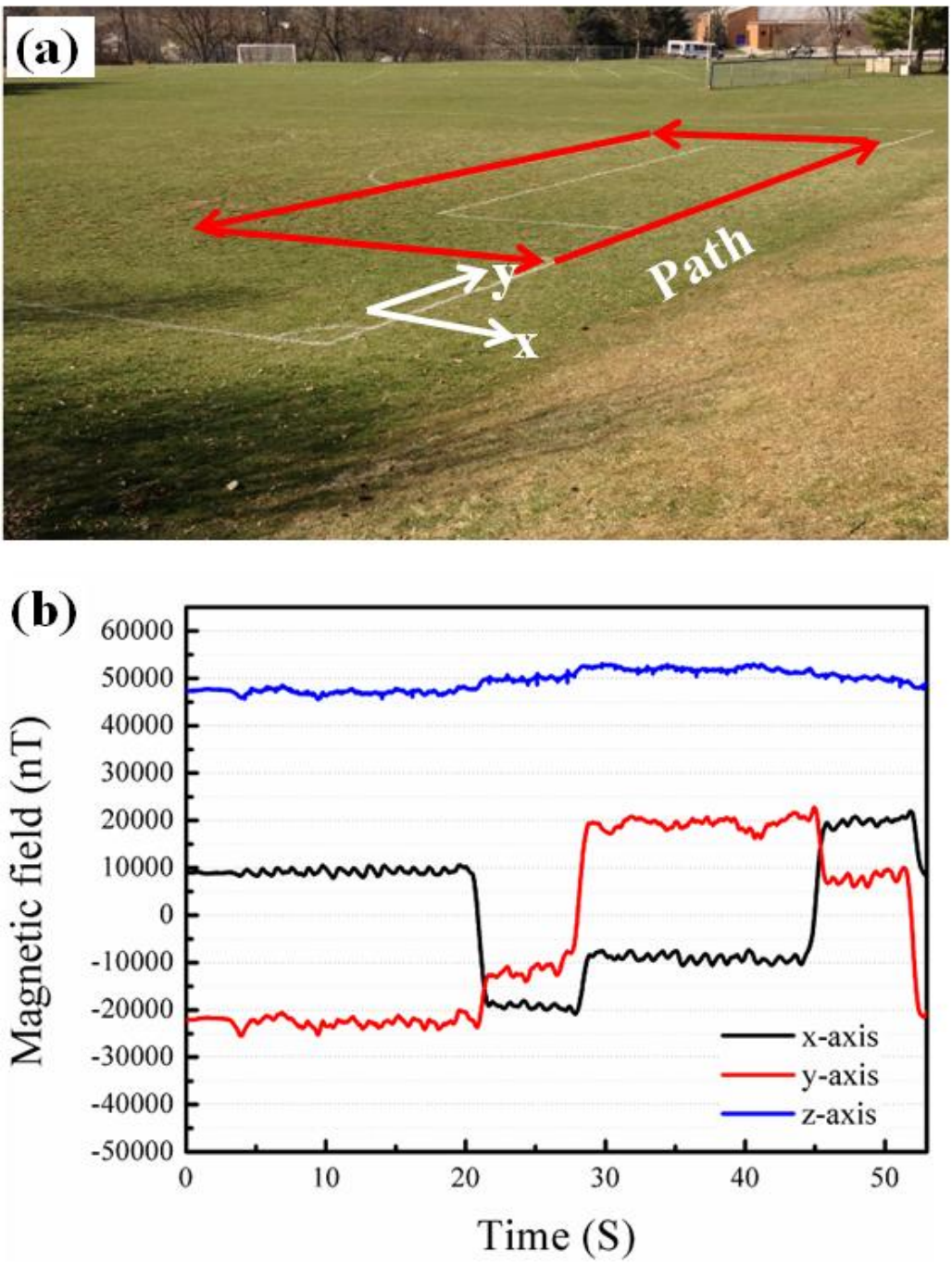

Figure 5.21 (a) Geomagnetic field sensing in an open environment; and (b) magnetic fields for the process.

5.5 Summary of this section

A highly-sensitive, man-portable DC magnetic sensor was developed that displayed the sensitivity in the range of 10 nT. This DC magnetic sensor has potential for use in magnetic target localization, magnetic field mapping etc. An important result from this study is that we were able to detect geomagnetic field with high accuracy using the DC magnetic sensor. Moreover, a multi-axial geomagnetic field device was shown to be able to monitor the orientation, magnetic field mapping and motion control based on the presence of the geomagnetic field.

6. Other devices based on ME effect

6.1 Introduction

Previous chapters have chiefly described the development and use of a magnetic sensor based on Metglas/piezo-fibers with multi-push pull configurations. Since ME composites can be designed with different structures, this section will investigate the use of unsymmetrical bi-layered ME composites, which have been shown to display markedly different resonant effect compared to conventional multi-push pull configurations. The inherent characteristics of bi-layered ME composites make them applicable for the design of a magnetic resonator at various frequencies. Moreover, the resonant frequency can be tuned to a significant degree by altering the layers of the Metglas or by applying an active tip mass. In short, the wide-ranging tenability of bi-layered ME composites makes them promising for practical applications at various frequency ranges.

Although they can be used in magnetic sensor applications, there are several other devices can be developed based on these functional composites, including energy harvesters, magnetic memory devices, etc. In this section, I will further investigate their use in magnetic energy harvesters. Based on conditional structures, highly effective harvesters have been demonstrated to power battery with great efficiency. Moreover, the 60 Hz harvester was also designed based on bi-layered ME composites, which can be used to capture the magnetic energy generated by

instruments. Finally, the frequency multiplication effect that can be tuned by the geomagnetic field in Metglas/piezo-fibers composites has also been investigated. Such effects show promise for applications in frequency multiplier and geomagnetic guidance devices.

6.2 Bi-layered ME composites

Recently, a number of scholars have investigated the development of multifunctional devices based on ME composites,[81, 91] as well as the influences of various environmental conditions on the performances of these devices.[85, 92] However, one of the biggest challenges for the practical application of such devices has been the ME coefficient α_{ME}, which limits the performance of the ME devices. Thus, it is highly desirable to enhance the value of α_{ME} in order to optimize the property of ME devices. Recent investigations have reported that driving ME composites under a resonance frequency (f_r) can improve α_{ME} by up to a factor of 100×,[93] and improve the sensitivity of ME magnetic sensor dramatically.[29] However, such EMR gains in L-L mode structures are only possible at high frequencies of fr≈30 kHz over narrow bandwidths. Therefore, it would be desirable to shift this gain in α_{ME} to lower frequency, while limiting the compromise in bandwidth.

In this section, we have investigated bending mode structures for bi-layer Metglas/PZT laminates. Near a fundamental bending frequency (FBR) of 210 Hz, the value of α_{ME} was enhanced by a factor of >10×, compared to a corresponding L-L mode of the same size. Using a charge amplifier detection method, magnetic noise floors of ≤ 0.3pT/√Hz were achieved near the FBR, which was about 100×

lower than at 1 Hz and about 10× lower than that of L-L mode at the same frequency.

6.2.1 Design of bi-layered ME composites

We obtained PZT fibers (Smart Materials, Sarasota, FL) and Metglas foils (Vitrovac Inc., Hanau, Germany) to fabricate the laminates. Five pieces of 180 um thick piezoelectric fibers were oriented along the long axes to form a layer that was in total 10 mm wide and 40 mm long. Two interdigited Kapton®-based electrodes were then bonded to the top and bottom surfaces of the piezoelectric layer in a multi push-pull mode configuration. To fabricate symmetrical longitudinal mode sensors, three Metglas foils of 80 mm in length and 10 mm in width were first laminated to each other, and subsequently laminated to both the top and bottom surfaces of the PZT fiber layer. To fabricate an asymmetrical bending mode, six Metglas foils of the same size were bonded together, and subsequently laminated to only the bottom surface of the PZT fiber layer. A schematic comparison of the symmetrical L-L and asymmetrical bending modes can be seen in Figure 6.1. Due to the symmetric structure of the L-L mode, strains generated by the top and bottom layers of the Metglas are identical under magnetic field: thus, the L-L mode elongates or shrinks along the horizontal plane. However, the asymmetrical structure undergoes a flexural deformation under magnetic field.

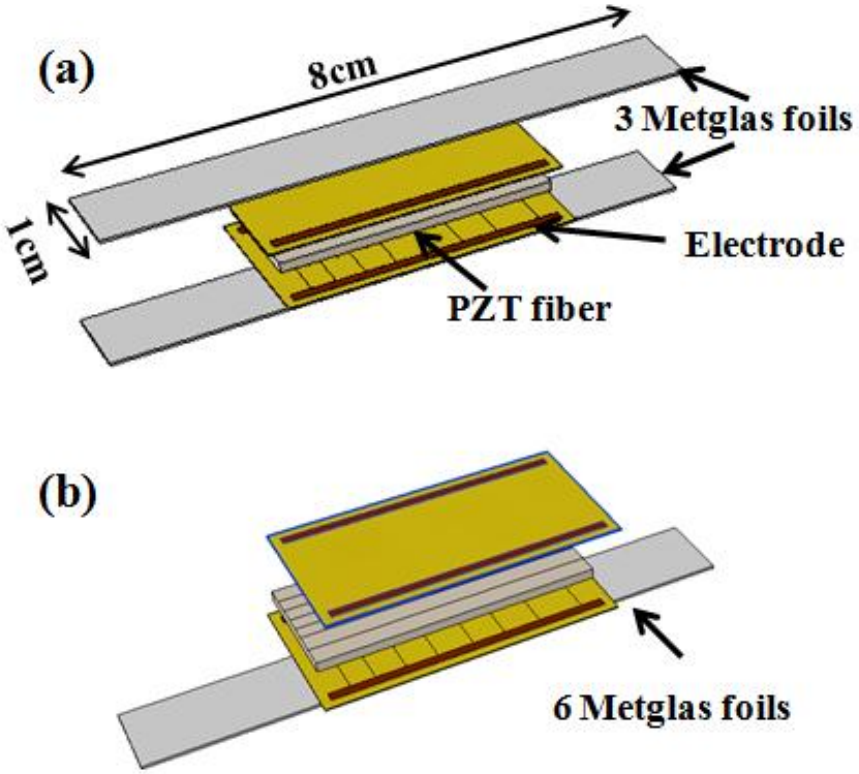

Figure 6.1 Schematics of Metglas/PZT ME laminate sensors: (a) L-L mode sensor, and (b) bending mode.

First, α_{ME} for both L-L and bending mode structures was measured as a function of dc magnetic bias H_{dc}, as shown in Figure 6.2(a). A lock-in amplifier (SR-850) was used to drive a pair of Helmholtz coils to generate an ac magnetic field of H_{ac}=1 Oe at a frequency of f=1 kHz. The dc magnetic bias H_{dc} was applied along the long axis of the ME laminates. As can be seen in Figure 6.2(a), α_{ME} for both modes exhibited similar trends with increasing $H_{dc.}$ At a frequency of 1 kHz, the maximum value of α_{ME} for the bending mode was 24 V/cm-Oe, which was a little larger than the 20 V/cm-Oe for the L-L mode. We were surprised by these results, since the L-L multi-push pull mode has been believed to have the highest ME coefficient.[27]

Figure 6.2(b) shows α_{ME} as a function of the ac magnetic field frequency. In this figure, we can see a notable difference in α_{ME} between the L-L and bending modes over the frequency range of 10^2 Hz<f<10^3 Hz. The value of α_{ME} for the L-L mode was nearly constant over this frequency range at 20 V/cm-Oe. However, the bending mode exhibited a strong EMR enhancement at 210 Hz, achieving values of α_{ME}=400 V/cm-Oe. This demonstrates that α_{ME} for the bending mode can be improved by a factor of 20× at the FBR relative to the value for the L-L mode at the same frequency. The insert in Figure 2(b) shows α_{ME} for the L-L mode sensor as a function of frequency: where the EMR frequency can be seen to be about 30 kHz, as previously reported.[27]

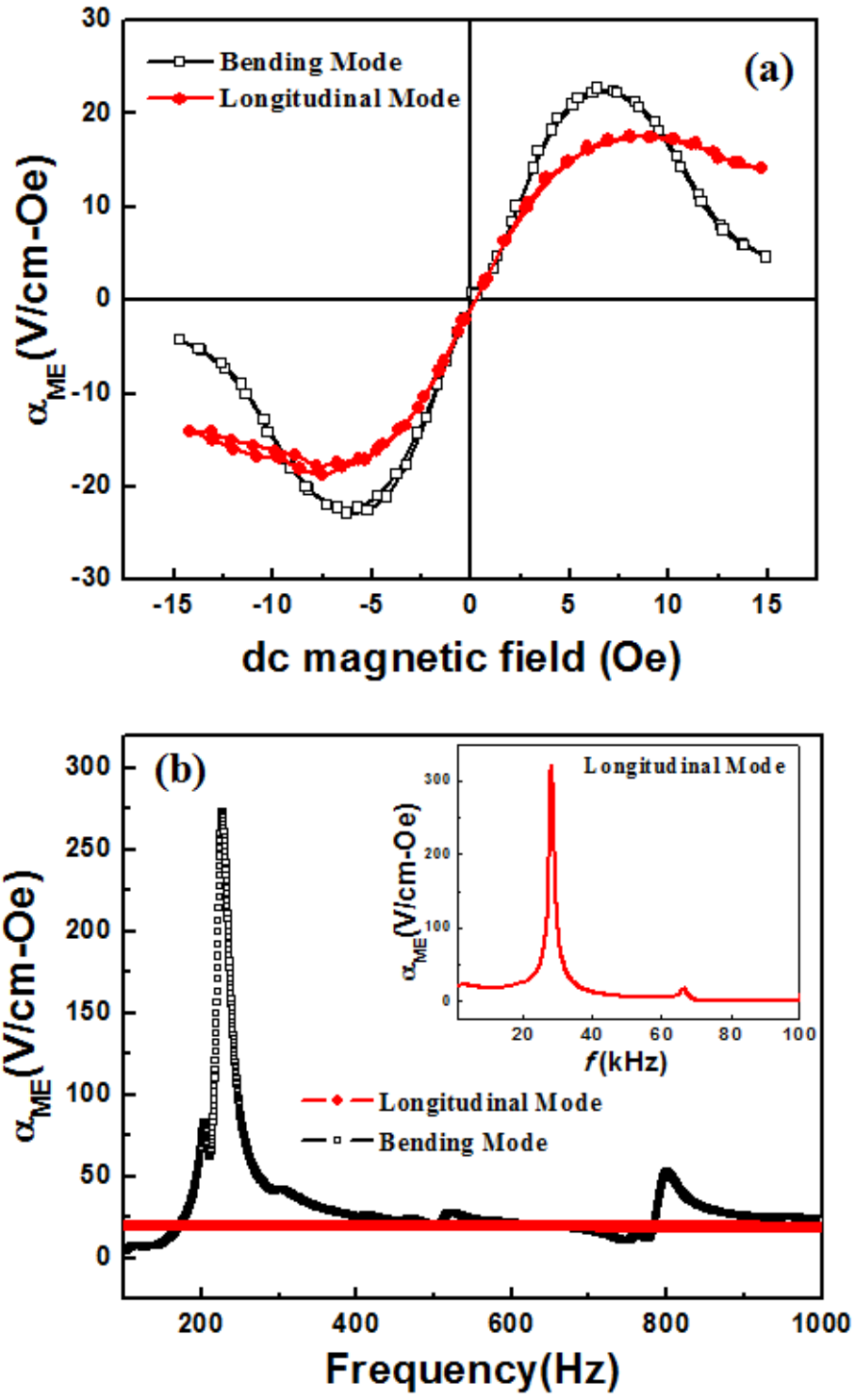

Figure 6.2 ME voltage coefficients of L-L and bending mode ME laminates: (a) α_{ME} as a function of dc magnetic bias H_{dc} at f = 1 kHz, and (b) α_{ME} as a function of ac magnetic drive frequency. The insert shows α_{ME} for the L-L mode for $10^3 < f < 10^5$ Hz.

Second, the ac magnetic sensitivity was measured using an operational amplifier based detection circuit.[45] Helmholtz coils were used to apply a small ac magnetic field along the long axis of the laminates by inputting an ac signal generated by the lock-in amplifier at f=210 Hz. Small permanent dc magnets were attached to the ME laminates along the long axis, in order to bias the laminates to the maximum value of α_{ME}, as identified in the α_{ME}- H_{dc} data of Figure 6.2(a). Details about the detection unit can be found in Ref [79]. The noise levels of the detection units and induced ac voltage from the laminates were monitored in the time domain using an oscilloscope (Agilent 54624A). Details of the setup and measurement can be found in Ref [94]. Figure 6.3 (a) shows the noise levels of the L-L and bending mode ME sensors under H_{ac}=0 Oe. In this figure, one can see that the peak-to-peak value of the noise for the L-L mode sensor was about 25 mV, which was smaller than that of the bending value of 80 mV. An applied H_{ac} was then modulated to keep the peak-to-peak value of the output voltage constant at about 50 mV for the L-L and 160 mV for the bending mode sensors: which corresponded in both cases to a constant signal-to-noise ratio of SNR=2. This was done in order to compare the ac magnetic field sensitivities for different laminates under the same condition. Figure 6.3 (b) shows the ac magnetic sensitivity at 210 Hz. In this figure, one can see that the ac magnetic field sensitivity for the bending mode was about 0.05 nT at 210 Hz, which was about a factor of 10× lower than that of the L-L mode at the same frequency.

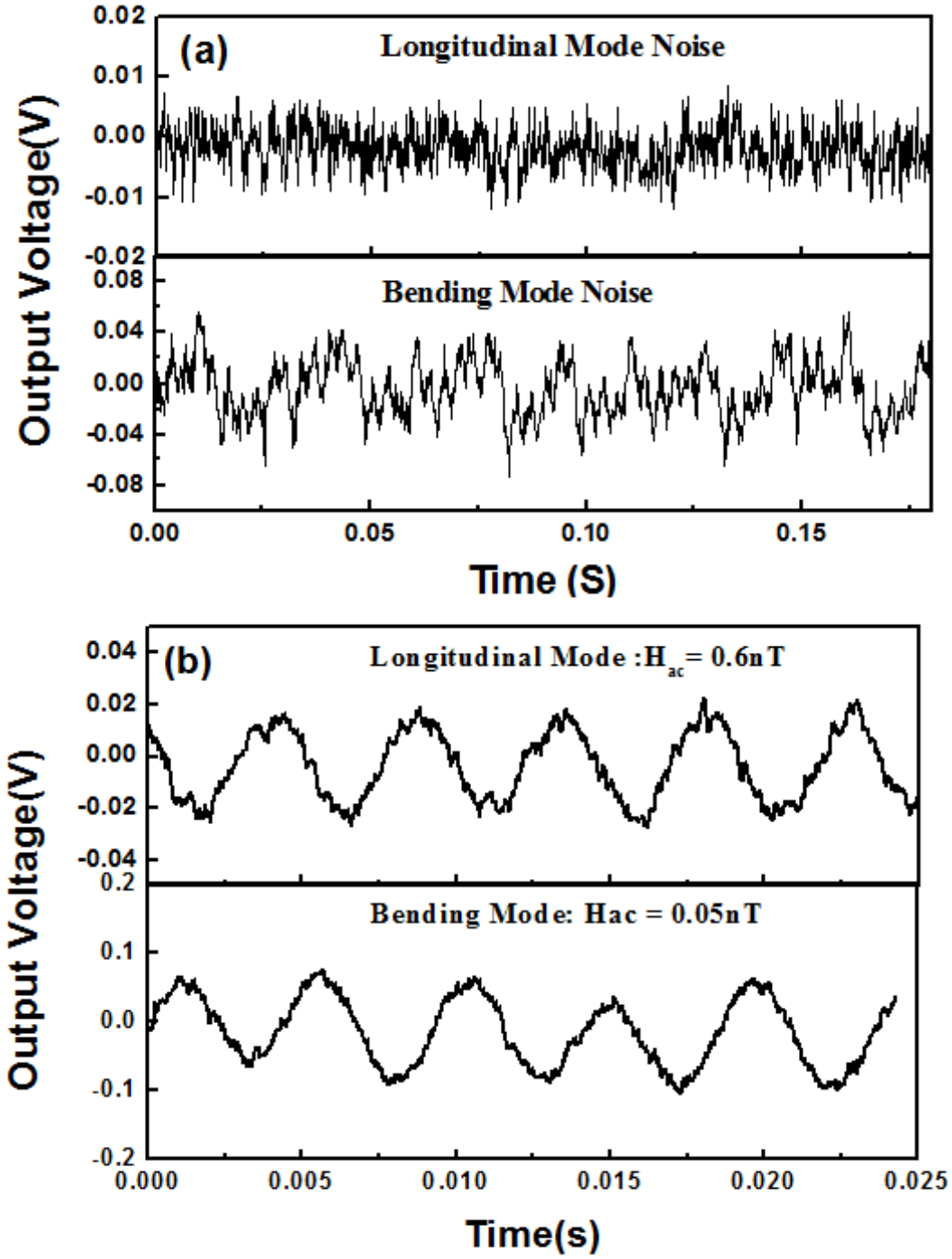

Figure 6.3 (a) Noise levels for the L-L and bending mode sensors; and (b) ME output voltage as a function of time for the L-L and bending mode sensors. The corresponding peak-to-peak ac field sensitivities are listed in the figures.

Finally, the equivalent magnetic noise floors for both types of ME laminate sensors were measured over the frequency range of $10^2<f<10^3$ Hz. During the tests, the ME sensors were placed in a magnetically shielded chamber in order to reject environmental magnetic noise. A dynamic signal analyzer (SR-785) was used to measure the noise power density of the ME sensors in V/√Hz. We then used the following sensor transfer function to convert the noise floor in V/√Hz to that in T/√Hz:

$$\begin{aligned} Conversion\ factor(V/T) &= \frac{\alpha_{ME}(pC/10^{-4}T)}{gain\ of\ \ amplifier\ \ (pC/V)}; \\ Noise\ floor\ \ (T/\sqrt{Hz}) &= \frac{Noise\ \ floor(V/\sqrt{Hz})}{Conversion\ factor(V/T)}. \end{aligned} \tag{6.1}$$

Over the frequency range of $10^2<f<10^3$ Hz, the gain factor of the amplifier in V/pC was 1 V/pC.[79]

Figure 6.4 shows the equivalent magnetic noise floor spectra for both L-L and bending modes. In this figure, we can observe that the noise floor for the L-L mode sensor was constant at about 5 *p*T/√Hz over the frequency range of 100 to 1000 Hz: the constancy was due to the frequency independence of α_{ME}. In this same figure, the magnetic noise floor for the bending mode sensor can be seen to depend dramatically on frequency. In particular, near the FBR at 210 Hz, the noise floor was decreased to 0.3 *p*T/√Hz: which was a direct consequence of the FBR enhanced α_{ME}. Comparisons of the data in Fig.4 will show the magnetic noise floor of the bending was decreased by (i) a factor ~100× at 210 Hz, relative to that of 1 Hz; and (ii) a factor of ~20× at 210Hz, relative to the of the L-L mode at the same frequency. At frequencies below the FBR, the noise floor of the bending mode was higher that of

the L-L by a factor of 4-5×. But at frequencies greater than the FBR, the noise floors were nearly equivalent at a value of 5 pT/√Hz. These results may indicate that the bending mode laminates are more sensitive to low frequency vibrations than the L-L ones which are environmental noise sources. Nonetheless, due to the dramatic increase in α_{ME} near the FBR, the signal-to-noise ratio was enhanced.

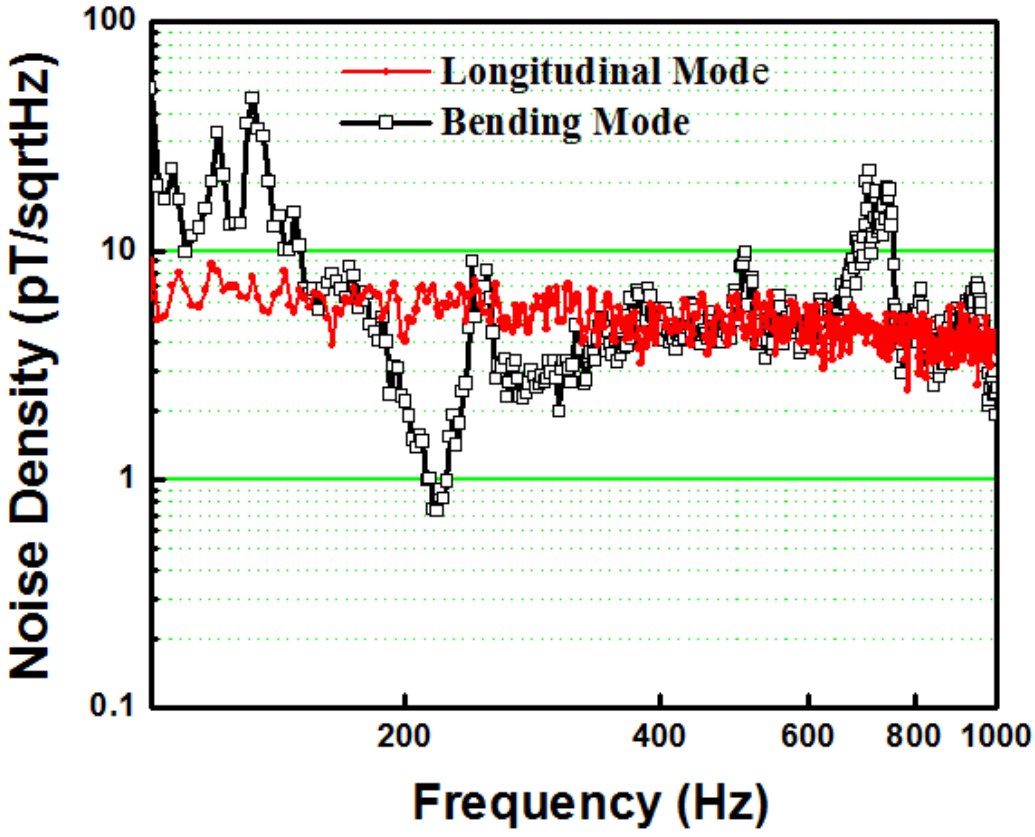

Figure 6.4 Equivalent magnetic noise spectra for the L-L and bending mode sensors for $10^2 < f < 10^3$ Hz.

6.2.2 Tunability of resonant frequency

The previous section described the dramatic low resonant frequency for bi-layered ME composites, as well as how the sensitivity of ME magnetic sensor can be improved by incorporating these composites.[29] The benefit, however, is only useful for a very narrow responsive frequency bandwidth, which limits their potential applications. In order to apply resonant ME effect at various frequencies, a number of approaches have been studied to tune the resonant frequency of ME composites.[32, 95, 96] In prior investigations, however, centain restrictive experimental conditions were imposed in these studies, such as the use of double-side clamped edges. Otherwise, the resonant ME coefficients may not be impressive and may limit the performance of related device. Thus, strong resonant ME effect that can be easily tuned is highly desirable.

In this section, we present a simple approach for tuning the resonant frequency (f_r) of Metglas/PZT bi-layer composites without losing the value of α_{ME} in any significant way. Investigations show that bi-layered Metglas/PZT composites with multi-push pull configuration have giant resonant ME coefficients of > 400 V/cm-Oe. Moreover, by loading tip mass on two edges of the composites, the resonant frequency of f_r was shifted from 70 Hz to 220 Hz easily, which will enable the design of devices working at various frequencies. A theoretical model for bi-layered ME composites was developed to describe the resonant frequency tunability with tip mass. The predicted results match the experimental data well.

Bi-layered ME composites have been fabricated following the similar process described in the previous section. First, the shift in f_r with tip mass weight was

measured using an impedance analyzer (Agilent 4294 A). Tip masses were added to the two edges of the bi-layered composites, as shown in the insert of Figure 6.5 (a). Commercial permanent magnets D41 with mass of 0.377 gram from K&J Magnetics (USA) were used as the tip mass. Using small magnets can provide the tip mass and the DC bias at the same time. Thus, there is no necessary to apply an external DC magnetic field during measurement. Accordingly, the resonant frequency measured by the impedance analyzer was a compositive effect of magnetomechanical resonance (MMR) in Metglas and electromechanical resonance (EMR) in the piezo-layers, as shown in Figure 6.5(a). One can see that the fundamental resonant frequency was observed at f =215 Hz without loading of a tip mass. The value of f_r was then decreased to about 74 Hz by continuously adding more tip mass.

Next, the ME voltage coefficient α_{ME} for the bi-layered ME composites was measured as a function of frequency. A lock-in amplifier was used to drive a pair of Helmholtz coils, generating an ac magnetic field of H_{ac}=0.1 Oe over a frequency range of 1 Hz < f < 300 Hz. The induced voltage from the ME composites was measured by the lock-in amplifier as well. In Figure 6.5 (b), one can see that the ME resonant peak positions were well matched to those of the impedance peaks (Figure 6.5 (a)). The ME voltage coefficients reached values of $\alpha_{ME} \geq 400$ V/cm-Oe at f_r = 215 Hz without tip mass, consistent with previous reports.[29] The resonant peak positions then exhibited significant tunability on loading with tip mass: shifting from 75 Hz to 215 Hz. Furthermore, α_{ME} was increased to 500 V/cm-Oe with 2 magnets load, but decreased to 380 V/cm-Oe and 260 V/cm-Oe with 4 and 6 magnets load. However, the values were still much larger than described in prior reports.[95, 96]

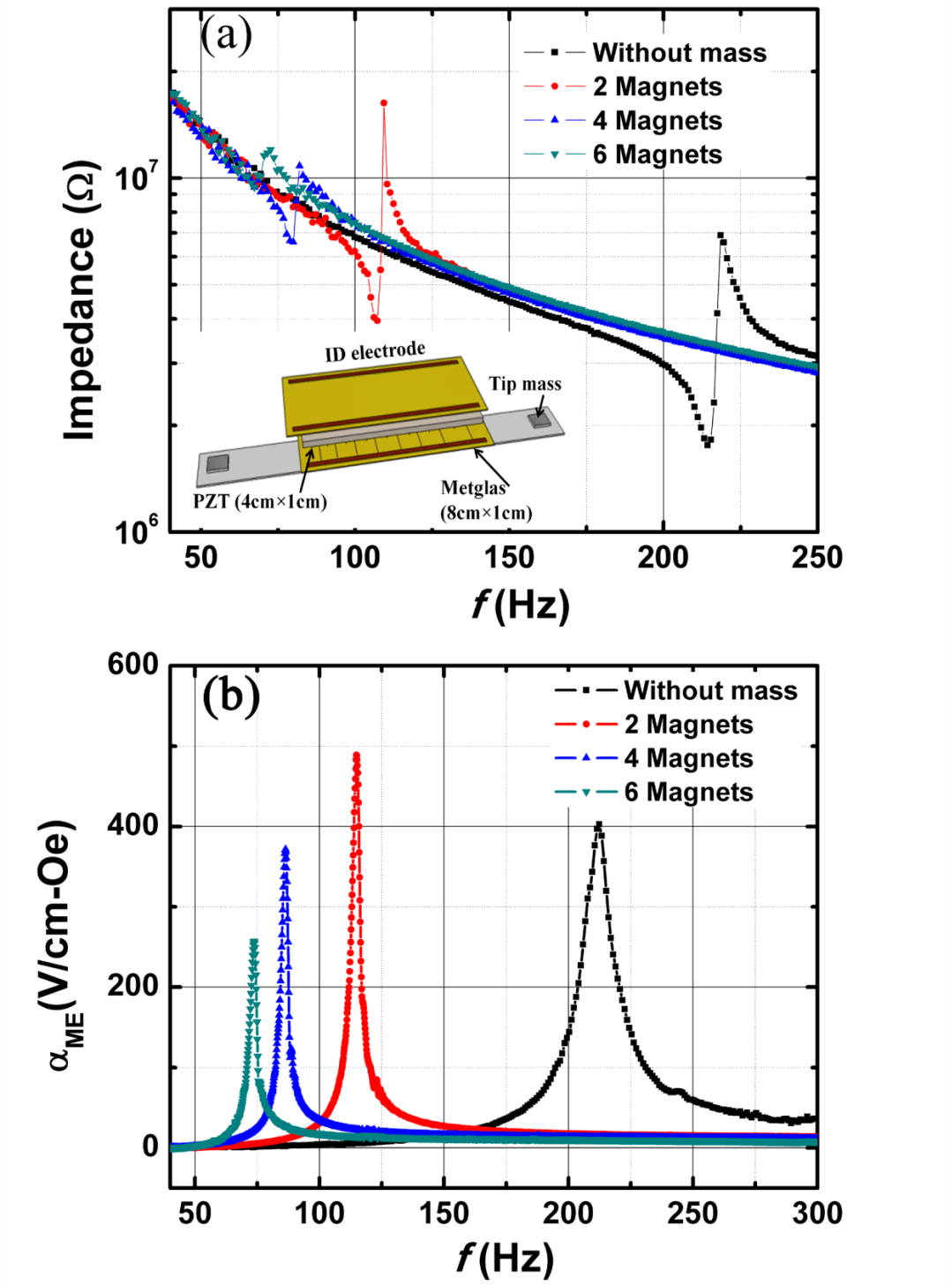

Figure 6.5 (a) Impedance spectra of Metglass/PZT bending laminates with various tip masses; and (b) ME voltage coefficients for Metglas/PZT laminates as a function of frequency with various tip masses. The insert is a schematic of the bending mode laminates.

A theoretical model for ME bending mode laminates was then developed to predict the behavior of the laminates. Figure 6.6 describes the model of the bi-layered structure. To simplify the model, a 2-D bar was used to describe the mechanical performance of the ME bi-layer structure. The x_1-axis in Cartesian coordinates is along the length direction of the bar, the x_2-axis is directed across the width, and the x_3-axis is orthogonal to them. It was assumed that the piezoelectric layers were polarized in the x_1 direction and that a magnetic field was incident along the same orientation. During the calculations, only small-amplitude oscillations of the bi-layer were considered.

In our theoretical analysis, the following assumptions were made: (i) the length of composites was notably larger than the thickness; (ii) the boundary conditions between the two layers were ideal; (iii) linear elasticity could describe each layer; (iv) the stains and displacements were small; and (v) the transverse shear stresses on the top and bottom surfaces were zero. In addition, we assumed that Kirchoff's hypothesis was valid for all layers, i.e., the displacements in x_1 and x_3 directions can be represented as:

$$\begin{cases} u_1(x_1, x_3) = u(x_1) - x_3 \dfrac{\partial w}{\partial x_1} \\ u_3(x_1, x_3) = w(x_1) \end{cases} . \tag{6.2}$$

The equations for the strain tensor S_{1m} in the magnetostrictive layer (cubic symmetry) and the strain tensor S_{1p} in the piezoelectric one (∞m symmetry) under a magnetic field H_1 and an electric field E_1 were expressed as:

$$\begin{cases} S_{1m} = {}^{m}s_{11}\,{}^{m}T_1 + {}^{m}q_{11}\,{}^{m}H_1 \\ S_{1p} = {}^{p}s_{11}\,{}^{p}T_1 + {}^{p}d_{11}\,{}^{p}E_1 \end{cases} ; \tag{6.3}$$

where ${}^{m}s_{11}$ and ${}^{p}s_{11}$ are the elastic compliance tensor components of the magnetostrictive and piezoelectric layers, respectively; and ${}^{m}q_{11}$ and ${}^{p}d_{11}$ are the piezomagnetic and piezoelectric coefficients.

Under the above mentioned assumptions, equations and free-free boundary conditions with a concentrated mass on both ends of the bi-layer, we determined all relevant fields: i.e., stress, strain, magnetic and electric fields. Finally, under the open circuit condition of

$$\int_{-L}^{L} D_{1p}\,dx_1 = 0\ ; \tag{6.4}$$

where, D_{1p} is the electric displacement. The ME voltage coefficient was determined to be:

$$\alpha_{ME} = \frac{E_1}{H_1} = -\frac{{}^{m}q_{11}\,{}^{p}d_{11}}{{}^{p}s_{11}\varepsilon_{11}}\frac{h_p}{h_p+h_m}\{\frac{\gamma_0}{\gamma_0+1}\frac{\tan(\lambda_T L)}{\lambda_T L}-\frac{3}{2}\frac{\gamma_1}{\gamma_2+1}\frac{\sin h(\lambda_B L)\sin(\lambda_B L)}{\lambda_B L[\sin h(\lambda_B L)\cos(\lambda_B L)+\sin(\lambda_B L)\cos h(\lambda_B L)]}\}$$
$$\times\{1-K_1^2+K_1^2\frac{1}{\gamma_0+1}\frac{\tan(\lambda_T L)}{\lambda_T L}+\frac{3}{2}\frac{1}{\gamma_2+1}\frac{\sin h(\lambda_B L)\sin(\lambda_B L)}{\lambda_B L[\sin h(\lambda_B L)\cos(\lambda_B L)+\sin(\lambda_B L)\cos h(\lambda_B L)]}\}^{-1}\ , \tag{6.5}$$

where, h_m and h_p are the thicknesses of the magnetostrictive and piezoelectric layers; ρ_m and ρ_p are the densities of these two layers. The other notations in (4) are given by the following expressions:

$$\lambda_T = \sqrt{\frac{\rho\omega^2}{A}};\ \lambda_B = \sqrt{\frac{\rho\omega^2}{D}};\ \gamma_0 = \frac{{}^{p}s_{11}}{{}^{m}s_{11}}\frac{h_m}{h_p};\ \gamma_1 = \frac{{}^{p}s_{11}}{{}^{m}s_{11}}(\frac{h_m}{h_p})^2;$$
$$\gamma_2 = \frac{{}^{p}s_{11}}{{}^{m}s_{11}}(\frac{h_m}{h_p})^3; A = \frac{h_p}{{}^{p}s_{11}}+\frac{h_m}{{}^{m}s_{11}}; D = \frac{1}{3}(\frac{h_p^3}{{}^{p}s_{11}}+\frac{h_m^3}{{}^{m}s_{11}});$$
$$\rho = (\rho_p h_p+\rho_m h_m)(1+m_0); K_1^2 = \frac{{}^{p}d_{11}^2}{{}^{p}s_{11}\cdot\varepsilon_0}; m_0 = \frac{m_c}{m_t}.$$

where, ω is angular frequency, m_c is the tip mass and m_t is the mass of ME composites. The material parameters for Metglas and PZT are listed in Table 6.1.

Table 6.1 Materials parameters for Metglas, PZT used for theoretical modeling

Materials	${}^{m}s_{11}$ or ${}^{p}s_{11}$ ($10^{-12}m^2/N$)	${}^{p}d_{11}$ ($10^{-12}C/N$)	${}^{m}q_{11}$ ($10^{-9}m/A$)	$\varepsilon_{11}/\varepsilon_0$	h_p or h_p ($10^{-6}m$)	$2L$ (m)	Width (m)	ρ_m or ρ_p (kg/m^3)
Metglas[a)]	10	…	50.3	…	66	0.06	0.01	7180
PZT[b)]	15.3	400	…	1750	180	0.06	0.01	5675

a) Cited from Ref.[97]

b) Cited from Ref.[98]

The theoretical ME voltage coefficients for bi-layered Metglas/PZT composites as function of frequency can be established using material parameters given in Table 6.1. Figure 6.6 (b) shows the simulation results of α_{ME} versus frequency for various tip mass loadings. From this figure, one can see that the predictions from the model were in very good agreement with the experimental observations in Figure 6.5 (b). The value of f_r was about 210 Hz without tip mass, which was quite closed to the observed one. Furthermore, a huge resonant peak shift was predicted by the model, whose values were comparable to the experimental data. Thus, our model can provide reasonable estimated values and a sound basis for predicting further shifts with additional increasing tip masses.

In summary, the resonant magnetoelectric (ME) effect in an unsymmetrical bi-layered ME composites can be tuned simply by applying the active permanents: Moreover, the actual measured and predicted results present similar resonant frequency shifting behaviors for ME composites. Such greatly-tunable resonant effect facilitate the design of ME composites for practical applications at various frequency ranges.

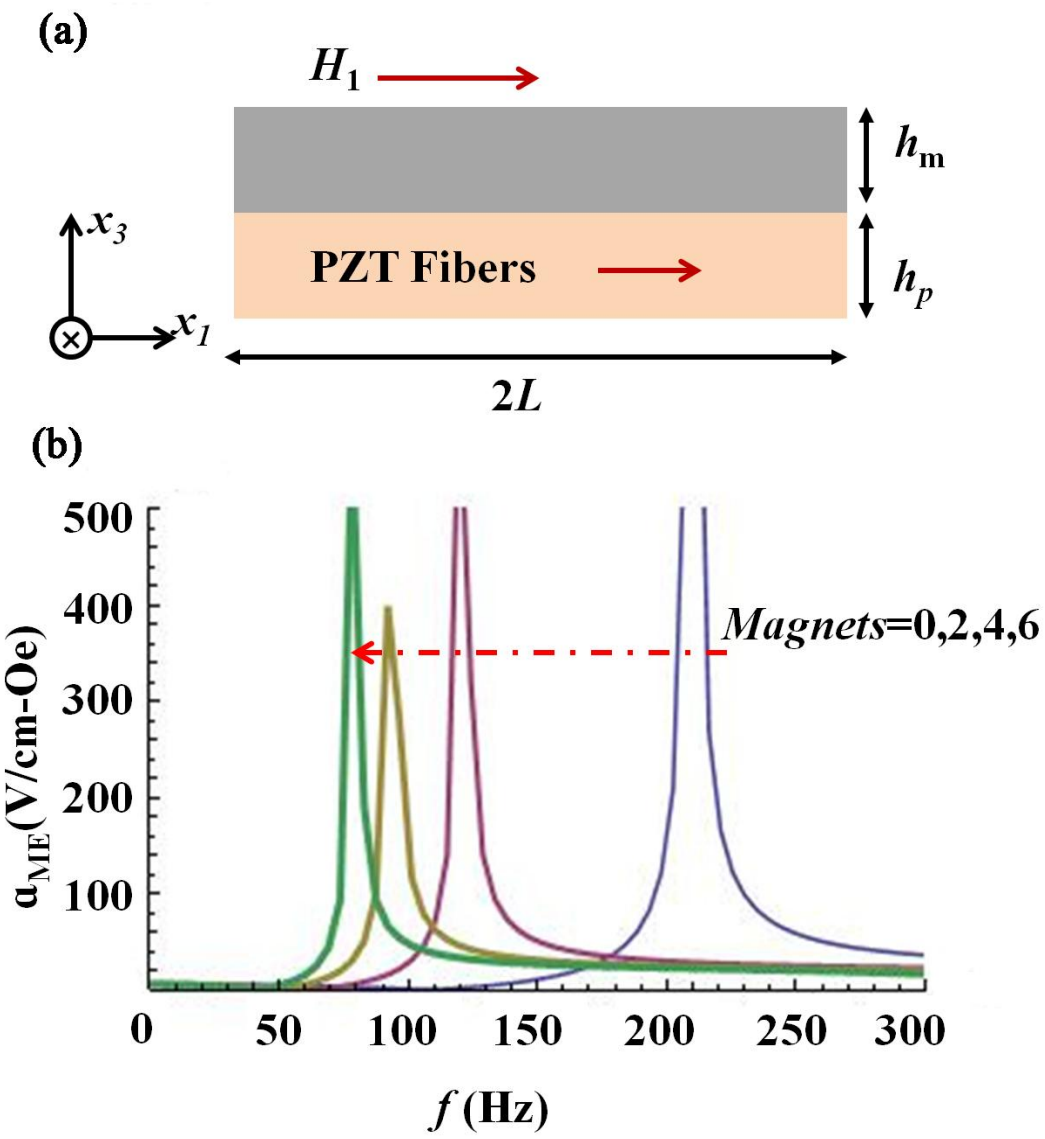

Figure 6.6 (a) Theoretical model for magnetoelectric bi-layer laminates, and (b) estimated ME voltage coefficients as a function of frequency.

6.3 Energy harvester

The use of ME composites can assist the establishing the relationship between the magnetic field and the electric field. Therefore, they have potential in applications designed to capture magnetic energy for electronic devices. In response, this section describes the possible development of magnetic energy harvesters using composites.

6.3.1 Multi-push pull ME harvester

Since ME composites can be used to harvest magnetic energy, ME-based sensor units could be designed to be self-powered systems capable of very long deployment times. Based on this relationship, the following investigation was conducted.

First, the harvested output power and voltage were measured. A lock-in amplifier was used to generate a driving signal to a pair of Helmholtz coils that generated a magnetic field at a frequency of f =25.5 kHz, which was the fundamental longitudinal resonance frequency. A resistance decade box was directly connected to the ME laminates as an electrical load, and the voltage across it was then measured by an oscilloscope. Figure 6.7 shows the induced voltage as a function of load resistance. It can be seen that the normalized voltage reached ~42 Vp.p./Oe at the optimum R_{load}. Correspondingly, the maximum harvested power output was 8 mW/Oe under a 11 kohm load resistance.

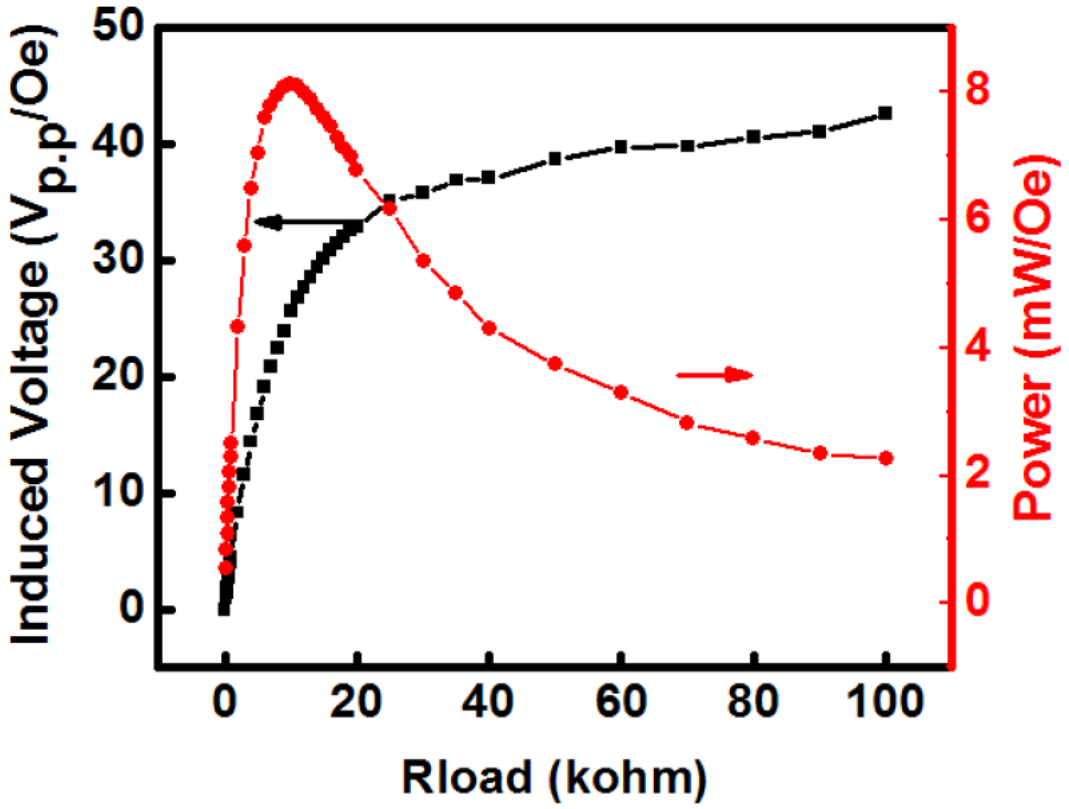

Figure 6.7 Output voltage and power as a function of load resistance load for Metglas/PMN-PT laminates at their fundamental resonance frequency.

Using this ME magnetic energy harvester, a circuit was setup to charge Nickel Metal Hydride (NiMH) batteries which had a capacity of 330 mAh, as shown in Figure 6.8(a). The charging circuit consisted of a full wave rectifier, capacitor and battery to be charged. The voltage from the Metglas/PMN-PT laminate was first converted to a DC output and subsequently stored on a super-capacitor. The voltage used to charge the battery was in parallel with the capacitor.

At the beginning of the measurement, the battery was initially discharged by connecting it to a resistor for 8 hours until the remaining voltage was below 1 volt, and then was subsequently connected to the charging circuit. During the measurements, an ac magnetic field (f =25.5 kHz) was generated by the H-coils driven by a lock-in. The induced voltage from the ME laminates was rectified and then used to power the batteries. The charging cycle is shown in Figure 4(b). From this figure, one can see that it took 1.5 hours to charge the battery from <1 V to 3.2 V: i.e., a 90% charging was achieved. These results demonstrate that Metglas/PMN-PT laminates can be used in magnetic energy harvesters at their resonance frequency range; these harvesters can then charge batteries to power the charge amplifier detection circuits for low frequency ME magnetic sensors.

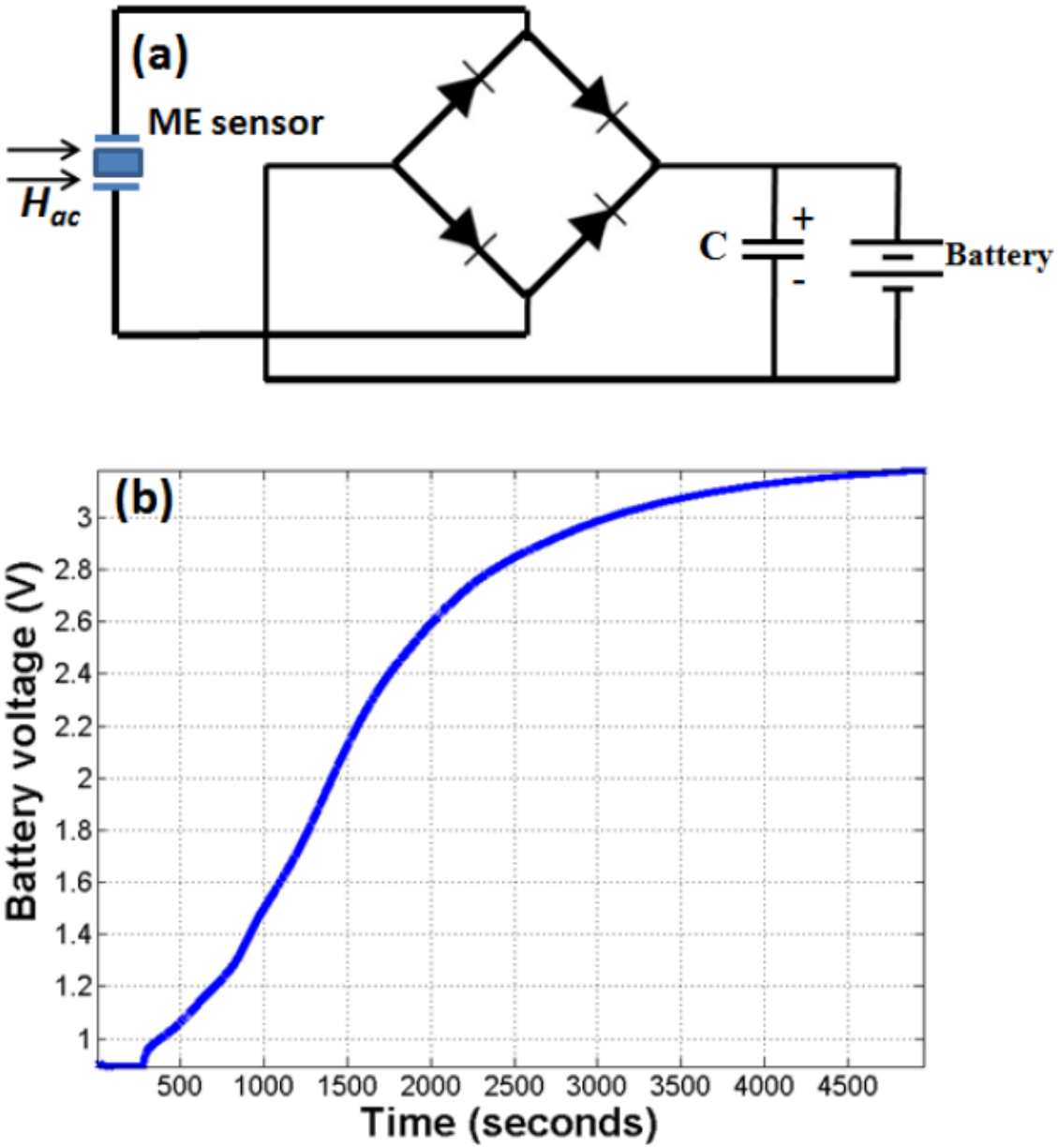

Figure 6.8 Illustration of ability to charge batteries of ME detection units by magnetic energy harvesting: (a) experimental setup, and (b) testing results.

6.3.2 Bi-layered ME harvester

Based on this tunability of f_r for bending mode laminates, a 60 Hz magnetic field energy harvester was designed with a suitable tip mass. The ME voltage coefficient was found to reach 274 V/cm-Oe at f = 60 Hz, as shown in Figure 6.9 (a). The high coupling effect made it possible to more efficiently harvest stray 60 Hz magnetic energy. The output power of the energy harvester was characterized. A lock-in amplifier (SR 850) was used to generate a driving signal for a pair of Helmholtz coils that generated a magnetic field at a frequency of f =60 Hz. A resistance decade box was then directly connected to the ME laminates as an electrical load, and the voltage across it was measured by an oscilloscope. Figure 6.9(b) shows the output voltage and power as a function of load resistance R_{load}. It can be seen that the normalized voltage reached ~13 *V*rms/Oe at an optimum R_{load}. Correspondingly, the maximum harvested power output was 16×10^{-6} W/Oe under R_{load} =6 Mohm.

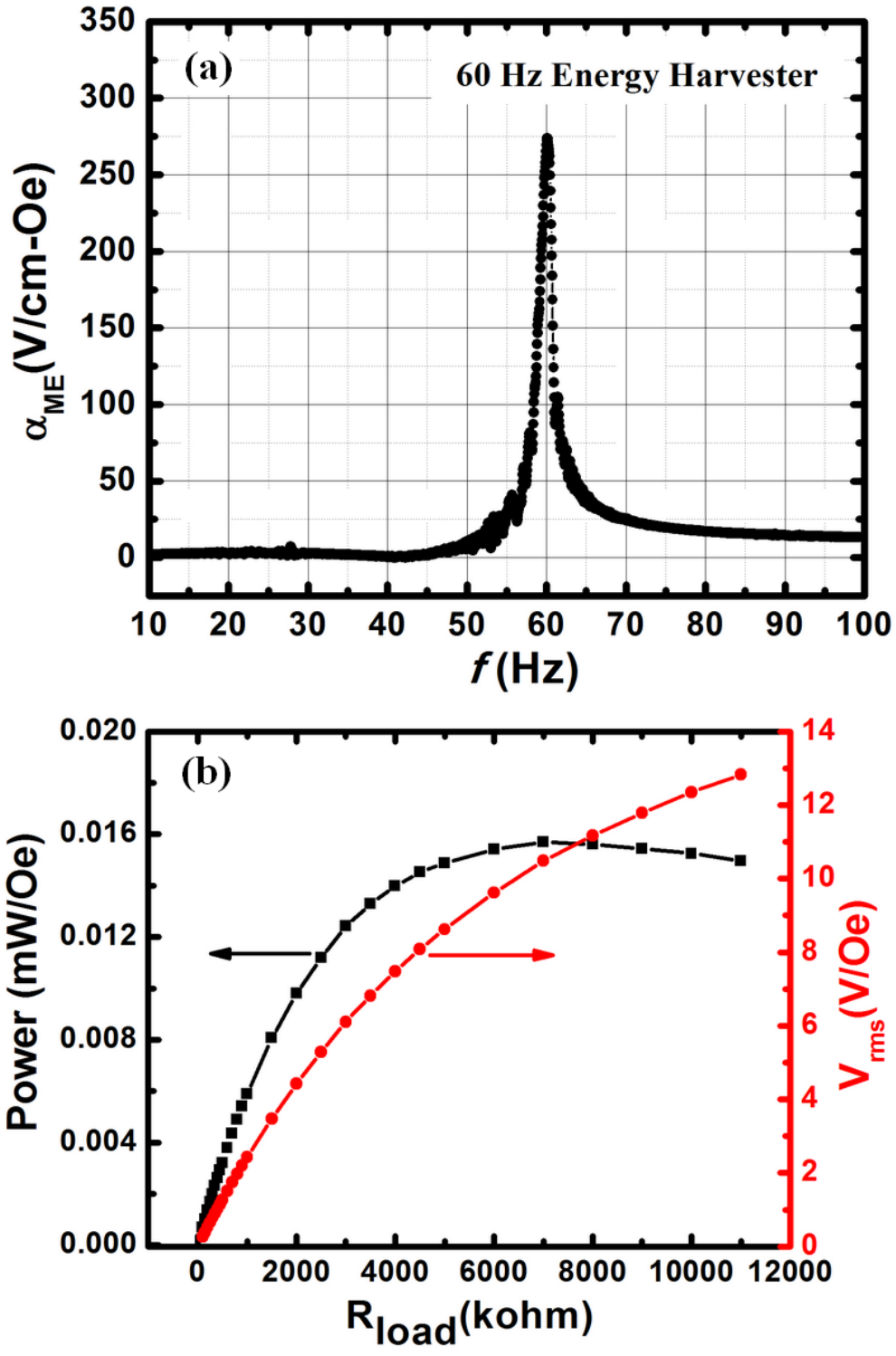

Figure 6.9 (a) ME voltage coefficient of 60 Hz magnetic energy harvester as a function of AC magnetic drive frequency; and (b) output voltage and power as a function of resistance load at the bending mode resonance frequency.

Finally, we used our energy harvester to capture 60 Hz magnetic energy in an open laboratory setting. Figure 6.10 (a) shows a photo of the harvesting system and source. A power cable was placed across the harvester which generated a 60 Hz magnetic field due to a flowing current. Figure 6.10 (b) shows the output voltage from the harvester in the time domain when current was flowing through the cable. The output voltage reached 80 mV under open circuit conditions. The period of the signal can be seen to be 16.7 ms, corresponding to 60 Hz. Thus, this test confirmed that the harvester was able to capture 60 Hz magnetic energy from an ambient environment and convert it to useable electric energy.

The bi-layered laminated composites have been demonstrated to be used to harvest 60 Hz electromagnetic energy. Presently, the optimized output power for this harvester can reach 16 μW/Oe with a 6 Mohm resistance load, with the power density of $\geq$ 200 μW/cm^3. The power density was found to be limited by the high internal impedance of the ME laminates; however, it can be reduced by using a ME laminates array configuration.[66] Since ME harvesters could be integrated into power source cables or instruments, they could have important applications for harvesting 60 Hz magnetic energy.

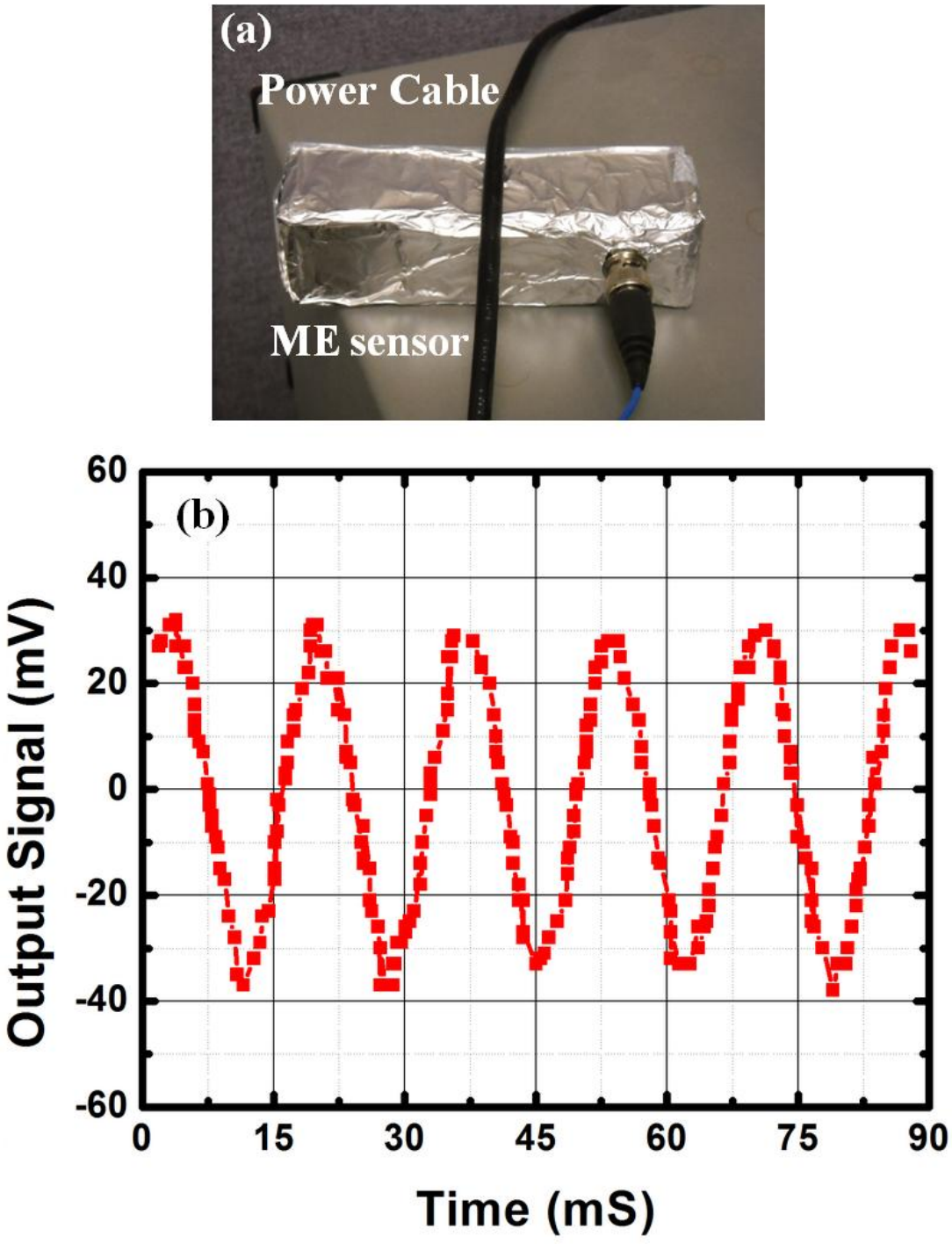

Figure 6.10 Demonstration of ability to capture 60 Hz electromagnetic energy by using ME magnetic harvester: (a) photo of experimental setup, and (b) output voltage signal in the time domain.

6.4 Frequency multiplier

ME composites with giant ME coefficients have been developed for potential devices, such as magnetic sensors,[71, 92] and data memory devices.[37] Moreover, potential frequency doubling devices based on ME composites have recently been proposed.[53, 54] We obtained PZT fibers from Smart Materials (Sarasota, FL) and Metglas foils from Vitrovac Inc. (Hanau, Germany) to fabricate ME composites with a multi-push pull configuration.[94] The detailed process can be found in Ref [75]. Finally, a 100-turn driving coil was wrapped around the composites directly, as shown in the insert of Figure 1 (a).

To observe frequency multiplication, a commercial lock-in amplifier (SR-850) was used to generate an ac input signal to the driving coils wrapped around the ME composites, generating an ac magnetic field of H_{ac}=0.2 Oe at a frequency of f =1 kHz. The amplitude of the H_{ac} and the induced signal V_{out} from the ME composites were then monitored by an oscilloscope (Agilent 54624A). It should be noted that during this measurement, a dc magnetic bias was not applied to the composites. Thus, the strain generated by Metglas was completely influenced by $H_{ac.}$ On applying a sine wave signal of frequency f = 1 kHz to our ME composite frequency multiplier, a steady output signal at a frequency of f = 2 kHz was monitored in the time domain, as shown in Figure 6.11 (a). The results demonstrated that the frequency multiplication in Metglas/PZT composites was significant as absence of dc magnetic bias. Moreover, we characterized the influence of dc magnetic bias on frequency multiplying behaviors. During measurements, the same ac magnetic field was generated. Meanwhile, a dc magnetic bias H_{dc} was applied along the longitudinal

axis of the multiplier, and the induced voltage at a frequency of 2 kHz from the composites was then measured by the lock-in amplifier. The results are shown in Figure 6.11 (b), which indicates that the amplitude of V_{out} was affected by dc biases greatly: reaching maximum values for H_{dc} ≈0 Oe, decreasing sharply at small dc biases (-4 Oe< H_{dc} < 4 Oe), and subsequently increasing with further increasing. The results indicated that even small dc biases can effectively tune the frequency multiplication. In fact, by applying H_{dc}=1 Oe, no obvious frequency doubling effect was observed in time domain, as shown in the insert of Figure 6.11 (b).

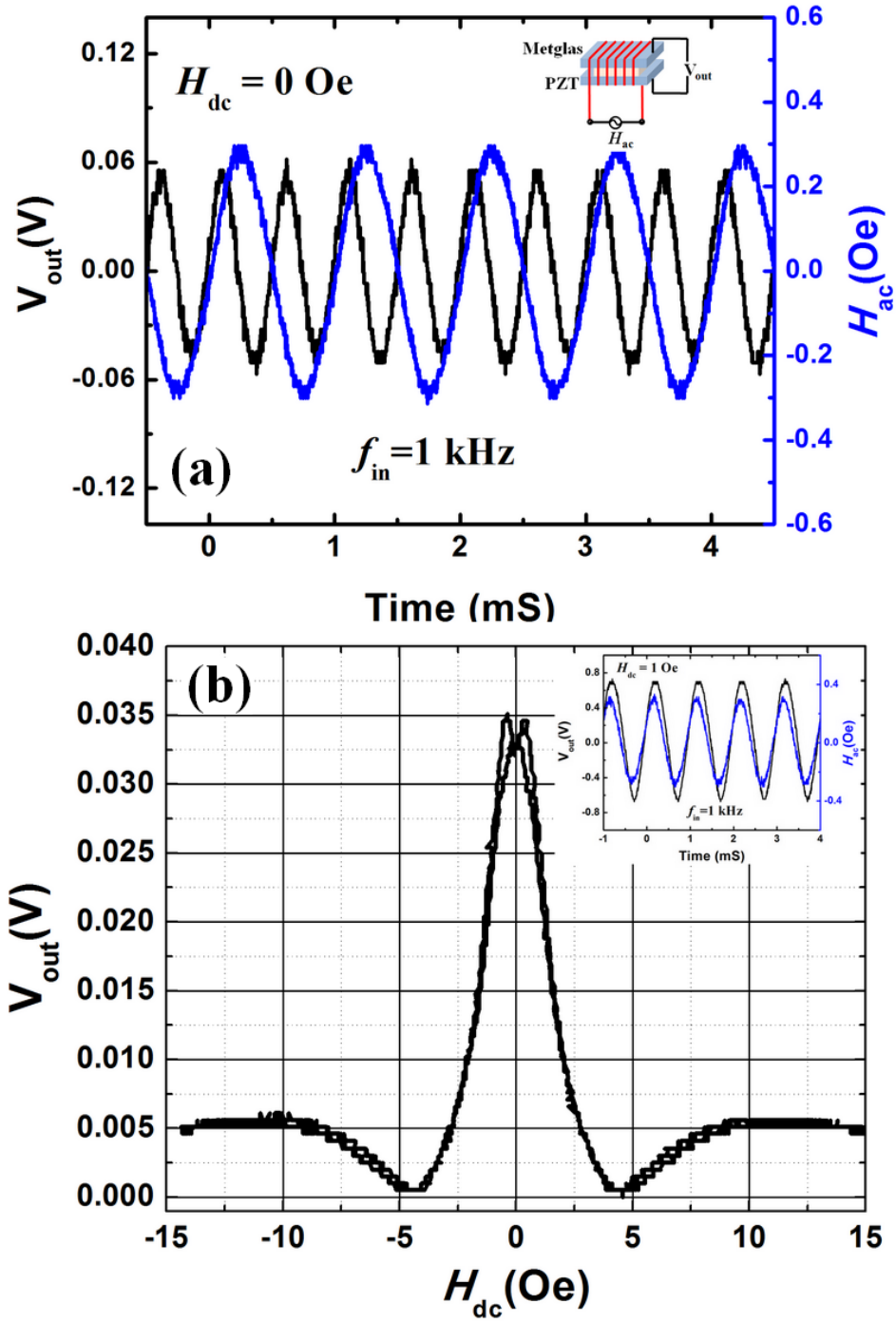

Figure 6.11 (a) Waveforms of driving ac magnetic field and output signal in time domain; and (b) induced frequency doubling signal as a function of dc magnetic bias H_{dc}. The insert shows schematic of frequency multiplier based on Metglas/PZT ME composites.

Furthermore, frequency multiplication can be achieved over a wide bandwidth below the electromechanical resonant frequency ($f_r \approx 28$ kHz), since the ME coefficient is frequency independent.[29] Considering the inductance of driving coils changed at various frequencies, the modulated ac signals were applied to the coils to generate the consistent ac magnetic fields of H_{ac}=0.2 Oe. Figure 6.12 presents the waveforms in the time domain of the output signal in response to an input signal of various frequencies between 100 Hz and 2000 Hz. Frequency doubling of near constant amplitude was found at all frequencies studied.

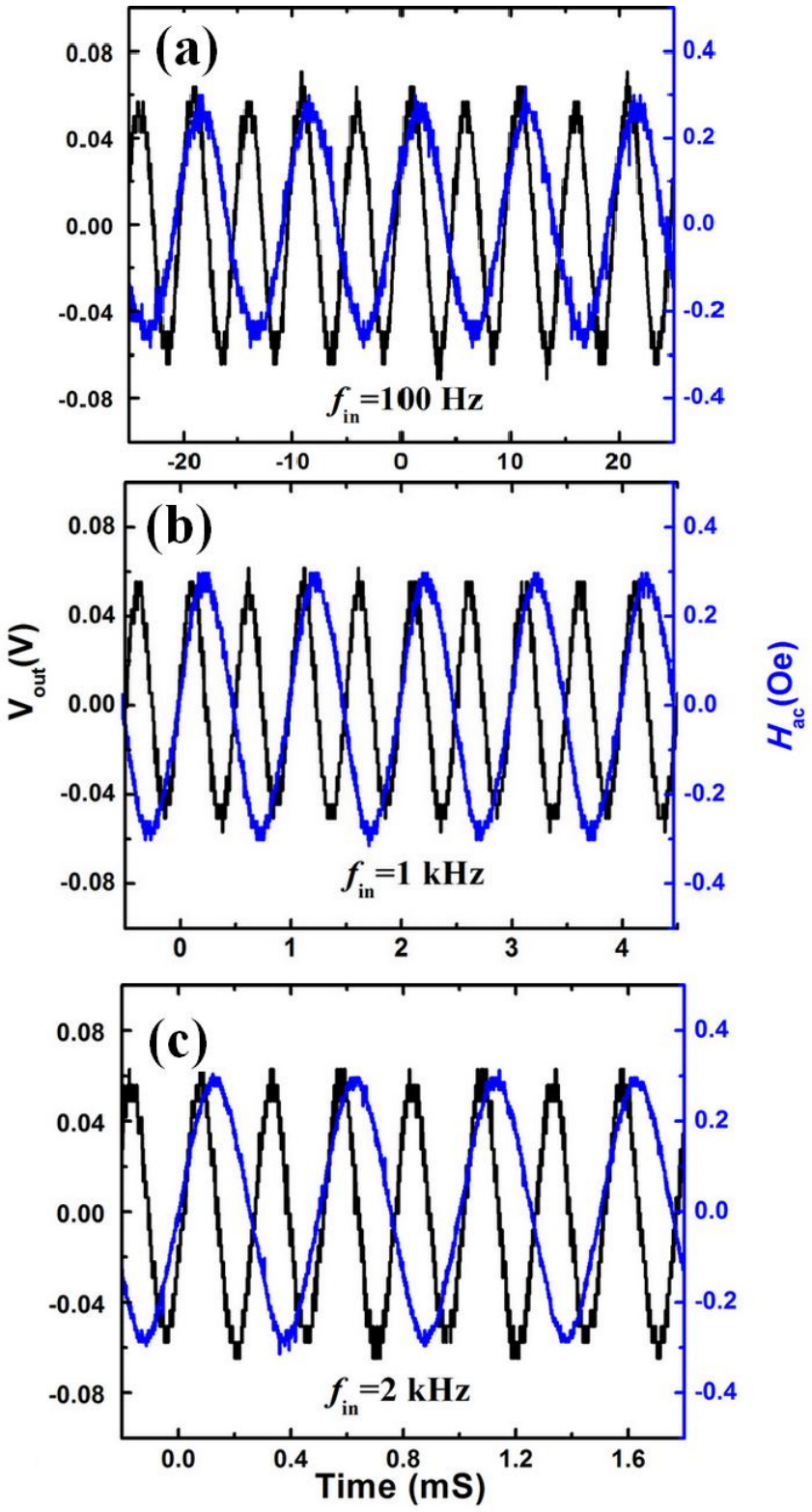

Figure 6.12 Waveforms of driving ac magnetic field and output signal in the time domain at various frequencies: (a) 100 Hz, (b) 1 kHz, and (c) 2 kHz.

Prior studies have found that the frequency doubling can be turned off by applying H_{dc} = 62 Oe.[53] However, the physical means required to apply an external field is not convenient with regards to packaging considerations. By improving magnetic flux concentration, much smaller required dc biases can be achieved, allowing adjustments in these important considerations.[89] Here, our frequency multiplier was designed to be modulated by the geomagnetic fields. Table 6.2 presents the parameters for local geomagnetic fields. It can be seen that the magnetic field intensities along different directions have significant differences, which provide an easy and natural switch for the frequency multiplier devices.

Table 6.2 Geomagnetic field intensity [a)] in the Virginia Tech area

Location	***North Component +North -South***	***East Component +East -West***	***Vertical Component +Down -Up***
Lat: 37 °13' 55" Lon: - 80 °25' 17"	21,240.4 nT	-3048.4 nT	46,756.1 nT

a) Cited from National Oceanic and Atmospheric Administration, United State

Figure 6.13 shows the geomagnetic field operated as an on-off switch for frequency multiplication. Part (a) presents a photo of the experimental setup, and the insert shows the 3-D coordinate system for the test: the east direction is along the x-axis, the north direction is along the y-axis, and the up direction is along the z-axis. We characterized the frequency multiplication along different directions, including the horizontal and vertical planes. In the horizontal plane, we defined the angle between device and north direction as θ. And we defined the angle between device and east direction as φ in vertical plane. During the test, an input H_{ac} = 0.2 Oe at f =

1 kHz was applied to the device. The output signals at frequency of 1 kHz and 2 kHz from multiplier were then monitored by dynamic signal analyzer (SR-785). Figures 3 (b) and 3 (c) show the results of the ratio of V_{2f}/V_f as function of θ and φ, respectively. In Figure 3 (b), one can see the ratio of V_{2f}/V_f along east (θ=90˚) or west (θ=270˚) directions reached maximum values (V_{2f}/V_f >8). Thus, the waveform in time domain shows the frequency multiplication, as shown in the insert of Figure 3 (b). This is the "ON" state. However, when the device was oriented along the north or south direction, the ratio of the second to first harmonics V_{2f}/V_f was approaching 1. Thus, there was no obvious frequency doubling behavior, which is the "OFF" state. Accordingly, it can be seen that the device performed in the "OFF" state as orientating at the range of -30˚ <θ < 30˚ and -150˚ <θ < 210˚, and performed in the "ON" state as placing along rest of directions in the horizontal plane. Similarly, the geomagnetic field effect in vertical plane (θ = 90˚) was also studied, as shown in Figure 3 (c). Since the magnitude of geomagnetic field in vertical direction was larger than the value in horizontal plane, the device was switched to "ON" state along east (φ=0˚) or west (φ=180˚) direction. The slight tilt can tune it to the "OFF" state. The insert shows the waveforms in time domain as φ=90˚. Thus, it can achieve a transition from "ON" to "OFF" just by using the geomagnetic field bias. One could simply develop logic between "ON" and "OFF" states by using a stage whose orientation could be rotated by an actuator. Furthermore, a simple guidance device based on frequency multiplication might be enabled which could lock onto the largest component of Earth's field, or to an object with the highest local magnetic fields.

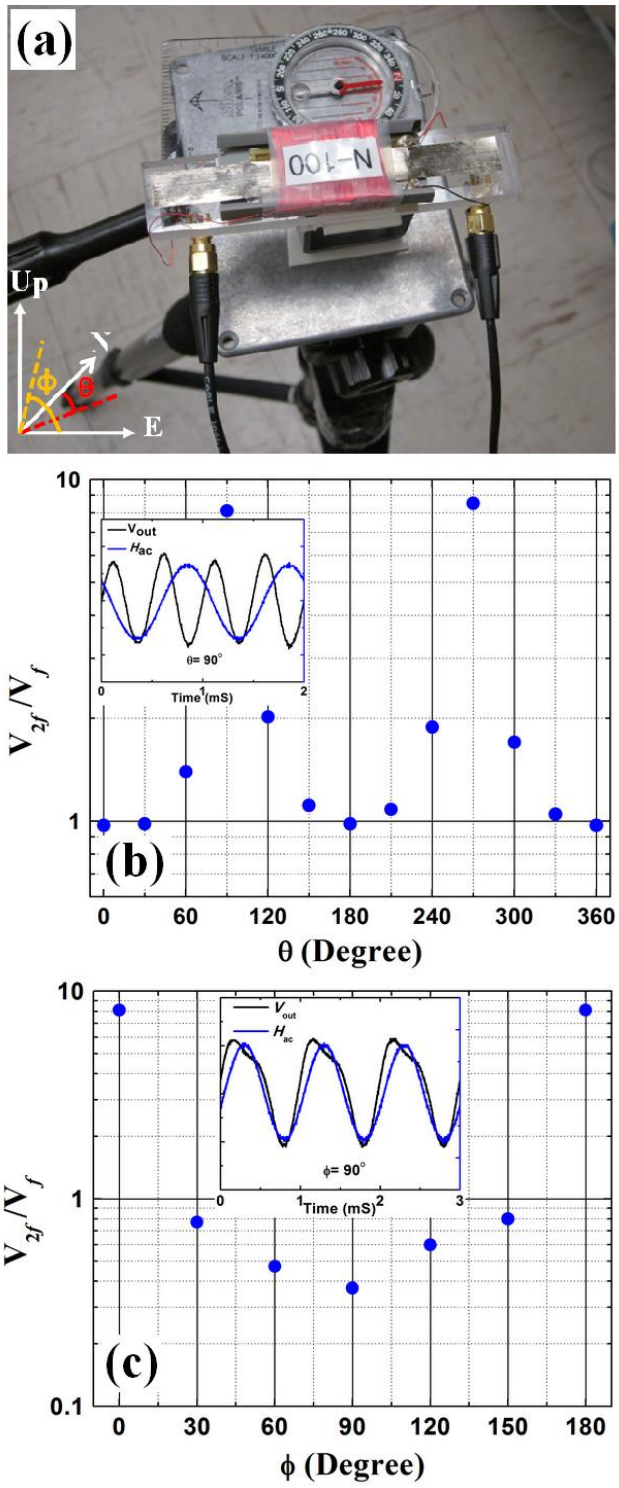

Figure 6.13 (a) Schematics of frequency multiplier under geomagnetic field; the ratio of the induced second to first harmonic signals V_{2f}/V_f along various directions: (b) in horizontal plane, and (c) in vertical plane. The inserts show the waveforms in the time domain.

Finally, the origin of frequency multiplication was studied. Previous investigations have shown the ME effect in composites was achieved through a magneto-elasto-electric interaction mediated at the interlayer boundaries.[9] Thus, induced voltage from PZT layer was directly dependent on strain transferred from Metglas layer.[53, 99] To understand the frequency multiplication in Metglas/PZT composites, we studied the effective magnetostriction coefficient (λ) as function of dc magnetic field (H_{dc}). The magnetostriction influenced by H_{dc} was characterized by a bridge module BCM-1 (Omega: Stamford, CT, USA). Figure 6.14 shows the magnetostriction and effective linear piezomagnetic coefficients. One can see that the magnetostriction was independent on the direction of the applied H_{dc} but dependent on its amplitude. During the above measurements, for H_{dc} = 0 Oe, the magnetostriction was affected by the applied H_{ac}. In response to a sine wave, both positive and negative input signals generated a strain with the same direction: thus, the induced strain had a doubled frequency multiplication. Accordingly, the output signal from the PZT layer affected by this strain has a significant second harmonic component. This can explain why the device when oriented along the east direction had significant frequency multiplication. On the other hand, the geomagnetic field intensity along the up direction is able to reach 46,000 nT (0.46 Oe): at which the effective linear piezomagnetic coefficient begins to become larger. Thus, when oriented along the north direction, the first harmonic was increased; however, the waveform exhibited significant distortion from a sine wave (see insert in Figure6.13 (c)).

In summary, a geomagnetic field tuned frequency multiplication has been studied based on Metglas/PZT tri-layered ME composites. The steady frequency multiplication arises when operated under low dc magnetic biases. The geomagnetic field can serve as a switch to control this multiplication between "ON" and "OFF" thresholds. Thus, there are potential unique applications with respect to guidance and logic.

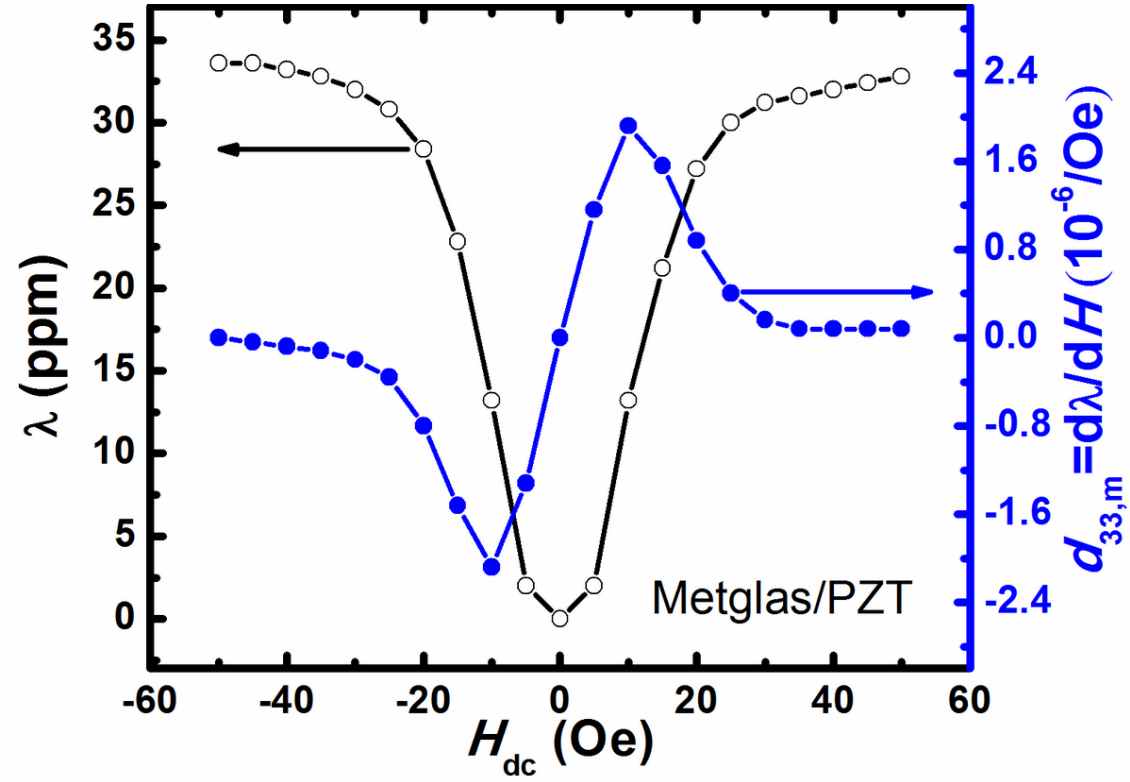

Figure 6.14 Magnetostriction and effective linear piezomagnetic coefficient for the Metglas/PZT ME composites.

6.5 Summary of this section

In this section, one bi-layered bending mode structure was proposed for Metglas/Piezo-fiber ME composites. The completely different resonant effect associated with these materials allows us to design sensors capable of working in much lower frequency ranges with higher sensitivity compared to conventional structures. Meanwhile, the resonant frequency can be tuned by simply applying the active tip mass.

In addition to the magnetic sensor, two other devices were investigated: (1) a magnetic energy harvester capable of charging a battery under resonant frequency; (2) one 60 Hz magnetic sensor designed to harvest the magnetic energy from instruments; and (3) frequency multiplication effect in ME composites is greatly dependent on the geomagnetic field. Based on these results, possible applications include the development of a frequency multiplier and/or geomagnetic guidance devices can be developed.

References

1. M. Fiebig, J Phys D Appl Phys **38** (8), R123-R152 (2005).
2. W. Eerenstein, N. D. Mathur and J. F. Scott, Nature **442** (7104), 759-765 (2006).
3. C. W. Nan, Z Metallkd **94** (10), 1148-1152 (2003).
4. M. I. Bichurin, D. A. Filippov, V. M. Petrov, V. M. Laletsin, N. Paddubnaya and G. Srinivasan, Phys Rev B **68** (13) (2003).
5. J. Ma, J. M. Hu, Z. Li and C. W. Nan, Adv Mater **23** (9), 1062-1087 (2011).
6. P. Curie, J.Physique **3**, 393 (1894).
7. D.N.Astrov, Sov. Phys. **10**, 628 (1960).
8. G. T. Rado, Phys. Rev. Lett. **7**, 310 (1961).
9. C. W. Nan, M. I. Bichurin, S. X. Dong, D. Viehland and G. Srinivasan, J Appl Phys **103** (3) (2008).
10. J. Vandenboomgaard, A. M. J. G. Vanrun and J. Vansuchtelen, Ferroelectrics **14** (1-2), 727-728 (1976).
11. C. W. Nan, M. Li and J. H. Huang, Phys Rev B **63** (14) (2001).
12. J. H. Ryu, S. Priya, A. V. Carazo, K. Uchino and H. E. Kim, J Am Ceram Soc **84** (12), 2905-2908 (2001).
13. S. X. Dong, J. R. Cheng, J. F. Li and D. Viehland, Appl Phys Lett **83** (23), 4812-4814 (2003).
14. G. Srinivasan, E. T. Rasmussen, J. Gallegos, R. Srinivasan, Y. I. Bokhan and V. M. Laletin, Phys Rev B **64** (21), art. no.-214408 (2001).
15. G. Srinivasan, E. T. Rasmussen, J. Gallegos, R. Srinivasan, Y. I. Bokhan and V. M. Laletin, Phys Rev B **66** (2) (2002).
16. S. Dong, J. Zhai, F. Bai, J. F. Li and D. Viehland, Appl Phys Lett **87** (6) (2005).
17. J. Y. Zhai, N. Cai, Z. Shi, Y. H. Lin and C. W. Nan, J Appl Phys **95** (10), 5685-5690 (2004).
18. J. P. Zhou, H. C. He, Z. Shi, G. Liu and C. W. Nan, J Appl Phys **100** (9) (2006).
19. I. V. Lisnevskaya, I. A. Bobrova, E. A. Bikyashev and T. G. Lupeiko, Inorg Mater+ **42** (10), 1147-1151 (2006).
20. S. X. Dong, J. F. Li and D. Viehland, Ieee T Ultrason Ferr **51** (7), 794-799 (2004).
21. J. Y. Zhai, S. X. Dong, Z. P. Xing, J. F. Li and D. Viehland, Appl Phys Lett **89** (8) (2006).
22. S. X. Dong, J. Y. Zhai, J. F. Li and D. Viehland, Appl Phys Lett **89** (12) (2006).
23. R. A. Islam and S. Priya, J Mater Sci **43** (10), 3560-3568 (2008).
24. R. A. Islam, Y. Ni, A. G. Khachaturyan and S. Priya, J Appl Phys **104** (4) (2008).
25. J. Ryu, S. Priya, K. Uchino and H. E. Kim, J Electroceram **8** (2), 107-119 (2002).
26. K. Mori and M. Wuttig, Appl Phys Lett **81** (1), 100-101 (2002).
27. S. X. Dong, J. Y. Zhai, J. F. Li and D. Viehland, Appl Phys Lett **89** (25) (2006).
28. J. Zhai, Z. Xing, S. Dong, J. Li and D. Viehland, J Am Ceram Soc **91** (2), 351-358 (2008).
29. J. Q. Gao, Y. Shen, Y. J. Wang, P. Finkel, J. F. Li and D. Viehland, Ieee T Ultrason Ferr **58** (8), 1545-1549 (2011).

30. L. Y. Fetisov, N. S. Perov, Y. K. Fetisov, G. Srinivasan and V. M. Petrov, J Appl Phys **109** (5) (2011).
31. Z. P. Xing, S. X. Dong, J. Y. Zhai, L. Yan, J. F. Li and D. Viehland, Appl Phys Lett **89** (11) (2006).
32. P. Finkel, J. Bonini, E. Garrity, K. Bussman, J. Gao, J. F. Li, S. E. Lofland and D. Viehland, Appl Phys Lett **98** (9) (2011).
33. S. K. Mandal, G. Sreenivasulu, V. M. Petrov and G. Srinivasan, Phys Rev B **84** (1) (2011).
34. S. C. Yang, K. H. Cho, C. S. Park and S. Priya, Appl Phys Lett **99** (20) (2011).
35. J. Y. Zhai, S. X. Dong, Z. P. Xing, J. F. Li and D. Viehland, Appl Phys Lett **91** (12) (2007).
36. V. Bedekar, M. I. Bichurin, S. N. Ivanov, Y. J. Pukinski and S. Priya, Rev Sci Instrum **81** (3) (2010).
37. J. M. Hu, Z. Li, J. Wang and C. W. Nan, J Appl Phys **107** (9) (2010).
38. J. M. Hu, Z. Li, Y. H. Lin and C. W. Nan, Phys Status Solidi-R **4** (5-6), 106-108 (2010).
39. P. Li, Y. M. Wen, C. B. Jia and X. S. Li, Ieee T Ind Electron **58** (7), 2944-2951 (2011).
40. S. D. Moss, J. E. McLeod, I. G. Powlesland and S. C. Galea, Sensor Actuat a-Phys **175**, 165-168 (2012).
41. Y. J. Wang, C. M. Leung, F. F. Wang, S. W. Or, X. Y. Zhao and H. S. Luo, J Phys D Appl Phys **42** (13) (2009).
42. M. N. Baibich, J. M. Broto, A. Fert, F. N. Vandau, F. Petroff, P. Eitenne, G. Creuzet, A. Friederich and J. Chazelas, Phys Rev Lett **61** (21), 2472-2475 (1988).
43. K. Shirae, Ieee T Magn **20** (5), 1299-1301 (1984).
44. H. J. Barthelmess, M. Halverscheid, B. Schiefenhovel, E. Heim, M. Schilling and R. Zimmermann, Ieee T Appl Supercon **11** (1), 657-660 (2001).
45. Z. P. Xing, J. Y. Zhai, S. X. Dong, J. F. Li, D. Viehland and W. G. Odendaal, Meas Sci Technol **19** (1) (2008).
46. J. Y. Zhai, Z. P. Xing, S. X. Dong, J. F. Li and D. Viehland, Appl Phys Lett **88** (6) (2006).
47. S. X. Dong, J. Y. Zhai, J. F. Li and D. Viehland, Appl Phys Lett **88** (8) (2006).
48. S. X. Dong, J. Y. Zhai, J. F. Li, D. Viehland and S. Priya, Appl Phys Lett **93** (10) (2008).
49. X. Z. Dai, Y. M. Wen, P. Li, J. Yang and X. F. Jiang, Acta Phys Sin-Ch Ed **59** (3), 2137-2146 (2010).
50. X. Z. Dai, Y. M. Wen, P. Li, J. Yang and M. Li, Sensor Actuat a-Phys **166** (1), 94-101 (2011).
51. S. X. Dong, J. F. Li and D. Viehland, J Mater Sci **41** (1), 97-106 (2006).
52. J. Zhai, J. Gao, C. De Vreugd, J. Li, D. Viehland, A. V. Filippov, M. I. Bichurin, D. V. Drozdov, G. A. Semenov and S. X. Dong, Eur Phys J B **71** (3), 383-385 (2009).
53. J. Ma, Z. Li, Y. H. Lin and C. W. Nan, J Magn Magn Mater **323** (1), 101-103 (2011).
54. W. H. Zhang, G. Yin, J. W. Cao, J. M. Bai and F. L. Wei, Appl Phys Lett **100** (3) (2012).
55. S. Franco, (2002).
56. R. W. Whatmore, Rep Prog Phys **49** (12), 1335-1386 (1986).
57. J. Y. Zhai, Z. P. Xing, S. X. Dong, J. F. Li and D. Viehland, Appl Phys Lett **93** (7) (2008).

58. Z. P. Xing, J. Y. Zhai, J. F. Li and D. Viehland, J Appl Phys **106** (2) (2009).
59. W.O.Henry, (1988).
60. W. M. Leach, P Ieee **82** (10), 1515-1538 (1994).
61. M. S. Keshner, P Ieee **70** (3), 212-218 (1982).
62. J. B. Johnson, IEEE Spectr. **8**, 42 (1971).
63. D. Abbott, B. R. Davis, N. J. Phillips and K. Eshraghian, Ieee T Educ **39** (1), 1-13 (1996).
64. Z. P. Xing, J. F. Li and D. Viehland, Appl Phys Lett **91** (14) (2007).
65. Z. P. Xing, J. F. Li and D. Viehland, Appl Phys Lett **91** (18) (2007).
66. Z. P. Xing, J. Y. Zhai, J. Q. Gao, J. F. Li and D. Viehland, Ieee Electr Device L **30** (5), 445-447 (2009).
67. T. Egami, Rep Prog Phys **47** (12), 1601-1725 (1984).
68. R. Roy and A. K. Majumdar, J Magn Magn Mater **25** (1), 83-89 (1981).
69. S. X. Dong, J. Y. Zhai, Z. P. Xing, J. F. Li and D. Viehland, Appl Phys Lett **91** (2) (2007).
70. D. Zhou, F. F. Wang, L. H. Luo, J. Chen, W. W. Ge, X. Y. Zhao and H. S. Luo, J Phys D Appl Phys **41** (18) (2008).
71. Y. J. Wang, D. Gray, D. Berry, J. Q. Gao, M. H. Li, J. F. Li and D. Viehland, Adv Mater **23** (35), 4111-+ (2011).
72. C. R. Bowen, L. J. Nelson, R. Stevens, M. G. Cain and M. Stewart, J Electroceram **16** (4), 263-269 (2006).
73. J. Q. Gao, D. Hasanyan, Y. Shen, Y. J. Wang, J. F. Li and D. Viehland, J Appl Phys **112** (10) (2012).
74. M. Li, D. Hasanyan, Y. Wang, J. Gao, J. Li and D. Viehland, J Phys D Appl Phys **45** (35) (2012).
75. M. H. Li, D. Berry, J. Das, D. Gray, J. F. Li and D. Viehland, J Am Ceram Soc **94** (11), 3738-3741 (2011).
76. Y. D. Yang, J. Q. Gao, Z. G. Wang, M. H. Li, J. F. Li, J. Das and D. Viehland, Mater Res Bull **46** (2), 266-270 (2011).
77. C. Modzelewski, H. T. Savage, L. T. Kabacoff and A. E. Clark, Ieee T Magn **17** (6), 2837-2839 (1981).
78. J. Q. Gao, J. Y. Zhai, Y. Shen, L. G. Shen, D. Gray, J. F. Li, P. Finkel and D. Viehland, Ieee T Ultrason Ferr **58** (8), 1541-1544 (2011).
79. J. Q. Gao, J. Das, Z. P. Xing, J. F. Li and D. Viehland, J Appl Phys **108** (8) (2010).
80. J. Vrba and S. E. Robinson, Methods **25** (2), 249-271 (2001).
81. J. Q. Gao, Z. G. Wang, Y. Shen, M. H. Li, Y. J. Wang, P. Finkel, J. F. Li and D. Viehland, Mater Lett **82**, 178-180 (2012).
82. J. Q. Gao, Y. J. Wang, M. H. Li, Y. Shen, J. F. Li and D. Viehland, Mater Lett **85**, 84-87 (2012).
83. X. Zhuang, C. Cordier, S. Saez, M. L. C. Sing, C. Dolabdjian, J. Gao, J. F. Li and D. Viehland, J Appl Phys **109** (12) (2011).
84. X. Zhuang, M. L. C. Sing, C. Cordier, S. Saez, C. Dolabdjian, J. Das, J. Q. Gao, J. F. Li and D. Viehland, Ieee Sens J **11** (10), 2183-2188 (2011).
85. Y. Shen, J. Gao, L. Shen, D. Gray, J. Li, P. Finkel, D. Viehland, X. Zhuang, S. Saez and C. Dolabdjian, Sensor Actuat a-Phys **171** (2), 63-68 (2011).
86. S. Marauska, R. Jahns, C. Kirchhof, M. Claus, E. Quandt, R. Knochel and B. Wagner, Sensor Actuat a-Phys **189**, 321-327 (2013).
87. L. G. Shen, M. H. Li, J. Q. Gao, Y. Shen, J. F. Li, D. Viehland, X. Zhuang, M. L. C. Sing, C. Cordier, S. Saez and C. Dolabdjian, J Appl Phys **110** (11) (2011).
88. X. Zhuang, M. L. C. Sing, C. Cordier, S. Saez, C. Dolabdjian, L. G. Shen, J. F. Li, M. H. Li and D. Viehland, Ieee Sens J **11** (10), 2266-2272 (2011).

89. J. Q. Gao, D. Gray, Y. Shen, J. F. Li and D. Viehland, Appl Phys Lett **99** (15) (2011).
90. Y. Shen, J. Q. Gao, D. Hasanyan, Y. J. Wang, M. H. Li, J. F. Li and D. Viehland, Smart Mater Struct **21** (11) (2012).
91. J. M. Hu, Z. Li, J. Wang, J. Ma, Y. H. Lin and C. W. Nan, J Appl Phys **108** (4) (2010).
92. Y. Shen, J. Q. Gao, Y. J. Wang, J. F. Li and D. Viehland, Appl Phys Lett **100** (17) (2012).
93. J. Q. Gao, L. G. Shen, Y. J. Wang, D. Gray, J. F. Li and D. Viehland, J Appl Phys **109** (7) (2011).
94. J. Das, J. Gao, Z. Xing, J. F. Li and D. Viehland, Appl Phys Lett **95** (9) (2009).
95. C. S. Park, D. Avirovik, S. Bressers and S. Priya, Appl Phys Lett **98** (6) (2011).
96. M. Zeng, S. W. Or and H. L. W. Chan, Appl Phys Lett **96** (20) (2010).
97. M. I. Bichurin, V. M. Petrov and G. Srinivasan, Phys Rev B **68** (5) (2003).
98. Y. J. Wang, D. Hasanyan, M. H. Li, J. Q. Gao, J. F. Li, D. Viehland and H. S. Luo, J Appl Phys **111** (12) (2012).
99. K. E. Kamentsev, Y. K. Fetisov and G. Srinivasana, Appl Phys Lett **89** (14) (2006).